Concurrent Modelling and Experimental Analysis
of Meso-Scale Strain Fields and Damage in Woven Composites
under Static and Fatigue Tensile Loading

Gecombineerd numeriek en experimenteel onderzoek
van de rekvelden en schade op meso-schaal in textielcomposieten
onder statische en cyclische trekbelasting

Subbareddy Daggumati

UNIVERSITEIT
GENT

Promoters:

Prof. dr. ir. Wim Van Paepegem
Ghent University
Faculty of Engineering and Architecture
Department of Materials Science and Engineering

Prof. dr. ir. Joris Degrieck
Ghent University
Faculty of Engineering and Architecture
Department of Materials Science and Engineering

Examination Committee:

Prof. Ronny Verhoeven (chairman)	Ghent University
Prof. Paul Kiekens (secretary)	Ghent University
Prof. Wim Van Paepegem	Ghent University
Prof. Joris Degrieck	Ghent University
Prof. Benedict Verhegghe	Ghent University
Prof. Stepan Vladimirovich Lomov	K.U.Leuven
Prof. Ignaas Verpoest	K.U.Leuven
Dr. Sebastiaan Wijskamp	TenCate Advanced Composites, The Netherlands
Prof. Christian Hochard	University de Marseille, France

Research Institute:

Ghent University
Department of Materials Science and Engineering
Sint-Pietersnieuwstraat 41
B9000 Ghent, Belgium

ACKNOWLEDGEMENTS

Summary

The growing usage of textile reinforced composites in advanced structural applications demands the detailed investigation of their structural response under the applied static and fatigue loads. In comparison to the labor intensive and time consuming experimental testing, detailed structural analysis within the framework of multiscale modeling using Representative Unit Cell (RUC) Finite Element (FE) analysis proves to be a valuable technique. Although many researchers tried to develop the RUC based meso-FE analysis procedure for predicting the progressive damage behavior in textile composites, there lacks a suitable experimental validation at each and every stage of the meso-FE analysis development procedure. And hence there lacks a unified procedure for predicting the damage initiation and progression in textile composites. As it is well known that the applied external tensile load (static and fatigue) causes the reduction in the composite macroscopic stiffness, triggered by the progressive failure (local) of the composite constituents. In this regard, predicting the progressive failure of the composite constituents through meso-FE simulations highly depends on the accurate prediction of the local stress (strain) and damage locations in the RUC.

In view of the ultimate goal of predicting the progressive damage behavior of textile reinforced composites based on the RUC meso-FE simulations, a systematic approach is employed in the current research work with the following objectives: i) as observed in the experimental local strain analysis, predicting the local strain profiles and their spatial distribution using RUC meso-FE simulations; ii) prediction of the local damage initiation strain as well as the damage locations in the RUC, which are in correlation with the experimental observations; iii) developing an accurate numerical procedure requires a thorough understanding of the material and structural behavior. Hence, it is aimed to investigate the composite structural response using various experimental techniques under static and fatigue loads. In addition, the obtained experimental results set a benchmark for the numerical meso-FE analysis. Later, the developed meso-FE analysis procedure can be extended to the ultimate goal of progressive damage prediction using RUC FE simulations. For the numerical meso-FE analysis and subsequent experimental validation purpose, a thermoplastic carbon-PPS (PolyPhenylene Sulfide) 5-harness satin weave composite (CETEX$^®$) is used.

In the current research work, the developing process of the RUC meso-FE analysis procedure starts with validating the obtained numerical local strain profiles against the experimental full-field (Digital Image Correlation) strain profiles obtained under uni-axial static tensile load.

Comparison between the experimental and numerical strain profiles indicates that, the existing single RUC FE analysis procedure must be changed to predict the local surface strain profiles and their spatial distribution as observed in the experiments. This is due to the fact that the RUC with infinite laminate conditions is unable to represent the adjacent ply interaction, and hence unable to compute the spatial strain distribution as observed in the experiments. Moreover, instead of having a single strain profile from the numerical predictions to compare with the experimental strain profiles that are obtained from a randomly stacked (stochastic) laminate, different RUC stacking configurations are developed for the FE analysis. From the FE simulations of the aforementioned RUC stacks, the upper and lower bounds for the experimental strain are computed. In addition, the FE analysis of different RUC stacks indicates that the local strain profiles are sensitive to the stacking sequence as well as to the applied boundary conditions.

After comprehensive analysis of the heterogeneous local strain profiles and their spatial distribution, the RUC FE simulation procedure is extended to the local damage analysis. Initially, experimental damage analysis is conducted on the satin weave composite. Both experimental damage monitoring techniques (acoustic emission and microscopic analysis) used for detecting the crack initiation as well as progression during the static tensile test indicate that the damage initiation in the satin weave composite is a sequential process. Further complicating the structural analysis procedure, the experimental damage analysis reveals that the damage initiation in the plies of a satin weave composite depends on the ply placement in the laminate, indicating the component(s) of stress that causes the damage initiation varies over the laminate cross-section. Initial damage events in the satin weave composite are detected in the laminate inner layers, followed by the damage initiation on the surface layers. In order to investigate the observed experimental sequential damage and the responsible stress components, numerical damage analysis is conducted using different RUC stacks. Meso-FE damage analysis and the subsequent local stress and deformation analysis at the damage regions reveals that: i) local ply deformation in the satin weave laminate varies according to the ply placement in the laminate (local ply constraints); ii) according to the local deformation behavior, the stress components that cause the damage in the laminate inner layers vary substantially compared to the outer layers. In the above said terms, analysis of the detailed local structural response using primary variable (displacement) and derivatives (stress, strain), a unified knowledge is achieved regarding the sequential damage initiation process in the plies of a satin weave composite.

However, the observed experimental microscopic damage (weft yarn) in the satin weave composite under uni-axial static tensile load does not decrease the composite macroscopic stiffness. Instead, progressive composite stiffening is observed starting from the beginning of the load process until the composite final failure.

As an extension to the static damage analysis, experimental tension-tension fatigue damage analysis is conducted on the satin weave composite. The composite macroscopic stiffness is monitored throughout the fatigue testing process. In addition, according to the observed change in the composite stiffness (macro-scale), the damage events that are initiating at different time intervals of the fatigue life of the composite are monitored. At higher tensile loads (larger than 65% of ultimate static tensile strength), the reduction in longitudinal stiffness of the composite specimen occurs in the first one hundred thousand cycles. Consequently, microscopic analysis indicates that the composite specimen sustains the fibre breaks as well as meta-delimitations. The other damage mechanisms such as interply delaminations are detected at the later stages of the fatigue test. Moreover, residual strength analysis of the fatigue tested satin weave composite specimens indicates that the induced fatigue damage does not show any influence on the ultimate tensile strength of the composite specimen. Similar to the static case, the residual stress-strain analysis of the fatigue tested composite specimens indicates the substantial stiffening of the composite specimen.

Finally, the possible reasons for the satin weave composite stiffening are explored from the material as well as the geometrical point of view. Detailed structural analysis leads to the conclusion that the observed non-Hookean stress-strain behavior of the carbon-PPS satin weave composite can be attributed to: i) stiffening of the load carrying carbon fibres under external tensile load (non-Hookean material); ii) increased straightening of the warp yarns due to the meta-delaminations caused by the fatigue load.

Samenvatting (Summary in Dutch)

Het toenemend gebruik van textielvezelversterkte composietmaterialen in structurele toepassingen vereist ook een gedetailleerde studie van hun mechanische respons onder statische en cyclische belasting. In vergelijking met het intensieve karakter van experimentele testen, kan structurele numerieke analyse in het kader van multischaalmodellering een zeer bruikbaar instrument zijn. Daarbij wordt dan typisch gebruik gemaakt van eindige-elementenmodellen van een Representatieve Eenheidscel (E: Representative Unit Cell (RUC)). Heel wat onderzoekers hebben reeds gebruik gemaakt van eindige-elementenmodellering van dergelijke eenheidscellen op meso-schaal, om het progressief faalgedrag van textielcomposieten te voorspellen. Toch ontbreekt het nog aan een grondige experimentele validering van deze modellering op meso-schaal in al haar stappen: van beschrijving van geometrie, over randvoorwaarden, naar voorspelde rekken, schadepatronen en spanningen. Momenteel ontbreekt het dan ook aan een generieke procedure voor voorspelling van schade-initiatie en –propagatie in textielcomposieten. Verder is het bekend dat de extern aangelegde belasting (statisch of vermoeiing) kan leiden tot een afname in de macroscopische stijfheid, als gevolg van het progressief lokaal falen van de individuele componenten. De voorspelling van het progressief falen van textielcomposieten m.b.v. eindige-elementenmodellering op meso-schaal hangt dan ook sterk af van de accurate voorspelling van de lokale spanning/rek en schade-lokaties in de eenheidscel.

Om dit finale doel van simulatie van progressief faalgedrag van textielcomposieten op meso-schaal te bereiken, zijn een aantal stappen in de modellering cruciaal, en deze vormen precies het doel van dit doctoraatsonderzoek: (i) voorspelling van de lokale rekpatronen en hun spatiale verdeling in de eenheidscel, in overeenstemming met experimentele rekmetingen, (ii) voorspelling van de lokale rek voor schade-initiatie en van de schade-lokaties in de eenheidscel, die in overeenstemming zijn met experimentele waarnemingen, en (iii) ontwikkeling van een numerieke procedure voor de berekening van de structurele respons van textielcomposieten. De nauwe koppeling tussen eindige-elementenmodellering op meso-schaal en de experimentele validering moet toelaten om de ontwikkelde procedures voor mesoschaalmodellering later uit te breiden naar progressieve schademodellering. Voor de numerieke modellering op meso-schaal en de experimentele validering is gewerkt met een textielcomposiet van polyphenyleensulfide hars met koolstof satijnweefsel als vezelversterking (CETEX®).

Het onderzoekswerk is gestart met de validering van de lokale rekpatronen die berekend worden met eindige-elementenmodellering van de eenheidscel op meso-schaal. Daartoe werden de rekvelden opgemeten in quasi-statische trektesten m.b.v. digitale beeldcorrelatie. Vergelijking tussen de experimentele en numerieke rekvelden toont aan dat de bestaande procedure met één enkele eenheidscel op

meso-schaal niet voldoet om de rekvelden aan het oppervlak en hun spatiale verdeling correct te voorspellen. Dit is te wijten aan het feit dat de eenheidscel met periodische randvoorwaarden in de drie richtingen geen rekening houdt met de interactie van de lagen onderling, en de vrijere vervorming van de lagen aan het oppervlak. In plaats van de simulatie van één enkele eenheidscel met periodische randvoorwaarden, is het aangewezen om verschillende stapelingen van eenheidscellen te simuleren. Uit deze simulaties van stapelingen van eenheidscellen kunnen de onder- en bovengrenzen voor de experimentele rekwaarden berekend worden. Bovendien geven deze eindige-elementensimulaties aan dat de lokale rekvelden gevoelig zijn voor de stapeling en de toegepaste randvoorwaarden.

Vervolgens zijn de numerieke simulaties uitgebreid naar de lokale schade-analyse. Daartoe werden experimenten uitgevoerd op het koolstof/PPS composiet. Akoestische emissie en microscopische beeldvorming werden gebruikt voor het bepalen van de lokaties van schade-initiatie en –propagatie tijdens een statische trektest. Beide technieken geven aan dat de schade-initiatie in een textielcomposiet een sequentieel proces is. Verder is ook duidelijk dat de schade-initiatie in de afzonderlijke lagen van het textielcomposiet afhangt van de positie van de laag binnen het laminaat, wat er op wijst dat het aandeel van de verschillende spanningscomponenten dat de schade veroorzaakt, wijzigt doorheen de lagen van het laminaat. Schade wordt eerst gedetecteerd in de binnenste lagen van het laminaat, en pas nadien treedt initiatie op in de buitenste lagen van het laminaat. Om de geobserveerde sequentiële schade te simuleren, worden opnieuw simulaties uitgevoerd met een stapeling van eenheidscellen. Analyse van de lokale spanningen en vervormingen op meso-schaal leert dat (i) de lokale vervorming van de lagen in het textielcomposiet varieert naargelang de lokale positie van de lagen binnen het laminaat, en (ii) de lokale spanningscomponenten die de schade veroorzaken, zijn verschillend voor de binnenste en buitenste lagen van het laminaat. De gecombineerde analyse van lokale vervormingen, spanningen en rekken binnen de stapeling van eenheidscellen levert belangrijke inzichten in het sequentieel schadeproces in de lagen van een textielcomposiet.

Niettegenstaande de duidelijk waarneembare schade in de inslagbundels van het textielcomposiet onder statische trekbelasting, neemt de macroscopische stijfheid in de langsrichting niet af. In tegendeel, progressieve toename van de stijfheid wordt waargenomen tijdens verhoging van de aangelegde belasting.

Tenslotte zijn vermoeiingsproeven in trek-trek uitgevoerd op hetzelfde koolstof/PPS textielcomposiet, als uitbreiding t.o.v. de statische experimenten. De evolutie van de macroscopische stijfheid wordt continu opgevolgd tijdens de vermoeiingstesten. Daarnaast wordt m.b.v. microscopische inspectie de evolutie van de microscopische schademechanismen opgevolgd. Bij hogere amplitudes van de vermoeiingsbelasting treedt een reductie op van de longitudinale stijfheid in de eerste honderdduizend belastingscycli. De microscopische beelden tonen ook de aanwezigheid van lokale vezelbreuk en meta-delaminaties. Andere schademechanismen zoals delaminatie tussen verschillende lagen treden op in een later stadium van de vermoeiingstesten. Statische bepaling van de residuele sterkte na de vermoeiingstesten toont aan dat de sterkte na vermoeiing niet daalt, en dat, in analogie met de statische testen, de stijfheid progressief toeneemt tijdens het oplopen van de statische belasting na vermoeiing.

De redenen voor de progressieve toename van de stijfheid in de aanwezigheid van vermoeiingsschade zijn verder onderzocht. Op basis van de experimenten, microscopische observaties en bestaande literatuur kan besloten worden dat het niet-lineair gedrag in trek van het koolstof/PPS textielcomposiet na vermoeiing kan toegeschreven worden aan twee simultane effecten: (i) verstijving van de koolstofvezels onder toenemende trekbelasting, en (ii) toenemende aligneering van de scheringbundels van de textielvezelversterking onder oplopende belasting, t.g.v. de meta-delaminaties in vermoeiing.

Curriculum

Subbareddy Daggumati was born on December 27, 1979 in Rudravaram, India. In 2005 he received his M.Sc. degree in Computational Engineering from the RUHR University in Bochum, Germany. Shortly after his return to India he started to work as a finite element analysis engineer in Robert Bosch India LTD. However, with the interest in the field of advanced composite materials, he started his research work in the department of Materials Science and Engineering at Ghent University in April 2007. The work presented in this dissertation has been performed under the guidance of Prof. dr. ir. W. Van Paepegem and Prof. dr. ir. J. Degrieck, in collaboration with Prof. dr. ir. S. V. Lomov and Prof. dr. ir. I. Verpoest from KULeuven. The research work has been financially supported by the PhD grant of F.W.O-Vlaanderen for the project "Micro-meso-macro-homogenization of fatigue damage models in textile composites". Subbareddy Daggumati is author of 4 publications in international journals of the Science citation index and 9 publications in international conference proceedings.

List of publications

Publications in international journals of the Science Citation Index (SCI)

[1] **Daggumati, S.,** Van Paepegem, W., De Baere, I., Degrieck, J., Xu, J., Lomov, S.V. and Verpoest, I., *Local damage in a 5-harness satin weave composite under static tension: part I - Experimental analysis*. *Composites Science and Technology*. **70**(13): p. 1926-1933. (SCI-IF: 2.901)

[2] **Daggumati, S.,** Van Paepegem, W., Degrieck, J., Xu, J., Lomov, S.V. and Verpoest, I., *Local damage in a 5-harness satin weave composite under static tension: Part II - Meso-FE modelling*. *Composites Science and Technology*. **70**(13): p. 1934-1941. (SCI-IF: 2.901)

[3] **Daggumati, S.,** Voet, E., Van Paepegem, W., Degrieck, J., Xu, J., Lomov, S.V. and Verpoest, I. (2011). *Local damage in a 5-harness satin weave composite under static tension: part I - Experimental analysis*. Accepted for *Composites Science and Technology*. (SCI-IF: 2.901)

[4] **Daggumati, S.,** Van Paepegem, W., Degrieck, J., Praet, T., Verhegghe, B., Xu, J., Lomov, S.V. and Verpoest, I. (2011). *Local strain analysis in a 5-harness satin weave composite under static tension: part II-Meso-FE analysis*. Accepted for *Composites Science and Technology*. (SCI-IF: 2.901)

Publications under preparation

[5] **Daggumati, S.,** Van Paepegem, W., De Baere, I., Degrieck, J., Xu, J., Lomov, S.V. and Verpoest, I. *Fatigue and post-fatigue stress-strain analysis of a 5-harness satin weave composite under tensile load*. To be submitted to *Composites Science and Technology*.(SCI-IF: 2.901)

[6] Xu, J., Lomov, S.V. and Verpoest, I., **Daggumati, S.,** Van Paepegem, W., Degrieck, J. A progressive fatigue damage model of textile composites on meso-scale using finite element method. submitted to *Computers & structures* (SCI-IF: 1.440)

Publications in international conference proceedings

[7] Xu, J., Lomov, S.V., Verpoest, I., **Daggumati, S.,** Van Paepegem, W. and Degrieck, J. (2009). A New Meso-scale Modelling of Static and Fatigue Damage in Woven Composite Materials with Finite Element Method. *Proceedings of the 17th International Conference on Composite Materials (ICCM-17)*, Edinburgh, United Kingdom, 27-31 July 2009.

[8] **Daggumati, S.,** Van Paepegem, W., Degrieck, J., Xu, J., Lomov, S.V. and Verpoest, I. (2009). Meso-scale modelling in thermoplastic 5-harness satin weave composite. *Proceedings of the 17th International Conference on Composite Materials (ICCM-17)*, Edinburgh, United Kingdom, 27-31 July 2009.

[9] **Daggumati, S.,** Van Paepegem, W., Degrieck, J., Xu, J., Lomov, S.V. and Verpoest, I. (2010). Meso-scale modelling in a thermoplastic 5-harness satin weave composite. *SAMPE Benelux Student Meeting*, Bergeyk, the Netherlands January 2009. *(Best presentation award)*

[10] Xu, J., Lomov, S.V., Verpoest, I., **Daggumati, S.,** Van Paepegem, W. and Degrieck, J. (2010). Progressive fatigue Damage Modelling of Textile Composite on Meso-Scale with Finite Element Method, Materials Characterization and Experimental Verification. *10th International Conference on Textile Composites (TEXCOMP10)*, Lille, France, 26-28 October, 2010.

[11] **Daggumati, S.,** Voet, E., Van Paepegem, W., Degrieck, J., Praet, T., Verhegghe, B., Xu, J., Lomov, S.V. and Verpoest, I. (2010). Effect of ply stacking on the variation in local strain and damage behaviour in a 5-harness satin weave composite. *10th International Conference on Textile Composites (TEXCOMP10)*, Lille, France, 26-28 October, 2010.

[12] Xu, J., Lomov, S.V., Verpoest, I., **Daggumati, S.,** Van Paepegem, W. and Degrieck, J. (2010). Progressive fatigue Damage Modelling of Textile Composite on Meso-Scale with Finite Element Method, Materials Characterization and Experimental Verification. *Proceedings of the 14th European Conference on Composite Materials (ECCM-14)*, June 7-10, 2010, Budapest, Hungary.

[13] **Daggumati, S.,** Voet, E., Van Paepegem, W., Degrieck, J., Praet, T., Verhegghe, B., Xu, J., Lomov, S.V. and Verpoest, I. (2010). Evaluation of local strain profiles in a satin weave composite: experimental vs. meso-FE modelling. *Proceedings of the 14th European Conference on Composite Materials (ECCM-14)*, June 7-10, 2010, Budapest, Hungary.

[14] Voet, E., **Daggumati, S.,** Luyckx, G., Van Paepegem, W., Degrieck, J., Xu, J., Lomov, S.V. and Verpoest, I. (2010). Evaluation of local strain distribution in a satin weave composite using fibre Bragg gratings. *Proceedings of the 14th European Conference on Composite Materials (ECCM-14)*, June 7-10, 2010, Budapest, Hungary.

[15] Xu, J., Lomov, S.V., Verpoest, I., **Daggumati, S.,** Van Paepegem, W. and Degrieck, J. (2010). Progressive fatigue damage modelling of textile composite on meso-scale with FE-method. *Proceedings of the SAMPE EUROPE 31st International Technical Conference*, Hotel Mercure Paris Porte de Versaille Expo, France, 12-14 April 2010.

[16] **Daggumati, S.,** Voet, E., Van Paepegem, W., Degrieck, J., Praet, T., Verhegghe, B., Xu, J., Lomov, S.V. and Verpoest, I. (2011).Local strain variation in the plies of a satin weave composite: Experimental vs. Numerical. _Photo mechanics conference,_ Brussels, Belgium, *7-9th February 2011.*

TABLE OF CONTENTS

Chapter 1

Introduction

The first part of this chapter briefly describes the background and scope of the research work. Later, it explains the problem statement of current research work. Finally, this chapter ends with a brief summary of the content of the different chapters of this manuscript.

1. 1.   Background and scope

1. 1. 1.   Background of the advanced composite materials

Although composite materials had been known in various forms throughout the history of mankind, the history of modern composites probably began in 1937 when salesmen from the Owens Corning Fibreglass Company began to sell fibreglass to interested parties around the United States. "Fibreglass had been made, almost by accident in 1930, when an engineer became intrigued by a fibre that was formed during the process of applying lettering to a glass milk bottle. The fibreglass salesmen realized that the aircraft industry was, in particular, a likely customer for this new type of material because the many small and vigorous aircraft companies seemed to be creating new aircraft designs and innovative concepts in manufacturing almost daily with many of these innovations requiring new materials. One company, Douglas Aircraft, bought the first roll of fibreglass because they believed that the fibreglass would help them to solve a production problem. They had a bottleneck in the making of metal molds for their sheet metal forming process (called hydro press forming).

Each changed aircraft design needed new molds and metal molds were expensive and had long lead times. Douglas engineers tried using cast plastic molds, but they could not withstand the forces of the forging process. Maybe if the plastic molds were reinforced with fibreglass they would be strong enough to allow at least a few parts to be made so that the new designs could be quickly verified. If the parts proved to be acceptable, then metal dies could be made for full production runs. In collaboration with Owens Corning Fibreglass, dies were made using the new fibreglass material and phenolic resin (the only resin available at the time).With that success, reinforced plastic dies for prototype parts became the standard" [1]. Nowadays, innovation in the field of fibre reinforced plastics is continuously growing and composites made of different types of fibres as well as resin materials can be found in numerous advanced structures ranging from aerospace industry to sports and recreation. The following sections of this chapter introduce different types of available fibres as well as resin materials. In addition, extended discussion is presented on advanced textile composites.

1. 2.   Fibre-reinforced plastic composites

Composite materials are engineering materials made from two or more constituent materials that remain separate and distinct at micro level while forming a single component. There are two categories of constituent materials: matrix and reinforcement. The matrix material surrounds and supports the reinforcement materials by maintaining their relative positions. Reinforcements impart their special mechanical and physical properties to enhance the matrix properties. A synergy produces material properties unavailable from the individual constituent materials.

"From the engineering point of view the most important type of composites are fibre reinforced plastics. The idea behind this kind of material is that the very high strength of various kinds of fibres of minute cross sections is exploited by embedding them in a relatively soft matrix. It thus becomes possible to manufacture materials whose strength and stiffness is comparable to that of the strongest metals and whose specific weight is as low as one third of metals" [2]. The combination of high stiffness (controls deflections and dynamic behaviour of structure) and strength (controls load carrying capability and resistance to damage of structure) with low weight makes these materials natural candidates for aerospace applications. Such applications are the chief motivation for the intense research and development activity concerning fibre reinforced materials.

1. 2. 1. a.   Different types of fibres

The most important types of reinforcing fibres are **glass fibres**, **carbon fibres** and **organic fibres** [3]. Glass fibre-reinforced plastics were among the first structural composites. Composites incorporating glass or other relatively low modulus fibres are used in many high-volume applications because of their low cost. E-glass (named for its electrical properties) accounts for most of the glass fibre production and is the most widely used reinforcement for composites. Glass/epoxy and glass/polyester composites are used extensively in applications ranging from fishing rods to storage tanks and aircraft parts. Carbon (<95% C) or graphite (>99% C) fibres are the most widely used 'advanced' fibres, and graphite/epoxy or carbon/epoxy composites are now used routinely in aerospace structures where their higher cost can be justified based on improved performance. (Poly)aramid fibres are the most widespread organic fibres. Well-known are the Kevlar®-fibres produced by DuPont. These fibres were originally developed for use in radial tires but are now more extensively used in structural applications. The density of Kevlar® is about half that of glass and its specific strength is among the highest of currently available fibres. Kevlar® also has excellent toughness, ductility, and impact resistance, unlike brittle glass or graphite fibres. Table 1-1 provides a glance of different advanced fibres, and comparison of their structural properties to the conventional metals.

Table 1-1.   Comparison of tensile strengths between various materials [4].

Material	Tensile strength (MPa)	Density (gm/cm^3)	Specific tensile strength (KN.m/kg)
Aluminum (Alloy)	600	2.70	222
Steel (martensite)	2000	7.86	254
Titanium (Alloy)	1300	4.51	288
Glass fibre (Virgin)	3400	2.60	1307
Carbon fibre (AS4)	4300	1.74	2457
Kevlar (grade 49)	3620	1.44	3619

1. 2. 1. b.   Matrix (resin) materials

In the advanced development of composite materials, the focus on the next generation has shifted from the structural fibre to the matrix materials. Resin or matrix materials used in the composite manufacturing can be divided into two major categories, thermoset and thermoplastic. Thermoset resins (epoxy, polyester…) generally come in liquid form, when mixed with a catalyst, upon curing forms a solid. Thermoset molecules crosslink with each other during curing, thus once cured, they cannot change. Thermoplastics (Polyimide, polyethylene, polypropylene...) are high molecular weight polymers which, unlike thermosetting resins, do not form a rigid three dimensional cross-linked chemical after processing. This allows thermoplastic resins to be readily re-melted and re-formed; something that cannot be achieved with the traditional thermoset resins [5]. The general advantages of the thermoplastic resins are: a) unlimited shelf life; b) short processing time; c) improved impact resistance; d) ability to be reformed and high chemical resistance. At the same time there are certain disadvantages of thermoplastic resins compared to the thermoset resins: 1) high processing temperature; 2) high pressure required to manufacture; 3) high raw material cost; 4) repairing procedures are not fully matured.

Based on the structural requirements, the fibre and matrix material are chosen and composites are manufactured. The following sections provide a short discussion of the different forms of reinforcements used in the advanced composite materials.

1. 3.   Textile preforms as a reinforcement

"The main objective of textile processing is to join two or more sets of fibres/yarns, using mechanical rather than adhesive bonding, so that a resulting dry preform can be handled, draped and mould into a finished composite" [6]. Reinforcement of these composites is formed by weaving, braiding or knitting, etc. Once textile preforms are constructed, then they are impregnated with resin or matrix material, stacked in a desired orientation, and cured to obtain a composite laminate. The interlacing fibre bundles have several advantages compared to the traditional UD composites such as increase in the intra- and inter-laminar strength, greater damage tolerance, as well as providing a possibility to produce near net shape structural components. Such capabilities are very important for producing thick laminates.

However, the above stated advantages come at the expense of some loss in the in-plane stiffness and strength, which depends on the weave architecture [7]. Textile composites have potentially better fatigue and impact resistance than laminated composites. Another benefit is in the reduction of manufacturing cost due to the part count reduction. With the above stated advantages of textile composites, "a number of structures for the Airbus A380 passenger aircraft rely on textile composites. These structures include six metre diameter dome-shaped pressure bulk head and wing trailing edge panels, both manufactured by resin film infusion (RFI) with the carbon non-crimp fabrics, wing stiffeners and spars made by RTM, the vertical tail plane by vacuum infusion (VI), and thermoplastic composite (glass/polyphenlyne sulphide) wing leading edges" [8].

1. 3. 1.   Types of textile preforms

Figure 1-1 shows the most commonly used textile preforms as reinforcement for composite manufacturing process. The following sections explain the details regarding their manufacturing, and the parameters that affect the structural properties.
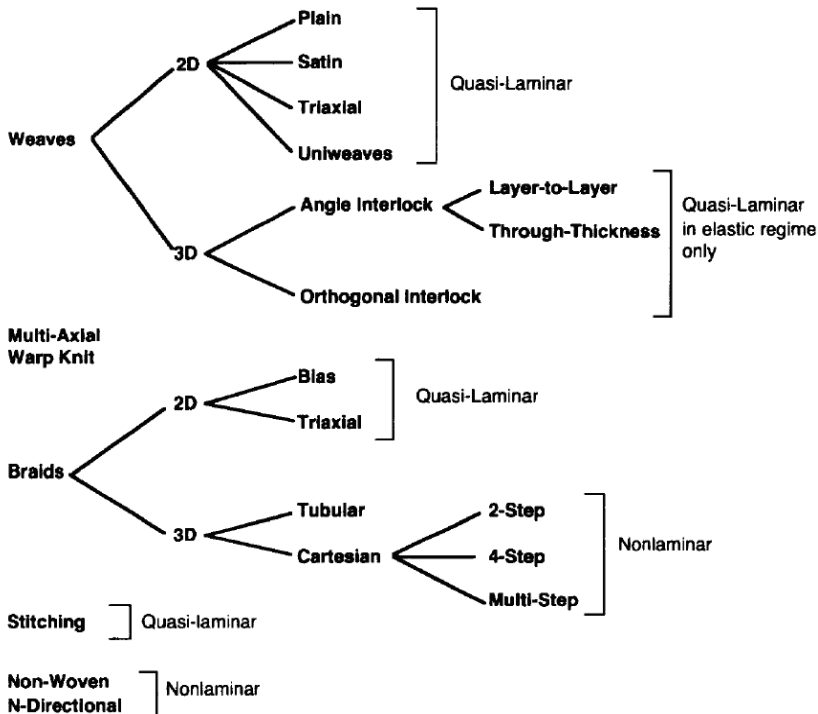
Figure. 1-1.   Classification of textile pre-forms [9].

1. 3. 1. a.   Woven composites

Woven fabrics generally consist of two sets of interlaced yarn components, known as warp and weft yarns according to the yarn orientation. Each yarn is a bundle of fibres (filaments) and its size is measured by the number of filaments in the yarn. 3D woven fabrics have additional yarns placed trough-the-thickness direction. They have higher resistance for delamination and damage tolerance than 2D woven laminates. Most of the pure and hybrid woven fabrics used in textile composites are simple 2D fundamental weaves, i.e., plain, twill, and satin weaves (Figure 1-2a-e), which are identified by the repeating patterns of the interlaced regions in the warp and weft directions.

- Plain weave is the most commonly used basic reinforcement of woven composite. In a plain woven structure, one warp yarn is repetitively woven over and under the weft yarn (Figure 1-2a).

- Twill weave has a looser interlacing and the weave is characterized by a diagonal line. In twill weave structure, each warp yarn floats ($2/2$) over two consecutive weft yarns (Figure 1-2b).

- In satin weave, one warp yarn is woven over successive weft yarns, and then under one weft yarn. This weave structure, with interlaced regions that are not connected, is called harness satin weave (Figure 1-2c-e).

a)
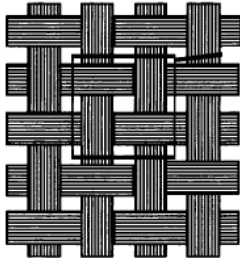
b)
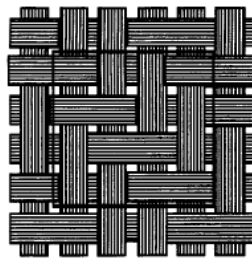
c)
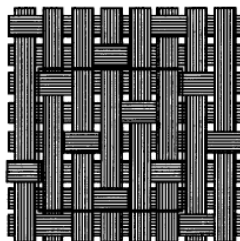
d)
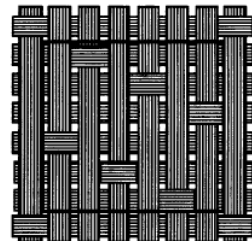
e)
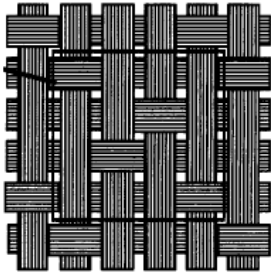
Figure. 1-2. **Schematics of common 2D weaves: a) plain weave; b)** $2/2$ **twill weave; c) 5 harness satin weave; d) 8 harness satin weave; e) crows-foot satin weave [10].**

Mechanical properties of woven composites are generally controlled by: (1) weave parameters such as weave architecture, yarn size, yarn spacing, fibre orientation angle, and fibre volume fraction; (2) laminate parameters such as stacking orientation and overall fibre volume fraction. In addition to the aforementioned parameters, yarn crimp is another important parameter that directly controls the textile composite mechanical properties. It is defined as the difference in length of the stretched yarn to the crimped yarn (Δl) over the entire length of the stretched yarn ($l + \Delta l$) [11]. Figure 1-3 shows the parameters related to the definitions of distances for defining the fibre architectures in single woven layer.
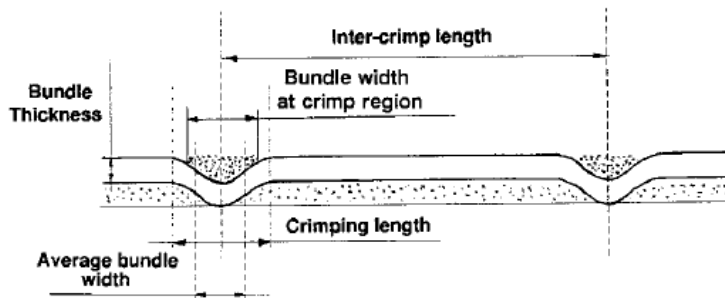
Figure. 1-3. **Parameters related to the weave architecture in woven composite [12].**

l - length of the crimped yarn
Δl - difference in the length between the stretched yarn to the crimped yarn

1. 3. 1. b.   Braided composites

Braided fabrics are constructed by orthogonally interlacing two or more sets of yarns to form an integral structure. One set of yarns are called axial yarns while the others are braiding yarns. Hence the structure of braided fabric consists of parallel axial yarns, interconnected with braided yarns that are placed along the complex spatial orientations (Figure 1-4).

The major parameters affecting the mechanical properties of a braided fabric include: (1) braid parameters such as braid architecture, yarn sizes, yarn spacing length, fibre volume fraction and fibre orientation angle, and (2) material parameters such as mechanical properties of fibres and matrix.
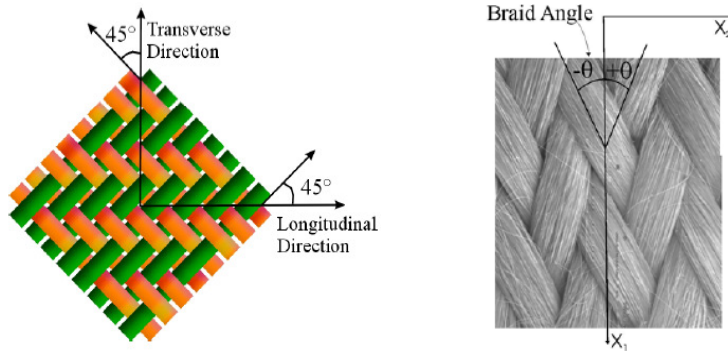
Figure. 1-4.   2D braided composite [10].

1. 3. 1. c.   Knitted composites

Knitted fabrics are characterized by their interlocking loop of yarns. Generally knitted fabrics can be divided into 2 types, i.e., the weft-knitted and warp-knitted fabric composites (Figure 1-5). In the weft-knitted fabric, the yarns run width-wise, and loops are formed by a single weft yarn. A row of loops in the longitudinal direction is called wale or warp, and that in the width direction is named as course or weft. In warp-knitted fabric, overlaps in alternative courses are produced with one thread crossing between adjacent wales in which loops incline in the course direction.

a)   b)
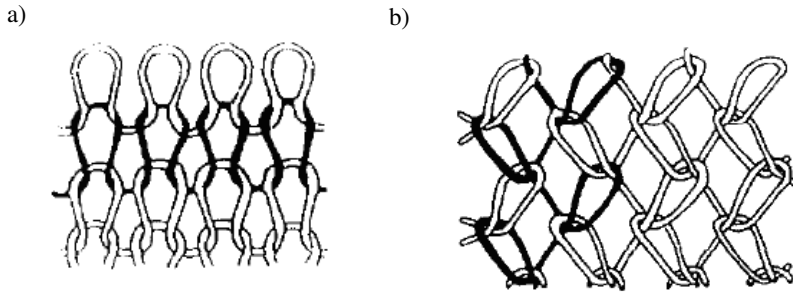
Figure. 1-5.   Knitted fabrics: a) weft-knitting; b) warp-knitting [13].

Based on the structural requirement, one of the above specified preform combined with the appropriate resin material, textile composite are produced. And the commercial application of these composite ranges from bio-medical components, aircraft and space structures to automotive and other applications. In the case of aircraft structures, woven or braided composites can be used for a wide variety of cross sectional forms such as stiffeners, truss members, rotor blades and spars etc. Having introduced the different types of textile composite and their importance in structural applications, the following sections will provide an argument for necessity of a numerical procedure for mechanical characterisation of the textile composites.

1. 4.   Background of the multi-scale modelling

The above specified textile composite parts such as stiffeners and truss members used in structural applications are constantly subjected to static and/or fatigue loads. Hence the mechanical characterization of textile composites under the aforementioned loads becomes very important from the structural design point of view. However, since the material properties are anisotropic and inhomogeneous in nature, the mechanical properties and the local stress-strain state in the composite constituents is controlled by numerous parameters, such as fibre architecture, fibre properties, matrix properties, etc. In the past 30 years, many researchers have continuously devoted their efforts to predict the mechanical properties of textile composites by making various assumptions. Earlier researches were carried out based on a large number of assumptions for simplifying the analysis procedures. The relevant approaches involved various rules of mixture approximations and composite cylinder models [13, 14].

These methods provided an approximate estimation of mechanical properties, but they cannot be used to analyze variations of mechanical properties with some important architecture parameters due to the introduction of oversimplified assumptions. On the other hand, it is almost impractical to investigate experimentally the mechanical properties of textile composites and their dependence on the major architecture parameters because of their complexity in geometry and spatial organisation, and labor intensity. In this regard, researchers developed mathematical formulations for the estimation of the homogenized macro-scale elastic constants within the framework of multi-scale modeling. Later, the developed homogenization formulas combined with the representative section of the textile composite (known as a unit cell), fully orthotropic material properties of the textile composite can be estimated using the commercial finite element software's [15]. The aforementioned procedure is firmly established and can be found in the literature [16, 17].

As a continuation to the above stated work, with the advances in computational resources, many researchers are focused on predicting the progressive damage behavior of textile composites under the static and fatigue loads using unit cell meso-FE simulations [18, 19]. In general, design criteria of textile composites under static and fatigue loads are usually determined by experiments. However, due to the complex and variable architectures and design parameters of the reinforcement and considerable time consumption of the tests, a reliable numerical method for evaluation of the composite behavior under damage (static and/or fatigue) would be of great value [20]. Moreover, apart from the experimental testing, understanding the stress and damage mechanics obtained from the numerical simulations provide an added advantage to the structural engineer to design the textile composites which have better resistance to the static and fatigue damage. In this regard, a recent publication of Lomov et al. [21] clearly established the data flow between different layers in the multi-scale modeling for both linear and non-linear cases.

Based on the simulations required, multi-scale modelling can be classified into two kinds of approaches, the hierarchical and simultaneous multi-scale modelling [22]. Within a hierarchical multi-scale model, the model parameters of the macro-scale are determined by means of homogenization associated with the micro-mechanical field variables, here a scale transition takes place. After the determination of effective elastic properties of the composite material no more microscopic analysis is required for the application of the macroscopic model. On the other hand the simultaneous or concurrent or integrated multi-scale modelling solves the model on all scales at the same time. Therefore the macroscopic model is affected by the response of the microscopic model and vice versa.

The aforementioned phenomena occur, if the macroscopic stress redistribution takes place due to the non-linear (such as damage) behavior of the micro-scale models. Hence, according to the given problem the class of multi-scale modelling has to be chosen.

1. 4. 1. a.   Hierarchical modelling in textile composites

Textile composites are structured, hierarchical materials, having three structural levels (Figure 1-6): 10^0 m-composite parts, 10^{-1} m-fabrics, 10^{-3} m-yarns/tows, 10^{-5} m-fibres [21].

i. "The micro (μ - 10^{-5} m)-level defines the arrangement of the fibres in the RVE (Representative Volume Element) of the impregnated yarn or fibrous ply. Local data on μ -level means the properties of fibre and matrix and their interface. Homogenized global parameters of μ -level are used as local parameters on meso-level".

ii. "The meso (m- 10^{-3} m)-level defines the internal structure of the reinforcement and variations of the fibre direction and the fibre volume fraction inside the yarns and the fibrous plies. The internal structure is defined by the reinforcement textile architecture and deformations applied to the reinforcement during part forming. Local on m-level means averaging (homogenization) on the scale of fibres. Global on m-level means local on M-level".

iii. "The macro (M- 10^0 m)-level defines the 3D geometry of the composite part and the distribution of local reinforcement properties. The local parameters of the reinforcement (such as fibre volume fraction, reinforcement thickness and shear angle, hence local stiffness) are defined by the draping process during the forming of the part. Local on the macro (M)-level means averaging (homogenization) of the properties of one or several adjacent unit cells of the material, and corresponds to the global on meso-level. Global on the M-level means overall loading conditions of the part".

Without the presence of micro-cracks, the hierarchical modelling ends with the evaluation of structural properties of composites such as engineering constants using RVE on meso-level (global on m-lelvel). The data flow in hierarchical modelling is shown in Figure 1-7(a).
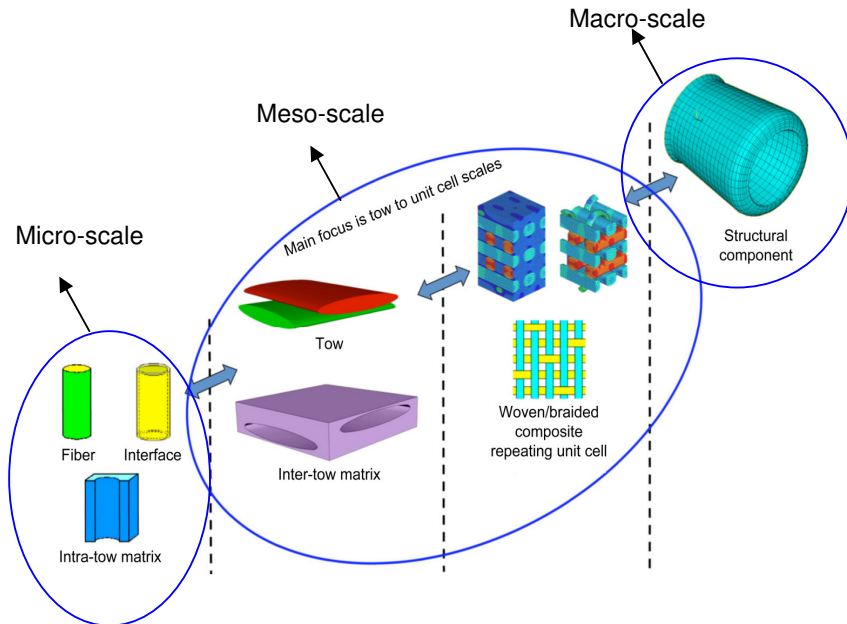
Figure 1-6.   **Schematic representation of the textile composite hierarchical scales [23].**

1. 4. 1. b.   Concurrent multilevel modelling

Concurrent multi-scale modelling is an adaptive computational model for multi-scale analysis of composite structures undergoing damage initiation and growth due to micro-structural damage induced by either debonding at the fibre matrix interface or damage initiated in individual yarns or matrix [24]. The concurrent multi-level model consists of three levels of hierarchy viz. level-1 (macro), level-2 (meso), and level-3 (micro), which evolve in sequence. The global loading condition on the unit cell is acquired from the level-1, in level-2 continuous damage modelling (CDM) will be applied on the unit cell for non-linear computations. The level-2 domain is used as a 'swing region' to establish the criteria for switching from macroscopic to microscopic calculations as shown in Figure 1-7 (b). A transition layer is placed in between the macroscopic and microscopic domains for smooth transition from one scale to the other. The transition layer is called meso-level modelling.

a)
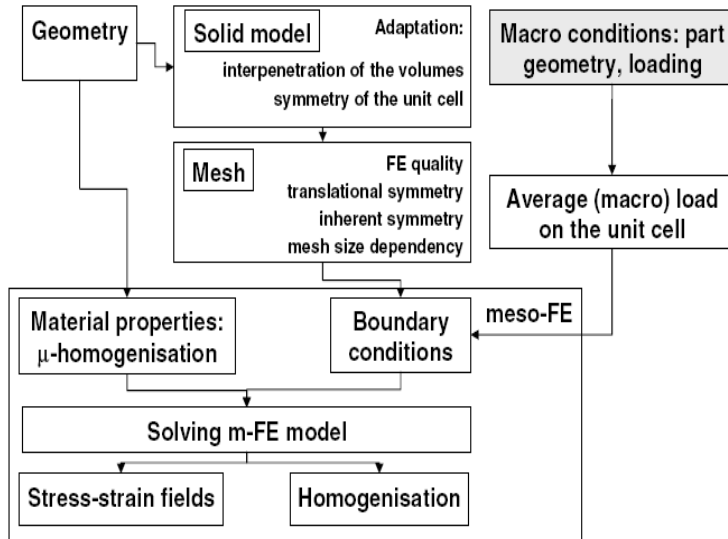
b)
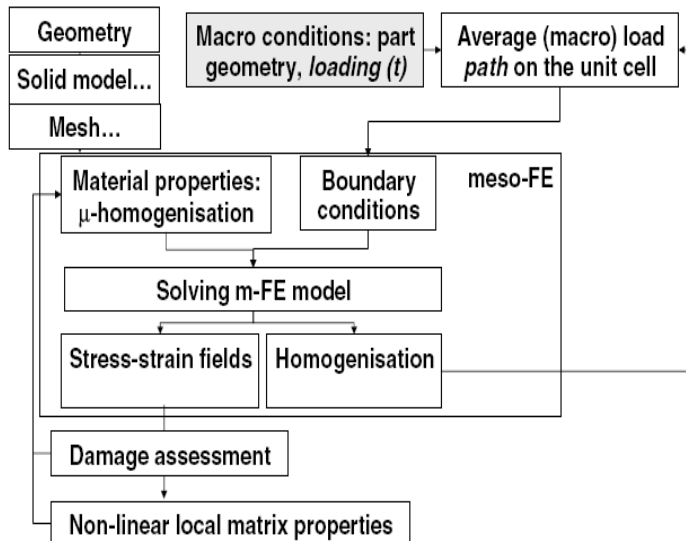
Figure 1-7.   **Road maps for meso-FE analysis: a) linear simulations; b) simulations in the presence of damage [21].**

1. 5.   State of the art of multiscale modelling

In general, composite structures under static and fatigue loads exhibit different types of damage starting from: (i) weft yarn cracks; (ii) fibre/matrix interface debonding; (iii) bundle debonding (meta-delminations or intra-ply delaminations); (iv) inter-ply delamination (v) fibre pull-out; and (vi) fibre fracture [25]. Under the applied external load, one of the above mentioned damage mechanism initiates early in the loading process at one particular location or at several locations of the textile laminate simultaneously. With the continuation of the external load, propagation of the existing damage or initiation of the new damage mechanisms occurs until the composite final failure, indicating that the damage initiation and propagation in textile composite is a sequential and progressive process. Based on the hierarchical nature of the textile composites, damage initiation and progression is influenced by the heterogeneities that are present in all three structural levels. At the micro-scale, parameter such as intra-yarn fibre volume fraction and fibre packing fraction shows considerable influence on the damage initiation in the plies of a textile composite. It is generally accepted that the poorer in-plane properties of 2D woven composites, relative to unidirectional (UD) ones, originate from the fibre crimping introduced by the interlacing of the tows. The understanding of the interlacing region's behavior and its role on failure is thus a key issue in the failure prediction of woven composites (meso-scale). Finally, at the macro-level, traditional textile composite manufacturing process introduces variability's such as the random shift between the adjacent layers, a variation in the shape of the yarn.

The above discussed parameters in textile composites at different length scales produces the complex local deformation pattern, and hence the local stress/strain concentration causing damage evolution, which is often difficult to asses [26]. Especially, the complex three dimensional local stress states that govern the local damage initiation in the composite constituent's begin with the composite manufacturing process (thermal residual-stress) [27]. Subsequent external load applied to the composite structure induces and increases the local stress concentration, consequently damage initiations occur when the induced local stress in the constituent material reaches the individual yarn or matrix strength. Hence, understanding the damage phenomena and the stress components that are responsible for the damage initiation is very important from the structural design point of view. Due to the fact that, based on the damage initiation strain, fatigue and durability life of the composite can be estimated [28]. Moreover, understanding the local stress-strain behaviour facilitates in developing the physically based meso-FE analysis procedure.

Regarding the state of the art of the damage analysis in textile composites using multi scale simulations, according to the recent doctoral dissertation of Ivanov [11]: *"despite of many successful examples of damage modelling for textile composites, it can be concluded that the technologies and intitutive engineering guesses have gone far ahead of the systematic analysis of the structures"*. In specific, recent publication by Carvalho et al. [29] stated that: *"virtually there are no publications in the field of damage analysis of textile composites which explicitly considered the effect of the variation in the reinforcement geometry on the resulting damage mechanisms"*. Finally, according to the anonymous reviewer of the journal papers submitted as a direct output of the current research work (chapter 3 and chapter 4), the actual state of the art of the damage analysis in textile composites is formulated in his own words: *"failure analysis of woven composites is a very wide area of research. There are numerous models, and very often these are not suitably validated. Partly, this is due to the lack of good and detailed experimental data, which this research work tried to provide"*.

1. 6.   Objectives of the research work

From the above discussed state of the art, it is justified to reach the conclusion that the research work in the field of damage modelling in textile composite is far from complete. From the literature [12, 30, 31] it can be concluded that there are numerous parameters that control the damage initiation and progression in textile composites. However, from the existing literature one cannot obtain a unified knowledge regarding the damage initiation and propagation in a textile composites. This can be attributed to the lack of through validation of the meso-FE development procedure against the suitable experiments. As it is well known that the damage initiation and progression in the composite constituents depends on the local strain (stress) state. In this perspective, in order to obtain a comprehensive and thorough procedure for the analysis of damage behaviour in textile composites, the current research work and the chapters of this dissertation are directed to realise the following objectives:

    i.   Initially, it is intended to understand the local strain behaviour in the plies of a textile composite under investigation using various experimental techniques. Due to the fact that the maximum local strain (stress) locations indicate the probable damage initiation locations.

ii.   Following the objective of this research work, it is intended to develop a unit cell meso-FE analysis procedure to predict the local strain profiles both qualitatively and quantitatively comparable to the observed experimental strain profiles.

iii.   After the experimental strain analysis, it is intended to characterise the damage initiation and propagation in the plies of a woven composite using experimental analysis.

iv.   In order to predict the observed experimental local damage behaviour using meso-FE simulations, a meso-FE analysis procedure should be developed. Moreover, the stress analysis at the damage regions of the textile composite should provide a step-wise understanding of the damage initiation. And this may lead to identify the influence of the local stress components on the damage development in the textile composites.

v.   After the stepwise understanding of the damage behaviour in woven composites using the experimental and the obtained numerical results under static loads, it is intended to extend the procedure for predicting the damage behaviour under fatigue loads using meso-FE simulations.

With the approval of the F.W.O-project in 2006 on the research topic "Micro-Meso-Macro homogenization of fatigue damage models in textile composites" this work became possible. This project is a collaborative work between the Department of Materials Science and Engineering at UGent and Metaalkunde en Toegepaste Materiaalkunde (MTM) at K.U.Leuven. In mid 2007 ir. Jian XU started his research work at MTM, where as the author of this dissertation started his work in April 2007 at UGent with the common goal of modelling the damage behaviour of textile composites.

1. 7.   Organization of the dissertation

Within the guidelines of the above stated objectives, the following sections give an overview of the different chapters that are discussed in this manuscript. The contents of each chapter are briefly described here:

1. 7. 1.   Chapter 2: Construction of the unit cell geometrical model and estimation of the homogenized elastic constants

Initially, this chapter introduces the composite material under investigation. Later, this chapter presents the detailed discussion about the creation of the RUC (Representative Unit Cell) geometrical model and estimation of the homogenized elastic constants of the textile composite under study. In order to create the unit cell (RUC and unit cell names are synonymously used throughout the manuscript) geometrical model, the textile parameters of the satin weave composite material were measured using the micro-CT analysis. With the obtained geometrical model, unit cell FE mesh is created and used to estimate the satin weave composite homogenised (macro-scale) material properties. In order to estimate the composite homogenized elastic properties, initial boundary value problems of the unit cell on the meso-scale are solved using different boundary conditions. Finally, estimated numerical homogenized elastic constants are compared to the experimental values.

1. 7. 2.   Chapter 3: Local strain analysis in the satin weave composite under uni-axial static tensile load

This chapter presents the detailed analysis of the local strain behaviour in the plies of a satin weave composite under uni-axial static tensile load. Initially, this chapter presents the experimental local strain analysis on the composite surface using the full-field strain measuring techniques (DIC), followed by the local strain analysis in the laminate inner layers using fibre optic sensors. The aforementioned experimental local strain analysis procedure describes the effect of internal yarn shifting (nesting) on the local longitudinal strain behaviour of the satin weave composite. Second part of this chapter presents the development of the unit cell meso-FE simulation procedure to predict the local strain profiles and their spatial distribution as observed in the experiments. Finally, a detailed discussion is presented based on the comparison between the experimental and numerical local strain analysis.

1. 7. 3.   Chapter 4: Experimental and numerical investigation of the local damage behaviour under uni-axial static tensile load

In this chapter, detailed investigation of the damage analysis in the plies of a satin weave composite under uni-axial static tensile load is presented. Starting from theoretical background of the accumulation of the thermal stresses due to the composite manufacturing process, investigation is extended to the variation of the micro, meso and macro-scale textile parameters and their influence on the composite damage initiation. In addition, studying the damage events that are initiating at the free edges facilitates the qualitative understanding of the observed sequential damage phenomena in the satin weave composite. The second part of this chapter presents the analysis of the observed experimental sequential damage phenomena using unit cell meso-FE simulations. Finally, investigation of the local stress components at the damaged regions provides a quantitative understanding of the observed sequential damage. Finally, the effect of the observed micro-scale damage events on the macroscopic composite stiffness is discussed.

1. 7. 4.   Chapter 5: Experimental damage analysis of the satin weave composite under tension-tension fatigue

As stated in the title, this chapter is devoted to the experimental fatigue damage analysis of a 5-harness satin weave composite. Evolution of the longitudinal strain as well as the composite in-plane stiffness (macro-scale) was monitored throughout the cyclic load process. During the fatigue test, instrumentation of the composite response is categorized into two parts: i) the first priority is to monitor the macro-scale structural response; ii) the second priority is to capture the microscopic damage events that are occurring in correlation with the observed macroscopic structural response. Moreover, comparison of the stress-strain behaviour as well as the strength of the virgin composite samples to the fatigue tested samples give an overview of the effect of the damage caused by fatigue load on the test specimen.

1. 7. 5.   Chapter 6: Conclusions and future work

The final chapter of this manuscript presents the concluding remarks of this dissertation. And the recommendations are provided for the future work in the area of damage analysis of textile composites using multi-scale simulations.

1. 8.   Original contributions

The original contributions from this dissertation are as follows:

- Development of an experimental procedure for estimating the local strain variation in different plies of the satin weave composite, which directly controls the local stress variation and hence the local damage initiation. The obtained experimental local strain results are published in *Composites Science and Technology [32]*.

- Prediction of the numerical local strain profiles using the unit cell meso-FE simulations, that are spatially (qualitatively) and quantitatively comparable to the experimental predictions. Comparison of the numerical and experimental local strain results has been published in *Composites Science and Technology [33]*.

- Development of an experimental procedure for detecting the damage initiation and progression in different plies of a satin weave composite under uni-axial static tensile load. The developed experimental methodology along with the sequential damage analysis has been published in *Composites Science and Technology [34]*.

- Using the unit cell meso-FE simulations, the observed experimental damage initiation in various plies of the satin weave composite is analyzed. From the unit cell meso-FE analysis, the damage phenomena and the various stress components contribution for the damage initiation in the ply of a satin weave composite is realized. The obtained results from the numerical local stress analysis combined with the local deformation and the local damage analysis in the satin weave composite has been published in *Composites Science and Technology [35]*.

- Finally, extensive experimental fatigue damage analysis is conducted on the satin weave composite. Evolution of the structural response parameters such as longitudinal strain as well as the stiffness of the composite is monitored throughout the fatigue life. In addition, according to the fluctuation in the monitored macro-scale structural repose, the micro-scale damage events are detected in the composite specimen. The effect of the induced fatigue damage on the satin weave composite load carrying behavior is investigated. As a result of the extensive static and fatigue damage analysis, conclusions are drawn from the material as well as numerical meso-FE analysis perspective. The results of above mentioned work are ready to publish.

1. 9.   References

[1]   Strong, A.B., *History of composite materials - Opportunities and Necessities.* Brigham Young University.

[2]   Hashin, Z., *Theory of fiber reinforced materials.* NASA CR 1974.

[3]   DEWAELE, W., *Structural monitoring of composite elements using optical fibres with Bragg-sensors.* PhD Thesis; Ghent University 2002.

[4]   Durão, L.M.P., *Machining of hybrid composites.* PhD Thesis; University of Porto, 2005.

[5]   Vodicka, R., *Thermoplastics for Airframe Applications A Review of the Properties and Repair Methods for Thermoplastic Composites.* DSTO Aeronautical and Maritime Research Laboratory, October 1996.

[6]   Potluri, P. and A. Manan, *Mechanics of non-orthogonally interlaced textile composites.* Composites Part A: Applied Science and Manufacturing, 2007. **38**(4): p. 1216-1226.

[7]   Mital, S.K. and L.N. Murthy, *Simplified Micomechanics of Plain Weave Composites.* NASA technical Memorandum 107165, 1996.

[8]   Long, A.C., *Design and manufacture of textile composites.* Woodhead Publishing in Textiles, 2005.

[9]   Cox, B.N. and G. Flanagan, *Handbook of Analytical Methods for textile composite.* NASA Contractor Report 4750, 1997.

[10]   Goyal, D., *Analysis of 2x2 braided composites, Master thesis, Texas A&M University.* August 2003.

[11]   Ivanov, d.S., *Damage analysis in textile composites.* PhD Thesis; KU Leuven - Faculty of Engineering, May 2009.

[12]   Gao, F., et al., *Damage accumulation in woven-fabric CFRP laminates under tensile loading: Part 1. Observations of damage accumulation.* Composites Science and Technology, 1999. **59**(1): p. 123-136.

[13]   Tan, P., L. Tong, and G.P. Steven, *Modelling for predicting the mechanical properties of textile composites--A review.* Composites Part A: Applied Science and Manufacturing, 1997. **28**(11): p. 903-922.

[14]   Pindera, M.-J., et al., *Micromechanics of spatially uniform heterogeneous media: A critical review and emerging approaches.* Composites Part B: Engineering, 2009. **40**(5): p. 349-378.

[15]   Kanouté, P., et al., *Multiscale Methods for Composites: A Review.* Archives of Computational Methods in Engineering, 2009. **16**(1): p. 31-75.

[16]   Hollister, S.J. and N. Kikuchi, *A comparison of homogenization and standard mechanics analyses for periodic porous composites.* Computational Mechanics, 1992. **10**(2): p. 73-95.

[17]   Byström, J., N. Jekabsons, and J. Varna, *An evaluation of different models for prediction of elastic properties of woven composites.* Composites Part B: Engineering, 2000. **31**(1): p. 7-20.

[18]   Whitcomb, J. and K. Srirengan, *Effect of various approximations on predicted progressive failure in plain weave composites.* Composite Structures, 1996. **34**(1): p. 13-20.

[19]   Tang, X., et al., *Progressive failure analysis of 2 x 2 braided composites exhibiting multiscale heterogeneity.* Composites Science and Technology, 2006. **66**(14): p. 2580-2590.

[20]   Xu, J., et al., *A new meso-scale modelling of static and fatigue damage in woven composite materials with finite element method.* 17th International Conference on Composite Materials (ICCM-17) ; Edinburgh, UK 2009.

[21]   Lomov, S.V., et al., *Meso-FE modelling of textile composites: Road map, data flow and algorithms.* Composites Science and Technology, 2007. **67**(9): p. 1870-1891.

[22]   Zastrau, B., I. Lepenies, and M. Richter, *Multi Scale Modeling of Textile Reinforced Concrete.* TECHNISCHE MECHANIK, Band 28, Heft 1, (2008), 53 – 63, August2007.

[23]   Nemeth, N.N., S. Mital, and J. Lang, *Evaluation of Solid Modeling Software for Finite Element Analysis of Woven Ceramic Matrix Composites.* NASA/TM—2010-216250, June2010.

[24]   Ghosh, S., J. Bai, and P. Raghavan, *Concurrent multi-level model for damage evolution in microstructurally debonding composites.* Mechanics of Materials, 2007. **39**(3): p. 241-266.

[25]   VanPaepegem, W., *Development and finite element implementation of a damage model for fatigue of fibre-reinforced polymers.* PhD Thesis; Ghent University Architectural and Engineering Press, 2002.

[26]   Fruehmann, R.K., J.M. Dulieu-Barton, and S. Quinn, *Assessment of fatigue damage evolution in woven composite materials using infra-red techniques.* Composites Science and Technology. **70**(6): p. 937-946.

[27]   Rupnowski, P. and M. Kumosa, *Meso- and micro-stress analyses in an 8HS graphite/polyimide woven composite subjected to biaxial in-plane loads at room temperature.* Composites Science and Technology, 2003. **63**(6): p. 785-799.

[28]   Ivanov, D.S., et al., *A comparative study of tensile properties of non-crimp 3D orthogonal weave and multi-layer plain weave E-glass composites. Part 2: Comprehensive experimental results.* Composites Part A: Applied Science and Manufacturing, 2009. **40**(8): p. 1144-1157.

[29]   Carvalho, N.V., S.T. Pinho, and P.Robinson, *Compressive failure of 2D woven composites.* ICCM-17 Conference proceedings, 2009.

[30]   Roy, A.K., *Comparison of in situ damage assessment in unbalanced fabric composite and model laminate of planar (one-directional) crimping.* Composites Science and Technology, 1998. **58**(11): p. 1793-1801.

[31]   Duplessis Kergomard, Y., et al., *Intralaminar and interlaminar damage in quasi-unidirectional stratified composite structures: Experimental analysis.* Composites Science and Technology. **70**(10): p. 1504-1512.

[32]   Daggumati, S., et al., *Local strain in a 5-harness satin weave composite: part I - experimental analysis.* Accepted for Composites Science and Technology, 2011.

[33]   Daggumati, S., et al., *Local strain analysis in a 5-harness satin weave composite under static tension : part II-meso-FE analysis.* Accepted for Composites Science and Technology, 2011.

[34]   Daggumati, S., et al., *Local damage in a 5-harness satin weave composite under static tension: Part I - Experimental analysis.* Composites Science and Technology. **70**(13): p. 1926-1933.

[35]   Daggumati, S., et al., *Local damage in a 5-harness satin weave composite under static tension: Part II - Meso-FE modelling.* Composites Science and Technology. **70**(13): p. 1934-1941.

Chapter 2

CONSTRUCTION OF THE UNIT CELL GEOMETRICAL MODEL AND ESTIMATION OF THE HOMOGENIZED ELASTIC CONSTANTS

The first part of this chapter introduces the textile composite material used in the current research work. The subsequent sections of this chapter present the estimation of the homogenized elastic constants of the material of interest using unit cell meso-FE simulations. For the aforementioned purpose, a unit cell geometrical model, namely, a <u>R</u>epresentative <u>U</u>nit <u>C</u>ell (RUC) of the satin weave composite is constructed. In order to compute the homogenized elastic properties using RUC FE simulations, different numerical procedures are presented. Finally, the computed effective elastic constants using RUC meso-FE simulations are compared to the analytical as well as the experimental (macro-scale) elastic constants obtained from the tensile test of a 5-harness satin weave composite.

2. 1.   INTRODUCTION

As described in the previous chapter, the mechanics of textile reinforced composites are not as well understood as those of unidirectional reinforced composites. The behaviour of a textile reinforced composite is related to the additional geometric parameters introduced by the complexity of the weave construction and modification caused by the composite fabrication process [1]. Reliable prediction of mechanical properties of composite materials is of primary importance for the successful usage of textile composites. In this regard, the current chapter begins with a detailed discussion regarding the textile composite under investigation. The weave architecture as well as the fibre and resin material used in the composite manufacturing process is presented. In addition, industrial applications of the material of interest are highlighted. The objective of the current chapter is to predict the macroscopic moduli of the textile composite under investigation based on the moduli of the individual phases and their geometric arrangement. This procedure has a distinct advantage that, at very fundamental level, numerical meso-mechanical analysis facilitates the understanding of how the local properties of constituent materials, phases and their arrangement influence the macroscopic material and structural behavior. In order to estimate the homogenized elastic constants using unit cell meso-FE simulations, a detailed discussion is presented in the following order: a) Capturing the textile reinforcement and construction of the satin weave unit cell geometrical model; b) Calculation of the micro-mechanical elastic constants; c) Applying different types of boundary conditions (BC's) to the unit cell for meso-FE simulations; d) Estimating the unit cell effective (macro-scale) elastic constants using different procedures. Finally, conclusions are drawn based on the comparison between numerical and analytical elastic constants as well as the experimental elastic constants. The current chapter deals with the hierarchical modeling wherein finite element analysis of the unit cell ends with the computation of the effective elastic constants of a textile composite [2-6].

2. 2.   Material under investigation

The material used in the current research work is a thermoplastic 5-harness satin weave composite (CETEX$^{®}$) with T300JB carbon fibre as reinforcement and PPS (PolyPhenylene Sulphide) as a matrix material. This material is supplied to us by TenCate advanced composites. Details of the satin weave reinforcement as well as the composite are presented in the following sections.

2. 2. 1.   Fibre and weave pattern

As mentioned in the previous section, the material used in the current research work is a 5-harness satin weave fabric with T300JB carbon fibre as a reinforcing material, which has a specific mass of 1750 kg/m^3. Detailed fabric specifications are listed in Table 2-1. Regarding the fabrication process, as explained in the previous chapter, the fabric yarns exchange their position frequently in plain weave composites. This waviness reduces the strength and stiffness of the composite. To reduce this waviness, 5-harness satin weave has 1-over and 4-under pattern and hence increases the length of the straight portion of the yarn known as float. The reduced yarn crimp in the satin weave composite is the main reason for the better structural performance compared to plain weave composites [7].

From the structural response perspective, as explained by Cox et al. [7] the individual layers of the satin weave fabric are asymmetric. One side of the fabric is predominantly warp yarns and other side is the weft yarns (Figure 2-1). Yarn exchange locations also break symmetry because they bend the yarns in an unsymmetrical way. Consequently, bending and stretching are coupled. There is also coupling between stretching and in-plane shear under the applied tensile load, because the yarn exchange locations are not symmetric about either in-plane axis. Moreover, coupling between bending and stretching causes the warping of the composite plates during the curing process because of the thermal strains (extended discussion can be found in the chapter 4 of this manuscript).

Table 2-1.   Satin weave carbon fabric information.

Carbon fibre type	*T300JB*
tex, g/km	*198*
End/Pick count, yarns per 10 cm	*70*
Yarn filament count	*3000 (3k)*
Filament diameter, mm	*0.007*
Carbon fibre density, g/cm^3	*1.75*
Fabric areal density, g/m^2	*285*

a)

b)
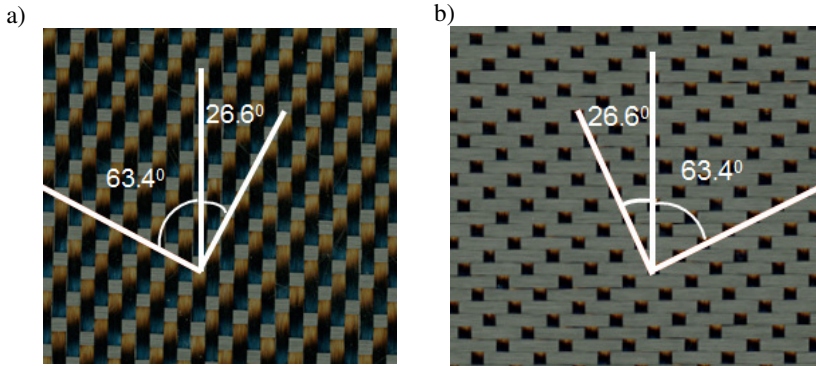
Figure. 2-1.   **Satin weave carbon fabric; a) warp dominant side; b) weft dominant side.**

2. 2. 2.   Matrix (resin) material

Using the hot-pressing technique, the above shown satin weave fabric (Figure 2-1) combined with the PolyPhenelyne Sulphide (PPS) resin composite plates are produced. PPS is a thermoplastic material with semi-crystalline structure possessing a high chemical resistance and good weldability. There are various types of this polymer commercially available, but for CETEX® the linear variant is used. It has a long chain structure with limited branching resulting in a low viscosity and a faster crystallisation than strongly branched polymers. PPS is a semi-crystalline thermoplastic, which means that the amorphous and the crystalline phase coexist. The portion between the both phases is determined by the preceding temperature cycle. The mechanical properties of PPS are listed in Table 2-2.

Table 2-2.   Mechanical properties of the PPS matrix (resin).

Melting temperature [8]	*280*
Glass transition temperature [^0C]	*90*
Optimal crystalline temperature [^0C]	*150-160*
Tensile strength, MPa	*90*
Shear strength, MPa	*63*
Ultimate strain	*0.08*
Young's modulus in tension, MPa	*3800*

In general, the higher the cooling rate, the more amorphous the structure becomes. Amorphous PPS starts to soften at a temperature of 90°C (T$_g$). This state of slightly altered viscosity lasts until the material starts to crystallise at 120°C. This crystallised material does not soften, and the structure is stable and can only be broken by melting. Melting of PPS starts at 280°C, the material is completely liquid at 300°C. At this temperature the material structure is highly disordered and the molecules have a high mobility. Since the molecular forces are very low, the melted material has very low viscosity. The cooling of the melt results in a second crystallisation. The number of crystals being formed depends on the cooling rate. Since crystallisation takes time, the lower the cooling rate, the higher the fraction of crystals. If the material is cooled down very fast, the disordered structure is frozen and the resulting material is amorphous.

2. 3. Manufacturing of the CETEX$^®$ material and its applications

Since PPS weakens at elevated temperatures, it is excellent for the hot pressing process (Figure 2-2a). This is a fast and flexible method for producing composite plates at a faster rate using semi-pregs. In order to produce the CETEX$^®$, 8 layers of carbon-PPS semi-pregs are stacked in $[(0^0,90^0)]_{4s}$ in a symmetrical way with respect to the mid-plane. Moreover, it should be noted that the $(0^0,90^0)$ represents a single fabric layer, in which 0^0 represents the warp direction and 90^0 represents the weft direction. A semi-preg consists of two layers: (i) a layer of fabric, for instance the satin weave carbon fabric and (ii) a thermoplastic film, for instance a PPS film. The two layers are bonded to each other simply by heating the two, so that the thermoplastic melts and bonds to the fabric. A semi-preg differs from the well known pre-preg, because for the former the two layers can still be distinguished, where as for the later the fabric is completely impregnated with a thermoplastic matrix.

a)

b)

7.4mm
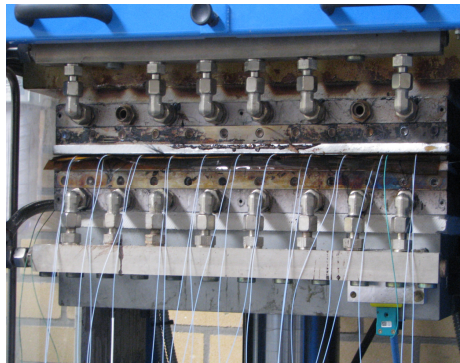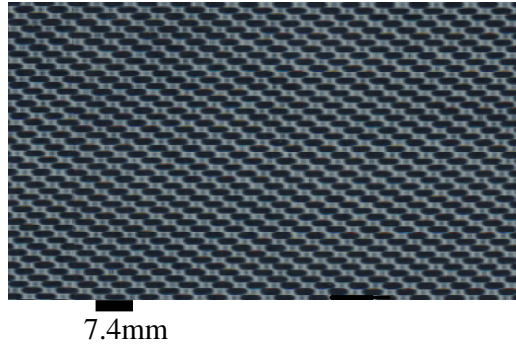
Figure. 2-2.   Manufacturing the thermoplastic 5-harness satin weave composite: a) small scale hot-press (TenCate); b) produced satin weave composite plate.

Using the hot press forming technique, the composite plates are produced (Figure 2-2c). The composite plates supplied by TenCate are usually around 45 cm by 48 cm in width and approximately 2.5 mm thick.

In general, thermoplastic composites have the advantage that they can be produced in an easy manner. However, due to the shrinkage of resin during recrystallisation, internal stresses are introduced between the fibre and matrix. When the bonding between the carbon fibre and PPS resin is insufficient, damage will occur at the fibre-matrix interface. However, by varying parameters such as cooling speed and sizing of the fibres, adhesion between fibre and matrix could be optimised.
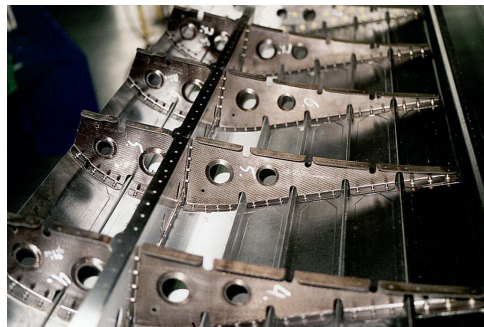
Satin weave composite rib flanges

Figure. 2-3.   Application of the CETEX® in the aerospace (series of wing stiffeners).

The primary application of CETEX® is in the aerospace industry. Some applications of CETEX® are the J nose part of the leading edge of the airplane wing, and the wing stiffeners (Figure 2-3) as well as heavy duty sandwich panels.

Having introduced the composite material, the following sections of this chapter present the detailed discussion regarding the estimation of the satin weave composite homogenized (macro-scale) elastic properties using meso-FE simulations.

2. 4.   Representative Volume Element (RVE) in a composite

In general, a common practice in structural mechanics when dealing with composite structures is to replace their highly nonhomogeneous constituents with homogenized materials. In this regard, a whole area of Solid Mechanics has been developed in the past forty years to predict theoretically the 'effective properties' of composite materials, directly from the constituents (or phases) and their distribution (or micro-structure) phases known as a homogenization procedure [9]. However, analysis of large composite (heterogeneous) structures on micro-scale is clearly an intractable problem. Analysis methods have therefore sought to approximate composite structural mechanics by analyzing a representative section of the composite micro-structure, commonly called as a Representative Volume Element (RVE) [10]. The microscopic scale is small enough for the heterogeneities to be separately identified. And the macroscopic scale is large enough for the heterogeneities to be 'smeared-out'. The effective properties at the macroscopic scale of the composite are determined from geometrical and material data available for the study of a RVE [9]. In addition, analysis of the RVE relies on the assumptions of spatial periodicity of the mesoscopic RVE's and the local uniformity of macroscopic fields within each RVE [11].

Consequently, RVE is clearly defined in two situations only: (i) Representative Unit Cell (RUC) in a periodic micro-structure; and (ii) a volume containing a very large set of micro-scale elements, possessing statistically homogeneous properties [12] (in case of particle reinforced composites). For textile composites, the micro-structure can be seen as a periodic array of RUC's. While for some other composites, such as unidirectional lamina or particle reinforced composites, a RUC can still be constructed after assuming a uniform distribution and the same geometry for the reinforcing phase. Therefore, in most micro-mechanical analysis the RUC is chosen as the RVE for the composite [13]. For the detailed discussion and the critical review about the differences between RVE and RUC the reader is referred to [14, 15].

In view of the current work, for a textile reinforced composite the RUC is defined by the requirement that the entire textile reinforcement can be constructed from spatially translated copies of it, without use of rotations or reflections [7]. The fundamental premise of a RUC is that it is representative of the entire textile composite. This implicitly assumes that the textile preform is not varying spatially but it is comprised of a repeating pattern of cells. The following sections present the detailed discussion regarding the construction of a 5-harness satin weave RUC geometrical model for the FE analysis.

2. 5.   Construction of a 5-harness satin weave RUC

As explained in the previous section, the properties of the composites are determined by the structure of the textile reinforcement, which is liable to change during the processing. An Adequate definition of the micro-structure is needed to predict the mechanical properties of textile composites. Moreover, knowledge of the micro-structure is important for predicting the composite part performance since the position and orientation of the reinforcement directly controls many of its properties. In the current study, the satin weave RUC geometric model will be used as an input to simulate the meso-mechanical behaviour of the textile composite. The results obtained from meso-FE simulations will be used to calculate the effective mechanical properties of the satin weave composite. Hence, the focus of this study is to investigate the meso-structure of a satin weave fabric in a processed composite. In this regard, preliminary investigations have shown that the micro-computed tomography scanning (micro-CT) is capable of visualizing each yarn dimension separately and the spacing between the yarns, thus providing the necessary input to create a reasonably accurate geometric model of the textile structure [16-18]. In the process of constructing the satin weave RUC geometrical model, the following steps are discussed in detail.

1)   Performing micro-CT analysis on a processed composite specimen

2)   Calculation of the textile parameters

3)   Construction of RUC geometrical model and translation into FE mesh.

2. 5. 1.   Overview of the micro-CT working procedure

Micro-computed tomography (micro-CT) has been originally used for biomedical purposes. It is a non-destructive method to get geometrical information about the internal microstructure of the object. In the past, destructive methods like serial sectioning were used to determine the fabric structure. In contrast, micro-CT is an alternate approach to image and quantify the textile architecture in 3D. Due to the above specified advantages, the micro-CT procedure is used for quantifying the internal geometry of the 5-harness satin weave composite. The working procedure is explained as follows.

An X-ray source illuminates the object. The transmitted X-rays are recorded on a detector that measures different intensities of the attenuated X-rays. The intensities vary due to the different X-ray absorption. High density materials absorb more X-rays than low density materials [17]. These intensities give information about the irradiated material density. The advantage of the CT is the possibility to X-ray the sample in all directions for every slice. Therefore either the object or the X-ray source must be rotated from 0 to 360 degrees. A high power directional tube of dual head 160 kV fine focus open-type tube X-ray source was used. This tube attenuates most of the X-ray below 10 keV and is equipped with a conical tungsten anode and an aluminium exit window. With a maximum power of 150W and a high X-ray power output, the directional tube is perfectly suited to penetrate thermoplastic composites. The X-ray detector, a remote Radeye EV CMOS flat panel (http://www.rad-icon.com) was applied. This detector provides a high contrast for micro-CT, with X-ray tube voltage up to 160 kV. Its active area is 24.6mm by 49.2 mm consisting of a 512 by 1024 matrix of silicon photodiodes on 48 μm centres. A thin straight fibre optic coupling is used to transport the visible light from the phosphor to the CMOS. The samples are positioned on a highly sensitive sample manipulator, consisting of seven motor stages. The samples are positioned between the X-ray tube and X-ray detector with an XYZ-translation stage with Berger Lahr stepper motors. To reach the high precision CT-scan, a rotation stage with air bearings is used. A standard air compressor and series of filters provide 4.5 bar air pressure of the stage. Additionally, a XY-piezo stage with 50 nm resolution and 20 mm travel range is fixed on the rotation platform to centre the sample on the rotation axis [19].

Using the above specified micro-CT equipment, the micro-structure of the satin weave fabric was investigated using three rectangular samples each with a size of $10.4 \times 10.4 \times 2.5$ mm (Figure 2-4). The sizes of the samples used for measurement were prepared according to the optimum dimensions of the RUC. Samples were cut from CFRP-plates produced by TenCate. All micro-CT scans were done in cooperation with the X-ray and CT-facility of the department of Subatomic and Radiation Physics (SSF) at the Faculty of Sciences, Ghent University. Using the micro-CT output images, the required information to construct the RUC geometrical model is measured as explained in the following section.
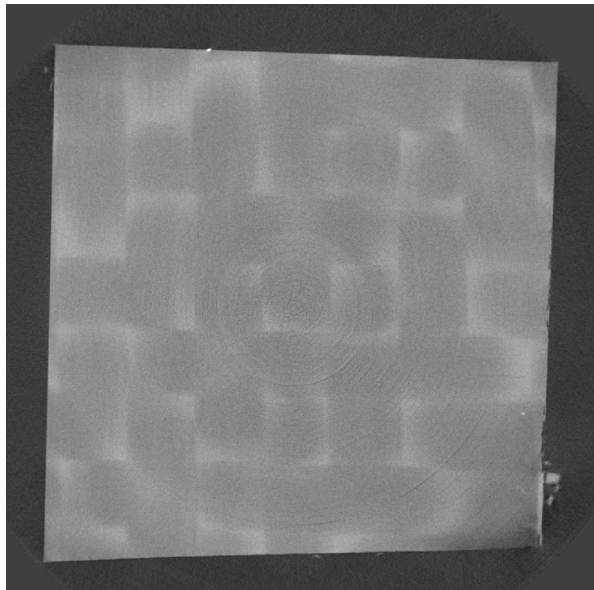
Figure 2.4.   Satin weave composite under micro-CT analysis.

2. 5. 2.   Calculating the textile parameters

In order to calculate the textile parameters, the obtained micro-CT data was reconstructed using the Octopus software (http://www.xraylab.com). From the reconstructed images, using a pixel size of 0.01mm (Figure 2-5a), the textile information required for the construction of the RUC geometry such as: a) spacing (distance between two warp or weft yarn heart lines); b) width and thickness of the yarns are measured at 20 different locations in both warp and weft yarn directions (Figure 2-5a-d). And the average of the measured textile parameters is listed in Table 2-3.

a)

b)

c)

d)

e)
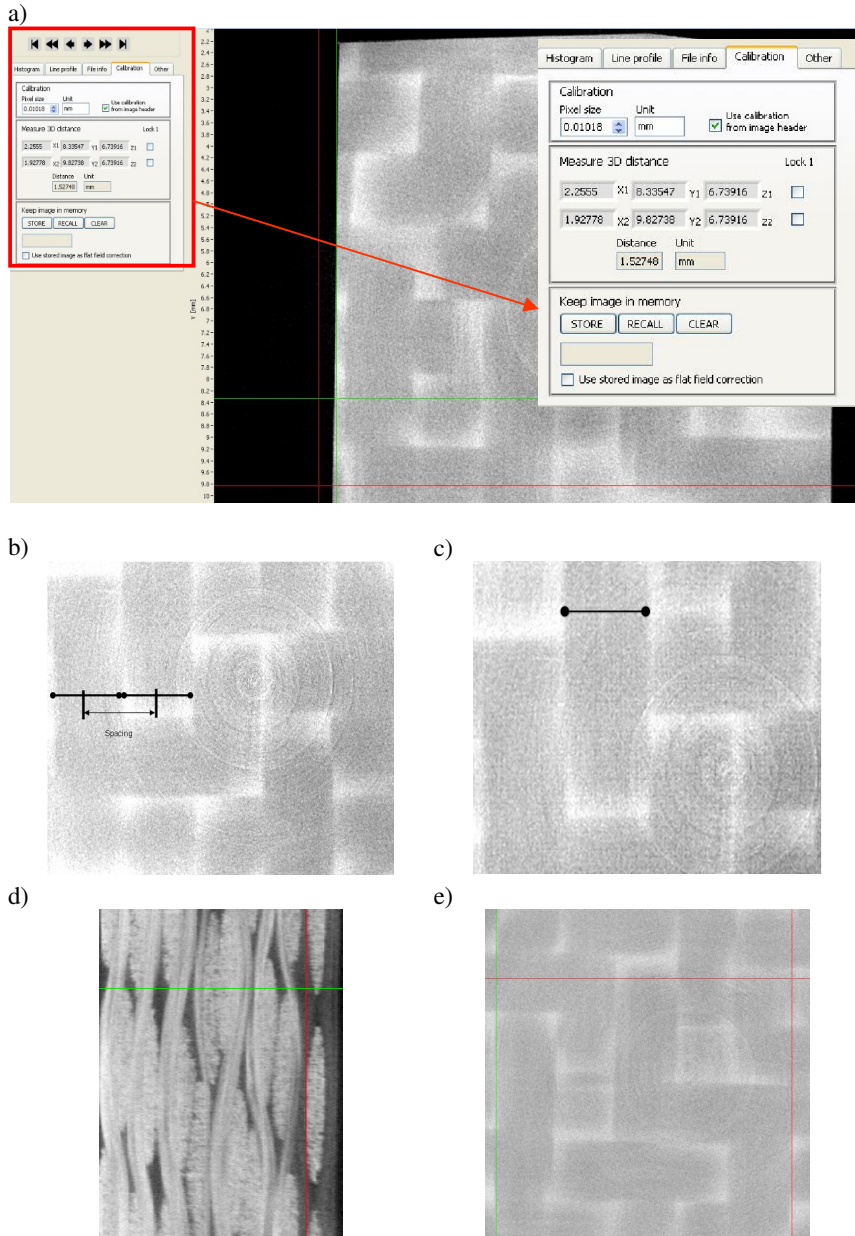
Figure 2.5.   Measurement of the textile parameters: a) measurement window in the 'Octopus' software: b) yarn spacing; c) yarn width; d) yarn thickness; e) 5-harwaness satin weave RUC.

Table 2-3. Textile parameters obtained from micro-CT as well as the individual yarn data.

Satin weave fabric information		
Property	5 harness satin weave warp	5 harness satin weave weft
RUC width, mm	7.4	
Number of measurements	20	20
Yarn width, mm	1.31 ± 0.01	1.32 ± 0.08
Yarn thickness, mm	0.162 ± 0.01	0.161 ± 0.06
Yarn spacing, mm	1.46 ± 0.04	1.48 ± 0.07
Yarn filament count	3000	
Filament diameter, mm	0.007	
Carbon fibre density, g/cm^3	1.75	

2. 5. 3.   Construction of the RUC geometrical model and translation into the FE mesh

In order to construct the satin weave unit cell geometrical model, 'WiseTex' software [20, 21] (developed by MTM at KU Leuven) is used. The required unit cell geometrical model is constructed using 'WiseTex' software based on the measured micro-CT data from the satin weave composite. The yarns of the satin weave composite in the geometrical modeller software 'WiseTex' are represented in elliptical shape having the major diameter of 1.32 mm and the minor diameter of 0.15 mm (Table 2-3). Along with the yarn cross-section dimensions, to construct the unit cell geometrical model the input data for 'WiseTex' at fabric level include: a) yarn interlacing pattern; b) yarn spacing in the textile fabric.

Along with the above specified fabric information, the carbon fibre data (Table 2-3) such as linear density and fibre diameter are used as input information in 'WiseTex' software. With the aforementioned information at fibre and fabric level, the satin weave unit cell (reinforcement) geometrical model is generated as explained in [20, 22, 23] (Figure 2-6a). In the 'WiseTex' software, the out-of-plane orientation of the warp and weft yarns at their cross-over points were taken into account in an approximate way, by presenting the curved yarns by a set of straight yarn segments [21]. Apart from the unit cell geometrical model (Figure 2-6a), the 'WiseTex' output includes: a) inter-yarn porosity; b) intra-yarn fibre volume fraction; c) overall fibre volume fraction; and d) areal density of the fabric. Comparison of the 'WiseTex' generated fabric output data with the supplier data (Table 2-4) proves the accuracy of the created satin weave unit cell geometrical model.

Later, the obtained 'WiseTex' generated unit cell geometrical model is translated into a FE mesh using 'MeshTex' software [21, 24] (developed by Prof. Zako at Osaka university, Japan).

Table 2-4.   Comparison of 'WiseTex' output with material supplier data.

Measurement	'WiseTex'	Supplier data
Unit cell size	$7.4 \times 7.4 \times 0.32$ mm	-NA-
Areal density of dry fabric	264.8 g/m^2	285 g/m^2
Fibre volume fraction (Yarn), %	70	-NA-
Fibre volume fraction (RUC),%	49.8	50 ± 3

Before meshing the unit cell geometrical model, the correction of the yarns interpenetration at the cross-over points (yarn crimps) for woven composites is accomplished as explained by Lomov et al. [23]. After correcting the yarn inter-penetrations, the obtained unit cell geometrical model is meshed using the sweep mesh operation: a mesh built on the first cross-section of the yarn is being "swept" throughout the yarn, creating a quite regular mesh. Later, the mesh in the matrix can be constructed. The resulting mesh obtained from 'MeshTex' has no yarn penetrations and is ready to use for FE simulations.

In 'MeshTex' quite regular meshing to the satin weave unit cell is accomplished. After meshing, the satin weave FE model consists of 53,200 elements. Moreover, it should be emphasized that perfect bonding is assumed at the interface between the yarns and matrix of the unit cell (Figure 2-6c): i.e. the yarn and the matrix share common nodes at the interface (Figure 2-6c), which has been justified by Gerlach et al. [25]. Finally, the overall fibre volume fraction of the unit cell geometrical model (49.8%) obtained from 'WiseTex' is almost unchanged after meshing in 'MeshTex' (49.2%). Figure 2.6 show the sequence of steps starting from the 'WiseTex' generated satin weave reinforcement and its translation into FE mesh, followed by the meshing of the entire unit cell in 'MeshTex' (reinforcement and matrix). Later, the obtained unit cell mesh will be transferred to the FE software ABAQUS® and assigned with the 8 node brick element (C3D8) for the numerical simulations.

a)
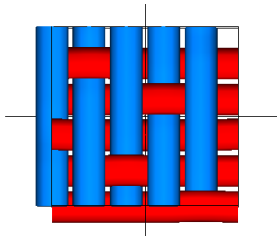
b)
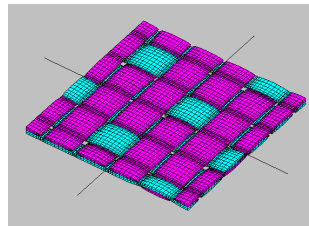
c)
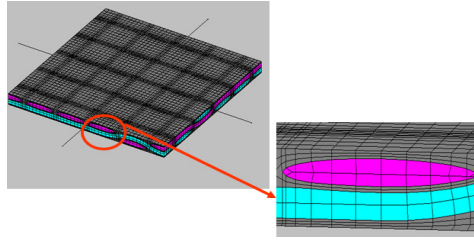
Figure 2-6.   **Satin weave RUC model: a) WiseTex generated RUC model; b) reinforcement FE mesh in 'MeshTex'; c) RUC FE mesh in 'MeshTex'.**

Having the unit cell geometrical model with the FE mesh, the following sections are focused on the detailed discussion of the assignment of material properties and boundary conditions to the unit cell FE model for the numerical simulations.

2. 6.   Micro-scale homogenization of the elastic constants

In order to assign the material properties to the complex unit cell FE model, yarns and fibrous piles are locally (on the scale of one finite element) represented as a uni-directional assembly of fibres [23]. Based on the above statement, to account for the yarn crimp in the FE model, the yarns are descretized in both warp and weft directions according to the local change in the yarn orientation angle (Figure 2-7)[6].
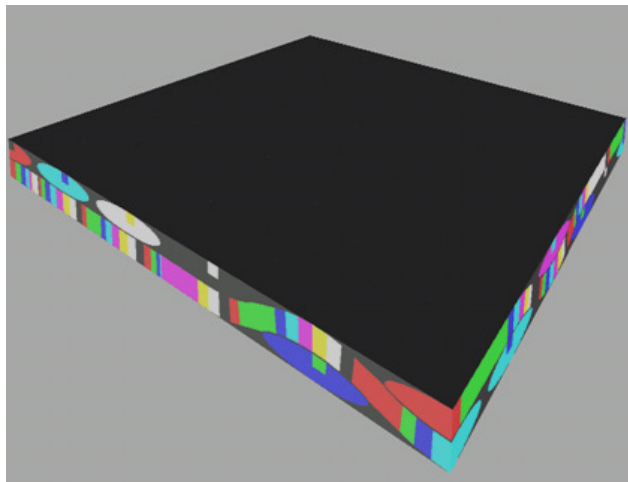
Figure 2-7.   RUC with the local yarn orientation (discreitized sections with different local orientations are shown in different colours).

In order to calculate the impregnated carbon-PPS unidirectional composite material properties, the individual material properties of T300JB carbon fibre and PPS resin (Table 2-5) are used as an input to the analytical Chamis micro-mechanical homogenization formulas [26] (Equation 2.1-2.6). The aforementioned rule-of-mixtures (Chamis) are used by many researchers [23, 27] to calculate the micro-scale material properties of the UD composites in a faster and efficient way. The intra-yarn fibre volume fraction in the satin weave composite impregnated yarn (K_f =0.7) is obtained from the 'WiseTex' software (Table 2-4), and is used to calculate the micro-mechanical elastic properties. In general, the intra-yarn volume fraction depends on the fibre morphology and usually amounts to $K_f = 0.7$ for general carbon fibres [28], which is equal to the fibre volume fraction obtained from the 'WiseTex' software.

Table 2-5.   T300JB carbon fibre and PPS material properties.

T300JB carbon fibre		PPS (resin)	
Longitudinal modulus E_{11}, GPa	231	Modulus of elasticity E , GPa	3.8
Transverse modulus E_{22}, GPa	28	Shear modulus G , GPa	1.38
In-plane shear modulus G_{12}, GPa	24	Poisson's ratio ν	0.37
Transverse shear modulus G_{23}, GPa	10.7		
In-plane Poisson's ratio ν_{12}	0.26		
Transverse Poisons' ratio ν_{23}	0.3		

Note: *T300JB carbon fibre material elastic properties are taken from TORAYCA technical datasheet No: CFA-002. PPS material properties are taken from Ticona PPS data sheet.*

By inserting the individual carbon fibre and PPS material properties (Table 2-5) into the equations 2.1-2.6, Carbon-PPS UD material properties at 70% fibre volume fraction are computed. Table 2-6 presents the comparison between the calculated analytical homogenized elastic constants of the carbon-PPS UD (micro-scale) to the other analytical method known as Concentric Cylindrical Assemblage (CCA) [29] and shows good correlation. The calculated homogenized micro-mechanical material properties are assigned to the yarn cross-sections in their local co ordinate system.

Longitudinal modulus: $E_{l11} = K_f E_{f11} + K_m E_m$ (2.1)

Transverse modulus: $E_{l22} = \dfrac{E_m}{1 - \sqrt{K_f}\,(1 - \dfrac{E_m}{E_{f22}})} = E_{l33}$ (2.2)

Shear modulus: $G_{l12} = \dfrac{G_m}{1 - \sqrt{K_f}\,(1 - \dfrac{G_m}{G_{f12}})} = G_{l13}$ (2.3)

Shear modulus: $G_{l23} = \dfrac{G_m}{1 - \sqrt{K_f}\,(1 - \dfrac{G_m}{G_{f23}})}$ (2.4)

Poisson's ratio: $\upsilon_{l12} = K_f \upsilon_{f12} + K_m \upsilon_m = \upsilon_{l13}$ (2.5)

Poisson's ratio: $\upsilon_{l23} = \dfrac{E_{l22}}{2G_{l23}} - 1$ (2.6)
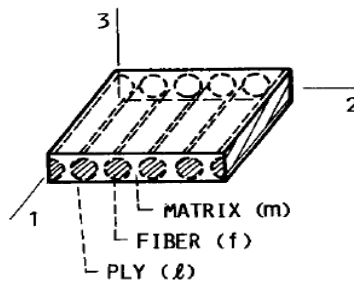
K_f represents the intra-yarn fibre volume fraction in an impregnated yarn.

E, G, υ represent the elastic, shear module and Poisson's ratio respectively

co-ordinate 1 represents the fibre direction

Table 2-6. **Comparison of the homogenized elastic properties of the Carbon-PPS UD between different techniques.**

$K_f = 0.7$	E_{11}, GPa	E_{22}, GPa	G_{12}, GPa	G_{23}, GPa	υ_{12}	υ_{23}
Chamis micro-mechanical homogenization	162.60	13.70	6.50	5.07	0.29	0.35
CCA [29] *Concentric Cylindrical Assemblage*	162.20	15.0	6.20	-	0.28	0.40

2. 7.   Meso-scale homogenization of the elastic constants

After assigning the transversely isotropic material properties to the yarn sections and isotropic material properties to the resin, the current section is focused on the estimation of the satin weave composite effective (macro-scale) elastic properties. To sum up the presented discussion in the previous sections, in order to predict the elastic properties of the satin weave composite, geometry based meso-FE approach is employed along with the application of the homogenization technique. The main point behind this approach is to treat the meso-volume as an assemblage of subcells (yarn sections). A geometric model of the meso-volume reinforcement is constructed, and this model is partitioned according to the change in the local yarn orientation. These subcells are taken as small volumes compared to the yarn size so that the reinforcement within each subcell can be considered as a straight line.

In order to compute the homogenized elastic constants at meso-scale, two different numerical approaches are used. The first approach uses the kinematic boundary conditions to solve the unit cell meso-FE problem [30, 31]. Later, the obtained reactions forces at the constrained unit cell surfaces are used to estimate the effective elastic constants of the satin weave composite (Table 2-7 *Column 3*). In the second approach, along with the application of periodic boundary conditions to the unit cell, volume averaging technique [23] is employed to calculate the homogenized elastic constants of the satin weave composite (Table 2-7 *Column 2*). The detailed description of the above mentioned two approaches is presented in the appendix of this manuscript.

Table 2-7.   **Elastic constants of 5-harness satin weave carbon-PPS composite.**

	PBC and Volume averaging	Kinematics and Surface reactions	Method of Inclusions (TexComp)	Experiment
E_{11}, GPa	56.49	59.5	61.7	57 ± 1
E_{22}, GPa	56.41	59.5	61.7	-NA-
E_{33}, GPa	10.53	10.55	10.56	-NA-
ν_{12}	0.08	0.057	0.053	0.05 ± 0.02
ν_{13}	0.41	0.41	0.44	-NA-
ν_{23}	0.41	0.41	0.44	-NA-
G_{12}, MPa	4280	4305	4297	4175 [19]
G_{13}, MPa	3048	3286	3375	-NA-
G_{23}, MPa	3045	3286	3375	-NA-

In addition to the above specified numerical procedures, the satin weave composite effective elastic constants are estimated using the analytical method of inclusions. The analytical macro-scale elastic constants are computed using 'TexComp' software [32] (developed by MTM at K.U. Leuven). The 'TexComp' software uses the 'WiseTex' geometrical model as an input along with the individual fibre and resin material properties. By using Mori-Tanaka method [33], the effective elastic constants of the satin weave unit cell are estimated (Table 2-7 *column 4*). After estimating the effective (macro-scale) elastic constants using different numerical and analytical procedures, the following section presents the evaluation of the experimental elastic constants. Moreover, comparison between the experimental and numerical elastic constants is accomplished.

2. 8.   Experimental elastic constants and comparison between different techniques

The tensile tests on the satin weave composite specimens were performed on a standard Instron machine (Instron 4505, test speed 0.1mm/min). The composite samples used for the tensile tests were prepared according to the ASTM D3479 standard (width = 25mm, length = 170mm, thickness= 2.5mm), with end tabs of the same material (Carbon-PPS). The local strain during the tensile test is measured using the digital image correlation technique (LIMESS). The global strain is computed over the entire strain window used for the full-field strain registration [34]. Figure 2-11 (a, b) show the evolution of stress vs. strain and Poisson's ratio of the 5-harness satin weave composite under uni-axial static tensile test. In order to obtain the experimental elastic constants, linear regression of the entire stress-strain curve is accomplished. The obtained experimental elastic constants are shown in (Table 2-7 *column 5*).

Finally, the effective elastic constants computed at the unit cell scale are compared to the obtained experimental macro-scale elastic constants. As listed in the Table 2-8, the difference in the value of elastic constants between the PBC's and kinematic boundary conditions is explained by Terada et al. [35]In correlation with the current observation, the authors [35] reported that the computed elastic constants for the $NiAl_2 - Cr$ MMC (Metal Matrix Composites) composite with different procedures show that the kinematic boundary conditions predict higher values than PBC's. The higher predicted values of the kinematic boundary conditions are might be caused by the over constraining of the unit cell faces.

a)
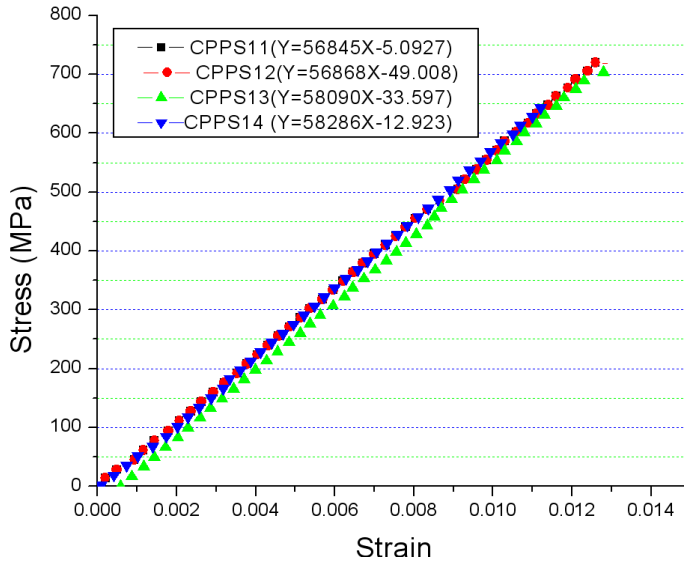
b)
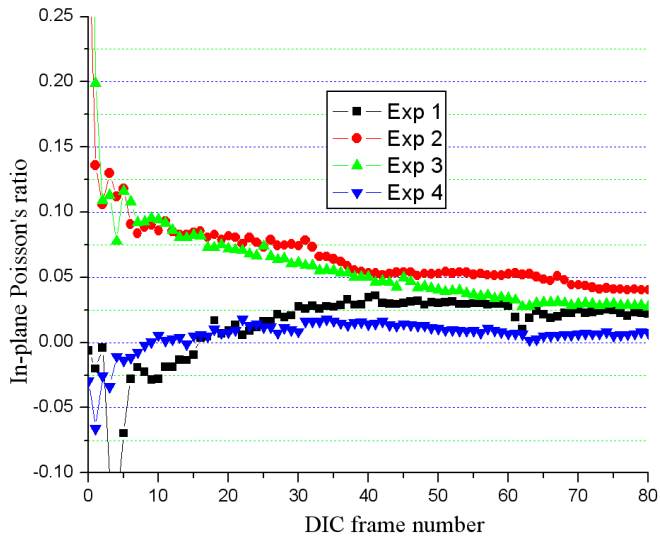
Figure 2-11.   **Experimental results: a) stress - strain curve; b) evolution of the Poisson's ratio.**

2. 9.   Conclusion

The current chapter presented the importance of unit cell FE analysis for the estimation of the homogenized elastic constants of a satin weave composite. A detailed procedure is presented regarding the capturing and construction of the unit cell of a 5-harness satin weave textile reinforcement. Construction of the unit cell geometrical model is accomplished using 'WiseTex' software. Creation of the FE mesh and translation into the FE software is accomplished using 'MeshTex' software. At the micro-scale, Chamis analytical homogenization formulas provide reasonably good material properties compared to the other analytical methods (CCA). At meso-scale, in order to solve the unit cell FE model, different boundary conditions are used. Initially, to estimate the effective elastic constants, homogeneous displacement BC's are applied to the unit cell. The other procedure involved in the estimation of the elastic constants at meso-scale is the application of PBC's along with the volume averaging technique. Among these procedures, PBC's with volume averaging technique predict the homogenized elastic constants that are approximately equal to the experimental elastic constants. On the contrary, kinematic BC's and the analytical methods tend to slightly overestimate the elastic constants.

As a concluding remark, it should be noted that the detailed experimental evaluation of the anisotropic elastic constants of a textile composite is a tedious process and almost impossible to determine with the conventional experimental setups. In this perspective, unit cell FE analysis provides an overall estimate of the homogenized elastic constants of the 5-harness satin weave composite, which are in good correlation to the experimental elastic constants. Moreover, the developed unit cell FE model and the micro-mechanical homogenized material properties will be used in the following chapters of this manuscript for the detailed stress-strain simulations and the damage analysis of a satin weave composite under tensile load.

2. 10.   REFERENCES

[1]   V.Ramanath, N. F.Dow, and B.W. Rosen, *Analysis of woven fabrics for reinforced composite materials* NASA MSC TFR 1715/0210, 1987.

[2]   Srirengan, K., J. Whitcomb, and C. Chapman, *Modal technique for three-dimensional global/ local stress analysis of plain weave composites.* Composite Structures, 1997. **39**(1-2): p. 145-156.

[3]   Whitcomb, J., K. Srirengan, and C. Chapman, *Evaluation of homogenization for global/local stress analysis of textile composites.* Composite Structures, 1995. **31**(2): p. 137-149.

[4]   Whitcomb, J.D., *Three-Dimensional Stress Analysis of Plain Weave Composites.* NASA Contractor Report 101672, 1989.

[5]   whitcomb, *Analysis of New Composite Architectures.* NASA Contractor Report 198506, 1996.

[6]   Lomov, S. and I. Verpoest, *Homogenisation of a sheared unit cell of textile composite FEA and approximate inclusion model.* Department of MTM, Katholieke Universiteit Leuven, 2004.

[7]   Cox, B.N. and G. Flanagan, *Handbook of Analytical Methods for textile composite.* NASA Contractor Report 4750, 1997.

[8]   Barbero, E.J., P. Lonetti, and K.K. Sikkil, *Finite element continuum damage modeling of plain weave reinforced composites.* Composites Part B: Engineering, 2006. **37**(2-3): p. 137-147.

[9]   Michel, J.C., H. Moulinec, and P. Suquet, *Effective properties of composite materials with periodic microstructure: a computational approach.* Computer Methods in Applied Mechanics and Engineering, 1999. **172**(1-4): p. 109-143.

[10]   Hollister, S.J. and N. Kikuchi, *A comparison of homogenization and standard mechanics analyses for periodic porous composites.* Computational Mechanics, 1992. **10**(2): p. 73-95.

[11]   Ghosh, S., K. Lee, and P. Raghavan, *A multi-level computational model for multi-scale damage analysis in composite and porous materials.* International Journal of Solids and Structures, 2001. **38**(14): p. 2335-2385.

[12]   Ostoja-Starzewski, M., *Material spatial randomness: From statistical to representative volume element.* Probabilistic Engineering Mechanics, 2006. **21**(2): p. 112-132.

[13]   Xia, Z., et al., *On selection of repeated unit cell model and application of unified periodic boundary conditions in micro-mechanical analysis of composites.* International Journal of Solids and Structures, 2006. **43**(2): p. 266-278.

[14]   Drago, A. and M.-J. Pindera, *Micro-macromechanical analysis of heterogeneous materials: Macroscopically homogeneous vs periodic microstructures.* Composites Science and Technology, 2007. **67**(6): p. 1243-1263.

[15]   Pindera, M.-J., et al., *Micromechanics of spatially uniform heterogeneous media: A critical review and emerging approaches.* Composites Part B: Engineering, 2009. **40**(5): p. 349-378.

[16]   Desplentere, F., et al., *Micro-CT characterization of variability in 3D textile architecture.* Composites Science and Technology, 2005. **65**(13): p. 1920-1930.

[17]   Schell, J.S.U., et al., *Micro-computed tomography determination of glass fibre reinforced polymer meso-structure.* Composites Science and Technology, 2006. **66**(13): p. 2016-2022.

[18]   Djukic, L.P., et al., *Contrast enhancement in visualisation of woven composite tow architecture using a MicroCT Scanner. Part 1: Fabric coating and resin additives.* Composites Part A: Applied Science and Manufacturing, 2009. **40**(5): p. 553-565.

[19]   Ives, D.B., *Experimental and Numerical Study of Different Setups for Conducting and Monitoring Fatigue Experiments of Fibre-Reinforced Thermoplastics.* PhD Thesis, Gent university, 2008.

[20]   Lomov, S.V., et al., *Textile composites: modelling strategies.* Composites Part A: Applied Science and Manufacturing, 2001. **32**(10): p. 1379-1394.

[21]   Verpoest, I. and S.V. Lomov, *Virtual textile composites software WiseTex: Integration with micro-mechanical, permeability and structural analysis.* Composites Science and Technology, 2005. **65**(15-16): p. 2563-2574.

[22]   Lomov, S.V., et al., *Nesting in textile laminates: geometrical modelling of the laminate.* Composites Science and Technology, 2003. **63**(7): p. 993-1007.

[23]   Lomov, S.V., et al., *Meso-FE modelling of textile composites: Road map, data flow and algorithms.* Composites Science and Technology, 2007. **67**(9): p. 1870-1891.

[24].   Zako, M., Y. Uetsuji, and T. Kurashiki, *Finite element analysis of damaged woven fabric composite materials.* Composites Science and Technology, 2003. **63**(3-4): p. 507-516.

[25]   Gerlach, R., et al., *The interface between matrix pockets and fibre bundles under impact loading.* Composites Science and Technology, 2009. **69**(11-12): p. 2024-2026.

[26].   Chamis, C.C., *Mechanics of Composite Materials Past, Present, and Future.* NASA Technical Memorandum 100793, 1984.

[27]   Xu, J., et al., *Progressive fatigue Damage Modeling of Textile Composite on Meso-Scale with Finite Element Method, Materials Characterization and Experimental Verification.* . 10th International Conference on Textile Composites (TEXCOMP10), Lille, France, 26-28 October, 2010.

[28]   Hofstee, J., H. de Boer, and F. van Keulen, *Elastic stiffness analysis of a thermo-formed plain-weave fabric composite--part III: experimental verification.* Composites Science and Technology, 2002. **62**(3): p. 401-418.

[29]   Hofstee, J. and F. van Keulen, *Elastic stiffness analysis of a thermo-formed plain-weave fabric composite Part II: analytical models.* Composites Science and Technology, 2000. **60**(8): p. 1249-1261.

[30]   He, H., Y.C. Roth, and N. Himmel, *Elastic constants estimation of stitched NCF CFRP laminates based on a finite element unit-cell model.* Composites Science and Technology, 2007. **67**(6): p. 1081-1095.

[31]   Heß, H. and N. Himmel, *Structurally Stitched NCF CFRP Laminates. Part 2: Finite Element Unit Cell Based Prediction of In-Plane Strength.* Composites Science and Technology. **In Press, Accepted Manuscript**.

[32]   S.V.Lomov, *Mechanics of heterogeneous media - Lecture notes.* Department of Metallurgy and Materials Engineering, Katholieke Universiteit Leuven.

[33]   Huysmans, G., I. Verpoest, and P. Van Houtte, *A poly-inclusion approach for the elastic modelling of knitted fabric composites.* Acta Materialia, 1998. **46**(9): p. 3003-3013.

[34.]   Ivanov, D., et al., *Strain mapping analysis of textile composites.* Optics and Lasers in Engineering. **47**(3-4): p. 360-370..

[35]   Terada, K., et al., *Simulation of the multi-scale convergence in computational homogenization approaches.* International Journal of Solids and Structures, 2000. **37**(16): p. 2285-2311.

Chapter 3

LOCAL STRAIN ANALYSIS IN THE SATIN WEAVE COMPOSITE UNDER UNI-AXIAL STATIC TENSILE LOAD

This chapter presents a comprehensive analysis of the local strain behavior in the plies of a satin weave composite. The first part of this chapter presents the various experimental techniques that are used to estimate the local strain behavior in the plies of a satin weave composite under uni-axial static tensile load. In the later sections, extensive meso-FE simulations are accomplished using the 5-harness satin weave unit cell as well as various configurations of unit cell stacks. The aforementioned simulations predict the local strain profiles on the surface as well as in the laminate inner layers of the composite. Finally, conclusions are drawn based on the comparison between the experimental and numerical local strain profiles as well as the strain contours. This work is conducted in the view of analyzing the variation in the local strain behavior of the satin weave composite, influenced by the random internal shifting and nesting of the plies.

3. 1.   INTRODUCTION

The first part of this chapter presents an experimental method for determining the strain distribution in the plies of a thermoplastic 5-harness satin weave composite under uni-axial static tensile load. In contrast to the unidirectionaly reinforced composites, the yarn interlacing pattern in textile composites causes heterogeneous strain fields with large strain gradients in the close locations of the composite, in particular, around the yarn crimp regions. In addition, depending on the local constraints that are posed by the surrounding plies, the deformation behaviour of the laminate inner layers may vary from that of the surface layers, which are relatively more free to deform, compared to the inner layers.

In order to validate the above hypothesis, the local strain on the composite surface was measured using digital image correlation technique (LIMESS). The aforementioned contact less strain measuring technique has a distinct advantage compared to the classical electrical resistance strain gauges, which do not have adequate spatial resolution [1]. The local strain measurements obtained from the full-field method will provide a qualitative (spatial strain distribution) as well as quantitative (local strain values) understanding of the maximum and minimum values of local strains, and their corresponding locations on the laminate traction free surface in the composite width direction. However, there are few publications [2-4] that have studied the effect of adjacent layers in the laminate on the local strain behaviour. The studies mentioned above suggest that the surface strain field is a representative strain field for all layers, which may not be a reliable assumption. As adjacent layers try to suppress the yarn undulation effects of the laminate inner layers, hence causes the local strain profile/gradient inside the laminate vary considerably compared to the surface layers [5, 6]. In this regard, understanding the maximum and minimum strain locations is very important due to the fact that these strain locations indicate the probable damage initiation zones in the composite [2, 7, 8]. In general, the local stress distribution (hence the local strain) in the ply of a textile laminate depends on: 1) the distance of the ply to the surface; 2) number of plies in the laminate; and 3) the stacking sequence and the internal yarn nesting [9].

In the above drawn guidelines from the literature, in order to quantify the local strain variation on the surface as well as inside the laminate, the following experimental approach is employed during the tensile test of a satin weave composite specimen: a) the local strain on the composite surface is quantified using the digital image correlation technique (LIMESS) together with surface mounted fibre optic sensors (FBG-Fibre Bragg Grating);

b) In order to obtain the maximum and minimum local strain values in the laminate inner layers, embedded fibre optic sensors were used. The motivation for the use of this experimental procedure was obtained from the work of [10, 11].

Using full-field strain measurements, the local strain profiles were evaluated on the composite surface both qualitatively and quantitatively. Moreover, surface mounted FBGs provided the quantitative local strain values. Comparison of the local strains obtained from the two independent experimental techniques proves the accuracy of the obtained local strain values. For the quantification of local strains in the laminate inner layers, the only possible experimental technique of fibre optic sensors is employed. Based on the comparison of the local strain values at different locations that were obtained using various experimental techniques, an attempt was made to understand the "shadowing" effects on the local strain behaviour caused by the interaction of randomly placed plies in the satin weave composite. Moreover, the large amount of available experimental data helps in the development of an accurate 5-harness satin weave unit cell computational model for evaluating the local strain profiles using meso-FE simulations.

3. 2.   Experimental methods

3. 2. 1.   Surface strain measurement using DIC

Digital Image correlation (DIC) is a non-contact method for measuring the whole-field displacements in 2D and 3D. In addition, DIC is able to capture severe strain gradients at a close location, thus indicating high spatial resolution [12]. The working principle of DIC as well as the theoretical background for the calculation of strains has been explained by many researchers [12-15]. In order to capture the surface strain field during the tensile test, an approximate length of 40mm ($\cong$ 5 unit cells) in the tensile direction and 25mm ($\cong$ 3 unit cells) in the transverse/width direction is painted with a white spray followed by a black speckle pattern on the surface of the white paint at the centre of the composite specimen (Figure 3-1). For the full-field strain registration during the loading process, the CCD camera was set to capture 2 images/sec over the entire speckle pattern ($40 \times 25 mm$). The details of the LIMESS equipment used for full-field strain registration are shown in Table 3-1.

Table 3-1.   **Details of the strain mapping (LIMESS) equipment [16].**

Software	LIMESS – Vic 2D
Camera	12 bit grayscale 1392×1040 pix
Lens focus distance, mm	16
Correlation subset size, pixels	21
Correlation step size, pixels	5
Strain window, pixels	5
Accuracy for strain, μ strains	200 (=0.02%)

Using the correlation between the initial image of the virgin specimen recorded before any loading and the consequent images taken until just before the final failure of the composite specimen (1.19% of average strain), the local strains were computed at different locations on the laminate surface with 'Vic 2D' software using the strain window settings shown in Table 3-1. The average strain is computed across the entire window of the speckle pattern used for full-field strain registration (Figure 3-1). However, it should be noted that DIC is a surface strain measuring technique. In order to quantify the local strains in the laminate inner layers, fibre Bragg gratings are introduced between the satin weave plies during the composite manufacturing process. The detailed discussion regarding the fibre Bragg grating working principle and the strain measuring procedure is explained in the following section.
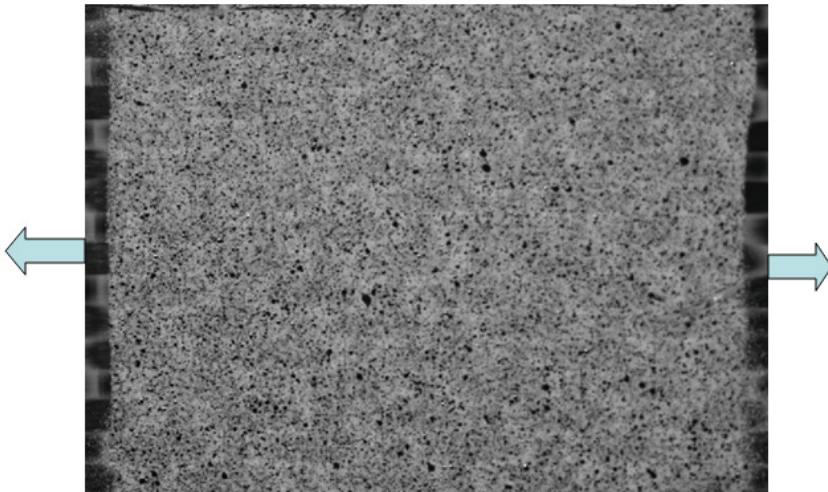
Figure 3-1.   **Specimen with speckle pattern (DIC) used for the tension test.**

3. 2. 2. Strain measurement using fibre Bragg grating sensors

Fibre optic sensors with fibre Bragg gratings (FBGs) are commonly used for local strain sensing, which makes them the optical counterpart to electrical strain gauges. The working principle of the Bragg grating within the optical fibre is explained in Figure 3-2 [17]. When a broadband light with a wide range of wavelengths travels through the optical fibre core containing a Bragg grating, a narrow band of wave length is reflected (λ_{ref}), while the other wavelengths pass through the grating (λ_{trans}). The central weave length of the reflected light is called the Bragg wave length λ_B and this is shown in Figure 3-3.
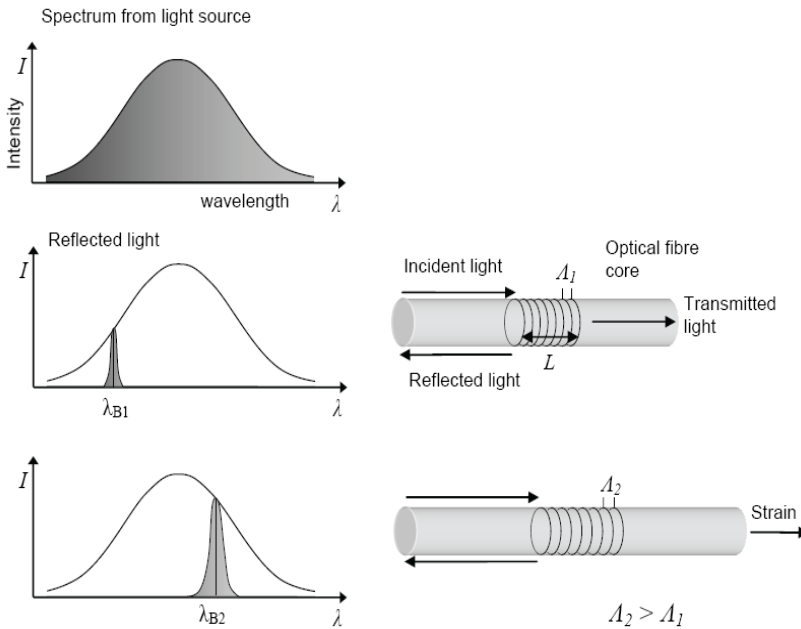
Figure 3-2.   **Schematic view of working principle of a fibre Bragg grating in a optical fibre [17].**

In detail, an FBG is a sensitive element written in the core of an optical fibre. The refractive index changes periodically along a definite length in the fibre, acting as a reflector for a specific wavelength (Figure 3-3). The reflection spectrum is centred on the Bragg-wavelength λ_B which is given by the condition $\lambda_B = 2n_{eff} \Lambda_{FBG}$, in which n_{eff} is the effective refractive index of the core of the optical fibre and Λ_{FBG} is the period of the grating. An FBG has typical dimensions of a few millimetres in length and a diameter of about 0.2 mm.

The reflected Bragg spectrum plot shows Power [dBm] on the y-axis versus Wavelength [nm] on the x-axis, with the relation:

$$\lambda_B = 2 \cdot n_{eff} \cdot \Lambda$$

$$\lambda_B = \lambda_{ref}$$
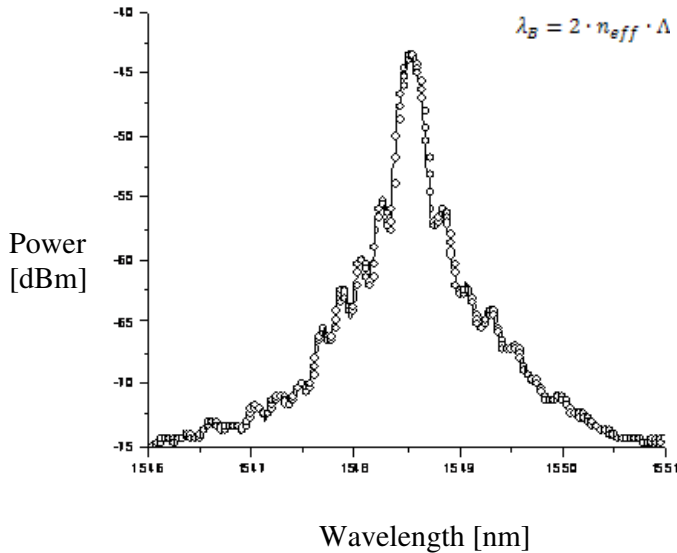
Figure 3-3. **Typical reflected Bragg spectrum and FBG sensor in the fibre core.**

In this study, high strength coated FBGs i.e. DTG®s (Draw Tower Gratings) were used. They can withstand high strain levels and have been found to be suitable for embedding in thermoplastic composites [18]. The approach employed with regard to the use of fibre optic sensors in the current study is twofold: 1) FBGs were being mounted on the surface of the test specimens to measure local surface strains (Figure 3-4); 2) in order to capture the interior strains around the sensor, FBGs were directly embedded between layers of satin weave fabric (Figure 3-5).

52

a)
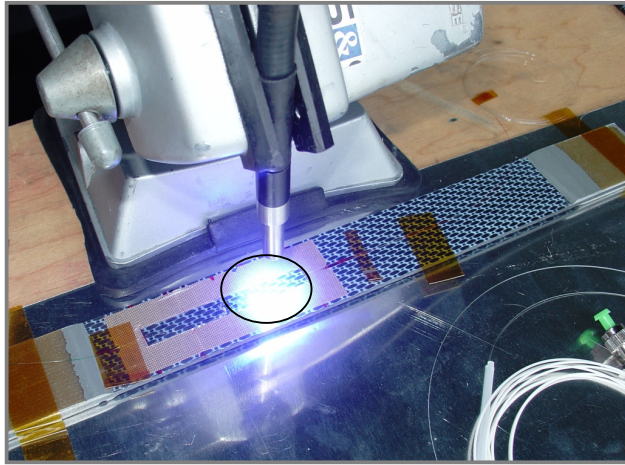
b)
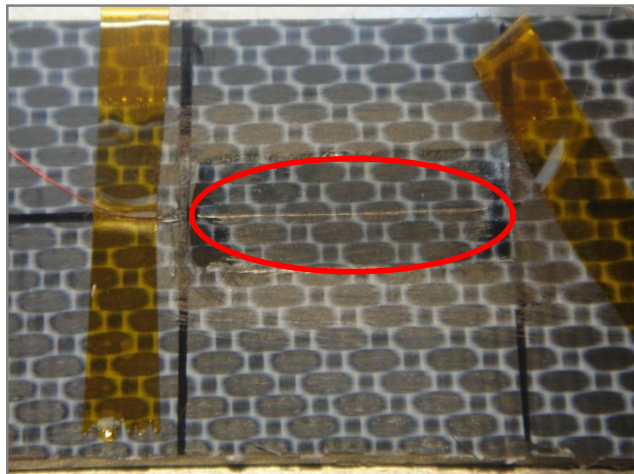
Figure 3-4. **Surface mounted optical fibre sensors; a) glueing of the optical fibre on the test coupon using UV technique; b) mounted optical fibre on the composite surface.**

In both approaches we have used sensors with a length of 8 mm (covering the complete length of one unit cell, i.e. 7.4 mm). All sensors were connected to a commercial Bragg interrogator from FOS&S (FBG-SCAN 608) with a depolarized optical source.

Both the Bragg interrogator and the test bench were linked to a PC and all read-out parameters (force, strain, Bragg spectra) were integrated in one software. During stepwise loading (quasi-static testing) of the composite specimens we were able to capture the response spectra from the composite at each load step. The full spectral response of the FBG sensors and thus the complete Bragg peak deformation was examined for strain analysis. Peak distortion induced by the local non-uniform strain along the grating resulted in multiple small Bragg peaks (Figure 3-3). By converting the individual Bragg peak shifts into strain it is possible to calculate the local longitudinal maximum and minimum strain values along the grating length (8 mm).

a)
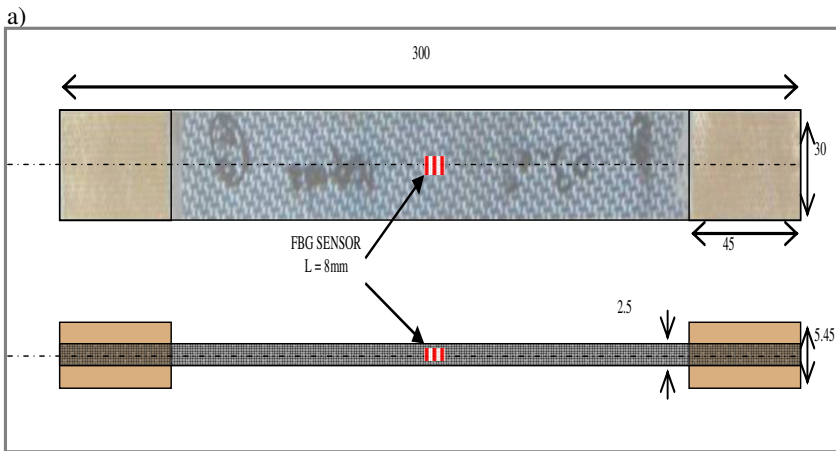
b)
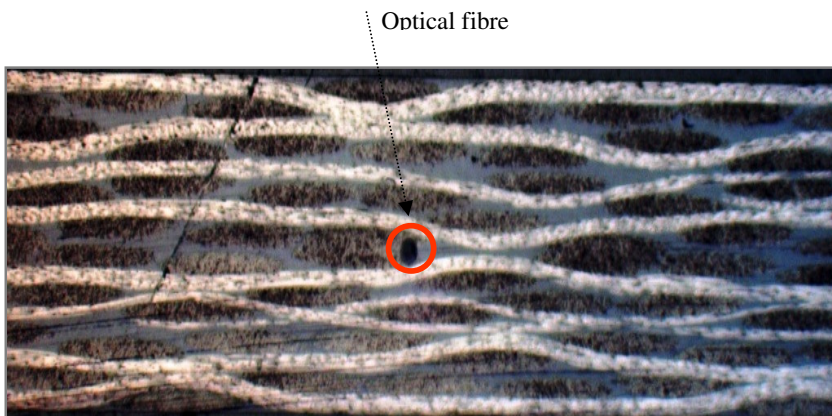
Figure 3-5.   Embedded optical fibre sensors; a) top view; b) side view.

3. 2. 2. a.   Surface strain measurement using FBGs

Three test coupons were prepared with each specimen having two surface bonded 80µm DTG® (high strength FBGs) sensors positioned in the central axis along the load carrying warp yarns (red line in Figure 3-6). The 80µm diameter sensors have a total diameter with ORMOCER® coating of approximately 140µm and an FBG length of 8mm. A special method of the company FOS&S has been employed to fix the sensors in a controlled manner using a UV adhesive and a special sensor pad (patent WO2009106576 (A1)) as shown in Figure 3-4a.

Figure 3-6.   Experimental tensile test set up for measuring the local strains in the composite inner layers using FBGs.

The goal is to measure the local longitudinal strain values (along a unit cell) during the tensile test, and to compare with the strain readings obtained the DIC measurements and FE simulations. In addition to that, the surface strain values were compared with the strain values obtained from the embedded sensors to obtain the influence of the 'shadowing' effects caused by the internal yarn shifting (nesting) on the local strain values.

3. 2. 2. b.   Strain measurement in the laminate inner layers using FBGs

In addition to the surface bonded sensors, the three test coupons mentioned above contain an embedded 125µm DTG$^®$ sensor placed in the central plane of the composite laminate (Figure 3-5b). The 125µm diameter sensors have a total diameter with ORMOCER$^®$ coating of approximately 190µm and an FBG length of 8mm.

It should be emphasized that the embedded sensor is surrounded by matrix material, yarns and warp and weft yarn cross-over points inducing a more complex strain field compared to the surface mounted sensors. It is therefore important to distinguish the transversal effects on the longitudinal strain measuring capabilities of the optical fibres. Previous research of Voet et al. [19] has shown that transversal strains cause: i) optical birefringence effects in the core of the optical fibre; ii) non-uniform strain along the length of the FBG causing an in-fibre strain distribution. Both effects can be characterized by looking into the reflected spectrum of the Bragg peak. In addition, there is a strong correlation between the strain field acting on the embedded grating and the deformation of the reflected Bragg spectrum [20, 21]. However, further investigations on this issue have shown that the birefringence effect in the thermoplastic test specimens is mainly caused by the residual transverse stresses induced during the composite manufacturing process, and does not change significantly during the load process; i.e. from the beginning to the end of the loading process this effect stays more or less the same (below strain levels of 0.05%). It can be stated that the Bragg peak deformations examined in this study were principally induced by longitudinal strain effects along the Bragg grating.

Finally, cross-sectional views of the composite laminate with an embedded optical fibre (Figure 3-7a, b) after the final failure of the composite showed that the optical fibre remained completely bonded to the host composite material, which ensured the correct and constant measuring of the local strains during the loading process.

a)
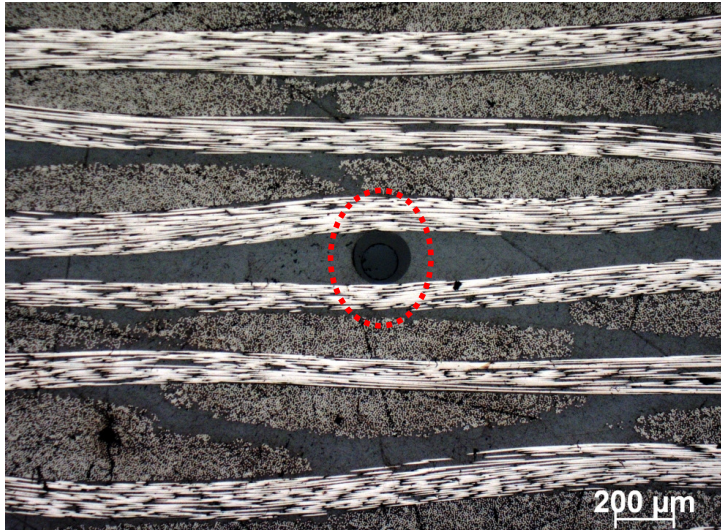
b)
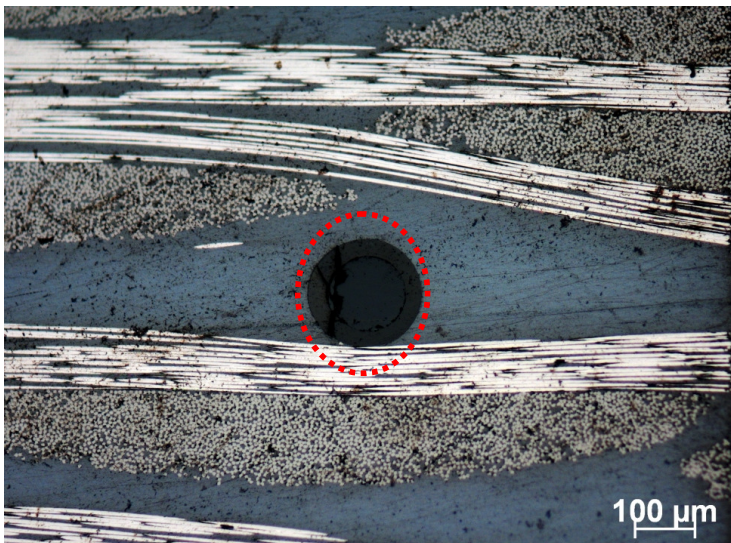
Figure 3-7.   a, b) Cross-sectional views of the optical fibre embedded in the composite inner layers.

3. 3.   Longitudinal strain calculation method

In order to calculate the longitudinal local strain from the reflected spectrum of the fibre optic sensors, a logarithmic approach has been employed. To measure the strain independent of the environmental temperature fluctuations, a temperature compensating plate with a cantilever design is used. A DTG is fixed on the surface of the temperature compensating plate. It is then fixed on the test-coupon using of some adhesive tape. The cantilever design ensures that no strain is applied on the temperature compensating plate, hence only thermal strain fluctuations are measured by the surface mounted DTG. With the above procedure, the strain induced in the composite specimen is calculated using the initial reference spectrum compared to the deformed spectrum under the applied tensile load. Moreover, for the strain formulation, temperature terms also added as shown in the below equation.

$$\Delta \varepsilon = \frac{\left(\ln \frac{\lambda_\varepsilon}{\lambda_{\varepsilon,0}} - \ln \frac{\lambda_T}{\lambda_{T,0}} \right)}{S_\varepsilon} = \frac{\left(\ln \frac{\lambda_\varepsilon}{\lambda_{\varepsilon,0}} - \ln \frac{\lambda_T}{\lambda_{T,0}} \right)}{0.777} \qquad (3.1)$$

The above equation is used to calculate the temperature compensated strain, where $\lambda_{\varepsilon,0}$ and $\lambda_{T,0}$ are the wavelength at the start of the measurement of the strain sensor and the temperature senor, respectively, λ_ε and λ_T are the respective measured wavelengths after applying the tensile load. Finally, the term S_ε represents the calibrated strain gauge factor [19]. Using the above mentioned experimental techniques, the obtained local strain values (surface, inside the laminate) are discussed in the following sections.

3. 4.   Analysis of the experimental local strain profiles

3. 4. 1.   Local strain analysis on the composite surface (DIC)

Initially, local surface strain analysis is performed using DIC data obtained from the uni-axial tensile tests. Figure 3-8(a, b) depicts the local surface strain evolution on the composite surface at different applied average tensile strains (0.5% and 1.19%) in the warp yarn direction.

a)

0.00407677   0.00631524

b)

0.009226   0.01529
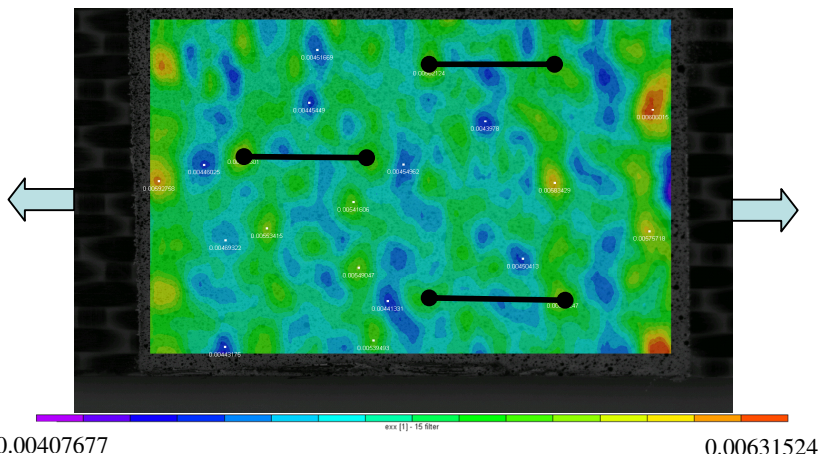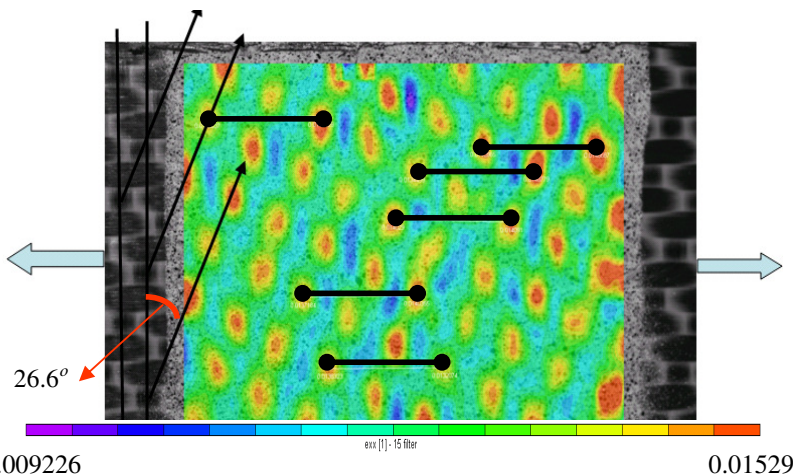
Figure 3-8.   Evolution of the local longitudinal strain profiles: a) surface strain contours at 0.5%; b) surface strain contours at 1.19%.

Based on the surface strain contours (Figure 3-8b), it is evident that the maximum and minimum strain concentration occurs in a periodic manner at an angle of 26.6^{o} from the perpendicular weft yarn at the yarn crimp location. Figure 3-9 shows the typical longitudinal (x-direction) local strain profiles and their evolution on the composite surface starting from 0.2% to 1.19% of the applied average tensile strain. By plotting the longitudinal local strain profile at various locations on the composite surface over the length of one unit cell (7.4 mm) starting from one yarn crimp location to another (marked locations in Figure 3-8b), the maximum local strain of 1.49% is observed at the centre of the weft yarn at the yarn crimp location for the applied 1.19% average tensile strain. From the observation of the strain profiles as well as strain contours, the entire local longitudinal strain distribution on the composite surface (Figure 3-9) can be categorized into three parts:

- the maximum local longitudinal strain (1.3-1.49%) on the composite surface occurred at the centre of the weft yarn at the yarn crimp locations (Section 1 in Figure 3-9).

- the minimum local longitudinal strain (1.0-1.15%) in the entire surface strain field is observed in the resin pockets at the geometrical transition location between the load carrying warp yarn and the perpendicular weft yarn (Section 2).

- finally, the third phase of the local longitudinal strain is detected at the straight position of the load carrying warp yarn, which varies (1.15-1.25%) in the close limits of the applied average tensile strain to the composite (1.19%) (Section 3).

Based on the local strain variation as well as the strain pattern observed from the DIC measurements, the strain gradient is computed as explained in [22]. From the maximum strain location at the centre of the weft yarn to the adjacent matrix pocket (minimum strain) over the length of 1.22 mm, the maximum strain gradient of $3.9 \times 10^{-3} \, mm^{-1}$ is observed in the marked location 1-2 (Figure 3-8).
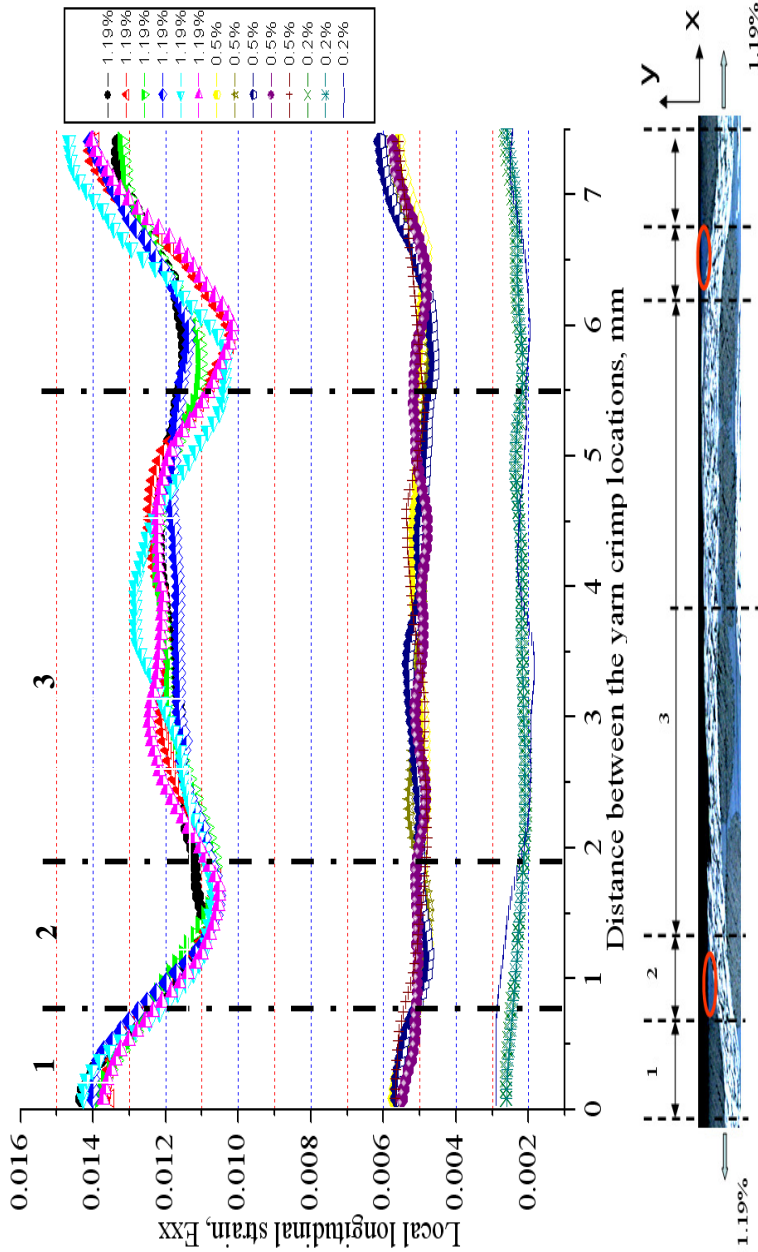
Figure 3-9. Evolution of the local strain profile from 0.2% to 1.19% of the applied average tensile strain.

From the in-plane transverse strain spatial distribution as well as the strain profiles (Figure 3-10(a, b)), it is observed that the compressive transverse strain caused by the Poisson's effect occurred at the load carrying warp yarn as well as in the resin rich regions. The positive transverse strain occurred at the centre of the weft yarn at the yarn crimp locations.

a)

-0.00402697   0.00626809
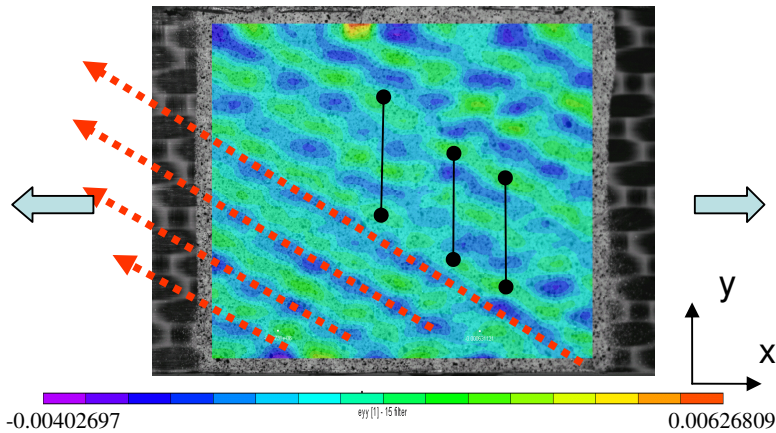
b)
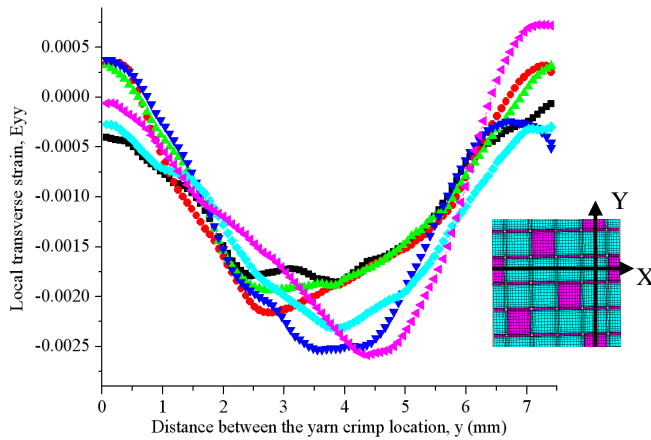
Figure 3-10. **Local transverse strain analysis at 1.19% of the applied longitudinal strain: a) transverse surface strain contours; b) transverse strain profiles between the yarn crimp locations of one unit cell.**

As marked in Figure 3-10a, the transverse strain profiles (Figure 3-10b) are plotted in the y-direction at different locations on the composite surface. As stated above, the initial phase of the strain profile starts from the centre of the weft yarn at the yarn crimp location with the slight positive transverse strain. The second and the third phase of the strain profile undergoes the compressive strain at the resin pockets as well as at the straight position of the load carrying warp yarn. The maximum compressive strain at around 0.027% is detected at the straight portion of the warp yarn.

Figure 3-11 presents the in-plane shear strain spatial distribution on the composite surface. The obtained in-plane shear strain contours are almost similar to the in-plane transverse strain contours (Figure 3-10a). The maximum local positive shear strain is about 0.03% and the similar value with the negative sign occurs at the other end of the strain spectrum, for the applied average tensile strain of 1.19%. Maximum and minimum shear strain locations seem to occur around the load carrying warp yarns (Figure 3-11). However, local shear strain analysis on the plain weave composite surface using the shear grating technique by Lee et al. [3] concludes that the shear strain reaches maximum values in the pure resin rich regions influenced by the tension/in-plane shear coupling effects at the yarn crimp region. Moreover, concerning the weft yarns, one side of the weft yarn sustains the positive shear strain while the other side undergoes the negative shear strain. In the following sections, detailed qualitative and quantitative analysis using unit cell meso-FE simulations provide the substantial evidence as well as the countercheck for the experimental strain locations.

-0.00350885   0.00675996
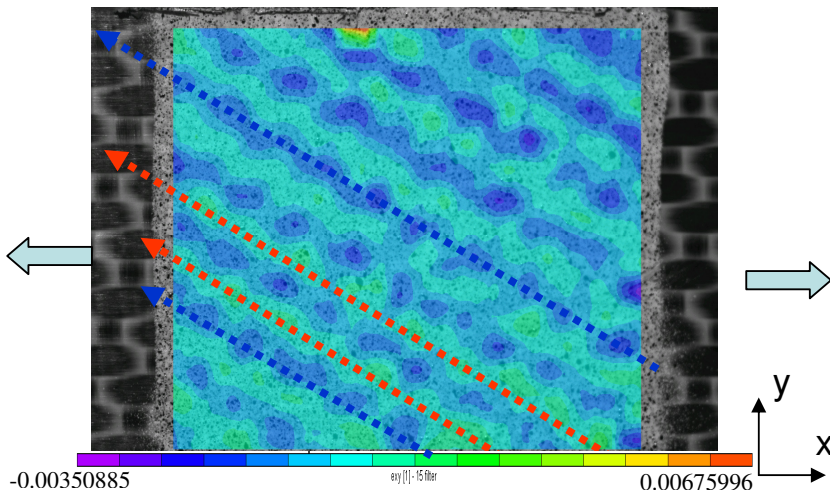
Figure 3-11.   **In-plane shear strain contours at 1.19% of the applied average tensile strain.**

The above section provides a detailed discussion of all in-plane strain components that are measured on the composite traction free surface in the width direction. However, it should be noted that the textile composite manufacturing process induces the lateral shift in the layers with respect to each other, and the compression of the layers causes the nesting (interpenetration of the yarns) between the adjacent plies in the composite in the thickness direction. Figure 3-12 (a, b) shows the difference in the periodic weave pattern on the composite free edges in the width and the shifted (nested) random pattern in the thickness direction.

As discussed in the previous sections, in correlation to the periodic weave pattern in the composite width direction (Figure 3-12a), all the local surface strain contours occurred in a periodic manner. In order to estimate the effect of ply shifting and nesting on the local strain behaviour in the composite inner layers (Figure 3-12b), following sections present the local strain data that is obtained from the embedded fibre optic sensors. Moreover, a comparison between the local strains on the traction free surface (DIC) and the laminate inner layers (FBGs) is presented.

a)
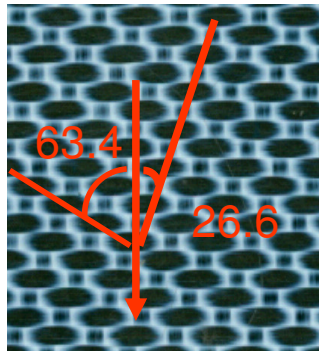
b)
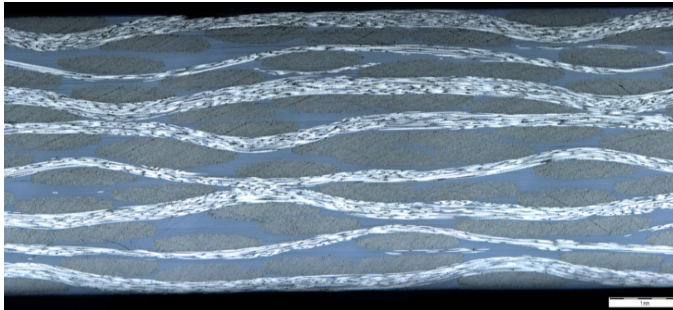
Figure 3-12.   5-harness satin weave composite weaving pattern: a) periodic weave pattern on the composite surface (width direction); b) randomly stacked and nested plies in the composite thickness direction.

3. 4. 2.   Local strain measurement using FBGs

In order to calculate the local strain in the composite inner layers, the following approach is employed. Based on experimental acoustic emission and microscopic analysis of the same composite material, it has been shown previously by the authors [23, 24] that the damage initiation in different layers of the satin weave composite is a sequential process (detailed discussion regarding the damage analysis is presented in Chapter 4). Damage initiation began in the laminate inner layers at 0.2%, followed by damage initiation on the surface layers at around 0.6% of the global tensile strain. In order to avoid the complexities posed by the damage initiation and propagation on the strain measuring capabilities of the optical fibre, the comparison of local strain between the traction free surface (DIC) to the laminate inner layers (FBG) is accomplished in the elastic range.

Figure 3-13a shows the embedded optical fibre response at various applied global tensile strain levels. Along with the thermal residual strains, the yarn crimp in the satin weave composite produces a deformed spectrum of the embedded sensor, without the application of any external structural load (dotted spectrum in Figure 3-13a). Subsequently, application of the external tensile load produces the deformed spectra. Using equation 3.1, the local strains in the composite inner layers as well as on the traction free surface (Figure 3-13(a, b)) are computed at different average tensile strains and listed in Table 3-2.

a)
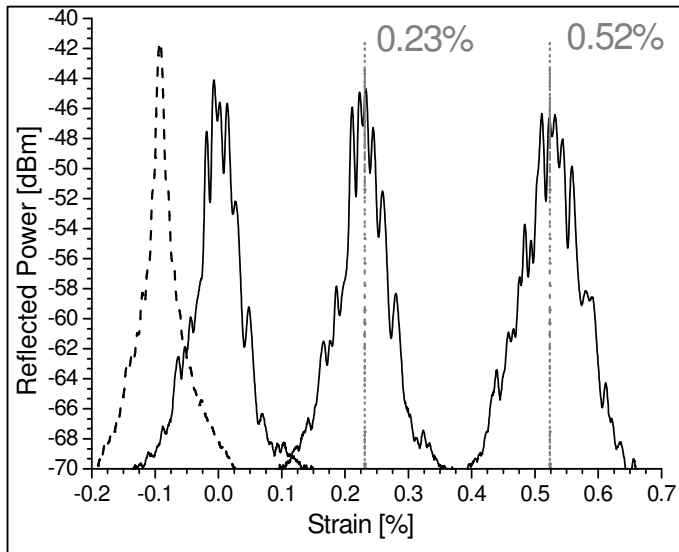
b)
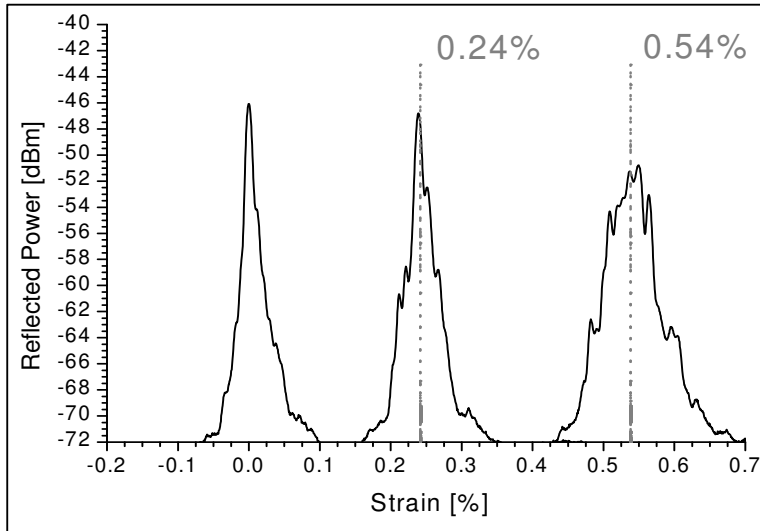
Figure 3-13.   **Optical fiber response spectrum at various strain levels: a) laminate inner layers; b) on the laminate traction free surface.**

From Table 3-2 it is evident that, for the applied average tensile strain at around 0.2% and 0.5%, embedded sensors detect the maximum local strain at around 0.25 and 0.55% respectively. Moreover, in correlation to the DIC strain data, the FBGs show a similar trend in the local maximum and minimum strain values. Comparison of the local strain values obtained from the DIC and the FBG (Figure 3-13b) on the composite surface is accomplished at the global tensile strain of $0.5 \pm 0.01\%$ in the load carrying warp direction, and shows very good correlation (Table 3-2).

Table 3-2.   **Comparison of the local strain values - DIC vs. FBGs.**

	Average strain	*Local strain at the yarn crimp(weft),%*	*Local strain at the flat yarn (warp),%*	*Local strain in the matrix,%*
FBGs –inside	$(0.2 \pm 0.01)\%$	0.25	-NA-	0.16
FBGs –inside	$(0.5 \pm 0.01)\%$	0.55-0.57	-NA-	0.43-0.45
FBGs - surface	$(0.5 \pm 0.01)\%$	0.56-0.57	-NA-	0.42-0.45
DIC	$(0.5 \pm 0.01)\%$	0.58-0.62	0.48-0.52	0.43-0.46

The obtained local strain values at different locations of the laminate show that the effect of the internal yarn shifting (nesting) is negligible on the local longitudinal strain behaviour of the satin weave composite. The obtained local strain behaviour in the plies of a satin weave is in correlation to the observation made by [25] on the intra-yarn damage analysis of a 4-harness satin weave composite. According to Duplessis Kergomard et al. [25], the local stress hence the local strain is affected mainly by the position of the ply in a weave structure, and the variability in the micro- and meso-structure. However, similar local strain behavior at various positions of the laminate suggests that the effect of internal yarn nesting is negligible on the local longitudinal strain values compared to the local strains induced at the yarn crimp region, by straightening of the weft yarns.

3. 5.   Summary of the experimental local strain analysis

Comprehensive experimental local strain analysis is performed on a thermoplastic carbon-PPS 5-harness satin weave composite under uni-axial static tensile load. For the analysis of local strain on the laminate surface, a full-field strain measuring technique (DIC) is applied along with fibre optic sensors. In order to detect the local strain inside the laminate, fibre optic sensors were embedded into the laminate during the composite manufacturing process. The detailed summary of the experimental results is presented here.

- The maximum local strain on the laminate surface occurs at the centre of the weft yarn at the yarn crimp location, while the minimum strain occurs in the resin pockets adjacent to the yarn crimp locations.

- Along the straight portion of the warp yarn, the local strain is almost equal to the average strain applied to the laminate.

- At the applied average tensile strain of 0.5%, the local maximum and minimum strain values obtained from the surface mounted and embedded optical fibres show almost the same strain, indicating that the 'shadowing' effects are negligible on the local longitudinal strain behaviour in the plies of a satin weave composite.

The qualitative strain locations observed in the current study are compared to the maximum and minimum strain locations that have been observed in other studies on the local strain analysis of plain and twill weave composites [4, 26] under uni-axial static tensile load. From the above observations, it might be concluded that for all 2D woven composites, the local in-plane strain components such as longitudinal, transverse and shear strains show similar behaviour on the composite traction free surface. Finally, consistency in the local strain values obtained from the different experimental techniques demonstrates the accuracy of the used experimental procedures.

With the above background of the experimental local strain analysis, the following sections of the current chapter are devoted to develop the unit cell FE analysis procedure for predicting the heterogeneous local strain fields both qualitatively and quantitatively comparable to the experimental strain profiles.

3. 6.   Numerical evaluation of the local strain profiles

In the process of developing a numerical procedure for the analysis of textile composites using the unit cell meso-FE simulations, the primary goal of the current chapter is to validate the obtained unit cell FE local strain profiles against the above discussed experimental local strains. Moreover, it is intended to achieve an inclusive knowledge regarding the maximum and minimum strain locations that are obtained from the above discussed experimental analysis. In the numerical simulations stand point, analysis of heterogeneous strain fields in the textile composites, recent publications [2, 4, 7] underscore the importance of the accurate prediction of local strain profiles as well as strain contours. Based on the evaluation of local strain profiles and gradients, reliable predictions of the damage initiation and strength can be accomplished. In this regard, developing a unit cell computational model which can predict the local strain profiles as observed in the experiments can be a challenging task. Previous research work [1, 12, 27] in this area dealt with the FE analysis of a single unit cell using infinite laminate boundary conditions (3D Periodic Boundary Conditions-PBCs). However, comparison of the experimental stress-strain profiles with the meso-FE results [2, 4, 5, 28, 29] leads to the conclusion that it is difficult to achieve an exact correspondence between the ideal unit cell computational strain profiles compared to the nested and more complicated composite laminates used in the experimental analysis.

In the process of improving the traditional unit cell FE analysis procedure, Owens et al. [30] and Ivanov et al. [5, 6] accomplished the unit cell FE analysis using finite and infinite laminate conditions. The above work concludes that there is a substantial difference in the stress (hence the strain) distribution in the laminate outer layers compared to the inner layers.

Based on the above observations from the literature, detailed local strain analysis in the plies of a 5-harness satin weave composite is accomplished using unit cell FE simulations as outlined in the current section: 1) computation of the local strain profiles inside the laminate is accomplished with the well established meso-FE procedure i.e. a single unit cell with 3D PBCs (infinite laminate). Later, the computed numerical strain profiles are compared to the optical fibre local strains obtained from the laminate inner layers; 2) for the computation of surface strain profiles, initially, a single unit cell with in-plane PBCs is used for the FE analysis. However, comparison of the single unit cell FE strain profiles and contours with the surface strain measurements obtained from the digital image correlation (DIC) reveals that neither 3D PBC nor in-plane PBC applied to the single unit cell are capable of capturing the local strain behaviour both qualitatively and quantitatively comparable to the DIC strain profiles.

From the above mentioned observations, to capture the 'shadowing' effects caused by internal ply shift of the beneath layers on the surface strain pattern, different unit cell stacks were developed as explained in [31]. The afore mentioned study shows that the increase in tension/bending coupling effects at the yarn crimp location for different ply stacking configurations will reduce the effective elastic modulus. And the order of the calculated numerical effective elastic constants for different unit cell stacking configurations in the ascending order is as follows: "cross-ply > random-phase stacking > out-of-phase stacking > iso-phase stacking > single lamina".

From the above observations, to compare the FE local surface strain profiles with the experimental DIC strain results, FE simulations are accomplished using different unit cell stacking configurations. The underlying principle in the FE analysis of the unit cell stacks with various ply configurations relies on the fact that by allowing or constraining the yarn undulation in different degrees at the yarn crimp location, FE analysis of the different unit cell stacks combined with appropriate boundary conditions provides an insight into the variation of the local strain values in the carbon-PPS 5-harness satin weave composite. Moreover, variations in maximum and minimum strain locations can be determined at different locations of the unit cell.

3. 7.   Evaluation of the numerical local strain profiles and comparison with the experimental results

3. 7. 1.   Local strain analysis in the laminate inner layers

For the local strain analysis using meso-FE simulations, the satin weave unit cell FE model developed in the previous chapter (Chapter 2) will be used for the purpose of computational exercise in the current chapter. As explained in the previous section, experimental AE (Acoustic Emission) and microscopic analysis of the composite specimen during quasi-static tensile tests on the carbon-PPS 5-harness satin weave composite [32] reveal that the weft yarn damage in the laminate inner layers occurs around the global tensile strain of 0.2%, followed by the surface layers weft yarn damage at a global tensile strain of around 0.6%. In order to calculate the local strains in the elastic regime and to compare with experimental fibre optic sensor results, an average tensile strain of 0.2% is applied to the unit cell in the warp yarn direction (Figure 3-14a) along with the 3D PBCs [27, 33]. Thus the computed local strain values belong to the composite inner layers.

Figure 3-14(a, b) shows the local strain pattern on the scale of a single unit cell with the matrix as well as on the reinforcement alone. Figure 3-14c depicts the local longitudinal strain profile plotted over the length of one unit cell in the load direction from one yarn crimp to the other as marked in the dotted line in Figure 3-14a. In correlation with the above stated experimental three stage surface strain behaviour, from Figure 3-14(b, c) it is evident that the maximum tensile strain (0.27%) in the unit cell occurs at the edges of the weft yarn at the yarn crimp location. The minimum local strain (0.17%) in the entire unit cell is detected in the matrix blocks at the geometrical transition location between the yarn crimp (weft) to the straight yarn position (warp). Finally, along the straight position of the load carrying warp yarn, the mean strain of 0.18 -0.19% is observed.

Comparison of the FE local strains (unit cell-3D PBCs) with the FOS (Fibre Optic Sensor) results measured in the laminate inner layers (Table 3-2) shows very good correlation starting from the maximum to the minimum strain values. Based on the heuristic approach, it is assumed that the local strain values measured from the optical fibre sensor inside the laminate (maximum, minimum) belong to the same locations as observed in the unit cell FE analysis.

a)

b)

Maximum   Average   Minimum
strain   strain   strain
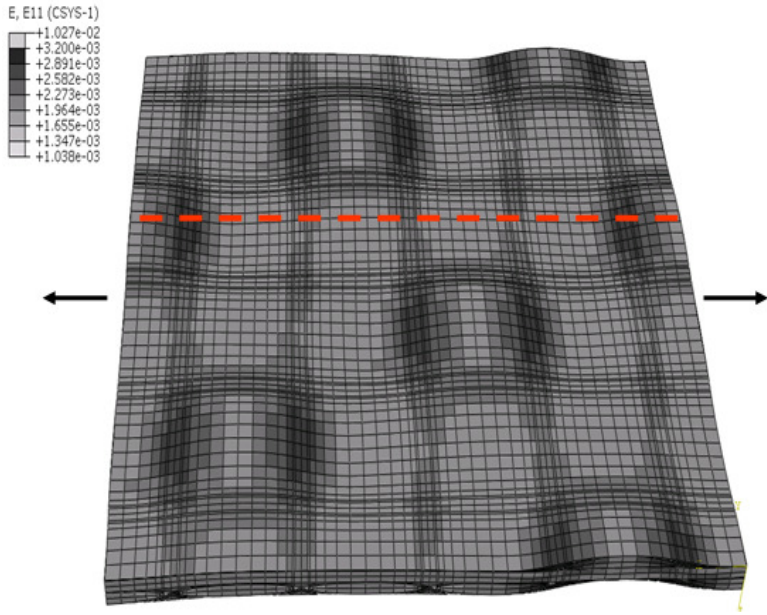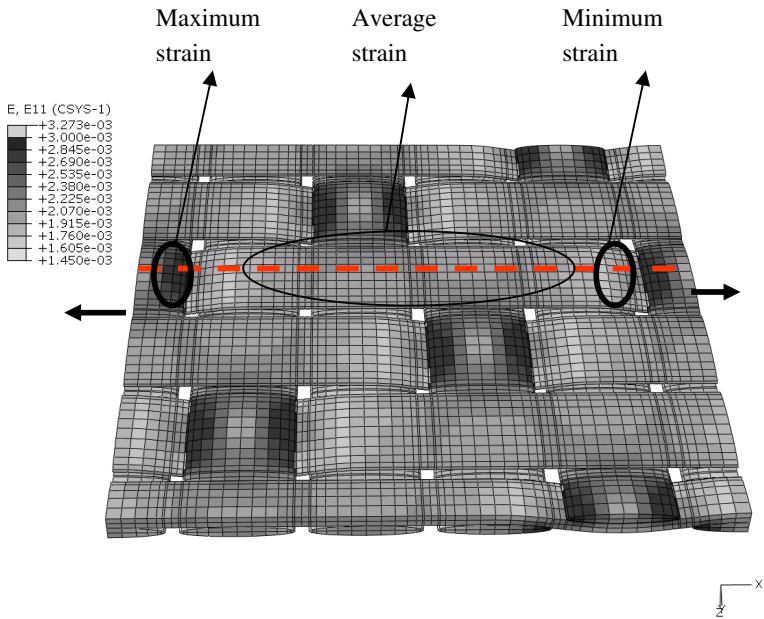
c)
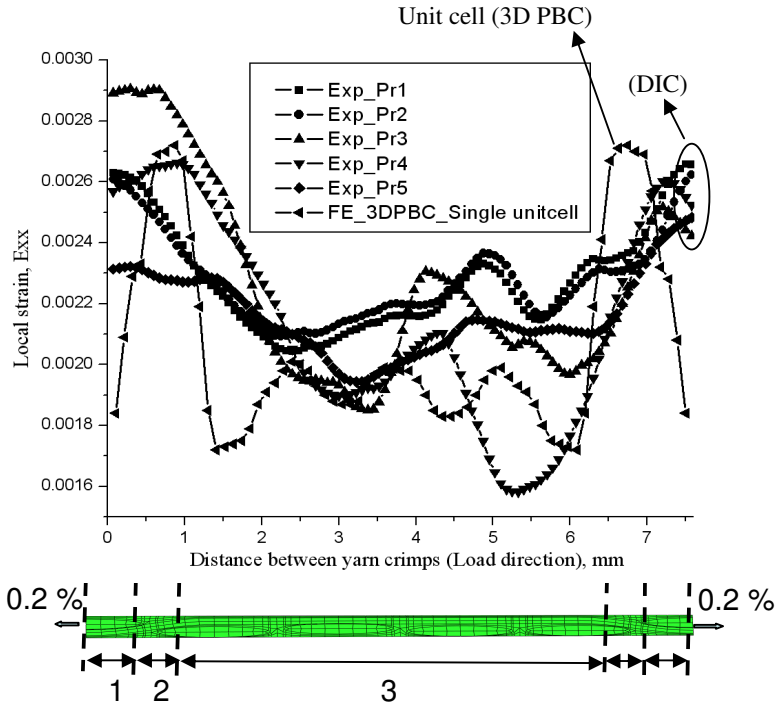
Figure 3-14.   **Analysis of the local strain contours using a unit cell with 3D PBC at 0.2% of the average tensile strain: a) local strain contours on the unit cell; b) local strain contours on the reinforcement; c) comparison between the experimental and numerical local strains.**

Moreover, comparison of the experimental (surface) and numerical (3D PBC-inside the laminate) local strain profiles (Figure 3-14c) shows that, quantitatively, the predicted FE local strain values are within the close limits of the experimental surface strain values. However, qualitative (spatial surface strain distribution) comparison of the experimental and numerical strain locations (Figure 3-14a and Figure 3-8b) indicates that there is a difference in the maximum and minimum strain locations.

Figure 3-15 presents the local in-plane shear strain locations and profile on the unit cell surface under the applied tensile load. From Figure 3-15a, it is observed that the maximum shear strain occurs in the resin pockets along the load carrying warp yarn. Moreover, the in-plane shear strain in the resin pockets is induced by the tension/in-plane shear load coupling effects caused by the weaving process.

a)

b)
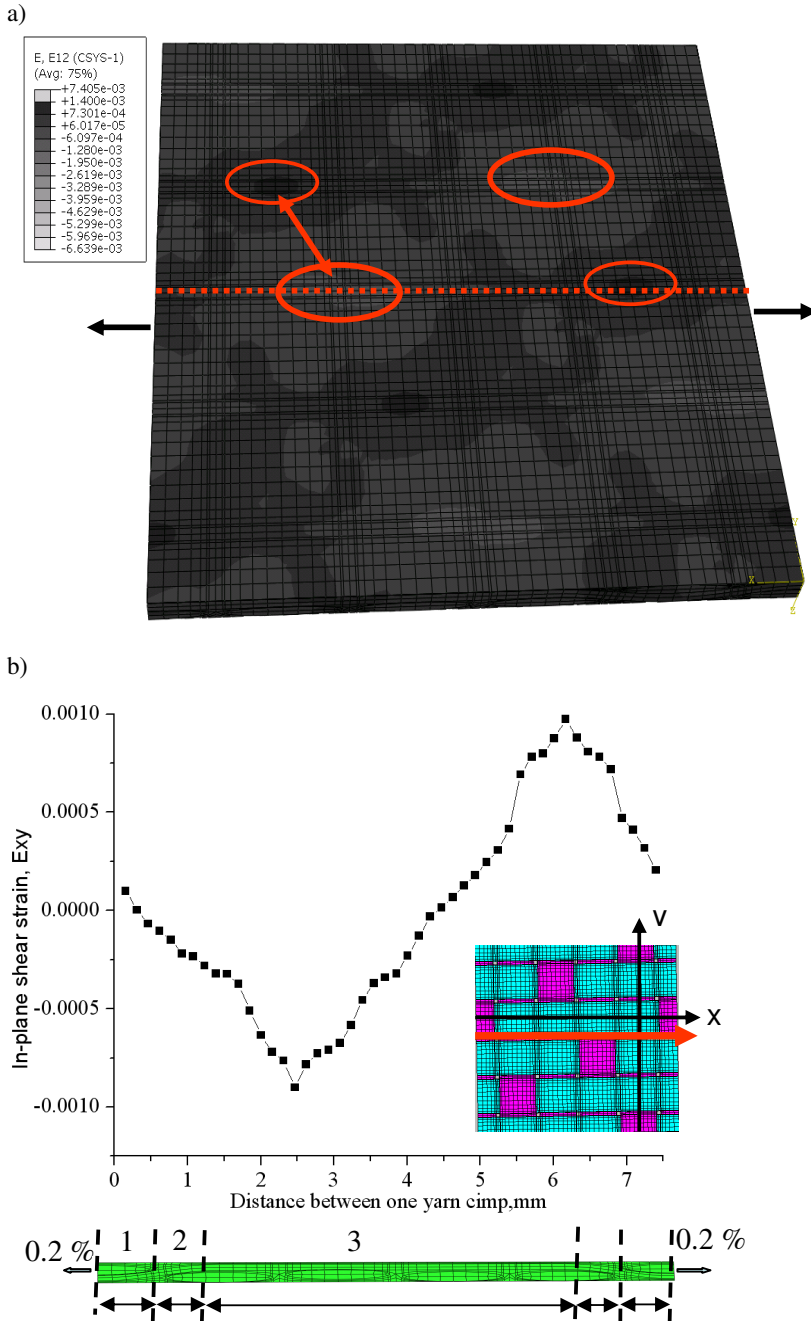
Figure 3-15.   **Local shear strain analysis (unit cell 3D PBC-0.2%): a) shear strain contours on the unit cell surface; b) shear strain variation between two yarn crimp locations.**

As shown in Figure 3-15b, the shear strain profile on the unit cell surface is plotted along the edge of the warp yarn between two yarn crimps. Almost zero shear strain is detected at the centre of the weft yarn at the yarn crimp locations. The negative shear strain value is detected at the edge of the warp on one side, and the same value with the positive sign is detected at the other side of the warp yarn at the straight portion. Moreover, the computed shear strain profiles are similar to the experimental shear strain profiles reported by [3, 4] on the twill and plain weave composite surface.

Concerning the longitudinal local strain values, the probable reason for the above stated qualitative difference in the local strains (profiles and contours) between the experimental and numerical strain profiles might be caused by the restriction of the local bending of the weft yarn at the yarn crimp location by the infinite laminate conditions (3D PBC). In addition, it should be noted that Figure 3-14c compares the traction free surface strain profiles (DIC) to the obtained numerical strain profile in the laminate inner layers. The afore mentioned observations underscore the necessity for improvement in the unit cell FE procedure used for the surface local strain analysis. In order to understand the obtained difference in the computed (inner) local strain profile compared to the surface local strain profiles (DIC), a unit cell stack should be developed with the internal yarn nesting that is present in the textile laminate. Consequently, BC's used for the meso-FE simulations should be changed according to the BC's that are prevailing in the composite laminate under the experimental tensile test. However, producing a unit cell stack with all nesting details that are present in a textile laminate is practically not feasible. The above mentioned problem can be circumvented by creating different unit cell stacking configurations for the FE analysis as explained in [31, 34]. Apart from the computation of the local strains at various locations of the composite, different unit cell stack FE analyses provide an insight into the effect of internal yarn shifting (nesting) on the surface local strain pattern.

3. 7. 2.   Local strain analysis on the laminate traction free surface

As explained in the previous section, for the calculation of local strain profiles in the elastic strain regime on the unit cell traction free surface, an average tensile strain of 0.5% is applied to the unit cell in the warp yarn direction. Initially, for the simulation of the surface strain profile, FE analysis is started with a single unit cell using in-plane periodic boundary conditions. Comparison of the FE local strain values with the DIC local strains at the average tensile strain of 0.5% (Figure 3-16b) shows that the single unit cell FE analysis predicts 50% higher local strain at the yarn crimp compared to the DIC results.

a)

b)
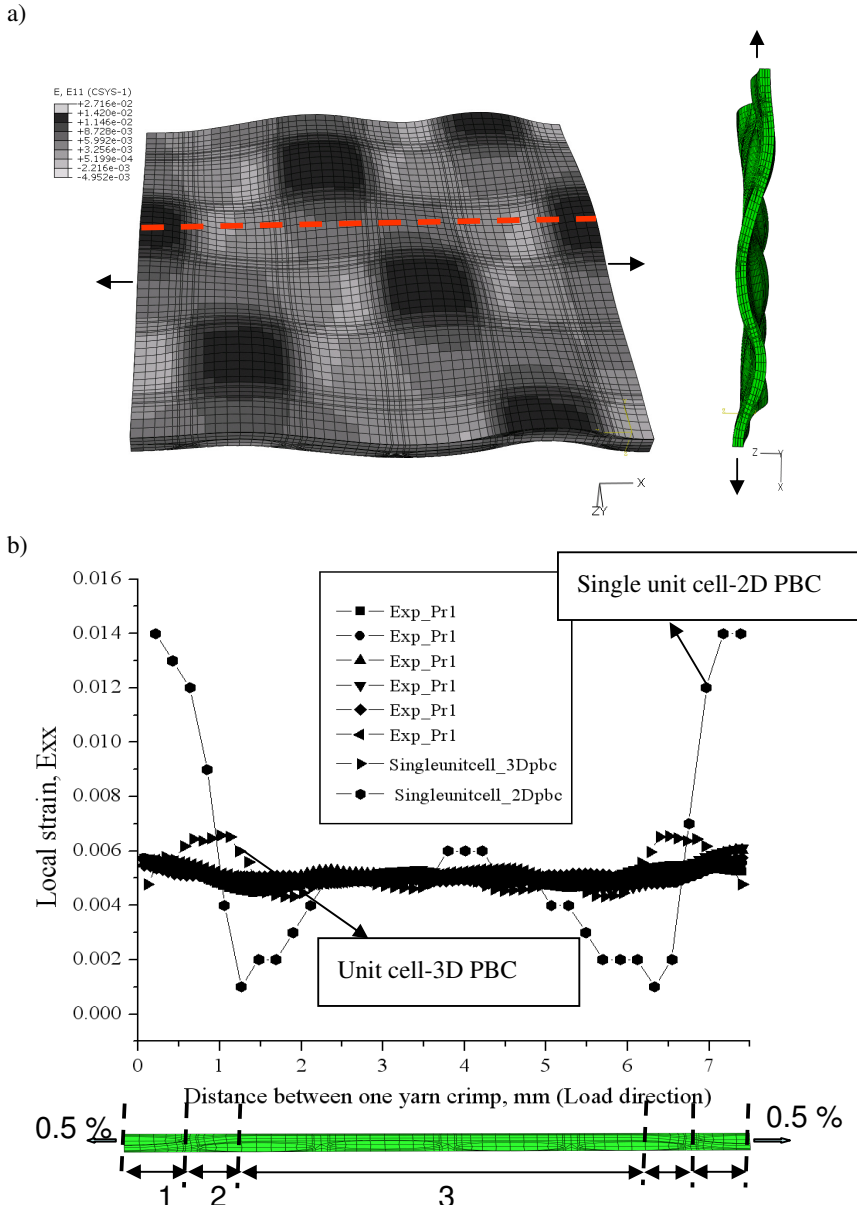

Figure 3-16.   **Local strain analysis in the finite laminate at 0.5% of the average tensile strain: a) local strain contours on the unit cell surface; b) comparison between the experimental and numerical local strain profiles.**

The difference in the local strain values between the numerical and experimental results can be attributed to the large tension/bending coupling effects caused by the unrestricted yarn undulation in a single ply lamina [3] used for the FE simulation. Moreover, FE (Figure 3-16a) and DIC (Figure 3-8b) strain contours show that the maximum local strain occurs at the centre of the weft yarn at the yarn crimp location. Comparing the local strain profile computed with the infinite laminate conditions to the free laminate that can deform in out-of-plane direction indicates that, large undulation effects in the free laminate causes the maximum weft yarn strain and minimum strain in the matrix pockets compared to the experimental as well as the strains computed with the infinite laminate conditions (Figure 3-16b).

In the process of improving the single unit cell FE strain profiles, and to predict the local surface strain profiles both qualitatively and quantitatively comparable to the experimental surface strain profiles, investigation of the local strain analysis is accomplished by developing several unit cell stacks as explained in [31, 35]. This allows us to find the bounding limits for the structural response, such as local stress - strain behaviour of the composite under the external tensile load. By allowing or constraining the yarn undulation effects at the yarn crimp location, variations in surface strain values as well as the surface strain locations are calculated using the following unit cell stack FE analysis.

- Unit cell stack with in-phase stacking
- Unit cell stack with step stacking
- Unit cell stack with out-of-phase stacking

The motivation for creating the above specified three unit cell stacks is obtained by examining the anticipated displacement pattern of the weft yarns caused by the straightening of the warp yarns under the applied tensile load. As shown in Figure 3-17, in region 1 of the randomly stacked satin weave laminate, yarn crimps are placed such that the weft yarn bending is an additive component. While in the region 2, the yarn crimps are placed such that the anticipated out-of-plane deformation is reduced by the straightening of the warp yarns.
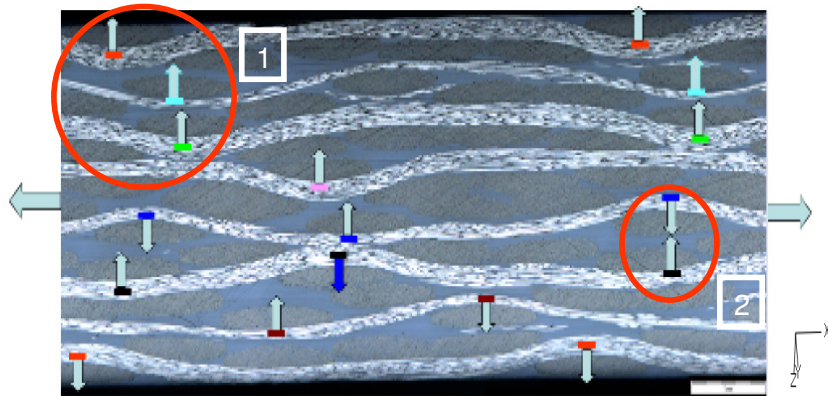
Figure 3-17.   Anticipated displacement pattern in a randomly stacked 5-harness satin weave laminate.

According to the above discussion, in the in-phase stacking, the unit cells are placed in such a way that the anticipated displacement at the yarn crimp location is compatible and in phase [29]. In contrast, for the out-of-phase stacking the anticipated displacement at the yarn crimp location is not compatible and will act to reduce the displacement of the weft yarn at the yarn crimp location. Finally, in case of step stacking, the yarn crimps of the unit cells are placed to form a step pattern at the yarn crimp location. In the above mentioned three unit cell stacks, in-phase and step stacking unit cell models are created using the 'WiseTex' software [4, 27, 36-38]. Whereas the third model (out-of-phase stacking) is developed using python scripting ('pyFormex' [39]) by performing series of translation and rotational operations on the single unit cell FE mesh obtained from 'MeshTex'.

In 'pyFormex' any arbitrary shift between the plies can be created. However, during the manipulations on the FE mesh, such as to produce the $1/4^{th}$ shift between the unit cells need cutting operation on the unit cell FE mesh (through the elements) and re-attaching the cut section to the other side unit cell FE mesh. The above specified operation produces the conflict elements at the joining faces (Figure 3-18a). However, cutting the FE mesh through the joining faces of the elements produces good quality unit cell stacks (Figure 3-18). Once the required shift is generated, the material orientation and the properties are assigned to the manipulated FE mesh, and the unit cell stack is ready for the FE analysis. Moreover, nodes at the joining faces of the unit cells are tied to each other so that perfect bonding is assured between the unit cells.

a)
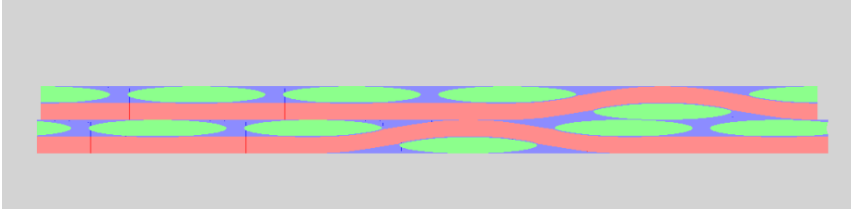
b)
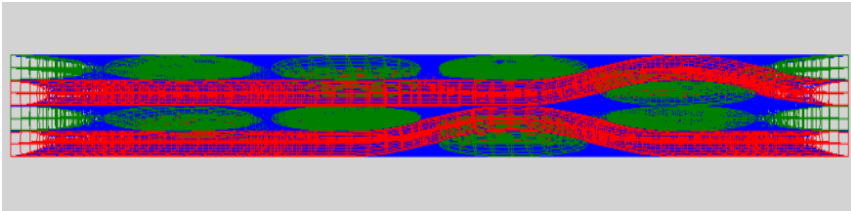
Figure 3-18.   Shifting operations using pyFormex: a) conflict of the elements at the joining faces for the 1/4th shift; b) out-of-phase stacking of the unit cells.

Choosing four unit cells in the stack (Figure 3-19a-c) from the laminate of eight layers, FE analysis of the unit cell stack is accomplished using in-plane periodic boundary conditions [40]. In addition, symmetry boundary conditions are applied at the bottom xz-surface and the top xz surface is allowed to deform in the out-of-plane direction (Figure 3-19a). FE analysis of the unit cell stacks is accomplished with the aforementioned BC's at 0.5% average tensile strain, and the results are presented in the current section.

Comparison of the experimental (Figure 3-8b) and numerical surface strain contours (Figure 3-19a-c) shows that, in correlation with the DIC and the single unit cell (2D PBC) FE strain contours, in-phase stacking of the unit cells (Figure 3-19a) predicts the maximum strain at the centre of the weft yarn at the yarn crimp location. It is also evident that a change in the unit cell stack and the applied BC's causes a shift in the maximum strain location form the centre to the edge of the weft yarn for the out-of-phase as well as the step stacking unit cell models (Figure 3-19b, c). Finally, comparison of the experimental surface strain profiles (DIC) to the numerical surface strain profiles (Figure 3-20a, b) obtained from the different unit cell stacks leads to the following conclusions:

- Depending on the unit cell stacking and boundary conditions used for the FE simulation, the maximum strain location on the weft yarn at yarn crimp location changes from the centre to the edge. Comparison of the local strain profiles computed from different unit cell stacks (Table 3-3) gives the following order of local strains at the yarn crimp: single unit cell (2D PBC) > in-phase stacking > step stacking > single unit cell with 3D PBC > out-of-phase stacking.

- The second part of the strain profile is associated with the minimum strain value adjacent to the yarn crimp location. The obtained minimum strain values from different unit cell stacks as well the experimental techniques prove very good correlation (excluding the single unit cell with 2D PBC).

- The final part of the strain profile belongs to the straight position of the load carrying warp yarn, whose values from all the measurements varies in between 0.48 - 0.53%.

Table 3-3.   Comparison of the local strain values - experiment vs. numerical simulations.

	Inside the laminate		Laminate surface	
Applied average strain in warp direction	*Max,%*	*Min,%*	*Max,%*	*Min,%*
FBG's –strain inside the laminate - 0.2%	0.25	0.16	-NA-	-NA-
Single unit cell -3D PBC 0.2%	0.27	0.17	-NA-	-NA-
Single unit cell -3D PBC 0.5%	0.65	0.47	-NA-	-NA-
LIMESS (DIC) – Surface strain 0.5%	-NA-	-NA-	0.58-0.62	0.43-0.46
Single unit cell -3D PBC 0.2%	-NA-	-NA-	1.4	0.1
4 Unit cells – out-of-phase stacking-0.5%	-NA-	-NA-	0.65	0.44
4 Unit cells – step stacking-0.5%	-NA-	-NA-	0.65-0.0.69	0.32-0.44
4 Unit cells – in-phase stacking-0.5%	-NA-	-NA-	0.73	0.35

a)

Warp – Load direction

Weft

b)

c)
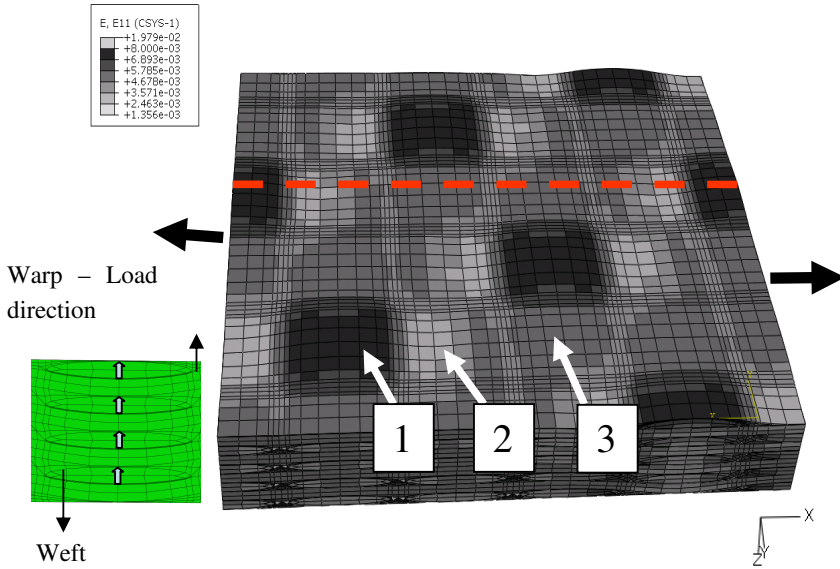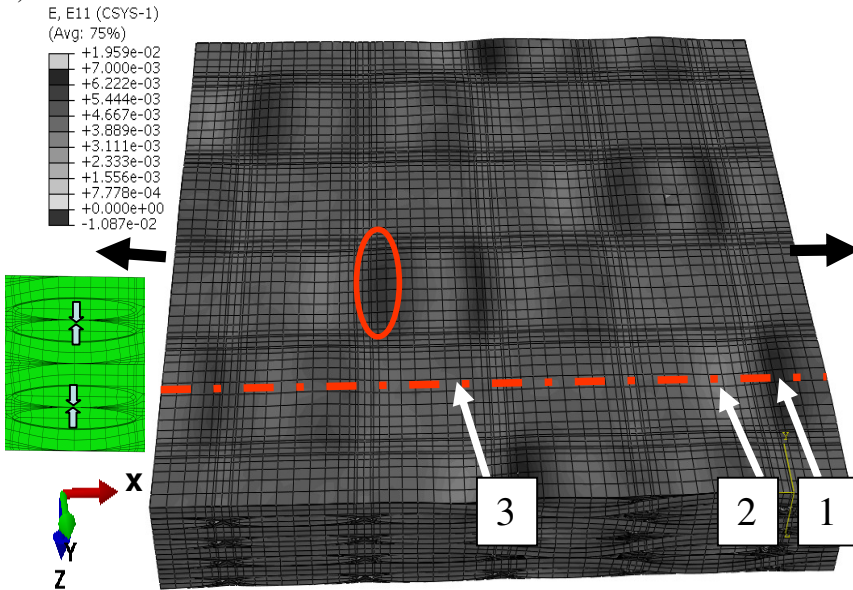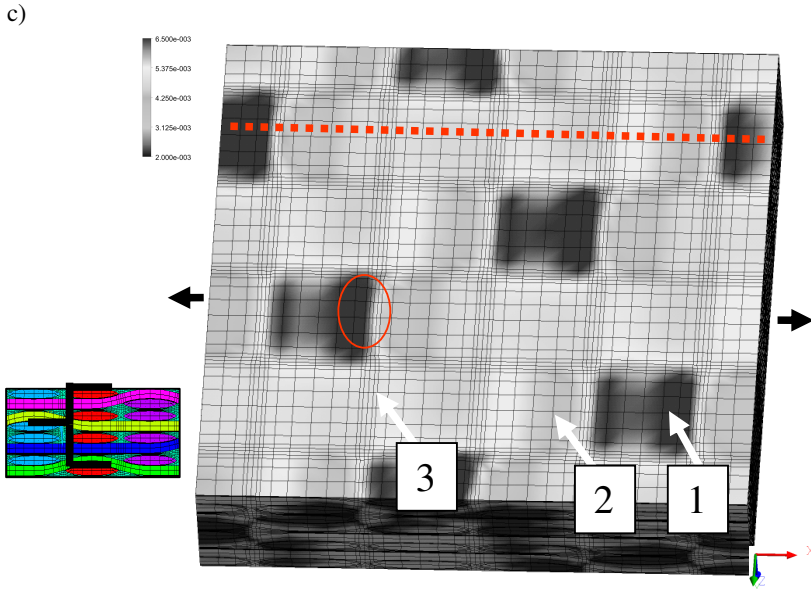
Figure 3-19.   Unit cell stack FE analysis at 0.5%: a) 4 unit cells with in-phase stacking; b) 4 unit cells with out-of-phase stacking; c) 4 unit cells with step stacking (2D PBC and Z-symmetry at bottom surface, top surface is traction free).

Finally, Figure 3-21 presents the comparison between the experimental and numerical local transverse strain, which shows good correlation. As observed in the experiment, meso-FE simulations predict the maximum positive transverse strain on the weft yarn at the yarn crimp location. And the resin pocket as well as the warp yarn undergoes the compressive transverse strain.

It should be noted that each yarn in the above mentioned unit cell stacks contains four or more elements over its cross section. In-phase and step stacking unit cell models contain 78500 elements, where as the out-of-phase model contains 319200 elements. Regarding the effect of mesh density on the local strain behavior, Lomov et al. [4] concludes that the mesh density shows minor influence on the local strain behavior. Also, from the investigation of the effect of mesh density on the unit cell local stress behavior [23] it appears that, when the yarn contains four of more elements over its cross-section, the local stress behaviour converges to the same value. Hence the local strain profiles shown in Figure 3-20 are highly reproducible.

a)

Weft

Warp – Load direction

Legend:
- Exp_Pr1
- Exp_Pr2
- Exp_Pr3
- Exp_Pr4
- Exp_Pr5
- Exp_Pr6
- 4unitcells_inphasestack_Zsymm
- 4unitcells_outofphasestack_Zsymm
- 4unitcells_step_Zsymm

Local longitudinal strain, Exx

Distance between one yarn crimp, mm (Load direction)

b)

Strain at the yarn crimp (1)

Single unit cell - 2D PBC	1.4%
In-phase stacking	0.73%
Out-of-phase stacking	0.65%
Step – stacking	0.65 – 0.69 %
Experiment [LIMESS]	0.59-0.62%

Strain at the flat yarn (3)

Single unit cell - 2D PBC	0.5%
In-phase stacking	0.48%
Out-of-phase stacking	0.48%
Step – stacking	0.5%
Experiment [LIMESS]	0.48-0.53%

Strain in the matrix (2)

Single unit cell – 2DPBC	0.1%
In-phase stacking	0.35%
Out-of-phase stacking	0.44%
Step – stacking	0.32-0.42%
Experiment [LIMESS]	0.45-0.46%

Figure 3-20.　　**Local surface strain analysis at 0.5% average tensile strain: a) comparison between the experimental and numerical surface strain profiles: b) experimental and numerical strain values at various location of the unit cell.**
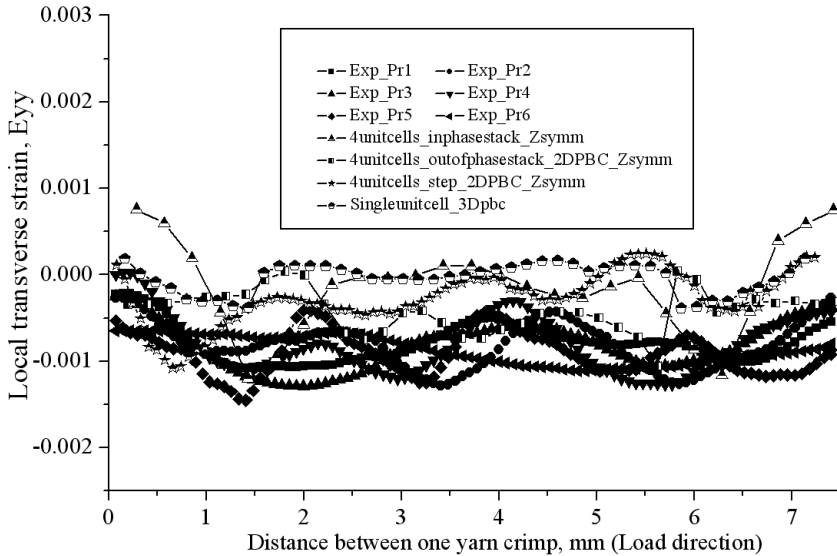
Figure 3-21. **Comparison between the experimental and numerical local transverse strain profiles at 0.5% of the applied tensile strain.**

3. 8. Conclusions

This chapter presents the detailed discussion regarding the experimental and numerical local strain behaviour in the plies of a satin weave composite under uni-axial static tensile load. In order to predict the local strain profiles as observed in the experimental analysis, meso-FE simulations are performed using various unit cell stack configurations. Comparison of experimental and numerical results leads to the following conclusions:

- The obtained experimental (DIC) local strain behaviour (longitudinal, transverse, in-plane shear) on the satin weave composite is similar to the local strain behaviour of other two-dimensional woven composites such as plain and twill weave composite [3, 4].

- From the experimental analysis, it is evident that the effect of the internal yarn shifting (nesting) is negligible on the local longitudinal strain behaviour of the composite.

- According to the traditional meso-FE simulations, the applied 3D PBCs to the single unit cell are unable to capture the adjacent ply interaction. And hence unable to compute the local strain spatial distribution as observed in the experiments.

- Meso-FE simulations show that the local strain profiles are sensitive to the unit cell geometrical model as well as the applied boundary conditions.

- Comparison of the experimental and numerical surface strain results implies that, by restricting the yarn undulation effects using 3D PBC or shifting of the beneath layers in the unit cell stack, quantitatively, numerical surface strain results approach to the experimental results. However, the maximum strain locations obtained from the FE simulations differ from those of the experimental strain contours.

As a summary, the current work emphasizes the effect of internal yarn shifting (nesting) on the local strain behaviour of a satin weave composite. To predict the FE surface local strains both qualitatively and quantitatively comparable to experimental results, unit cell geometry with maximum ply shift should be developed. However, it is a tedious process to develop a full scale unit cell stack with the detailed internal yarn shifting (nesting) for computational purposes. As a consequence, it is imperative to develop the above explained unit cell stacks to obtain an insight into the maximum and minimum limits for the surface local strain profiles as well as the variation in local strain contours.

Having the background of the maximum local strain locations, the following chapters of the current manuscript is focus on the local damage analysis in the plies of a satin weave composite.

3. 9.   REFERENCES

[1]   Nicoletto, G., G. Anzelotti, and E. Riva, *Mesoscopic strain fields in woven composites: Experiments vs. finite element modeling.* Optics and Lasers in Engineering. **47**(3-4): p. 352-359.

[2]   Potluri, P., et al., *Meso-scale strain mapping in UD woven composites.* Composites Part A: Applied Science and Manufacturing, 2009. **40**(12): p. 1838-1845.

[3]   Lee, J.-R., et al., *Digital phase-shifting grating shearography for experimental analysis of fabric composites under tension.* Composites Part A: Applied Science and Manufacturing, 2004. **35**(7-8): p. 849-859.

[4]   Lomov, S.V., et al., *Full-field strain measurements for validation of meso-FE analysis of textile composites.* Composites Part A: Applied Science and Manufacturing, 2008. **39**(8): p. 1218-1231.

[5]   Ivanov, D., et al., *Strain mapping analysis of textile composites.* Optics and Lasers in Engineering. **47**(3-4): p. 360-370.

[6]   Ivanov, d.S., *Damage analysis in textile composites.* PhD Thesis; KU Leuven - Faculty of Engineering, May 2009.

[7]   Summerscales, J. and P.M. Russel, *Observations on the fibre distribution and fibre strain in a woven fabric reinforcement.* Advanced composite letters 2004. **23 No.3, 2004**.

[8]   Littell, J.D. and W.K. Binienda, *Characterization of Damage in Triaxial Braid Composites Under Tensile Loading.* NASA/TM—2009-215645, May 2009.

[9]   Ivanov, D.S., et al., *Stress distribution in outer and inner plies of textile laminates and novel boundary conditions for unit cell analysis.* Composites Part A: Applied Science and Manufacturing. **41**(4): p. 571-580.

[10]   Bosia, F., et al., *Deformation characteristics of composite laminates--part I: speckle interferometry and embedded Bragg grating sensor measurements.* Composites Science and Technology, 2002. **62**(1): p. 41-54.

[11]   Bosia, F., T. Gmür, and J. Botsis, *Deformation characteristics of composite laminates--part II: an experimental/numerical study on equivalent single-layer theories.* Composites Science and Technology, 2002. **62**(1): p. 55-66.

[12]   Anzelotti, G., G. Nicoletto, and E. Riva, *Mesomechanic strain analysis of twill-weave composite lamina under unidirectional in-plane tension.* Composites Part A: Applied Science and Manufacturing, 2008. **39**(8): p. 1294-1301.

[13]   Takano, N., et al., *Study on large deformation characteristics of knitted fabric reinforced thermoplastic composites at forming temperature by digital image-based strain measurement technique.* Composites Science and Technology, 2004. **64**(13-14): p. 2153-2163.

[14]   Grédiac, M., *The use of full-field measurement methods in composite material characterization: interest and limitations.* Composites Part A: Applied Science and Manufacturing, 2004. **35**(7-8): p. 751-761.

[15]   Willems, A., et al., *Optical strain fields in shear and tensile testing of textile reinforcements.* Composites Science and Technology, 2008. **68**(3-4): p. 807-819.

[16]   Lomov, S.V., et al., *A comparative study of tensile properties of non-crimp 3D orthogonal weave and multi-layer plain weave E-glass composites. Part 1: Materials, methods and principal results.* Composites Part A: Applied Science and Manufacturing, 2009. **40**(8): p. 1134-1143.

[17]   Parlevliet, P.P., *Residual Strains in Thick Thermoplastic Composites - an Experimental Approach.* PhD Thesis; Delft University of Technology, 2010.

[18]   Ives, D.B., *Strain Monitoring in Thermoplastic Composites with Optical Fiber Sensors: Embedding Process, Visualization with Micro-tomography, and Fatigue Results.* Journal of Thermoplastic Composite Materials, 2007.

[19]   Voet, E., *High strain measurements during fatigue cycleing in fibre reinforced thermoplastic composites using imbedded draw tower fibre brag grating sensors* ECCM13 Conference procedings, 2008.

[20]   YipingWang, et al., *Characterization of a high birefringence fibre Bragg grating sensor subjected to non-homogeneous transverse strain fields.* Meas. Sci. Technol. 17 939-942 2006.

[21]   Ling, H.-Y., et al., *Characterization of dynamic strain measurement using reflection spectrum from a fiber Bragg grating.* Optics Communications, 2007. **270**(1): p. 25-30.

[22]   Lagattu, F., J. Brillaud, and M.-C. Lafarie-Frenot, *High strain gradient measurements by using digital image correlation technique.* Materials Characterization, 2004. **53**(1): p. 17-28.

[23]   Daggumati, S., et al., *Local damage in a 5-harness satin weave composite under static tension: Part II - Meso-FE modelling.* Composites Science and Technology. **70**(13): p. 1934-1941.

[24]   Daggumati, S., et al., *Local damage in a 5-harness satin weave composite under static tension: Part I - Experimental analysis.* Composites Science and Technology. **70**(13): p. 1926-1933.

[25]   Duplessis Kergomard, Y., et al., *Intralaminar and interlaminar damage in quasi-unidirectional stratified composite structures: Experimental analysis.* Composites Science and Technology. **70**(10): p. 1504-1512.

[26]   Lee, J.-R., et al., *Diffraction grating interferometers for mechanical characterisations of advanced fabric laminates.* Optics & Laser Technology, 2006. **38**(1): p. 51-66.

[27]   Lomov, S.V., et al., *Meso-FE modelling of textile composites: Road map, data flow and algorithms.* Composites Science and Technology, 2007. **67**(9): p. 1870-1891.

[28]   Hale, R.D., *An experimental investigation into strain distribution in 2D and 3D textile composites.* Composites Science and Technology, 2003. **63**(15): p. 2171-2185.

[29]   Carvalho, N.V., S.T. Pinho, and P.Robinson, *Compressive failure of 2D woven composites.* ICCM-17 Conference proceedings, 2009.

[30]   Owens, B.C., J.D. Whitcomb, and J. Varghese, *Effect of Finite Thickness and Free Edges on Stresses in Plain Weave Composites.* 2009. p. 0021998309347571.

[31]   Ito, M. and T.-W. Chou, *Elastic moduli and stress field of plain-weave composites under tensile loading.* Composites Science and Technology, 1997. **57**(7): p. 787-800.

[32]   Daggumati, S., et al., *Local damage in a 5-harness satin weave composite under static tension: Part I - Experimental analysis.* Composites Science and Technology. **70**(13): p. 1926-1933.

[33].   Whitcomb, J.D., C.D. Chapman, and X. Tang, *Derivation of Boundary Conditions for Micromechanics Analyses of Plain and Satin Weave Composites.* 2000. p. 724-747.

[34]   Le Page, B.H., et al., *Finite element simulation of woven fabric composites.* Composites Part A: Applied Science and Manufacturing, 2004. **35**(7-8): p. 861-872.

[35]   WOO, K. and Y.W. Suh, *Phase shift effect on the stress distribution for satin weave composites.* Journal of Composite Materials, 2001. **Vol. 36, No. 03/2002**.

[36]   Lomov, S.V., et al., *Textile composites: modelling strategies.* Composites Part A: Applied Science and Manufacturing, 2001. **32**(10): p. 1379-1394.

[37]   Verpoest, I. and S.V. Lomov, *Virtual textile composites software WiseTex: Integration with micro-mechanical, permeability and structural analysis.* Composites Science and Technology, 2005. **65**(15-16): p. 2563-2574.

[38]   Lomov, S.V., et al., *Nesting in textile laminates: geometrical modelling of the laminate.* Composites Science and Technology, 2003. **63**(7): p. 993-1007.

[39]   BAGGER, A., B. VERHEGGHE, and K.D. HERTZ, *Modeling plate shell structures using pyFormex.* Proceedings of the International Association for Shell and Spatial Structures (IASS) Symposium , Valencia, 2009.

[40]   Zako, M., Y. Uetsuji, and T. Kurashiki, *Finite element analysis of damaged woven fabric composite materials.* Composites Science and Technology, 2003. **63**(3-4): p. 507-516.

Chapter 4

EXPERIMENTAL AND NUMERICAL INVESTIGATION OF THE LOCAL DAMAGE BEHAVIOUR UNDER UNI-AXIAL TENSILE LOAD

This chapter is divided into two parts. The first part of this chapter presents the extensive investigation of the experimental damage initiation in the plies of a satin weave composite. In order to understand the local damage behaviour, tensile tests were performed and accompanied by Acoustic Emission (AE) and microscopic analysis of the composite specimen. These tests enable us to detect the damage initiation stress as well as the damage initiation location in the composite. Moreover, effect of the residual thermal stresses and their influence on the satin weave composite damage behaviour is highlighted. The experimental local damage analysis leads to the conclusion that the damage initiation in the plies of a satin weave composite is a sequential process. Subsequently, the second part of this chapter investigates deformation and stress mechanics that is responsible for the above stated sequential damage process, which is analyzed through the satin weave unit cell FE simulations. Finally, comparison between the experimental and numerical damage analysis is presented.

4. 1. INTRODUCTION

Damage accumulation in textile composites is a complicated process, and development begins on the micro-scale with the fibre matrix debonding, the matrix cracking and the fibre failure (the micro-scale defines the arrangement of fibres in an impregnated yarn or fibrous ply). On the meso-scale, damage develops by intra-yarn cracking and delaminations (the meso-scale defines the internal structure of the reinforcement, variation of the fibre direction and the fibre volume fraction inside the yarns and the fibrous plies). Finally, the macro-failure of the composite is characterized by dense cracking, intersection of several small cracks (crack conjunction) and fibre rupture [1] (the macro-scale defines the three-dimensional geometry of the composite part and the distribution of local reinforcement properties).

Starting from the micro-scale fibre matrix debonding, Figure 4-1 schematically depicts the weft yarn damage that is affected by the restriction of local ply deformation caused by the surrounding layers in a satin weave composite under uni-axial tensile test. The influence of local constraints is manifested by a change in the weft yarn crack location (edge/centre) based on the location of the chosen ply in the laminate (inner/surface). In order to obtain comprehensive knowledge of the damage phenomena occurring in textile composites, it is necessary to understand the factors that contribute to the damage at different length scales. Apart from the natural variability in yarn spacing and its dimensions, the unit cells of textile reinforcement are theoretically the same. However, parameters such as the fibre orientation, localized fibre spacing and packing often exhibit a wide statistical variation when evaluated on the micro-scale in a processed composite. Therefore, some localized micro volumes are stressed more than others. The stress inhomogeneity is further enhanced by the inhomogeneity of the elastic properties of the composite constituents. The inhomogeneity of the stress field, coupled with the inhomogeneity of the strength properties of the reinforcing elements, the matrix and the interface, lead to the gradual damage development in composites [2]. Moreover, the micro-scale stress-strain state defines the number of transverse cracks in a particular yarn and how they are placed over its entire cross-section [3].

In addition to the micro-scale parameters mentioned above, at the ply level (meso-scale), geometrical parameters such as the yarn crimp and the variations in intra-yarn volume fraction can contribute to the stochastic nature of the stress concentration in the micro-volumes [4, 5].

Finally on the scale of the laminate, in the textile composite, different layers have different ply shifting and nesting patterns. During the manufacturing process of woven fabric composites, fabric layup and lateral compression may cause fabric layers to nest with each other and also shift randomly between each other, altering the mechanical behaviour of the composite. The nesting conditions of the particular laminate are defined by the penetration of the yarns from one ply into another. Hence, the stress-strain state inside the ply (as in the micro volumes) depends on the placement of the ply inside the laminate [6-8]. Consequently, in addition to the above mentioned micro- and meso-scale parameters, weft yarn damage in the plies of a satin weave composite depends on the ply position in the laminate [9].
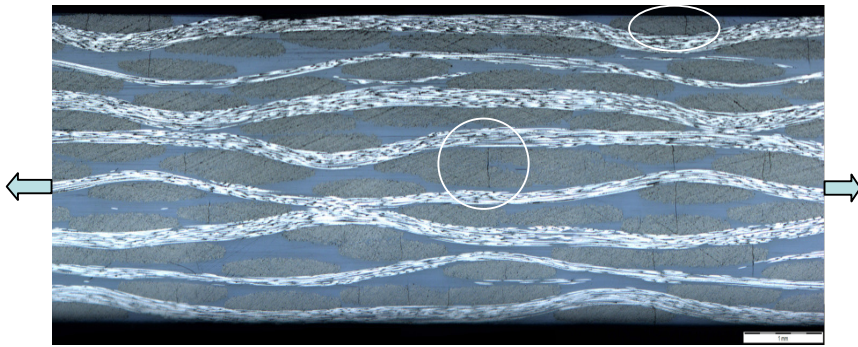
Weft yarn damage at the laminate level
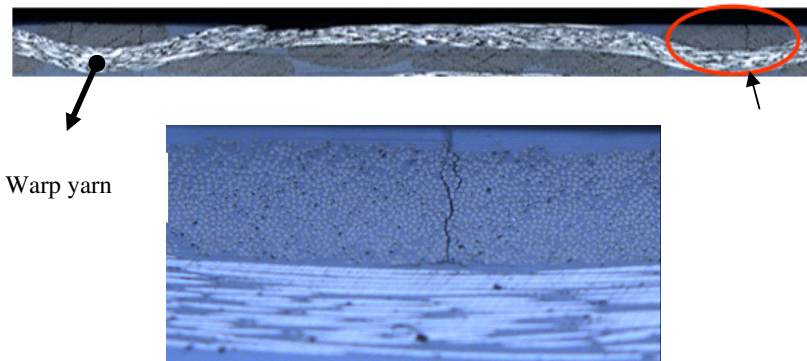
Ply level– Weft yarn damage on the surface layer (at the weft yarn centre)
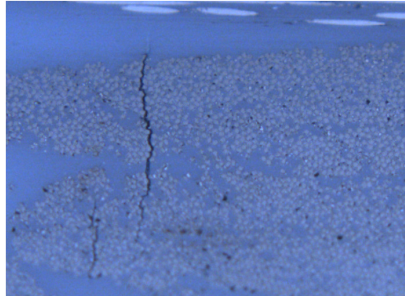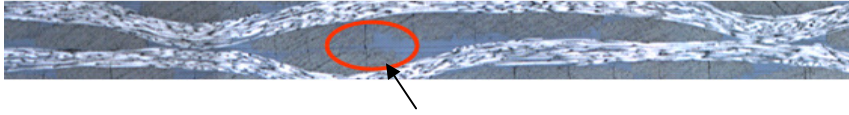
Ply level – Weft yarn damage at nested yarn configuration (at the edge of the weft yarn)
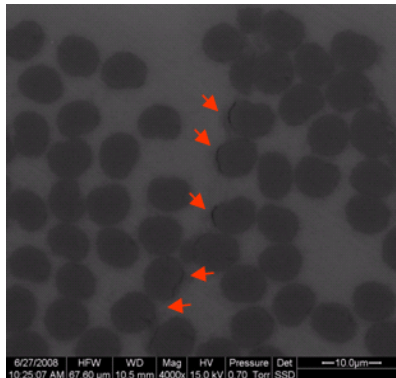
Micro level- fibre matrix debonding in the weft yarn

Figure 4-1.   Schematic representation of the damage at various levels in a satin weave carbon-PPS thermoplastic composite.

The above mentioned parameters of textile composites at various hierarchical levels combined with the thermal residual stresses accumulated at the relevant scale [10] during the composite manufacturing process can lead to different damage initiation conditions and different patterns of progressive damage in the chosen ply of a laminate. In general, micro-scale damage initiation in a textile composite is not only affected by the stochastic micro-level geometrical variables, but also by the meso- and laminate level geometrical parameters.

A combination of different experimental techniques is used in the current study to understand the detailed damage phenomena and the damage history in the satin weave composite. Damage initiation is detected using the acoustic emission (AE) technique during the tensile test. AE provides the damage initiation threshold and the critical stresses of the composite. In order to detect the location of the damage, microscopic analysis is used. The afore mentioned methodology has been proposed by many researchers [11-13] to study the damage initiation and propagation in textile composites. From the microscopic images captured during the tensile test, the major damage observed in the satin weave composite is weft yarn cracking before the final failure of the laminate. Based on the microscopic images, apart from the detection of damage initiation stress and locations, a novel procedure is introduced to interpret the layer-wise sequential damage at different locations in the laminate. The aim of using this procedure is to provide the information regarding the history of the weft yarn transverse damage in different layers of the laminate. This then also provides information on the influence of adjacent layers (internal yarn nesting) on the meso damage behaviour of a local ply. Finally, the correlation between AE event data and the microscopic crack density provided confidence in the interpretation of the complex damage behaviour.

The current chapter is divided into two parts: the primary focus of the first part is to conduct the in-depth experimental investigation on the parameters that are influencing the location as well as orientation of the weft yarn cracks in a thermoplastic 5-harness satin weave composite. Following the objective of the current research work, the second part of this chapter aimed at developing the unit cell meso-FE analysis procedure for predicting the observed experimental sequential damage phenomena. Later, numerical investigation is conducted using unit cell FE analysis for the stress and deformation mechanics that is responsible for the sequential damage process.

4. 2.   The mechanical testing procedure

Tensile tests on the composite specimens were performed using a standard Instron machine (Instron 4505, test speed 1 mm/min). Composite samples used for the tensile tests were prepared according to the ASTM D3479 standard (width 25mm, gauge length 170mm, thickness 2.5mm), with the end tabs of the same material (Carbon-PPS). As discussed in the previous chapter, local strain during the tension test is measured using the digital image correlation technique (LIMESS). At the end of the loading process, the average strain is computed across the entire window of the speckle pattern ($23\times37mm$) used for the full-field strain registration [14].

Along with the DIC registration, the AE measurement and data acquisition system (VALLEN) was used to detect the damage initiation stress followed by the microscopic analysis of the composite specimens for the inspection of the damage locations. The following sections present the detailed discussion regarding the experimental setup used for the damage analysis.

4. 2. 1.   Acoustic emission technique

As discussed above, composite materials under stress experience numerous damage mechanisms. For example, these may include fiber failure, delamination, matrix cracking, bundle debond etc. [15]. These damage mechanisms can occur at numerous locations throughout a composite beginning at very low stress levels. The task of keeping track of all of these damage sites and mechanisms is far more complex than simply monitoring crack growth at a few locations in a metallic material. Because the accumulation of damage in a composite is closely tied to the actual strength, life and stiffness of the composite, understanding this damage is very important for the structural applications of composite materials. Moreover, it is important to determine the damage initiation and the critical strains over the stress-strain curve obtained from the tension test on the textile composite specimen. Based on the damage initiation and critical strains observed, the composite fatigue and durability life can be determined [16, 17].

For the above mentioned purpose, several methods have been used to monitor the damage occurrences in composites. Among these techniques, acoustic emission has been widely used. AE is based on monitoring the stress waves that are generated by rapid local redistributions of stress which accompany the operation of many damage mechanisms [13]. AE offers a number of advantages and potential advantages which give the technique some unique capabilities. Among these are: (1) high sensitivity; (2) real-time capability; (3) total specimen volume sensitivity; (4) location of damage regions, and (5) sensitivity to any process or mechanism that generates stress waves. Nevertheless, the use of such techniques needs a clear understanding of relationships between the recorded signal and the damage process. And the stress waves resulting from the micro-structural changes depend on the propagation conditions including attenuation, damping and boundary surface interactions in a heterogeneous medium. So the signal delivered by the sensor is a strongly modified representation of the original source. However, it is realistic to consider that this signal contains some representative features of the source in such a manner that direct correlation exists between the damage mechanisms and the magnitude of the various AE parameters [13].

As shown in Figure 4-2, once the composite test specimen is mounted on the tensile machine, two sensors are attached at the ends of the specimen at a distance of 150 mm from each other. Special vacuum grease is used to mount the sensors onto the composite, which will transfer the acoustic events from the composite material to the AE sensors. The complete AE VALLEN system used in the current experiment can be obtained from the VALLEN data manual [18]. Details of the AE equipment used for the event registration are shown in Table 4-1.
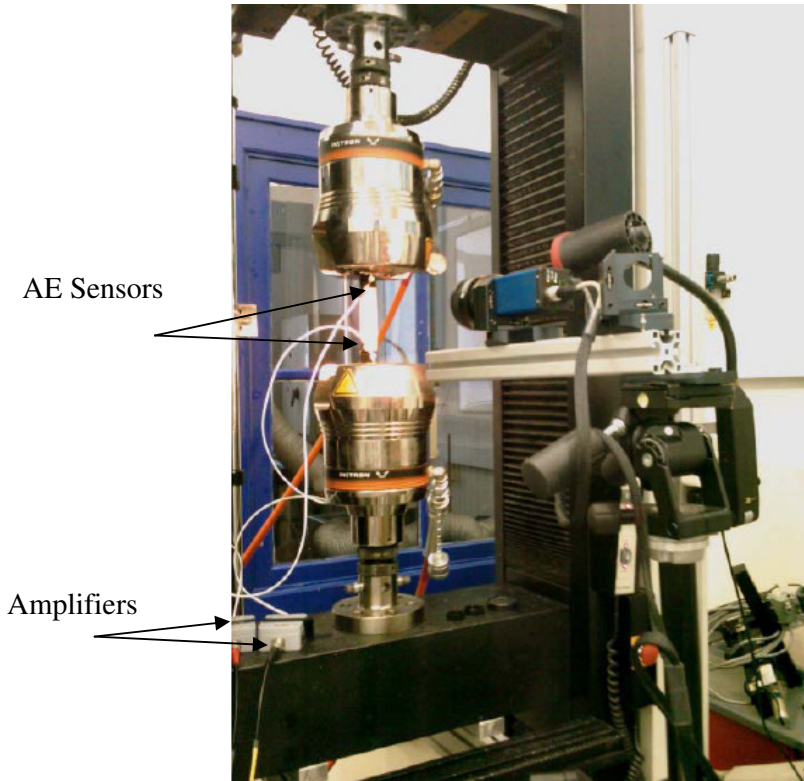
Figure 4-2.   Specimen with the AE sensors mounted on tensile machine.

As shown in Figure 4-3, the complex acoustic emission measurement chain consisting of many separate measuring components is schematically represented. The emitted stress wave propagating through the material is detected using acoustic emission sensors, which are fixed on the specimen via a coupling agent. The obtained acoustic emission signal is transmitted to a preamplifier which intensifies the electrical signal. The amplified signal is supplied to the acoustic emission analyser.

The downstream frequency filters undertake the task of eliminating background noises. The AE software processes the detected signals, converts the detected burst into feature data sheets, and displays them graphically and numerically in real time [19].

Table 4-1.   Parameters of the AE (Acoustic Emission) equipment.

Software	Vallen AMSY-5
Amplifiers	Vallen AEP4
Amplification, dB	34
Discrimination time, ms	0.4
Rearm time, ms	3.2
Range, MHz	0.025..1.6
Sample rate, MHz	5
Sensors	Digital wave 1025
Sensor diameter, cm	0.93
Threshold, dB	35

The obtained AE output is combined with the strain data, and results are plotted as a logarithm of cumulative acoustic energy versus tensile strain (Figure 4-4). By analyzing the different strain levels in Figure 4-4a, the critical stress at which damage occurs can be detected [17].
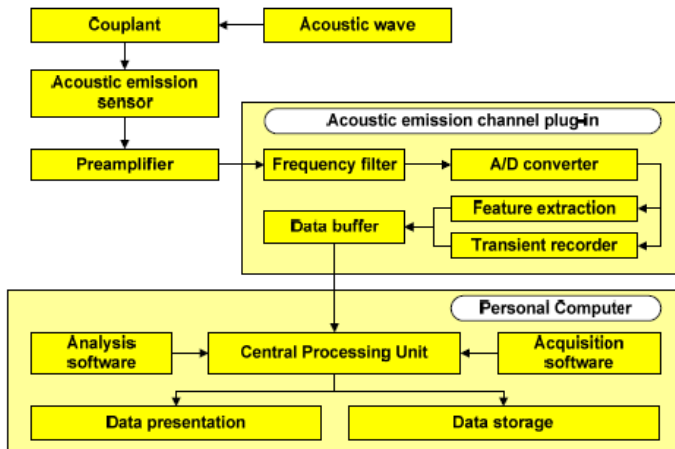
Figure 4-3.   AE process chain [19].

4. 2. 2.   Microscopic analysis

The AE technique described in the above section provides the damage initiation stress quantitatively, but it can not give any indication regarding the type of damage and the location of the detected event source. Although many researchers try to interpret fibre failure and other damage mechanisms based on the obtained AE frequency and energy levels [2, 20]. However, they lack sound physical interpretation. In the current study, AE data is only used for the indication of the critical stress levels. In order to visualize the damage locations, microscopic analysis of the composite specimen was considered to be the accurate method to analyze the damage progression [5, 21, 22]. The technique presented in this chapter (in later sections) is based on capturing and performing the qualitative as well as the quantitative analysis of the microscopic images. Quasi-static tensile tests were performed on the polished composite specimen to allow for the microscopic inspection of damage initiation and propagation. In order to visualize the damage, an OLYMPUS AX-70 microscope was used along with the 'cell-D' software (www.microscopy.olympus.eu) for the analysis of the microscopic images that were captured.

## 4. 3.   Experimental data analysis and results

4. 3. 1.   Analysis of AE data

In order to obtain critical strains for the damage analysis, the stress versus strain curve is plotted together with the strain versus acoustic energy (Figure 4-4a). To show consistency in the AE event pattern for different samples, the event distribution (in a linear scale) is plotted with the tensile stress (Figure 4-4b). These curves were plotted using the acoustic events obtained from the AE VALLEN, the stress data obtained from the INSTRON load cell and the LIMESS strain data.

The first phase of the AE data (Figure 4-4a) is associated with the occurrence of low energy events starting at the global tensile strain around 0.14% in the warp yarn direction (corresponding to approximately 80 MPa stress), which is designated as the damage initiation strain ε_{min} [16]. In the second phase (ε_{min} to ε_1 - 0.14 to 0.3%), the rise in the slope of the AE curve is very small, and this phase is related to the occurrence of sporadic cracks which were associated with a low energy release. In the next phase of the AE curve (ε_1 to ε_2 - 0.3 to 0.4%), the slope increases rapidly with the occurrence of low and middle energy acoustic events.

The final part of the AE curve (after $\mathcal{E}_2$) is associated with continuous events with high energy release, indicating the critical crack propagation and eventually catastrophic failure of the composite. Once the stress level reached around 500 MPa, the AE sensors were removed from the composite specimen to avoid damage to the sensors due to the catastrophic failure of the composite laminate.

a)
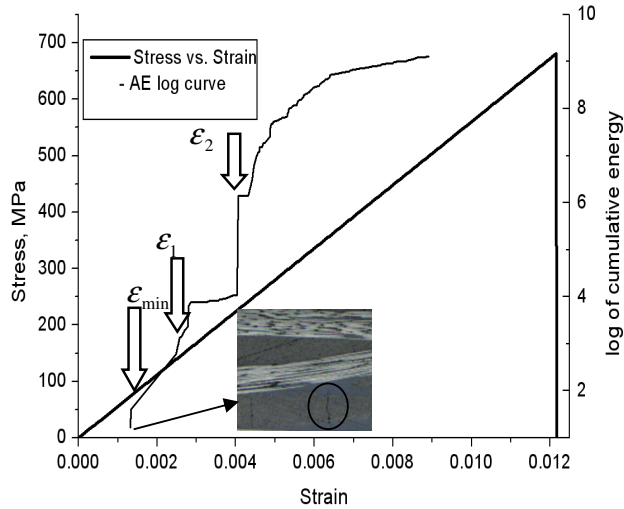
b)
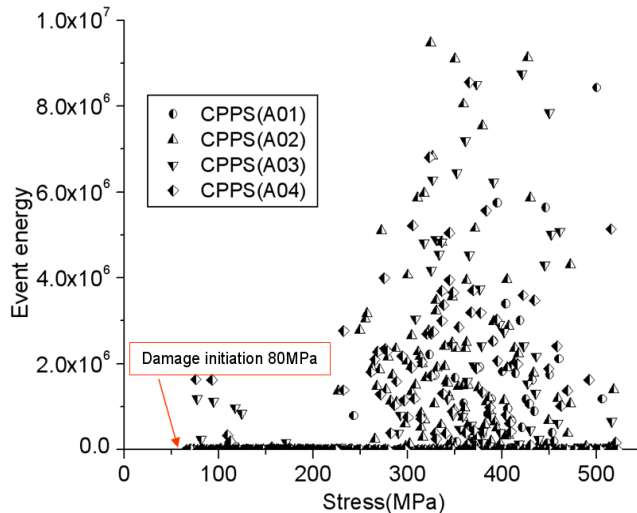
Figure 4-4.   Analysis of AE data: a) stress vs. strain and strain vs. AE registration curve (test1); b) AE event pattern (batch 1)

Moreover, based on the literature on thermoplastic composites [23-25], it is observed that the amount of thermal residual stresses accumulated during the manufacturing process can not be neglected. For the carbon-PPS composite plates, thermal stresses were accumulated immediately after processing and subsequent cooling to room temperature. And the accumulation of the thermal residual stresses is influenced by all three structural levels that are inherent in a textile composite (micro-meso-macro scales).

i.   At <u>micro-scale</u> thermal residual stresses are accumulated due to the mismatch of the thermal expansion coefficients between the fibre and matrix. Unlike thermoset matrix, thermoplastic matrix is heated to a processing temperature above its melting temperature and subsequently solidified upon cooling to the service temperature, where no chemical reaction should take place. The cooling involves volumetric shrinkage of the thermoplastic matrix, which is significantly higher than the fibre shrinkage. The aforementioned phenomenon is the main driving force for the formation of thermal stresses between the fibre and matrix at micro level. Moreover, fibre waviness also influences the formation of the thermal residual stresses.

ii.   At the unit cell scale <u>(meso-scale)</u> unsymmetrical weaving of the 5-harness satin weave fabric causes warping of the composite plates during the curing process. In general, due to the differences in processing conditions such as layer stacking (internal yarn nesting), different composite plates produced with the same constituent materials tend to exhibit differences in the local warping, which are manifested by the partial relief of thermal stresses.

iii. At the <u>macro-scale</u>, residual stresses are present on a ply-to-ply scale due to lamina anisotropy. The residual stresses are arising due to the difference in the transverse and longitudinal ply coefficient of thermal expansion.

In case of carbon-PPS 5-harness satin weave composite, warping is negligible on the entire composite plate supplied by TenCate (45 cm by 48 cm). However, from the composite test coupons obtained from water jet cutting, warping is clearly observed (Figure 4-5). Moreover, it is also observed that the different test coupons obtained at different locations of the whole plate (45 cm by 48 cm) possess different degrees of warping. As a result the accumulated thermal residual stresses from various hierarchical levels lead to the formation of the weft yarn transverse damage, referred as micro cracks in the composite laminate [24].
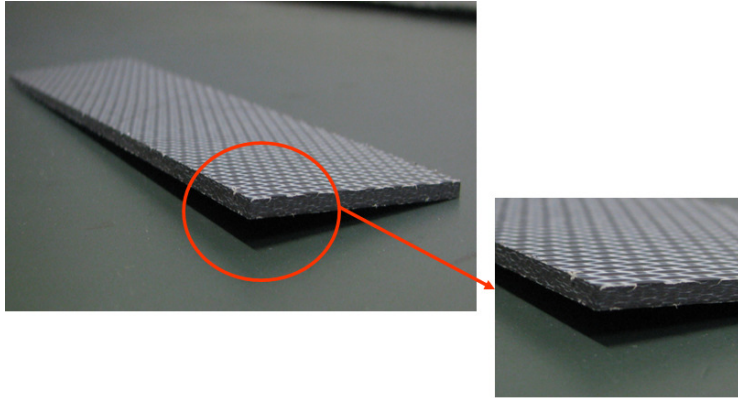
Figure 4-5.   Warped composite laminate specimen used for the tension test.

The main reason for the damage initiation is that the thermal residual stress in the matrix exceeds the yield strength of the resin and the fibre-matrix bond strength, and hence causes matrix cracking or fibre matrix debonding. In the context of analyzing the variations in thermal stresses in different composite plates, and their influence on the critical strains (ε_{min}, ε_1, ε_2), further investigations were carried out by testing the other batch of carbon-PPS test coupons obtained from a different plate. AE tests on the other batch of carbon-PPS samples predicted the damage initiation at an early strain of 0.09% (40 MPa) (Figure 4-6).
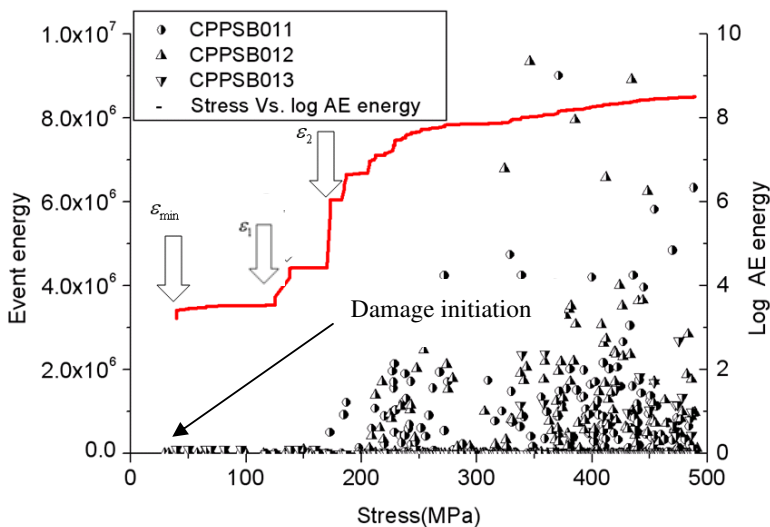
Figure 4-6.   AE event pattern (batch 2).

From the AE tests on batch 1 and 2 (Figure 4-4b) and (Figure 4-6), it is evident that there is almost a 50% difference in the damage initiation stress due to the variation in thermal residual stresses. Moreover, the aforementioned study provides evidence that thermal stresses cause the early damage events with low energy release, which is termed as the damage caused by manufacture induced inhomogeneities. However, in both the cases that are illustrated in Figure 4-4b and Figure 4-6, the rise in event count and the energy release is strongly increased approximately at around 200 MPa stress or 0.3-0.4% of average strain. This is a typical value for the intra-yarn damage onset observed experimentally for many textile composites [8]. Table 4-2 provides the summary of structural properties for the 5-harness satin weave carbon-PPS composite under tension.

Table 4-2. **Experimental mechanical properties of the carbon-PPS satin weave composite.**

	Warp direction	*Weft direction*
Young's modulus, GPa	*57 ± 1*	*57 ± 1*
In-plane Poisson's ratio v_{12}	0.05 ± 0.02	
In-plane shear modulus G_{12}, GPa [26]	4175	
Strength, MPa	*734*	*754*
Ultimate strain, %	*1.1 ± 0.1*	*1.1 ± 0.1*
Damage initiation ε_{min}, %	*0.09 -0.2*	*-NA-*
First damage threshold ε_1, %	*0.25-0.35*	*-NA-*
Second damage threshold ε_2, %	*0.4-0.45*	*-NA-*

4. 3. 2.   Microscopic damage analysis

4. 3. 2. a.   Effect of the layer stacking on the crack initiation

From the above section (AE event analysis) it is evident that the damage initiation in the satin weave composite is a sequential process and the damage initiation in the plies of a satin weave composite occurs at different stress levels over the entire stress-strain curve. Consequently, the current section investigates the type of damage and the sequence of the damage events occurring at different stress levels. For the aforementioned purpose, microscopic analysis of the composite specimens is a possible technique for evaluating the damage initiation and propagation in textile composites. Along with the AE, microscopic analysis allows for the study of the comprehensive damage behaviour of the composite [5, 27].

Quasi-static tensile tests were performed on the polished specimens of the composite laminate, which allowed for the microscopic inspection of the damage initiation and propagation along the thickness direction as well as on the traction free surface of the composite. From the captured microscopic images, apart from the traditional crack counting (crack density) on the polished edges, a novel procedure is introduced to study the effect of layer stacking on the local damage behaviour of the weft yarn.

According the above discussion in the previous sections, due to the sensitivity of the micro-scale geometrical parameters (fibre spacing, packing fraction…) on the damage behaviour, there is a special focus on investigation of the variation of the local yarn cross-section (which directly controls the fibre packing fraction) at various locations of the laminate (Figure 4-7a-d). The yarn dimensions, which were measured in different locations of the laminate revealed that the 5-harness satin weave weft yarn maintained its elliptical shape, with a major diameter of 1.32 ± 0.17 mm, and the minor diameter varying at around 0.15 ± 0.02 mm. The above measured yarn dimensions with 3000 filaments in each bundle showed a constant packing fraction that is independent of the location of the chosen weft yarn.

a)
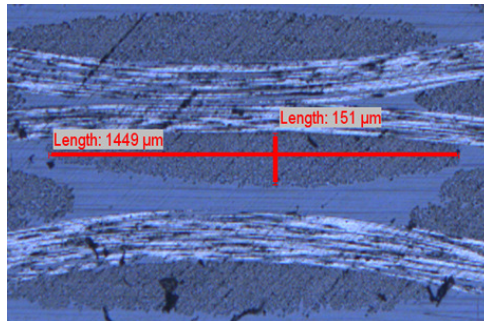
b)
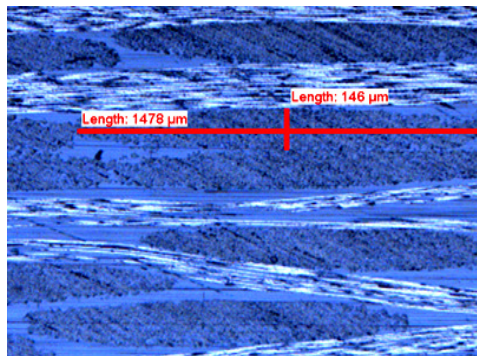
c)
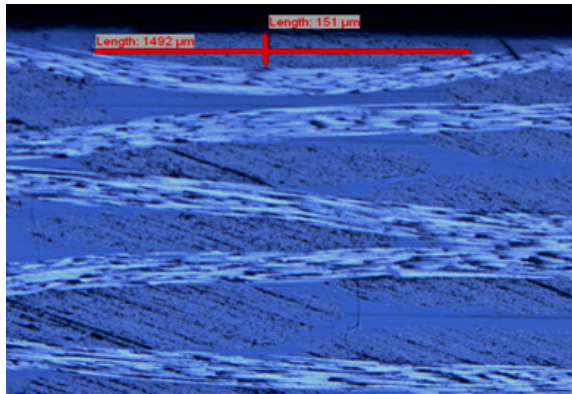
d)
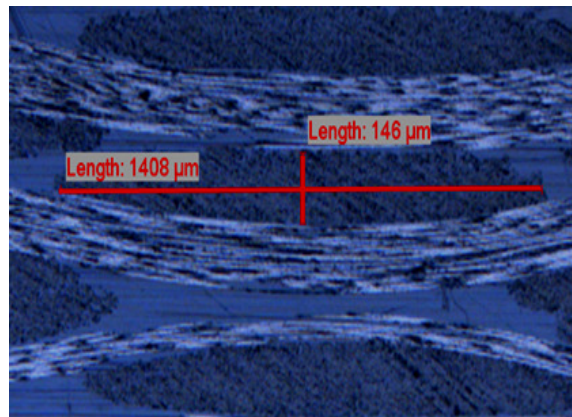
Figure 4-7.   **Weft yarn dimensions measured at a) yarn in the resin rich region; b) nested yarns; c) surface of the laminate; d) tightly packed by warp yarns.**

Having the background of the effects of manufacture induced stresses (thermal) as well as the variations in the local fabric geometries, the following sections are devoted to the local damage analysis in the plies of a satin weave composite under uni-axial tensile load (in fibre direction). Moreover, it should be emphasized that the following results are based on the damage locations observed over number of unit cell stacks along the laminate cross-section (for statistical significance).

Due to the sensitivity of the initial damage, up to 100 MPa average tensile stress, the load on the INSTRON machine is increased in two steps with a step size of 50 MPa. After the initial damage, the load is increased with a step size of 100 MPa until the composite final failure. Damage developed in the 5-harness satin weave composite under tensile load takes the form of weft yarn cracking, which is perpendicular to the loading direction (Figure 4-8a). Moreover, damage initiation occurs in the weft yarns at the yarn crimp location as well as the weft yarns away from the crimp location. This type of weft yarn cracking began early in the loading process and almost all weft yarns possess this kind of damage before the final failure of the composite.

In order to study the effect of local constraints that are posed by the surrounding composite constituents on the weft yarn damage, detailed sequential damage analysis was conducted on the composite specimen. The above mentioned four locations in the laminate (Figure 4-7a-d) were chosen for this purpose, which can represent different cases where the weft yarn local warping (bending) is allowed or constrained by the adjacent layers [28]. Also, the above mentioned four locations represent the various local fabric geometries that are available in the laminate. By constantly monitoring the weft yarn damage at the above mentioned locations during the loading process, the effects of local yarn constraints on the damage initiation stress and location can be realized.

During the loading process of the composite, initial damage is detected at around 100 MPa stress level on the polished edges of the composite. At these low stress levels, damage occurs at the edges of the weft yarn inside the laminate, in the region where there is no contact between the load carrying warp yarn and the perpendicular weft yarn (Figure 4-8a). By increasing the stress level from 100 to 400 MPa in three steps, the damage is observed at the nested yarn configurations at various locations in the laminate (Figure 4-8b). Moreover, the number of observed cracks between these stress levels can be compared to the event count obtained from AE. By increasing the tensile stress from 400 to 500 MPa, the next new damage location is observed on the laminate traction free surface (Figure 4-8c). Moreover, 80% of the microscopic images on the surface (top and bottom) of the laminate show the occurrence of intra-yarn damage at the centre of the weft yarn. At this stress level (400-500 MPa), along with the damage on the surface layers, the crack density in the nested yarns inside the laminate is increased at various locations.

a)
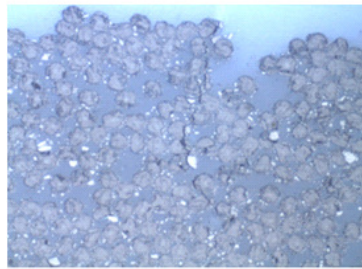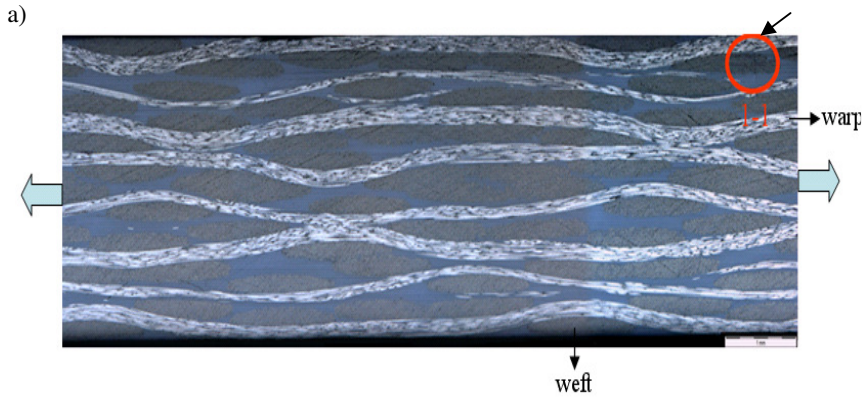
Damage 1-1

b)
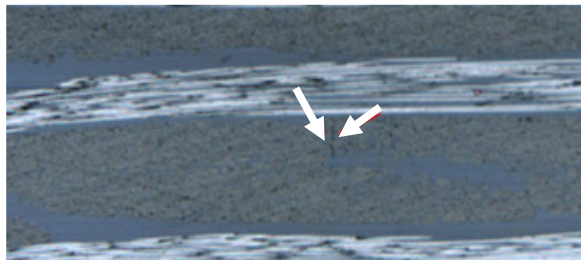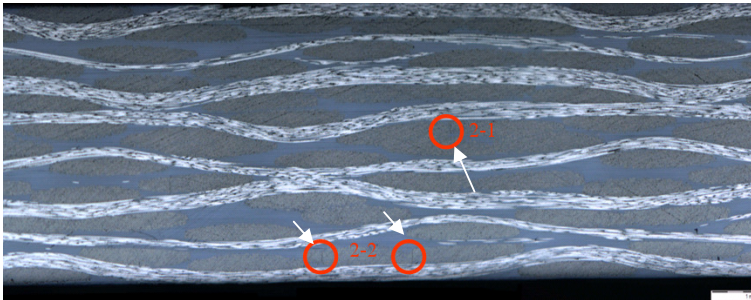
Damage location at 2-1(nested yarn)

c)

3-1
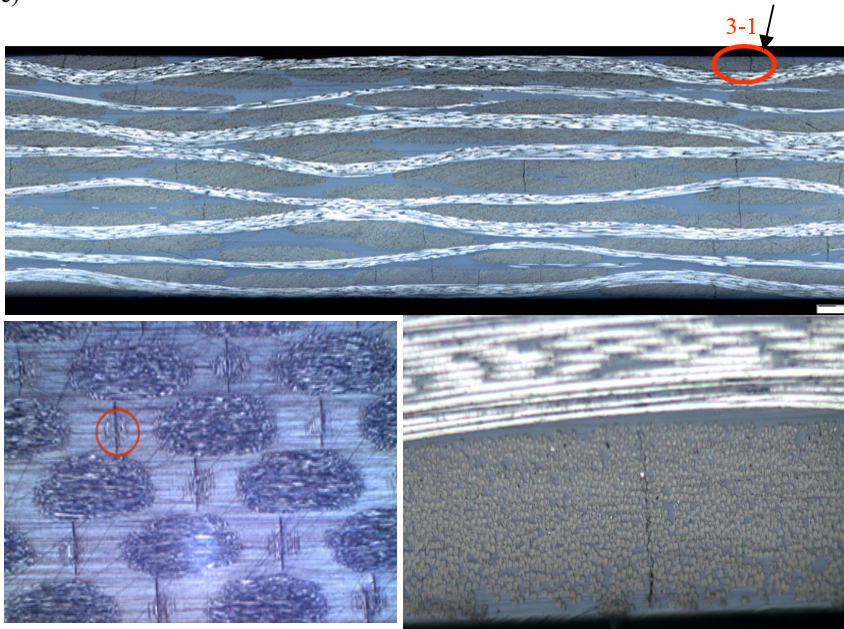
Damage location 3-1 (Surface yarn) top view

Damage location 3-1(Surface yarn) side view

Figure 4-8. **Microscopic sequential damage analysis: a) laminate at 100 MPa tensile stress; b) damage in the nested plies at the tensile stress between 100-400 MPa; c) surface damage at the tensile stress between 400-500 MPa.**

Finally, between the stress levels of 500-680 MPa, the next damage is observed at the edges of the weft yarn, where it is tightly packed by load carrying warp yarns (Figure 4-9). Any further loading causes the catastrophic failure (macro-scale) of the composite specimen. And this final failure always occurs near or within the tab area of the composite specimen (Figure 4-10).

From the above discussed sequential damage analysis, it can be observed that the local fabric geometry whose local bending is restricted by load carrying warp yarns tends to show the initial damage. In contrast, the yarn crimps on the surface layers are relatively more free to deform in the out-of-plane direction, which causes the damage on the surface weft yarns to start at later stages of the loading.
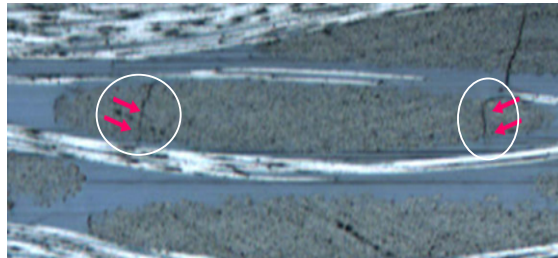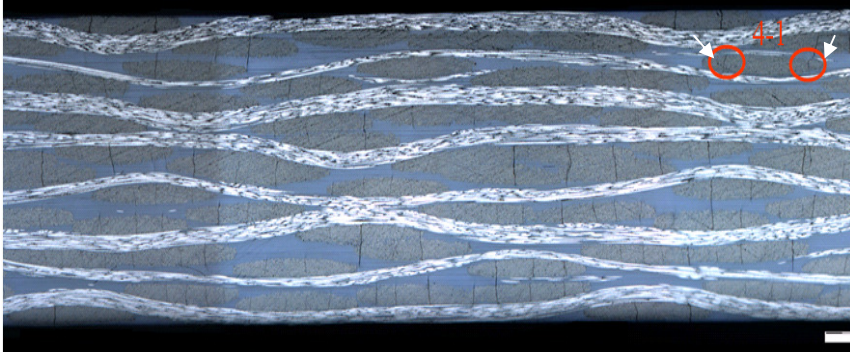
Damage at location 4-1

Figure 4-9.   Microscopic sequential damage analysis: damage in the weft yarn at the tensile stress between 500-680 MPa.

4. 3. 2. b.   Analysis of the sequential intra-laminar damage

The above observed sequence of the intra-laminar damage events at various locations of the satin weave laminate is entirely supported by [29]. In correlation to the observations of the current work, Duplessis Kergomard et al. [29] reported the damage mechanisms for the 4-harness satin weave glass fibre-epoxy composite (Figure 4-11). The author reported that the first stage of the micro-cracks appear adjacent to the yarn crimp region (case 1) (Figure 4-8a). In the nested yarns, the cracks appear far from the yarn crimp location (case 2). Finally, weft yarn damage is detected at the crimp region (case 3).
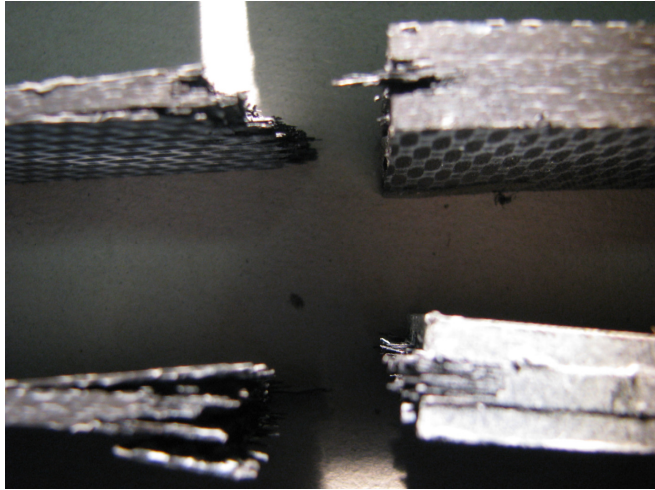
Figure 4-10.   Static failure of the carbon-PPS specimen under tensile load (in the tab region).
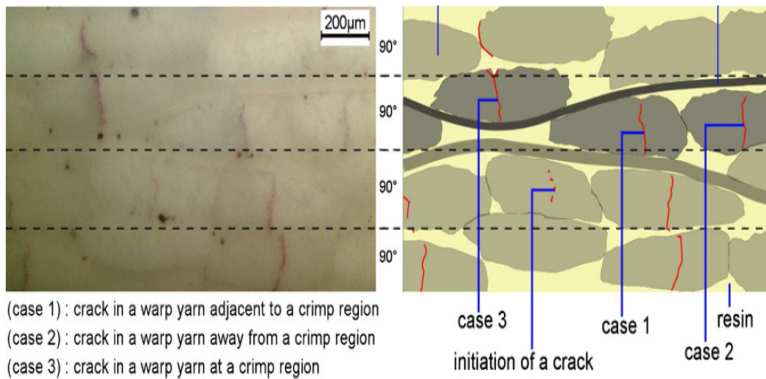
Figure 4-11.   Weft yarn damage locations and the sequence of the damage observed in a 4-harness satin weave composite (glass fibre - epoxy) [29].

The above stated different cracks at different locations are formed due to the straightening in the crimp region, thus inducing the highly localized 3D stress state. The induced stress state highly depends on the yarn crimp angle as well as the yarn dimensions. In addition, the variability at the micro- and meso-scale textile parameters produces the local stress variations in the supposed periodic stress field. However, the good repeatability of the crack locations indicate that these local stress variations must be small when compared to the level of stress concentration induced in the crimp region due to the straightening [29].

4. 3. 2. c.   Effect of the layer stacking on the crack orientation

The above section presented the detailed discussion regarding the effect of the local yarn constraints on the weft yarn damage initiation stress as well as the damage location. The current section is extended to the discussion of the weft yarn crack orientation in a particular ply of the laminate. The orientation of the cracks in the weft yarn of a particular ply depends on the stress components that are present at the location, which are dependent on the position and orientation of the ply within the laminate [5].

As explained by John et al. [5], during the tensile testing (along the warp direction) , the warps are subjected to the constant tensile stress (σ_x) (Figure 4-12). The crimped yarns under the pure tension try to occupy a straight position, and this straightening stress σ_s were introduced. The resolved stress σ_R has an orientation and a value dependent on σ_x and on the yarn crimp angle. The resulting stress direction is important because the cracks within the weft yarns (transverse cracks) are formed at 90^0 to the direction of σ_R .
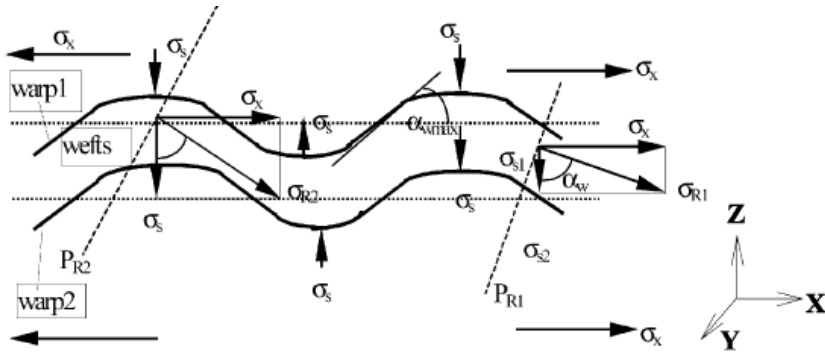
Figure 4-12.   **Implication of yarn geometry undulation on transverse micro cracks [5].**

In case of the satin weave composite surface layers (Figure 4-13a); weft yarn cracks are occurred perpendicular to the load direction due to the absence or minor influence of the shear stress components. However, in the laminate inner layers where the nesting is predominant, weft yarn carks are formed at an angle oblique to the load direction (Figure 4-13b). Here, the weft yarn damage is caused by the combination of transverse stress as well as the interlaminar shear stress [30].
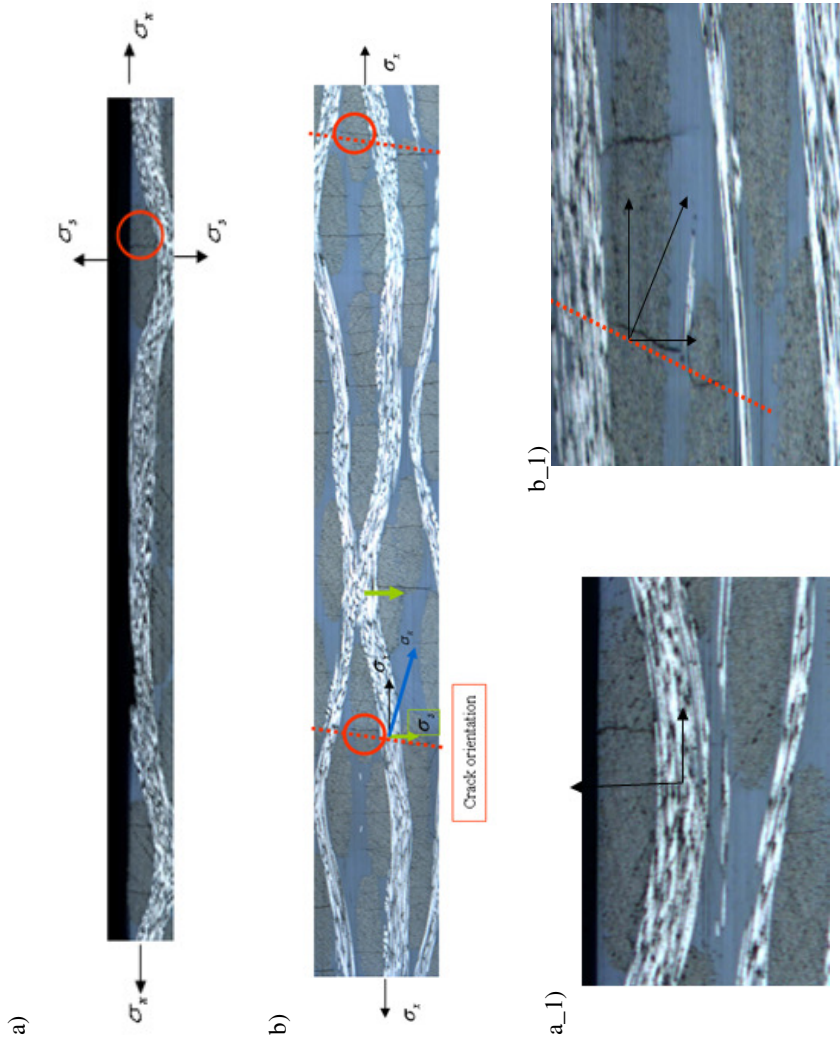
Figure 4-13.   **Effect of the local yarn constraints on the weft yarn crack orientation: a) crack orientation on the surface layer weft yarn; b) crack orientation in the nested yarns.**

4. 4.   Detecting the damage initiation on the composite traction free surface using the DIC data

As described in the previous chapter, once the local surface strain profiles are computed, damage initiation on the composite surface can be detected by plotting local strain at a point vs. average strain computed over the entire strain window as explained below. According to Summerscale et al. [31], by the application of a uni-axial tensile load to the warp yarns, fibres experiencing the highest tension (warp) are straightened more than those under lower strain (weft), as a consequence, the fibres at the non-contact edge of the weft yarn at the yarn crimp location take a longer path than those at the point of contact, thus indicating the possible damage initiation location. The damage initiation at the highest tension point, i.e. the weft yarn at the yarn crimp is detected using the LIMESS local strain data.

In order to detect the weft yarn damage, two different procedures can be found in the literature [32, 33], both using almost the same principle. According to [33, 34] at a certain value of the average tensile strain, the local strain ε_{xx} at a particular chosen point jumps abruptly, indicating the crack initiation transverse to the loading direction. Based on the above theory, the local strain is plotted as a function of the applied average strain at different locations of the surface weft yarns at the yarn crimp location. From Figure 4-14b, at an average tensile strain of around 0.7%, the jump in local strain is detected on the surface weft yarns indicating the damage initiation. The damage locations are marked in Figure 4-14a. As shown in Figure 4-14b, once the damage initiation occurred, the linear relationship between the local and global strain is disturbed. In addition, it is observed that the occurrence of damage on the laminate surface is not periodic, which is indicated by the localization of the strain concentration at random locations on the surface weft yarns (Figure 4-14a). In correlation with the damage initiation obtained from the DIC, microscopic analysis on the polished edges of the tensile tested composite laminate show that the surface plies weft yarn damage occurred at around 0.6-0.8% of the average tensile strain (Figure 4-8c) [35].

a)

b)
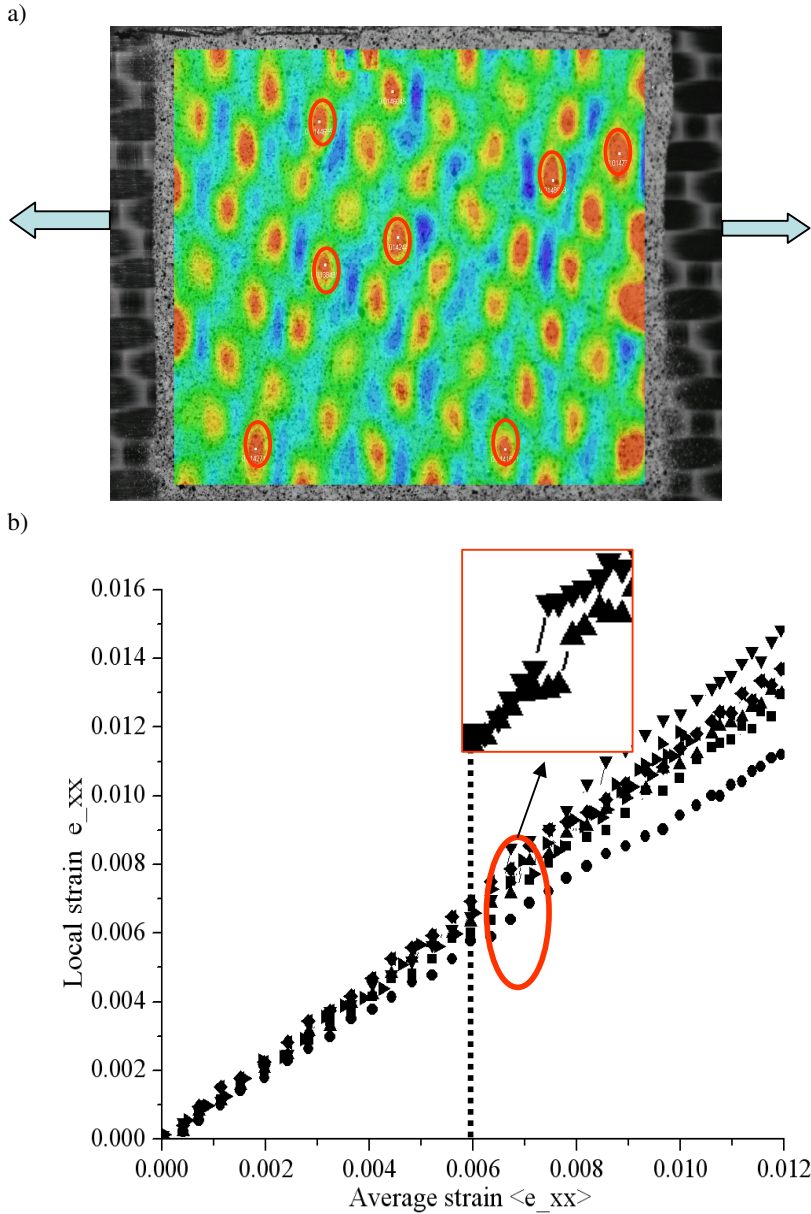
Figure 4-14.   Damage initiation on the traction free surface using DIC data: a) DIC local surface strain pattern at 1.19% of average tensile strain; b) local vs. average tensile strain.

4. 5.   Crack density analysis

Besides the qualitative analysis, microscopic images were used for the quantitative analysis as well. The accumulation of transverse weft yarn damage in the thickness direction is quantified on the polished edges of the composite. The crack density is measured as a function of the applied stress for the layers of the laminate, by dividing the number of cracks measured in each layer with the laminate gauge length [22]. Figure 4-15 shows the crack density as a function of applied tensile stress for three composite samples. The microscopic damage analysis described above is in correlation with the AE event pattern. At around the 250 MPa stress level ($\cong 0.37\%$ of average strain), the event count obtained from AE as well as the crack density tends to increase. The observed difference in the weft yarn crack density between different samples (Figure 4-15) is caused by: i) stochastic macro and meso level parameters; ii) micro-scale parameter such as variation in the fibre-matrix interface properties.
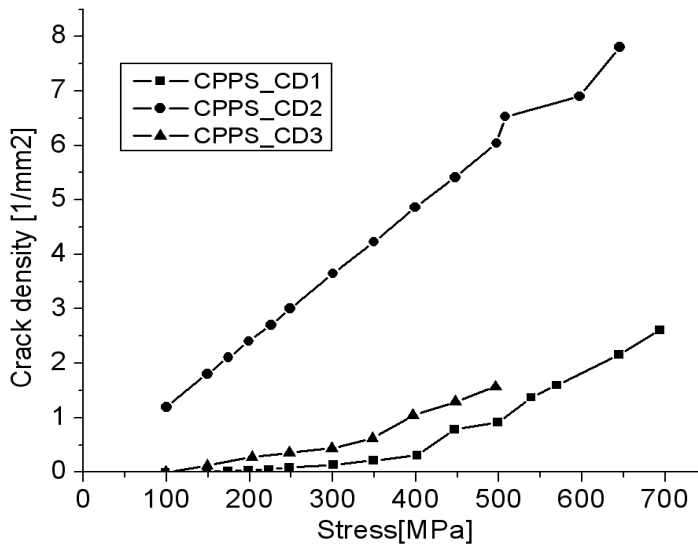
Figure 4-15.   Crack density as a function of applied tensile stress.

4. 6.   Macro-scale response of the satin weave composite

Previous sections of this chapter presented the detailed discussion regarding the micro-scale damage events that are initiating during the tensile test of the satin weave composite. In the current section, discussion is extended to the investigation of the influence of micro-scale damage events on the macroscopic composite stiffness. Starting from very low stress levels at around 40 MPa global tensile stress, the weft yarn damage (micro-scale) initiates. And the subsequent tensile load process increases the crack density in different plies of the satin weave composite until the final failure. However, the induced micro-scale damage does not show any influence on the macro-scale stress-strain (Figure 4-16) behaviour of the satin weave composite. Although satin weave composite seems to exhibit a linear stress-strain behaviour until composite failure (Figure 4-16), the local derivatives of the stress-strain curve shows substantial increase in the composite tangential modulus. At the beginning of the tensile load process, composite stiffness stands at around 55 GPa. Further tensile load process increases the composite stiffness and stands at around 60 GPa at the end of the tension test. For different carbon-PPS samples, the amount of stiffening varies from 6-8%.

As explained by [22, 36], the stiffening of the carbon fabric woven composites is caused by the straightening of the crimped yarns under the applied external tensile load. From the material perspective, the non-Hookean behaviour of the satin weave composite is attributed to the carbon fibre stiffening behaviour under the applied tensile load [37, 38]. In the following chapters of this manuscript (section 5.6), detailed discussion is presented regarding the composite stiffening from the geometrical as well as material perspective.

4. 7.   Summary of the experimental damage analysis

- Damage initiation in the carbon-PPS satin weave composite varies from 40 to 100 MPa applied average tensile stress. The variation of the experimental damage initiation stress in different composite plates can be attributed to the variation in micro-level (fibre spacing, intra yarn volume fraction, etc) as well as the laminate level (nesting) parameters combined with the residual thermal stresses in the composite.
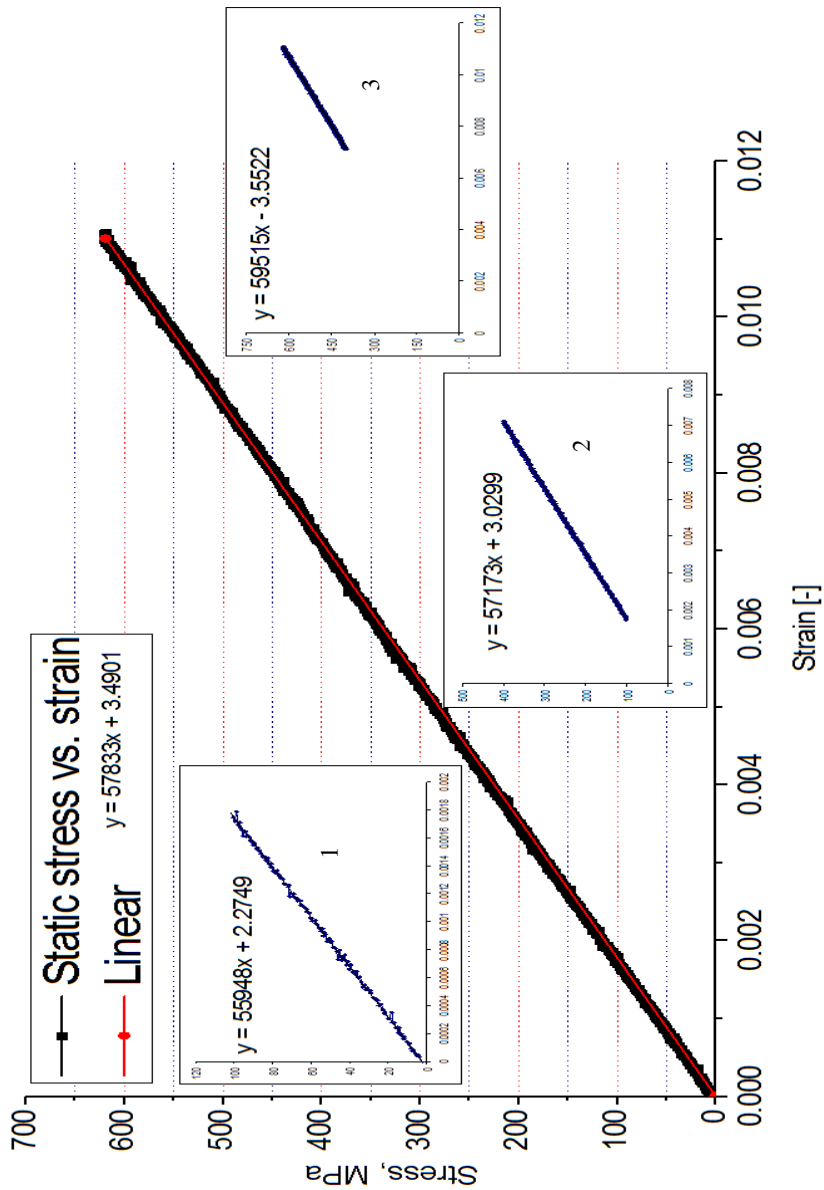
Figure 4-16.   **Macro-scale stress vs. strain behaviour of the carbon-PPS satin weave composite.**

- From the research output of Le Page et al. [39] and the AE event data obtained from the satin weave composite under tensile load, it can be concluded that the energy release rate and the associated local bending of the satin weave weft yarn increases approximately around 200 MPa global tensile stress.

- From the extensive microscopic analysis of damage in several satin weave laminates, in contrast to the experimental local strain analysis, the damage initiation in different plies of the satin weave composite depends on the ply position in the laminate. The earliest damage events occur in the inner layers, followed by the transverse cracking on the surface weft yarns. This behaviour is related to the constraints posed by the neighbouring layers on the local ply. Moreover, initial transverse cracks tend to be located near the edges of the weft yarns cross-section rather than the centre.

- The above observations are entirely supported by the work of Ivanov et al. [7], in which the author reported that the meso-stress distribution, and crack density is different for inner and outer layers of the laminate. Moreover, meso-stress distribution depends upon the stacking sequence, ply shift and the number of plies in the laminate [8].

- Although satin weave composite weft yarns posses numerous micro-scale damage locations under the applied tensile load, their influence on the global stiffness of the composite is negligible.

The damage phenomena discussed above focus mainly on the qualitative damage behaviour of the satin weave composite. In conclusion, it can be said that: a) damage in a satin weave composite is a sequential process; b) damage initiation in the particular yarn depends on the ply position in the laminate; c) moreover, it is also observed that the crack orientation is also influenced by the yarn location in the laminate. In order to understand the local variation in the ply deformation and stress components that are causing the above discussed sequential damage process, the following sections of this chapter provide the deterministic numerical simulations using a satin weave unit cell model.

4. 8.   Numerical damage analysis

Following by the above discussed comprehensive experimental damage analysis, in order to understand the mechanics that cause the sequential weft yarn damage process in the plies of the satin weave composite, meso-FE simulations are accomplished using the satin weave unit cell model. As explained in the previous chapter, FE analysis of a single unit cell with 3D PBC predicts the satin weave homogenized effective elastic constants that are in good correlation with the experimental elastic constants. However, the meso-FE procedure still needs to be improved for analysis of the local stress and damage behaviour of the composite using the unit cell FE simulations [7, 40]. The majority of the published numerical work regarding the analysis of local structural behaviour in the textile composite is based on the single unit cell FE simulations with 3D PBCs. The underlying principle in the application of 3D PBCs is that the unit cell is chosen from the middle of the laminate [41-44], which represents the entire stress/strain fields in the composite. However, recent publications [8, 45, 46] on the meso-FE analysis of the unit cell have emphasized the effect of free surface and free edges on local stress behaviour. Moreover, the influence of internal yarn shifting on the local stress behaviour of the unit cell has been highlighted.

In order to investigate the effect of local fabric geometries on the damage behaviour, Le Page et al. [39] developed two-dimensional plane strain FE models of woven composite with in-phase, out-of-phase and staggered shifted unit cell models. The above mentioned work concluded that the strain energy release rate associated with the crack formation is influenced significantly by the crack location. In addition, the formation of a crack is associated with the local bending deformation, and the energy release rate increases with the degree of bending. The research work of Zako et al. [4, 47] investigates the effect of yarn thickness and the crimp ratio in a plain weave composite, and its influence on the damage initiation and overall stress - strain behaviour of the composite. The aforementioned study concluded that the yarn thickness shows considerable effect on the damage initiation as well as the load carrying behaviour of the composite after damage initiation. Moreover, this study also reveals a relation between the overall tensile strength of unit cell versus unit cell thickness. According the Roy et al.[48], the stress analysis at the damage elements at the wavy region of the model laminate will provide a stepwise understanding to identify the influence of the local stress components on the different damages that are detected under the experimental tension test.

According to Adams et al. [49], the modelling approaches assume idealized textile architecture and generally consider a single unit cell. Due to the randomness of textile architecture produced using conventional processing techniques, the experimental data obtained has shown limited use for verifying the accuracy of these numerical models. In correlation with the above statement, in the previous chapter (Chapter 3) it is already shown that the applied 3D PBC to the single unit cell is unable to represent the adjacent ply interaction. As a consequence, in order to compare the numerical strain profiles with the experimental resunlts, different unit cell stacks are developed for the meso-FE analysis.

The first part of this chapter described the experimental observations of the sequence of damage events in different layers of the 5-harness satin weave carbon-PPS laminate, which are influenced by the local fabric geometries. The sequence of damage events in different layers implies that the damage initiation may have been influenced by the local constraints imposed by the surrounding plies. The above experimental observations are verified using the unit cell as well as laminate level 3D meso-FE simulations. The objective of the current numerical work is two fold: i) developing a meso-FE analysis procedure for predicting the observed experimental sequential damage in the weft yarns; ii) analysing the variation in the stress components and the deformation mechanics that causes the sequential damage.

4. 9.   Damage and stress analysis using unit cell FE simulations

4. 9. 1.   Micro-mechanical   homogenization   of   the   strength properties

In order to accomplish the unit cell FE damage analysis, initially, strength properties of the impregnated yarn are derived from the individual strength properties of the carbon fibre and PPS resin (Table 4-3) using the Chamis analytical strength homogenization formula (Table 4-4) [50]. The obtained homogenized UD strength properties (Table 4-5) are assigned to the unit cell sections in their local coordinate system. The micro-scale homogenization of strength properties of composite is accomplished by assuming the intra-yarn fibre volume fraction in the yarn being constant ($\phi_f = 70\%$).

Table 4-3   Strength properties of T300 JB carbon fibre and PPS matrix.

Property	T300 JB carbon fibre	PPS (resin)
Tensile strength, MPa	4210	90.3
Compressive strength, MPa	2616	148
Shear strength, MPa	-	63

Note: *T300 JB carbon material strength properties are taken from TORAYCA technical datasheet No: CFA-002. PPS material properties are taken from TECHTRON & RYTRON PPS data sheet.*

Table 4-4   Chamis strength homogenization formulas [50].

Property	Chamis
Longitudinal Tension, $F_L^{(t)}$	$\phi_f F_f$
Longitudinal Compression, $F_L^{(c)}$	$\phi_f F_c$
Transverse Tension, $F_T^{(t)}$	$\left[1 - (\sqrt{\phi_f} - \phi_f)(1 - E_m / E_{f22})\right] F_m^t$
Transverse Compression, $F_T^{(c)}$	$\left[1 - (\sqrt{\phi_f} - \phi_f)(1 - E_m / E_{f22})\right] F_m^c$
Intra-laminar shear, F_{LT}	$\left[1 - (\sqrt{\phi_f} - \phi_f)(1 - G_m / G_{f22})\right] F_m^s$

ϕ_f Intra-yarn fibre volume fraction F_f Fibre longitudinal tensile strength

E_{f22} Fibre transverse modulus G_{f22} Fibre transverse shear modules

F_c Fibre longitudinal compressive strength E_m Matrix elastic modulus

F_m^t Matrix transverse strength E_{fL} Fibre longitudinal modules

F_m^c Matrix compressive strength F_m^s Matrix shear modulus

E_T UD transverse modulus

Table 4-5.   **Homogenized strength properties of the carbon-PPS impregnated yarn.**

Mechanical property	*Carbon-PPS impregnated yarn (ϕ_f =0.7)*
Tensile strength, MPa	$F_L^t = 2947$ $F_T^t = 80$ $F_Z^t = 80$
Compressive strength, MPa	$F_L^c = 1832$ $F_T^c = 130$ $F_Z^c = 130$
Shear strength, MPa	$F_{TZ}^s = 56$ $F_{ZL}^s = 56$ $F_{LT}^s = 56$

4. 9. 2.   Selection and implementation of the failure criterion

Once the transversely isotropic strength properties of the yarns and the isotropic material properties of the matrix are assigned, for the damage analysis of the unit cell the following approach is employed. Generally, failure criteria fall into four basic categories: 1) limit theories; 2) polynomial theories; 3) strain energy theories and 4) direct mode determining theories. In order to determine the failure initiation in the fibre reinforced composites, polynomial theories are widely used [51]. The aforementioned theories use a polynomial in stress to describe the failure surface.

From the above discussion, initially, the occurrence of damage in the unit cell element is detected using the Hoffmann failure criteria [51] for a transversely isotropic material (Eq 4.1). Usage of the above mentioned failure criterion is justified by [4, 51, 52] for the prediction of damage initiation in composite materials. However, the above mentioned failure criterion cannot indicate the type of damage mode in the yarns, where the architecture of the fibre arrangement plays an important role.

$$F(\sigma,F)=(\frac{1}{F_L^t}+\frac{1}{F_L^c})\sigma_1+(\frac{1}{F_T^t}+\frac{1}{F_T^c})(\sigma_2+\sigma_3)-\frac{\sigma_2^2}{F_T^t F_T^c}-\frac{\sigma_1^2}{F_L^t F_L^c}+\frac{\sigma_1\sigma_2}{F_L^t F_L^c}+\frac{\sigma_4^2}{F_{TZ}^2}+\frac{(\sigma_5+\sigma_6)^2}{F_{LT}^2} \qquad (4.1)$$
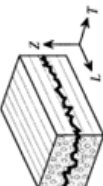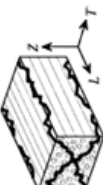
If $F(\sigma,F) \geq 1$ damage initiation

$$\sigma_1 = \sigma_{LL}$$

F_L^t - tensile strength in the fibre direction

$$\sigma_2 = \sigma_{TT}$$

F_L^c - compressive strength in the fibre direction

$$\sigma_3 = \sigma_{ZZ}$$

$F_T^{(t)}$ - tensile strength in the transverse direction

$$\sigma_4 = \sigma_{LZ}$$

$F_T^{(c)}$ - compressive strength in transverse direction

$$\sigma_5 = \sigma_{TZ}$$

F_{TZ} - transverse shear strength

$$\sigma_6 = \sigma_{LT}$$

F_{LT} - axial shear strength

According to Zako et al. [52] The modes of the damage are classified into four different types as shown in Table 4-6. The mode L represents the fibre breaking, T and Z modes represent the transverse and shear cracking. As shown in Table 4-6, by calculating the corresponding stress-to-strength ratios for the different modes, we consider that the damage mode that is taking place is the one whose stress-to-strength ratio has the maximum value. The above mentioned failure criteria and the and the following damage direction modes is implemented into the commercial FE software ABAQUS using UMAT Fortran routines, which enable us to simulate the damage in the unit cell. The results obtained from the FE modelling are compared with the experimental observations as follows:

   i.   validation of the FE damage initiation strain with the damage initiation strain obtained from the experimental acoustic emission technique.

  ii.   finding the FE damage initiation location in the unit cell, this could be verified with the microscopically observed damage initiation location on the quasi-static tensile tested composite specimen.

 iii.   finally, in the view of analyzing the variation in the stress components that are causing the sequential damage analysis in the plies of a satin weave composite, local stress analysis is conducted using different unit cell stacks.

Table 4-6.   The characteristics of the anisotropic damage model for fibre bundle and isotropic damage model for matrix [52].

| Damage mode	Anisotropic damage model for fiber bundle				Isotropic damage model for matrix
	Mode L	Mode T & LT	Mode Z & ZL	Mode TZ	
Maximum stress-to-strength ratio	$\dfrac{\sigma_L^2}{F_L^t F_L^c}$	$\dfrac{\sigma_T^2}{F_T^t F_T^c}$ or $\left(\dfrac{\tau_{LT}}{F_{LT}^s}\right)^2$	$\dfrac{\sigma_Z^2}{F_Z^t F_Z^c}$ or $\left(\dfrac{\tau_{ZL}}{F_{ZL}^s}\right)^2$	$\left(\dfrac{\tau_{TZ}}{F_{TZ}^s}\right)^2$	—
Damage tensor $\begin{bmatrix} D_L & 0 & 0 \\ 0 & D_T & 0 \\ 0 & 0 & D_Z \end{bmatrix}$	$\begin{bmatrix} 1 & 0 & 0 \\ 0 & 0 & 0 \\ 0 & 0 & 0 \end{bmatrix}$	$\begin{bmatrix} 0 & 0 & 0 \\ 0 & 1 & 0 \\ 0 & 0 & 0 \end{bmatrix}$	$\begin{bmatrix} 0 & 0 & 0 \\ 0 & 0 & 0 \\ 0 & 0 & 1 \end{bmatrix}$	$\begin{bmatrix} 0 & 0 & 0 \\ 0 & 1 & 0 \\ 0 & 0 & 1 \end{bmatrix}$	$\begin{bmatrix} 1 & 0 & 0 \\ 0 & 1 & 0 \\ 0 & 0 & 1 \end{bmatrix}$

4. 9. 3.   FE simulation of the damage in the laminate inner layers (CASE I)

In order to simulate the stress and damage behaviour inside the laminate, FE analysis is started with a single unit cell by applying 3D PBCs [41, 53], which corresponds to the unit cell located in the middle of the laminate. During the loading process, at 0.2% of the applied average tensile strain in the warp direction (Figure 4-17 X-direction), the damage initiation is detected at the edges of the weft yarn at the yarn crimp location by Hoffmann criteria (Figure 4-17). Once the Hoffmann criteria detect the damage initiation in the element, for the direction of the damage, the individual stress-to-strength ratios are calculated using the formulas shown in the Table4-6. And the values are listed below for the damaged elements.

$$\text{Mode L } (\frac{\sigma_l^2}{F_L^t F_L^c}) = \text{Negligible} \qquad \text{Mode T } (\frac{\sigma_t^2}{F_T^t F_T^c}) = 0.23$$

$$\text{Mode Z } (\frac{\sigma_z^2}{F_z^t F_z^c}) = 0.08 \qquad \text{Mode TZ } (\frac{\tau_{TZ}}{F_{TZ}^s})^2 = 0.16$$

Based on the above listed individual stress-to-strength ratios, the local transverse damage (meso-level) in a satin weave weft yarn is a combination of the micro-level transverse damage mode along with the out-of-plane shear damage mode. The predicted FE micro-level damage modes are in correlation with the theory of Cox [54] on the satin weave composite architecture. Cox reported that the asymmetric satin weave fabric causes the coupling of bending and stretching, and there is also coupling between stretching and in-plane shear under pure tensile load. In the present case, it is observed that the load coupling between stretching and in-plane shear is negligible compared to the load coupling between bending and stretching.

Followed by the local damage analysis, local stress analysis is conducted and the details are presented in the current section. From the transverse stress contours (Figure 4-18a), the maximum stress of 49 MPa is observed at the damaged elements of the weft yarn. Moreover, the transverse stress profile (Figure 4-18b) is plotted on the surface elements of the weft and warp yarns between the yarn crimp locations as marked in Figure 4-18a. In correlation to the local strain analysis (Chapter3), the variation in local transverse stress is divided into three parts (Figure 4-18b): starting from the centre of the weft yarn at the yarn crimp location, the transverse stress value increases from 30 MPa to the maximum value of 49 MPa at the edge of the weft yarn.
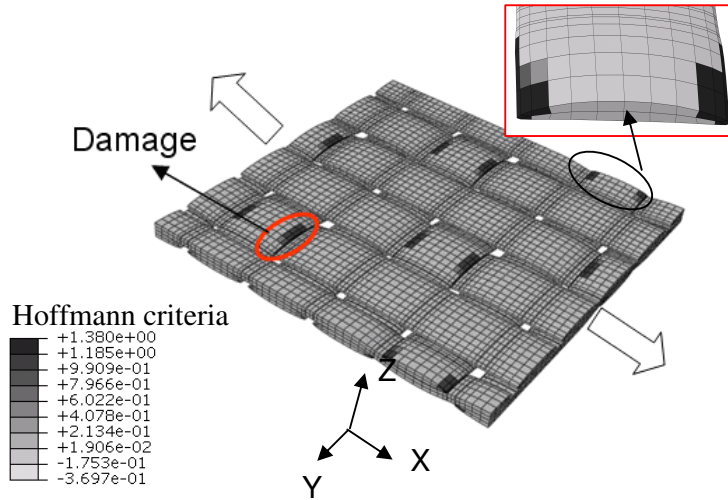
**Figure 4-17.   Damage initiation in the laminate inner layers (3D PBCs-0.2%
                     longitudinal strain).**

The second phase of the stress profile starts at the edge of the weft yarn, and
decreases to the minimum value (12 MPa) in the geometrical transition location
between the crimp regions to the flat position of the load carrying warp yarn. The
third phase in the stress profile is related to the constant transverse stress of 10 MPa
at the flat position of the load carrying warp yarn.

a)
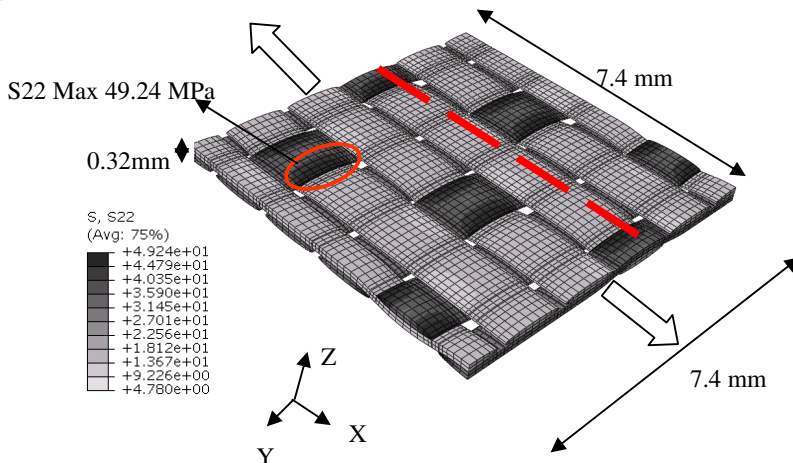
b)
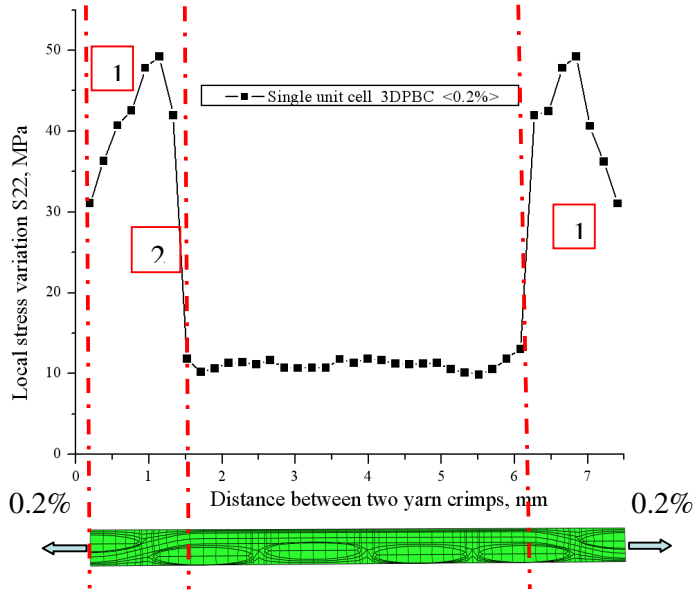
Figure 4-18.   **Local stress analysis: a) local transverse stress contours; b) local transverse stress profile (3D PBC-0.2% longitudinal strain)**

As explained above, apart from the transverse stress, the out-of-plane shear stress also shows considerable effect on the damage initiation in the unit cell. Figure 4-19(a, b) shows the out-of-plane shear stress contours and the variation of the stress profile along the length of the unit cell as depicted in Figure 4-19a, for the applied tensile load in the warp yarn direction.

a)
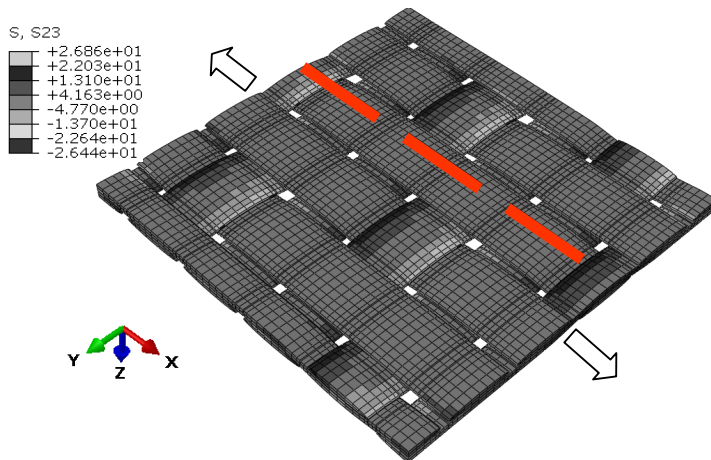
b)
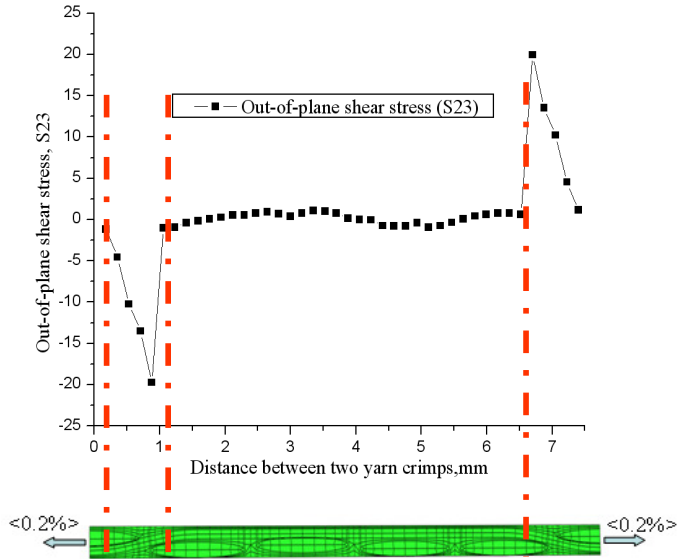
Figure 4-19.   **Local out-of-plane shear stress analysis: a) shear stress contours; b) shear stress profile (3D PBC-0.2% longitudinal strain)**

In the entire unit cell, the maximum out-of-plane shear stress at around 20 MPa is detected at the edge of the weft yarn where damage initiation is detected. At the flat position of the load carrying warp yarn, almost zero shear stress is observed.

4. 9. 4.   FE simulation of the damage on the surface layers (Case II)

The above section presents the damage and stress analysis in the laminate inner layers. Nevertheless, the above presented experimental analysis on the satin weave composite concludes that the damage initiation in the plies of a satin weave composite is a sequential process. And the damage initiation strain in the inner layers varies substantially from those of the surface layers. In order to understand the stress mechanics that is causing the sequential damage, the current section deals with the numerical simulation of the local stress and damage behaviour of the unit cell on the traction free surface. In order to understand the variation in local damage behaviour in the finite laminate compared to the infinite laminate, the single unit cell FE analysis with 3D PBCs is changed as explained below.

Initially, the surface stress analysis is performed using the single unit cell with in-plane PBCs. The top and bottom surfaces of the unit cell (Figure 4-20a) are free to deform in the out-of-plane direction. Under the above specified constraints, at 0.25% of the applied average strain in the warp yarn direction, weft yarn damage is detected at the yarn crimp location (Figure 4-20b). From the local stress analysis, it is observed that the maximum tensile stress (80 MPa) occurs at the centre of the weft yarn (Figure 4-20a). Due to the absence of textile reinforcement or supporting boundary conditions in the out-of-plane direction, the straight part of the warp yarn adjacent to the yarn crimp location is slightly compressed in the transverse direction (Figure 4-20c).

Comparison of the experimental (0.6%) and numerical (0.25%) surface damage initiation strains underlines the necessity for improvement in the unit cell model used for the surface stress analysis. In order to capture the effect of underlying layers on the surface stress profile, it is necessary to create a unit cell stack for the FE analysis. However, producing the unit cell stack with the same mesh size as a single unit cell is computationally very expensive. In this regard, comparison of the numerical local strain profiles with different mesh densities to the experimentally measured strains by Lomov et al. [55] leads to the conclusion that the effect of mesh size is minimal on the local strain variation.

In the current work, to study the effect of mesh size on the local stress behaviour, Figure 4-20c compares the local transverse stress profiles on the traction free surface with different unit cell mesh densities. The unit cell model with a coarse mesh has 8400 elements, and the fine mesh has 53200 elements. From the local stress profiles (Figure 4-20c), it is evident that the maximum and minimum stress locations are the same for different mesh densities. Further, there is a difference of approximately 10 MPa stress between the fine and coarse mesh at the yarn crimp location. The coarse mesh FE model contains two brick elements in the centre of the yarn (C_1). The fines mesh FE models (C_2, C_3) represented by six and eight brick elements respectively.

a)

b)

c)
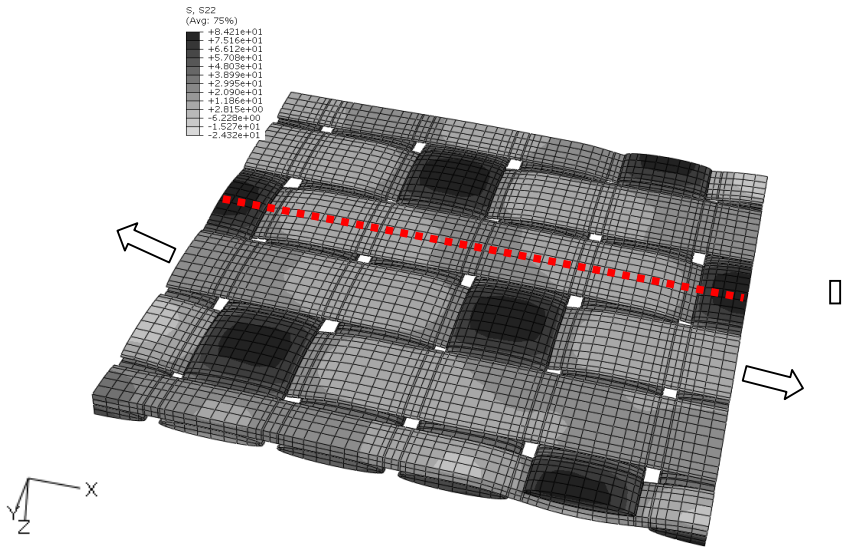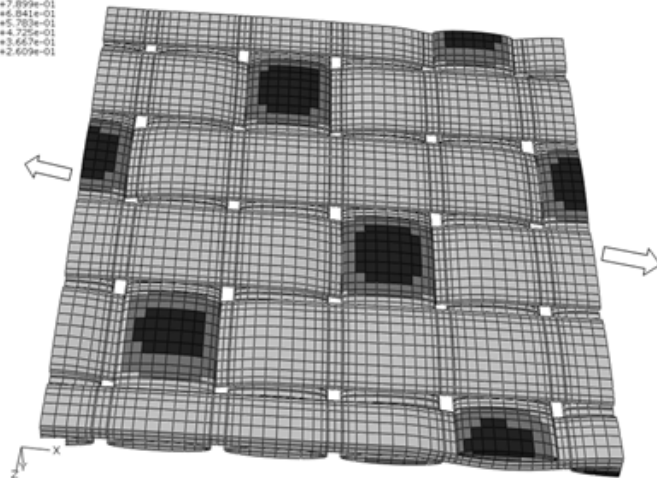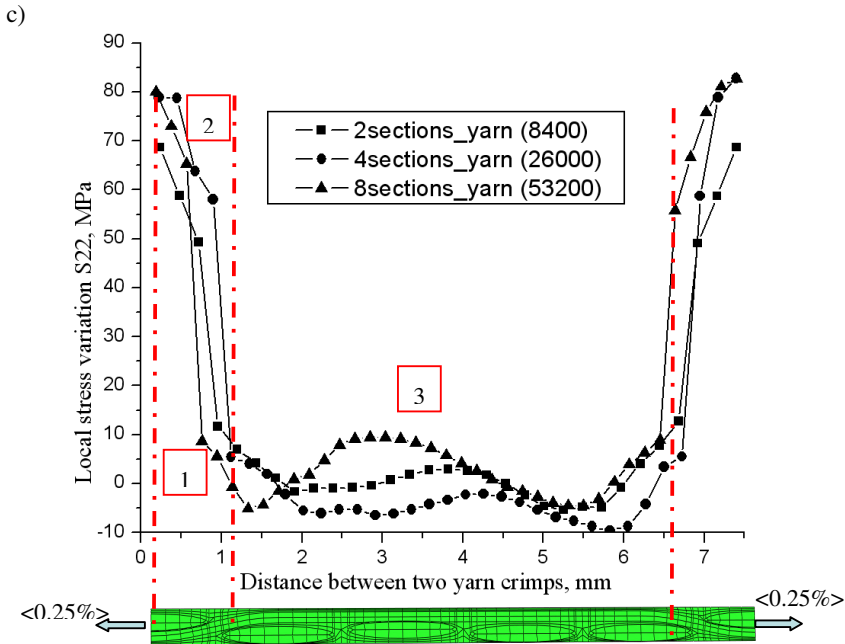
Figure 4-20.   **Single unit cell stress and damage profiles with in-plane PBC: a) transverse stress distribution on the weft yarn; b) transverse damage on the weft yarn at the yarn crimp location; c) transverse stress profiles between two yarn crimps with different mesh size.**

In the process of improving the unit cell FE analysis, four unit cells stacked together in such a way that the yarn crimp location are in-phase (Figure 4-21a). The boundary conditions were chosen in such a way that, one of the yz surfaces is restrained in the x direction and the tensile displacement is applied on the opposite face of yz surface. The periodic boundary conditions are applied to the both zx surfaces. Finally, z-symmetry applied to the top xy surface and bottom xy is free (Figure 4-21a).

a)

Hoffmann criterion
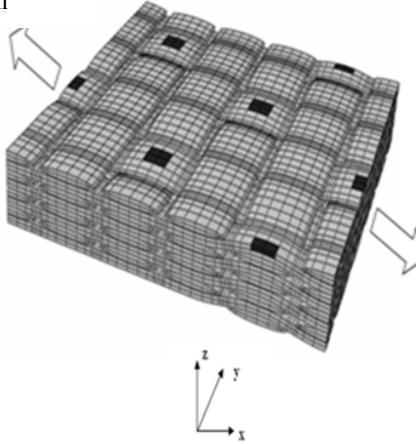
b)

Hoffmann criterion
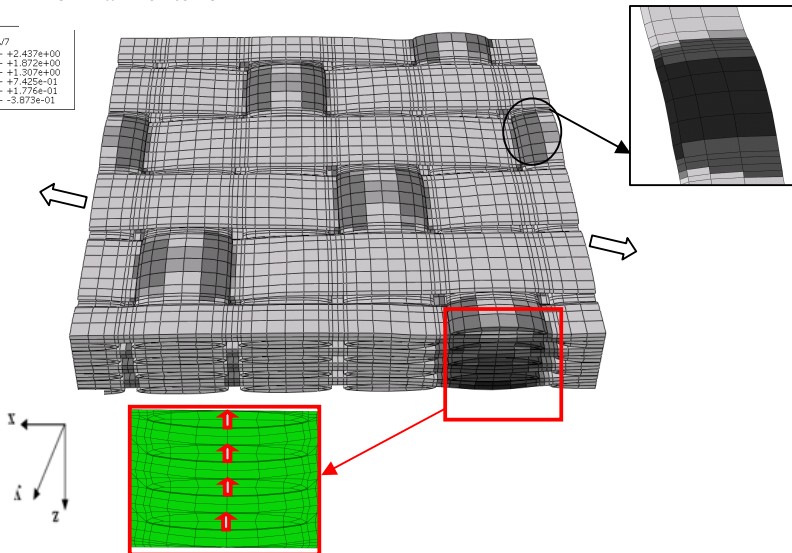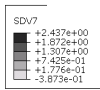
**Figure 4-21.   Four unit cell in-phase stack with in-plane PBC: a) damage
                      initiation on the warp yarn (Z symmetry face); b) transverse
                      damage on the weft yarn at the yarn crimp location on the
                      traction free surface;**

During the FE analysis of the in-phase stacking with the above mentioned BC's, the initial transverse damage is detected by Hoffman criteria at 0.2% average tensile strain on the surface where Z-symmetry is applied (Figure 4-21a), and the above mentioned damage is detected at the centre of the load carrying warp yarns, which is unrealistic. And this phenomenon is not observed during experimental damage analysis. By increasing the tensile strain from 0.2%, without reducing the homogenized elastic constants of the unit cell, weft yarn transverse damage is detected by Hoffmann criteria on the free surface of the unit cell at 0.44% of average strain, and the detected damage elements are situated towards the edge of the weft yarn (Figure 4-21b).

As stated in the previous chapter (Chapter3), in order to study the effect of stacking on the damage initiation, four unit cell out-of-phase stack with the above specified BC's is used for the FE analysis. During the tensile load process, as observed in the in-phase stacking, damage initiation on the warp yarn is detected on the z-symmetry face at 0.2% average tensile strain. Further increasing the tensile load, at 0.47% of the applied average tensile strain, damage is detected at the edge of the weft yarn on the traction free surface (Figure 4-22).

Hoffmann criteria
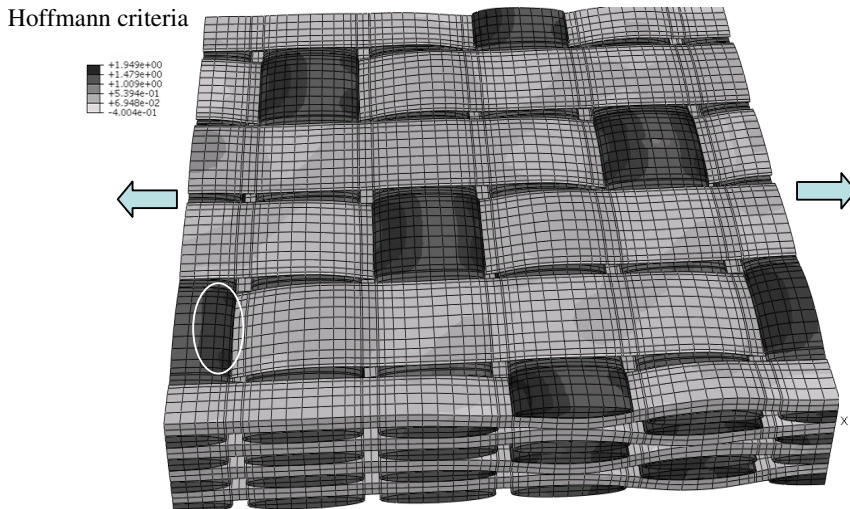
Figure 4-22.   **Four unit cell out-of-phase stack at 0.47% of the average tensile strain: transverse damage on the weft yarn at the yarn crimp location.**

At the damaged elements of the weft yarn on the traction free surface, the in-plane transverse stress (S22) varies in between 52 to 60 MPa. Moreover, the out-of-plane shear stress (S23) at around 15 MPa is detected.

Finally, in order to eliminate the artificial stress concentration at the z-symmetry surface which causes the early damage in the warp yarns, eight unit cells are stacked such that all the yarn crimp locations are in the same phase (Figure 4-23a). The aforementioned stress concentration at the warp yarns is mainly caused by the restriction of the yarn straitening under external load by the applied symmetrical boundary conditions. As an improvement, for the aforementioned eight unit cells stack in-plane PBCs are applied to the edges, while the top and bottom surfaces are free to deform. With the above specified loading conditions, at 0.44% of the global tensile strain in the warp yarn direction, transverse damage is detected at the weft yarn centre in the surface layer of the unit cell (Figure 4-23b). In addition, the transverse stress of 75 MPa is observed in the damaged elements (Figure 4-23a).

a)

132

b)
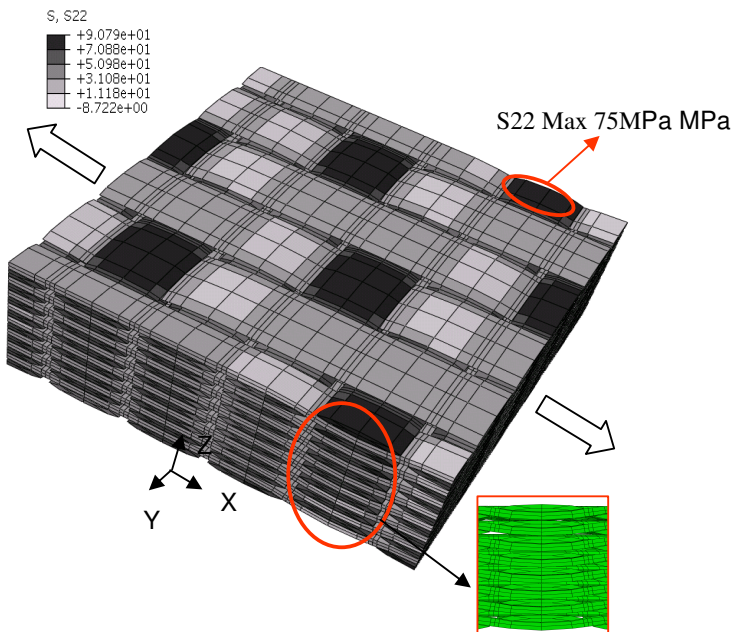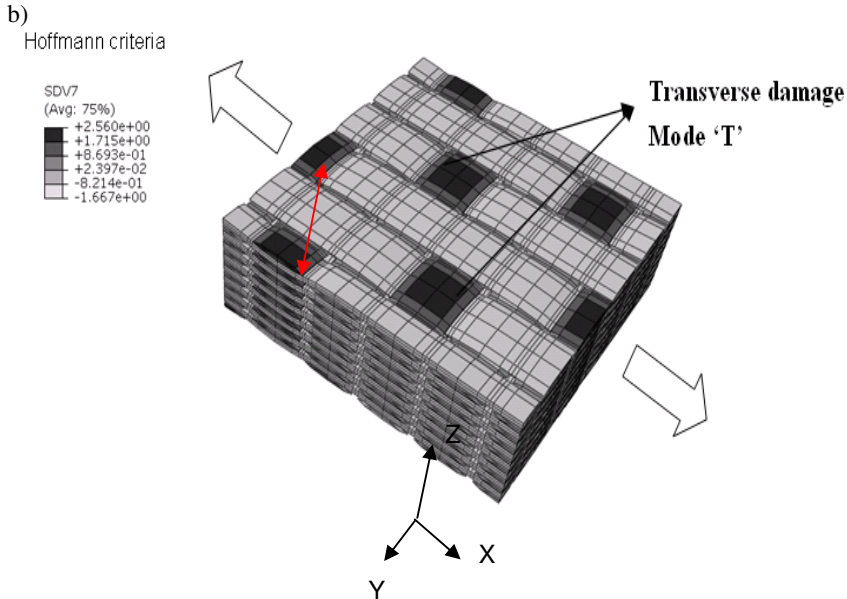
Figure 4-23.   8 unit cell stack FE analysis at 0.44% of the tensile strain with in-plane PBC: a) transverse stress distribution on the weft yarn; b) transverse damage locations on the weft yarn at the yarn crimp location.

From the comparison between the four unit cell stack with symmetry BC's to the eight unit cell stack FE analysis, it is evident that the change in mesh size does not show much influence on the damage initiation. However, the applied symmetry BC's at the bottom of the unit cell stack causes the shift in the damage location from the centre to the edge of the weft yarns on the traction free surface. Moreover, change in the unit cell stack from in-phase to out-of-phase configuration causes the change in the damage location as well as the damage initiation strain.

4. 10.   Comparison between the experimental and numerical results

In this section, the comparison between the experimental and numerical damage analysis is presented. This section is later extended to the analysis of unit cell local stress behaviour at different locations of the laminate. The experimental AE (Acoustic Emission) technique predicts the weft yarn damage in the laminate inner layers around 0.1-0.2% of the applied average tensile strain in the warp yarn direction.

Simulation of the single unit cell with 3D PBCs predicts the weft yarn damage at 0.2% of the global tensile strain, which proves to be a good correlation with the experimental results considering the fact that the computational model did not consider the residual thermal stress in the composite. In a sense, the damage initiation strain obtained from the FE simulations is a deterministic maximum value, which is within the limits of the experimental prediction. Moreover, the damage initiation location obtained from the FE simulation at the edge of the weft yarn (Case-I) shows a good correlation with the observed microscopic damage locations.

On the traction free surface, the single unit cell with in-plane PBCs and the 8 unit cell in-phase stack predict the weft yarn damage at around 0.25% and 0.44% of the global tensile strain respectively. Comparison of the numerical damage initiation strain with the microscopically observed damage initiation strain on the surface (around 0.6%) proves that the FE simulations predict the early damage initiation strain. In correlation with the experimental damage location, the numerical simulations predict the damage at the centre of the weft yarn. Based on the comparison of the experimental and numerical surface damage results, it is evident that without the presence of internal yarn shifting (nesting), by in-phase stacking of the yarn crimp locations, the maximum out-of-plane deformation in the surface layers is reached earlier than in the experimental counterpart (with the internal yarn nesting) and hence causes the early damage initiation [14, 40].

In addition to the local damage analysis, the unit cell local stress analysis provides insight into the active stress components and their variations depending on the ply position in the laminate. The major local stress components observed in the weft yarn at the yarn crimp location are the in-plane transverse stress (σ_{22}), the out-of-plane normal stress (σ_{33}) and the out-of-plane shear stress (σ_{23}) for the applied global tensile strain in the warp yarn direction. The local weft yarn stress values at the yarn crimp location for the single unit cell as well as the laminate are listed in Table 4-7. Comparison of the stress components inside the laminate (Case I) with the surface weft yarn stresses (CASE II) shows that the restriction of the yarn crimp inside the laminate causes a higher out-of-plane shear (σ_{23}) as well as out-of-plane normal stress (σ_{33}) compared to the surface layers. The stress behaviour observed above is in correlation with the research output of Lee et al. [56] on the local strain behaviour of a plain weave composite. The authors reported that the tension/in-plane shear and tension/bending coupling effects at the yarn crimp inside the laminate are restricted by the surrounding plies. In contrast, the unrestricted yarn crimp on the surface layers of the laminate caused weft yarn damage due to the maximum transverse and shear stress.

Finally, research work of Whitcomb et al. [57, 58] on the damage analysis of plain weave unit cell using infinite laminate conditions reported that almost similar stress components are responsible for the weft yarn damage as observed in current research work.

Table 4-7.   **Local stress distribution on the weft yarn cross sections at the damage initiation strain.**

	In-plane transverse stress(σ_{22}), MPa (edge/ centre of the yarn)	Normal out-of-plane stress (σ_{33}), MPa (edge/ centre of the yarn)	Out-of-plane shear stress (σ_{23}), MPa (edge/ centre of the yarn)
CASE I (Inside the laminate)-0.2%	49/31	14/14	22/2
CASE II-Single unit cell-2D pbc (on the surface)-0.25%	49/78	Negligible	16/7
CASE II-8 unit cell stack (on the surface)	62/75	Negligible	4/18
CASE II-8 unit cell stack (inside the laminate)-0.44%	55/60	8/12	15/15

Apart from the local stress and damage analysis, studying the deformation behaviour of the unit cell under the external load provides knowledge on the effect of stacking and the applied boundary conditions for the unit cell FE analysis. The literature [5, 31, 52] has shown that the tensile load applied to the unit cell causes the straightening of the yarn in the loading direction (warp). This straightening effect imposes the out-of-plane deformation on the perpendicular weft yarn. When the weft yarn deformation reaches its maximum value, damage will occur on the surface of the weft yarn. Figure 4-24(a, b) shows the 5-harness satin weave unit cell before and after the extension load. From Figure 4-24b, the out-of-plane deformation at the yarn crimp location under the extension load is evident.

a)
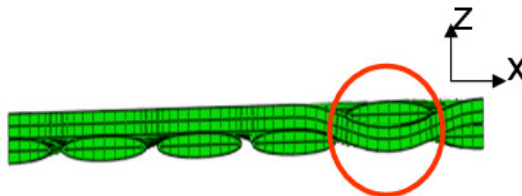
b)
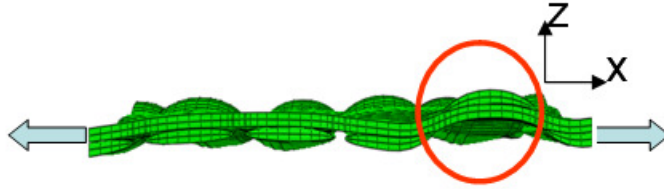
Figure 4-24. **Out-of-plane displacement at the yarn crimp: a) un deformed configuration; b) deformed configuration (10 times magnified).**

Moreover, the out-of-plane deformation is plotted on the surface of the above discussed unit cells in the positive z-direction between two yarn crimp locations at the moment of the respective damage initiation strains. Considering the absolute difference from maximum to minimum deformation, as expected, the out-of-plane deformation is restricted with 3D PBCs (Figure 4-25) causing an almost flat deformation starting from one yarn crimp to the other (peak points in the curves represent the yarn crossover position).
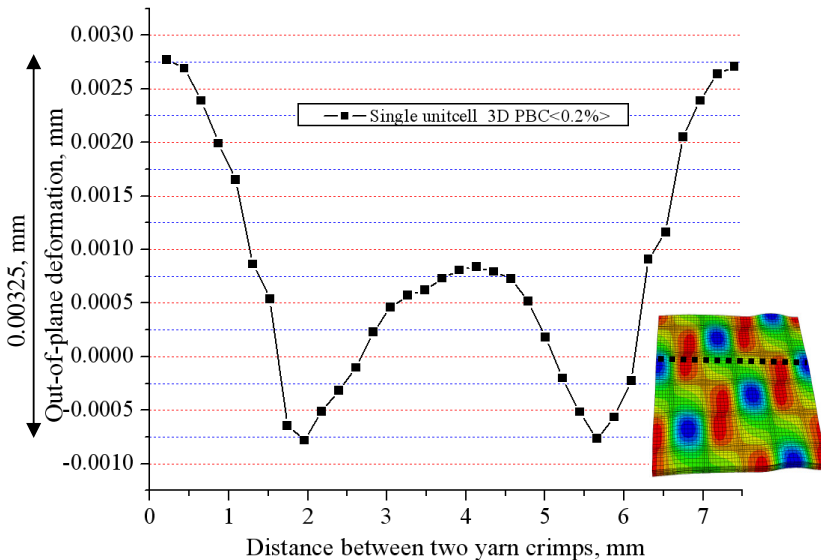
Figure 4-25. **Variation in the out-of-plane deformation on the unit cell surface under uni-axial static tensile load (3D PBC).**

a)
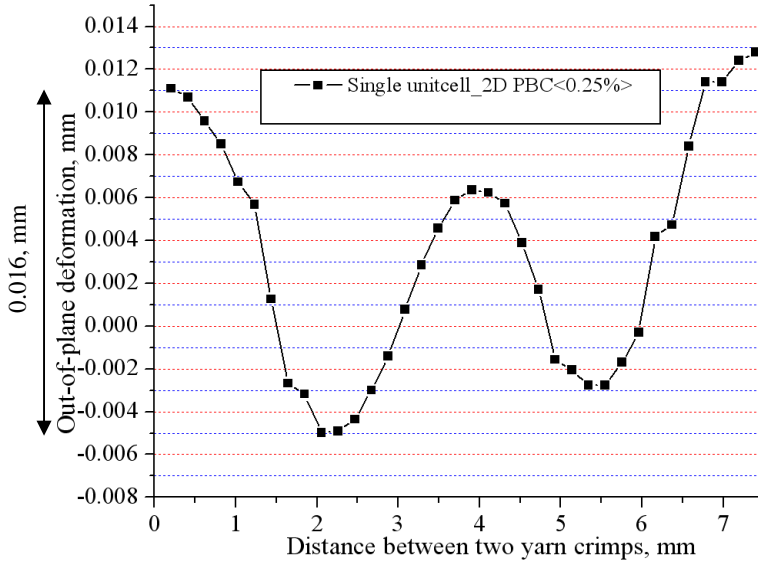
b)
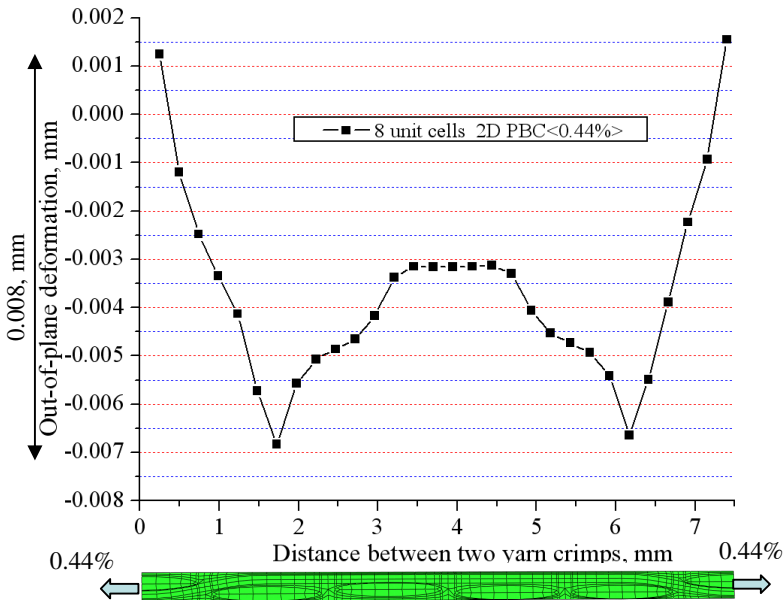
Figure 4-26.   Out-of-plane deformation on the traction free surface at the moment of damage initiation: a) single unit cell with in-plane PBC (0.25%); b) 8 unit cell stack with in-plane PBC (0.44%).

In contrast, the single unit cell with in-plane PBC predicts a large difference in the out-of-plane deformation (Figure 4-26a) between the yarn crimp and the flat yarn position. Moreover, the absolute difference in the out-of-plane deformation value for the 8 unit cell stack (Figure 4-26b) at 0.44% of the global strain is approximately twice the value of the infinite laminate at 0.2%. The aforementioned statement shows that, by increasing the number of unit cells in the stack, the out-of-plane deformation at the yarn crimp of the finite surface unit cell stack approaches the infinite laminate deformation [8].

4. 11.   Sequential damage in the satin weave composite and the varying stress components

As explained in the above sections, weft yarn damage in the satin weave composite is a sequential process. From the local longitudinal strain analysis from the previous chapters (Chapter 3), it is concluded that the effect of the internal yarn shifting (nesting) does not show any influence on the local longitudinal strain behaviour of the composite. However, from the above sections it is evident that the stress components such as transverse stress, out-of-plane normal and the out-of-plane shear stress vary considerably along the thickness direction in the composite plies. In correlation with the local longitudinal strain behaviour (Chapter 3), comparison of the local longitudinal stress profiles (Figure 4-27a) between the infinite and the finite laminate stacks shows very good correlation. However, at the applied average tensile strain of 0.5%, there is a difference of 23% in the local transverse stress for weft yarns at the yarn crimp location between the infinite laminate to the finite laminate (Figure 4-27b). Hence, for the same local longitudinal stress values, the transverse stress at the yarn crimp varies along the laminate in the thickness direction and causes the sequential weft yarn damage in the plies of the satin weave composite.
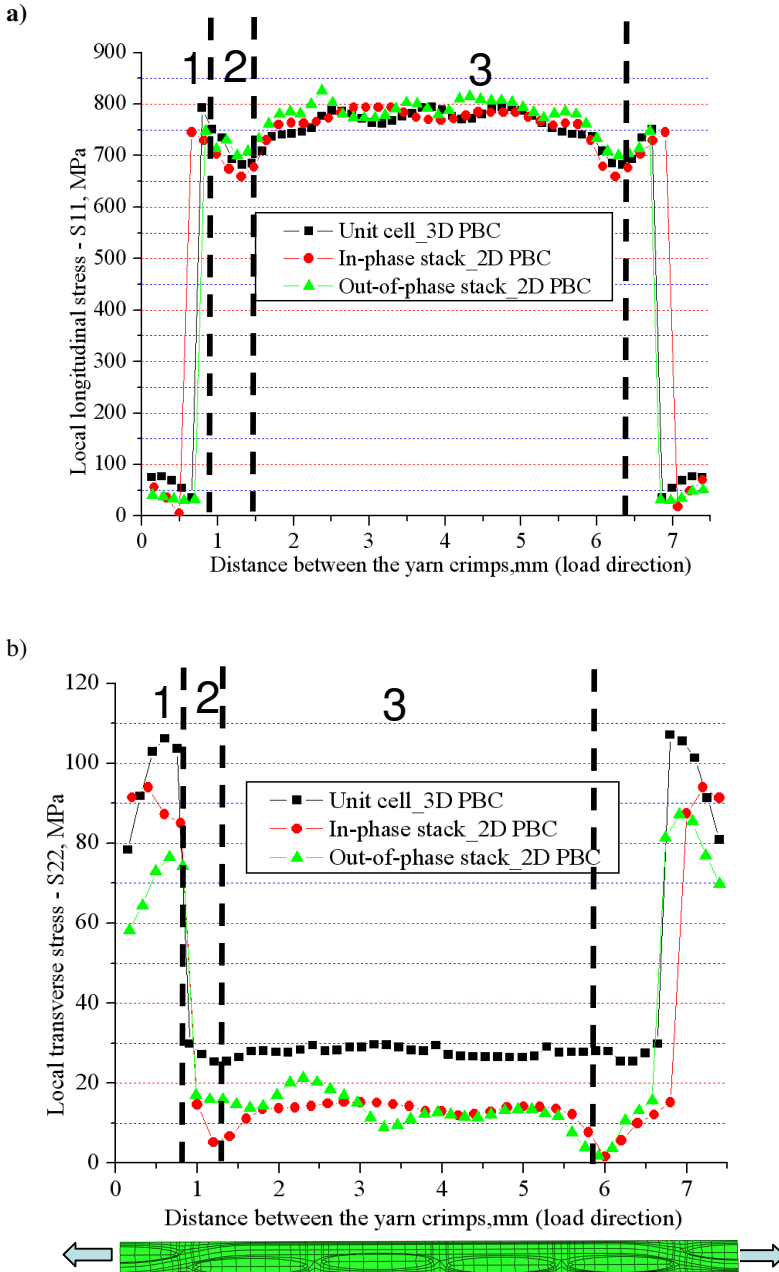
Figure 4-27.   Comparison of the local stress profiles at an average tensile strain of 0.5%: a) local longitudinal stress profiles; b) local transverse stress profiles (stress profiles on the reinforcement without the resin).

4. 12.   Conclusion

The first part of this chapter presented an experimental procedure for analyzing the damage initiation and the history of the damage in a 5-harness satin weave composite. The experimental procedure provided the qualitative as well as quantitative knowledge about the intra-yarn damage in various plies of the satin weave composite. In order to understand the stress behaviour and the mechanics of damage, the second part of this chapter dealt with the meso-FE analysis of a satin weave composite unit cell model. Numerical simulations provided insight into the mesoscopic damage locations and the local stress behaviour. In order to simulate the observed experimental damage at various positions of the laminate, apart from the traditional single unit cell FE analysis, unit cell stack FE analysis was accomplished. Comparison of the experimental and simulation results leads to the following conclusions:

- The predicted FE damage initiation (Unit cell with 3D PBCs) strain and location for the inner layers of the laminate are within the limits of the experimental observation. On the other hand, the single unit cell with 2D PBCs and in-phase stacking of an 8 unit cell laminate predict the early damage initiation strain of 0.25% and 0.44% on the surface layers, compared to the experimental damage initiation strain of 0.6%. This early damage initiation strain in the FE simulation can be attributed to the absence of internal yarn shifting (nesting) in the computational model.

- The local damage initiation trend obtained from the numerical simulations demonstrates that the infinite laminate predicts early damage initiation at the edges of the weft yarn. In contrast, the free surface unit cells predict damage in the later stage.

- In correlation with the experimental observations, the different weft yarn damage initiation strains at different locations of the laminate suggest that the transverse weft yarn damage in a textile composite is a sequential process.

- Extensive experimental microscopic damage analysis on the satin weave composite reveal that the only damage observed is the weft yarn cracks. And there is no change in the composite elastic modulus when composite is suffering this kind of damage.

- Depending on the unit cell model and the applied boundary conditions, the effective stress components that cause the transverse damage will change. Consequently, the damage initiation strain as well as the location of the weft yarn damage is changing from the centre (in-phase stacking) to the extreme edge (out-of-phase stacking).

- Apart from the experimental damage analysis in the plies of the satin weave composite, comprehensive numerical analysis starting from the primary variable (displacement) and the derivatives such as local strain (Chapter 3), stress and the damage parameters provide the in-depth knowledge regarding the structural response of the satin weave composite under the applied tensile load.

- In conclusion, the effect of internal yarn shifting (nesting) on the local structural response cannot be neglected and cannot be captured by the infinite laminate FE analysis.

The essence of the two parts of the current local damage analysis is summarized as follows. By observing the experimental microscopic damage phenomena on the scale of the laminate at the end of the loading process, formation of cracks in the weft yarn at different locations seems to be completely stochastic in nature. However, by segregating the entire damage mechanisms at different length scales, analyzing the factors contributing to the damage on the relevant scale, following the history of the damage and using the numerical simulations, the failure mechanism in textile composites can be understood in a certain deterministic way.

4. 13.   REFERENCES

[1]   Ivanov, D.S., et al., *Failure analysis of triaxial braided composite.* Composites Science and Technology, 2009. **69**(9): p. 1372-1380.

[2]   Dzenis, Y.A. and J. Qian, *Analysis of microdamage evolution histories in composites.* International Journal of Solids and Structures, 2001. **38**(10-13): p. 1831-1854.

[3]   Koissin, V. and D.S. Ivanov, *Fibre distribution inside yarns of textile composite: geometrical and FE modelling.* Proceedings of the 8th International Conference on Textile Composites (TexComp-8).Nottingham: CD edition, 2006.

[4]   Kurashiki, T., et al., *A numerical simulation of damage development for laminated woven composites* ECCM-13 Proceedings, 2008.

[5]   John, S., I. Herszberg, and F. Coman, *Longitudinal and transverse damage taxonomy in woven composite components.* Composites Part B: Engineering, 2001. **32**(8): p. 659-668.

[6]   Anzelotti, G., G. Nicoletto, and E. Riva, *Mesomechanic strain analysis of twill-weave composite lamina under unidirectional in-plane tension.* Composites Part A: Applied Science and Manufacturing, 2008. **39**(8): p. 1294-1301.

[7]   Ivanov, d.S., *Damage analysis in textile composites.* PhD Thesis; KU Leuven - Faculty of Engineering, May 2009.

[8]   Ivanov, D.S., et al., *Stress distribution in outer and inner plies of textile laminates and novel boundary conditions for unit cell analysis.* Composites Part A: Applied Science and Manufacturing. **41**(4): p. 571-580.

[9]   C.I.C.Manager, et al., *Damage development in plain weave GFRP.* Proceedings of the ICCM-11, Gold coast, Australia, 14th-18th July 1997.

[10]   Parlevliet, P.P., *Residual Strains in Thick Thermoplastic Composites - an Experimental Approach.* PhD Thesis; Delft University of Technology, 2010.

[11]   Mattsson, D., R. Joffe, and J. Varna, *Damage in NCF composites under tension: Effect of layer stacking sequence.* Engineering Fracture Mechanics, 2008. **75**(9): p. 2666-2682.

[12]   Morscher, G.N., *Modal acoustic emission of damage accumulation in a woven SiC/SiC composite.* Composites Science and Technology, 1999. **59**(5): p. 687-697.

[13]   Giordano, M., et al., *An acoustic-emission characterization of the failure modes in polymer-composite materials.* Composites Science and Technology, 1998. **58**(12): p. 1923-1928.

[14]   Ivanov, D., et al., *Strain mapping analysis of textile composites.* Optics and Lasers in Engineering. **47**(3-4): p. 360-370.

[15]   Huguet, S., et al., *Use of acoustic emission to identify damage modes in glass fibre reinforced polyester.* Composites Science and Technology, 2002. **62**(10-11): p. 1433-1444.

[16]   Lomov, S.V., et al., *A comparative study of tensile properties of non-crimp 3D orthogonal weave and multi-layer plain weave E-glass composites. Part 1: Materials, methods and principal results.* Composites Part A: Applied Science and Manufacturing, 2009. **40**(8): p. 1134-1143.

[17]   Ivanov, D.S., et al., *A comparative study of tensile properties of non-crimp 3D orthogonal weave and multi-layer plain weave E-glass composites. Part 2: Comprehensive experimental results.* Composites Part A: Applied Science and Manufacturing, 2009. **40**(8): p. 1144-1157.

[18]   Vallen, S.G.-. *AE Testing (AT) Fundamentals - Equipment - Data Analysis (Overview).*

[19]   W.Hufenbach, et al., *Application of acoustic emission analysis for damage investigation in fibre and textile reinforced composites.* Conference on damage in composite non-destructive testing and simulation (CDCM06) Stuttgart, 18.9-19.92006, to appear in NDT.net

[20]   Hamstad, M., *A review: Acoustic emission, a tool for composite-materials studies.* Experimental Mechanics, 1986. **26**(1): p. 7-13.

[21]   Searles, K., J. McCarthy, and M. Kumosa, *An image analysis technique for evaluating internal damage in graphite-fabric/polyimide composites.* Composites Science and Technology, 1998. **58**(10): p. 1607-1619.

[22]   Gao, F., et al., *Damage accumulation in woven-fabric CFRP laminates under tensile loading: Part 1. Observations of damage accumulation.* Composites Science and Technology, 1999. **59**(1): p. 123-136.

[23]   Parlevliet, P.P., H.E.N. Bersee, and A. Beukers, *Residual stresses in thermoplastic composites--A study of the literature--Part I: Formation of residual stresses.* Composites Part A: Applied Science and Manufacturing, 2006. **37**(11): p. 1847-1857.

[24]   Parlevliet, P.P., H.E.N. Bersee, and A. Beukers, *Residual stresses in thermoplastic composites - a study of the literature. Part III: Effects of thermal residual stresses.* Composites Part A: Applied Science and Manufacturing, 2007. **38**(6): p. 1581-1596.

[25]   Parlevliet, P.P., H.E.N. Bersee, and A. Beukers, *Residual stresses in thermoplastic composites--A study of the literature--Part II: Experimental techniques.* Composites Part A: Applied Science and Manufacturing, 2007. **38**(3): p. 651-665.

[26]   DeBaere, I., *Experimental and Numerical Study of Different Setups for Conducting and Monitoring Fatigue Experiments of Fibre-Reinforced Thermoplastics.* PhD Thesis, Gent university, 2008.

[27]   Lomov, S.V., et al., *Experimental methodology of study of damage initiation and development in textile composites in uniaxial tensile test.* Composites Science and Technology, 2008. **68**(12): p. 2340-2349.

[28]   Ito, M. and T.-W. Chou, *Elastic moduli and stress field of plain-weave composites under tensile loading.* Composites Science and Technology, 1997. **57**(7): p. 787-800.

[29]   Duplessis Kergomard, Y., et al., *Intralaminar and interlaminar damage in quasi-unidirectional stratified composite structures: Experimental analysis.* Composites Science and Technology. **70**(10): p. 1504-1512.

[30]   Shady, E. and Y. Gowayed, *Interlaminar shear stress distribution between nested layers of plain weave composites.* Polymer Composites. **31**(11): p. 1838-1845.

[31]   Summerscales, J. and P.M. Russel, *Observations on the fibre distribution and fibre strain in a woven fabric reinforcement.* Advanced composite letters 2004. **23 No.3, 2004**.

[32]   Littell, J.D. and W.K. Binienda, *Characterization of Damage in Triaxial Braid Composites Under Tensile Loading.* NASA/TM—2009-215645, May 2009.

[33]   Ivanov, D.S., et al., *A comparative study of tensile properties of non-crimp 3D orthogonal weave and multi-layer plain weave E-glass composites. Part 2: Comprehensive experimental results.* Composites Part A: Applied Science and Manufacturing, 2009. **40**(8): p. 1144-1157.

[34]   Koissin, V., et al., *Structurally stitched NCF preforms: Quasi-static response.* Composites Science and Technology, 2009. **69**(15-16): p. 2701-2710.

[35]   Daggumati, S., et al., *Local damage in a 5-harness satin weave composite under static tension: Part I - Experimental analysis.* Composites Science and Technology. **70**(13): p. 1926-1933.

[36]   Jekabsons, N. and J. Byström, *On the effect of stacked fabric layers on the stiffness of a woven composite.* Composites Part B: Engineering, 2002. **33**(8): p. 619-629.

[37]   Jones, W.R. and J.W. Johnson, *Intrinsic strength and non-hookean behaviour of carbon fibres.* Carbon, 1971. **9**(5): p. 645-650, IN15-IN18, 651-655.

[38]   DJORDJEVI, I.M., D.R. SEKULIC, and M.M. STEVANOVIC, *Non-linear elastic behavior of carbon fibres of different structural and mechanical characteristic.* J. Serb. Chem. Soc. 72 (5) 513–521 (2007), 2006. **JSCS–3582**.

[39]   Le Page, B.H., et al., *Finite element simulation of woven fabric composites.* Composites Part A: Applied Science and Manufacturing, 2004. **35**(7-8): p. 861-872.

[40]   Carvalho, N.V., S.T. Pinho, and P.Robinson, *Compressive failure of 2D woven composites.* ICCM-17 Conference proceedings, 2009.

[41]   Lomov, S.V., et al., *Meso-FE modelling of textile composites: Road map, data flow and algorithms.* Composites Science and Technology, 2007. **67**(9): p. 1870-1891.

[42]   Whitcomb, J.D., *Three-Dimensional Stress Analysis of Plain Weave Composites.* NASA Contractor Report 101672, 1989.

[43]   whitcomb, *Analysis of New Composite Architectures.* NASA Contractor Report 198506, 1996.

[44]   Bogdanovich, A.E., *Multi-scale modeling, stress and failure analyses of 3-D woven composites.* Journal of Materials Science, 2006.

[45]   Owens, B.C., J.D. Whitcomb, and J. Varghese, *Effect of Finite Thickness and Free Edges on Stresses in Plain Weave Composites.* 2009. p. 0021998309347571.

[46]   Lomov, S.V., et al., *Nesting in textile laminates: geometrical modelling of the laminate.* Composites Science and Technology, 2003. **63**(7): p. 993-1007.

[47]   Uetsuji, Y., T. Kurashiki, and M. Zako, *Three-Dimensional finite element analysis of plain weave fabric composites based on damage mechanics (Effect of geometric change in opened yarns on damage development).* J. Text. Mach. Soc. Japan, 2003.

[48]   Roy, A.K., *Comparison of in situ damage assessment in unbalanced fabric composite and model laminate of planar (one-directional) crimping.* Composites Science and Technology, 1998. **58**(11): p. 1793-1801.

[49]   Adams, D.O., *Idealized textile composites for experimental/analytical correlation.* NASA Technical Memorandum 19950016857 1994.

[50]   Chamis, C.C., *Mechanics of Composite Materials Past, Present, and Future.* NASA Technical Memorandum 100793, 1984.

[51]   Tolson, S. and N. Zabra, *Finite element analysis of progressive failure in laminated composite plates.* Compurers & Structures Vol. 38, No. 3, pp. 361-376, 1991, 1990.

[52]   Zako, M. and Y. Uetsuji, *On the damage behavior of fiber reinforced composite materials.* International Journal of damage mechanics, 2002.

[53]   Chapman, C.D., *Effect of assumed Tow architecture on the predicted moduli and stress in woven composites* NASA Contractor Report 195310, 1994.

[54]   Cox, B.N. and G. Flanagan, *Handbook of Analytical Methods for textile composite.* NASA Contractor Report 4750, 1997.

[55]   Lomov, S.V., et al., *Full-field strain measurements for validation of meso-FE analysis of textile composites.* Composites Part A: Applied Science and Manufacturing, 2008. **39**(8): p. 1218-1231.

[56]   Lee, J.-R., et al., *Digital phase-shifting grating shearography for experimental analysis of fabric composites under tension.* Composites Part A: Applied Science and Manufacturing, 2004. **35**(7-8): p. 849-859.

[57]   Whitcomb, J. and K. Srirengan, *Effect of various approximations on predicted progressive failure in plain weave composites.* Composite Structures, 1996. **34**(1): p. 13-20.

[58]   Whitcomb, J.D., *Failure analysis of 2D and 3D woven composites* NAG 1-1324, 1994.

Chapter 5

EXPERIMENTAL DAMAGE ANALYSIS OF THE SATIN WEAVE COMPOSITE UNDER TENSION-TENSION FATIGUE

This chapter is devoted to the experimental fatigue damage analysis of a 5-harness satin weave composite under tension-tension fatigue. Evolution of the longitudinal strain as well as the stiffness of the composite specimen was monitored throughout the cyclic load process. During the fatigue test, instrumentation of the composite structural response is categorized into two parts: i) the first priority is to monitor the macro-scale structural response such as the increase in the longitudinal strain and hence decrease in the composite longitudinal stiffness; ii) the second priority is to capture the micro-scale damage events that are occurring in correlation with the observed fluctuations in the macro-scale structural response. Finally, comparison of the stress-strain behaviour as well as strength of the virgin composite samples to the fatigue tested test coupons give an overview of the effect of the induced fatigue damage on the strength and stiffness of the satin weave composite.

5. 1.   Introduction

Fatigue failure for conventional engineering materials (metals) can be viewed as a two step process: crack initiation followed by crack propagation. Here the majority of the fatigue life is consumed for initiating a dominating crack. Once a dominant crack has been initiated, the principles of the fracture mechanics are utilized to predict crack growth and the remnant life. Unlike fatigue failure in conventional engineering materials, the accumulation and propagation of fatigue damage in composite materials is relatively complex. In addition, the basic damage mechanisms encountered in composite laminates are more numerous than in conventional materials [1]. In service, composite structures subjected to fatigue load develop fatigue damage, which intern decreases the in-plane mechanical properties of the composite such as strength and stiffness. The fatigue failure in composites consists of many modes including matrix cracking, fibre breakage, fibre-matrix debonds, void growth, and delamination [2]. Any one or a combination of these mechanisms may lead to the reduction of the overall modulus and strength. Therefore, fatigue failure is a progressive process during which the overall stiffness and strength decreases progressively until their values can no longer resist the applied loading, and hence causes the catastrophic composite failure.

In general, fatigue damage in a unidirectional composite starts with matrix cracks, and fibre matrix interface debonding, followed by fibre pull-out and fibre fracture. Figure 5-1 shows the well known three stage fatigue life mechanism for the UD composites under tensile fatigue load [3, 4]. The region I of the fatigue life diagram depicts the scatter band of the composite failure strain in tension, representing the non-progressive fibre breakage regime in which the random fibre failure mechanism governs. Region II is the regime of progressive fibre-bridged matrix cracking in which interfacial debonding plays a role. Finally, region III signifies the matrix cracking, which is effectively arrested by fibres, assisted possibly by interfacial debonding, such that the composite failure is not reached with in specified large number of cycles. The boundary between Region II and Region III is the so called fatigue limit.
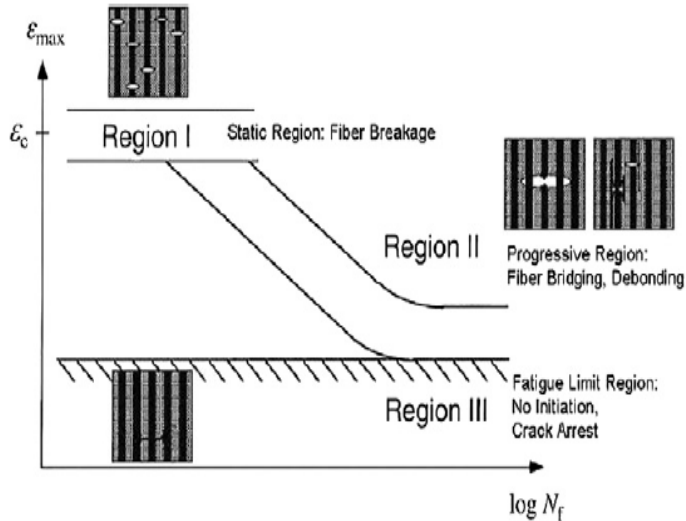
Figure 5-1.   Fatigue behaviour of UD composites under tensile load [4].

In contrary to the fatigue behaviour of UD composites, the weaving pattern in textile composites leads to a complex damage behaviour under fatigue load. As depicted in Figure 5-2, initiation of the damage in woven composites starts with cracking of the weft yarns which are perpendicular to the load direction. With the progress of the cyclic load, other damage mechanisms develop such as meta-delaminations (bundle debond), inter-ply delaminations as well as fibre fracture and eventually catastrophic failure of the composite specimen [5]. To further complicate the issue of damage accumulation, the sequence of initiation and propagation of the various cracks is a function of laminate lay-up, stacking sequence [1, 6], and loading conditions [7, 8]. Thus the fatigue damage accumulation is load path dependent and material dependent.

With regard to the fatigue damage analysis of satin weave composite, the current chapter provides a detailed discussion regarding:

i)   Estimating the evolution of strain as well as the longitudinal stiffness of the composite under cyclic load process.

ii)   In correlation to the observed fluctuations in the measured macroscopic composite stiffness, microscopic damage events are detected on the polished edges of the composite specimen (non-destructive) as well as in the laminate inner layers using the composite specimen using cut sections (destructive testing process).
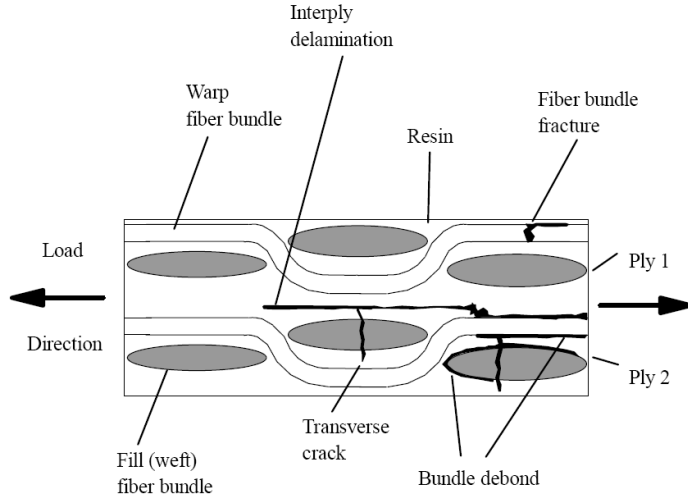
Figure 5-2.   Schematic representation of the fatigue damage in a woven composite [1].

iii)   In order to estimate the effect of the micro-scale damage events that have occurred during different stages of the fatigue test, and their influence on the load carrying behaviour as well as the strength of the composite, residual strength tests were performed and compared to the virgin samples stiffness and strength.

The planned fatigue tests were performed in a load-control manner. To obtain the composite response under fatigue load, such as the longitudinal strain variation, a dynamic extensometer was attached to the composite specimen. Moreover, to visualize the micro-scale damage events, microscopic analysis was performed on the polished edges of the composite in an interrupted fatigue testing process.

5. 2.   Experimental set-up and data-acquisition system

In order to accomplish the tension-tension fatigue tests, a servo-hydraulic INSTRON 8801 tensile testing machine with a FastTrack 8800 digital controller and a load cell of ±100kN was used. For the registration of the tensile data, a combination of a National Instruments 6251 data acquisition card for USB along with the SCB-68 pin shielded connector was used. In order to measure the strain during the cyclic load, a dynamic extensometer was attached to the composite specimen (Figure 5-3). After each cycle, the load, displacement and strain given by the FastTrack controller were sampled on the same time basis.
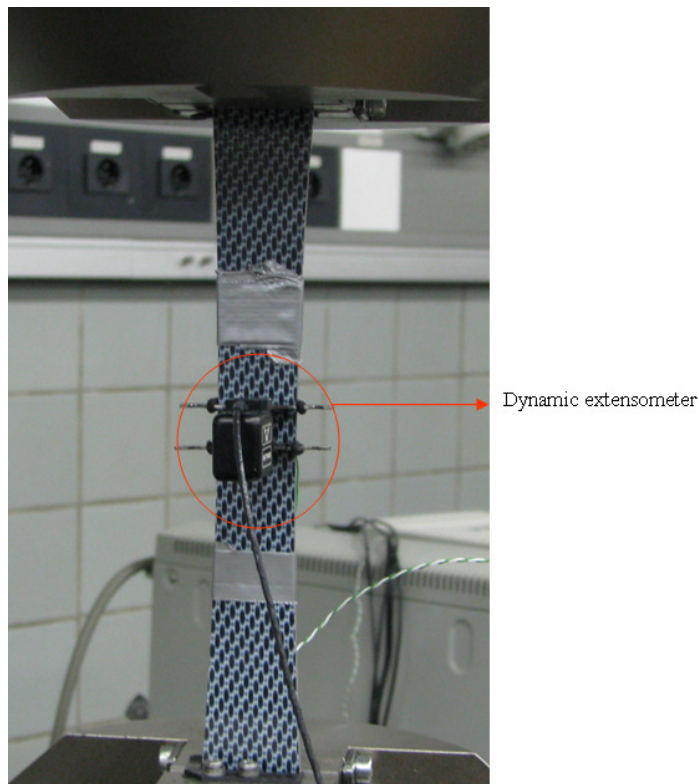
Figure 5-3.   Composite specimen mounted on the Instron for the tension-tension fatigue with the dynamic extensometer.

Regarding the fatigue test control mode, there are three possible choices: a) displacement-control; b) strain-control; and c) load-control [9]. The first mode is not so interesting due to the fact that there will be always some sliding in the grips.

 This makes it very difficult to perform two experiments with exactly the same load conditions, since the amount of sliding will differ. Furthermore, the amplitude and average values of both load and strain values will change throughout the composite fatigue life, making them difficult to interpret. Displacement-control test mode is useful when the fatigue parameter is a constant displacement (e.g. bending fatigue tests). In the strain-control test mode, the strain will vary between specified maximum and minimum values. As such, the amplitude and average values of the strain will remain the same throughout the test, making it easier to interpret the load signal. However, if the blades of the extensometer shift over the surface of the composite specimen, then the tensile machine would compensate for this shift, which corrupts the fatigue load data, since the strain no longer cycles between the desired maximum and minimum values. If the shift is quite large, failure of the specimen and even damage to the tensile machine or extensometer may occur.

Finally, in the load-control test, the load will vary between the specified maximum and minimum values. As a result, the amplitude and the average value of the load will remain the same throughout the fatigue test (Figure 5-4), making it easier to interpret the strain signal, with respect to permanent deformation and the evolution in stiffness. Furthermore, if the specimen fails, then the load will remain zero, which can be detected by the tensile machine if all corresponding limit settings were implemented correctly. Hence, under the load-control mode, fatigue tests were accomplished until the sample failure without the risk of damaging the equipment.

As a result of the above discussion, all the fatigue experiments explained in the current chapter (later sections) were accomplished under load-control mode. And the stress ratio 'R' is equal to zero, meaning the tensile stress varies between a minimum value zero (σ_{min} = 0 MPa) and a certain maximum stress σ_{max}. To avoid that the specimen would be loaded in compression as a result of the possible overshoot of the tensile machine, the specimen was always pre-stressed with a load of 0.5 kN meaning that σ_{min} is not exactly zero, but close to zero. Regarding the data-acquisition, due to the long duration of the fatigue experiment it is not possible to measure the fatigue data continuously at high frequencies. In order to have accurate results, the sampling frequency should be high enough to be able to accurately reproduce the sinusoidal signal.
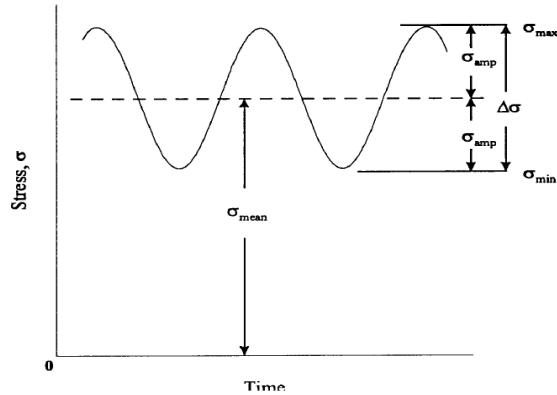
Figure 5-4.   **Schematic diagram of the load control tension-tension fatigue
                       test.**

However, measuring continuously with those high frequencies would yield very
large data files, which are difficult to process. Since it is expected that damage
grows slowly throughout the fatigue test, it would be sufficient to measure a few
cycles and then skip a certain number of cycles. The following procedure was
implemented: every five minutes, five cycles are registered and written as a single
line in a spread sheet. The used sample rate depends on the frequency of the signal
and the number of columns available in the used spread sheet. Furthermore, for each
burst, the maximum, minimum and the average value of the signal is calculated and
stored in a separate file, so a general image of the evolution of a parameter
throughout the fatigue experiment is obtained. Using the above specified procedure,
force, displacement and longitudinal strain data are measured continuously. With the
above specified experimental setup and the data acquisition procedure, tension-
tension fatigue experiments were accomplished and the results are presented in the
following sections.

5. 3.   Results and discussion

5. 3. 1.   Fatigue   damage   analysis   using   rectangular   test
                    specimens-ASTM standard

For the fatigue experiments, test coupons were prepared according to the ASTM
D3479 standard (Figure 5-5). Initial fatigue tests were performed at 5Hz frequency
with 300 MPa being the maximum stress, which is approximately 40% of the static
tensile strength of the carbon-PPS composite.
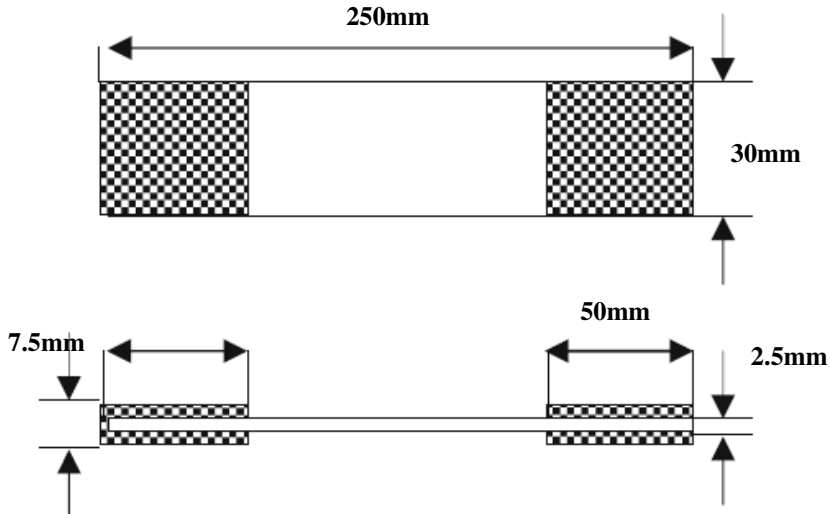
Figure 5-5.   **Dimensions of the test coupons for the fatigue damage analysis (ASTM D3479).**

It should be emphasized that the test frequency is chosen as a compromise between the expected heat generation and the duration of the fatigue test [9]. With the above mentioned load conditions, there is no observable change in the longitudinal displacement and hence the longitudinal stiffness of the composite until 8.5×10^5 cycles.

a)
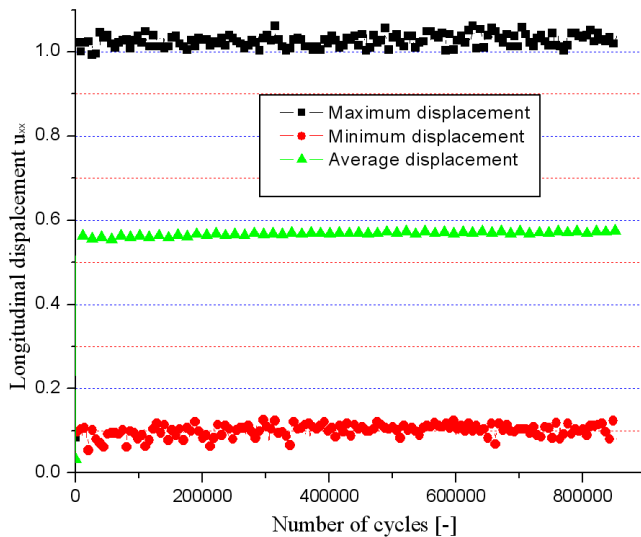
b)
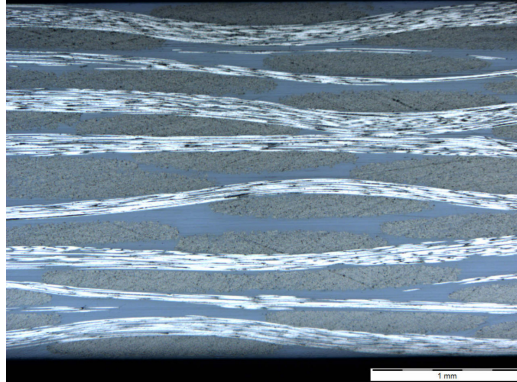
c)
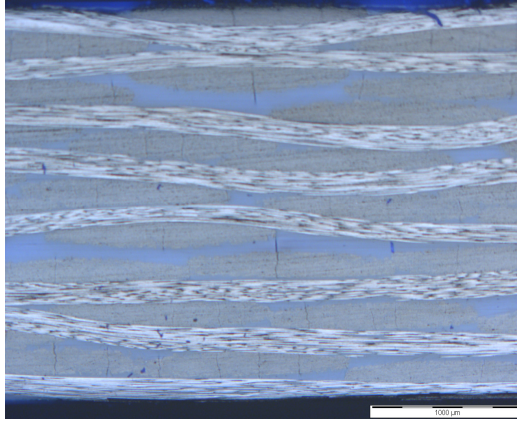
Figure 5-6.   Fatigue   damage   analysis   at   300   MPa   stress   and   5Hz frequency: a) displacement vs. number of cycles; b) microscopic view of the composite free edge before fatigue load; c) observed weft yarn damage at around 8.5×10^5 cycles.

Figure 5-6a presents the Instron displacement instead of the extensometer strain, due to sliding of the extensometer on the composite specimen during the test, which produced corrupted strain data[*]. However, the author's intention in presenting the displacement is to provide an estimate of the composite response under the applied fatigue load.

---

[*] More than 40% of the fatigue tests data was corrupted due to the sliding of the extensometer on the composite specimen. Hence, the corrupted test data is not considered for the analysis of composite structural response under the applied tensile load.

Figure 5-6(b, c) shows the microscopic images of the composite specimen before and after the fatigue test. Confirming the observation of the longitudinal displacement behaviour, microscopic analysis at 8.5×10^5 cycles reveals that the only observed damage is the weft yarn cracking, indicating the infinite fatigue life of the composite specimen under the applied load conditions. The following fatigue test is accomplished at 5Hz frequency with the maximum stress being 500 MPa ($\cong 65\%$ of the static tensile strength).

As depicted in Figure 5-7a, the maximum longitudinal strain values increase ($\cong 7E-04$) in the first few thousand cycles and afterwards the strain stays almost constant until the end of the fatigue test (1.42×10^6 cycles). In addition, the minimum strain value in Figure 5-7a gives an idea of the permanent strain in the composite, which stayed almost constant throughout the fatigue test. According to the observed fluctuations in the longitudinal strain, the longitudinal stiffness of the composite is calculated using the difference between maximum to minimum stress value over the difference between maximum to minimum strain values. Using the aforementioned procedure for calculating the longitudinal stiffness, the effect of the increase in permanent strain during the fatigue test is accounted on the stiffness fluctuations.

As shown in Figure 5-7b, in correlation with the increase in the longitudinal strain value, the longitudinal stiffness of the composite reduces from 59 GPa (initial elastic modulus[†]) to 57.5 GPa (secant modulus[‡]) in the first few thousand cycles. Later, no significant change in the composite stiffness is observed until the end of the fatigue test. At the end of 1.42×10^6 cycles, the fatigue test is aborted automatically due to adhesive failure between the end tab and the test specimen, which is not the actual composite failure. Finally, in correlation with the reduction in composite longitudinal stiffness, to observe the micro-scale damage events that are initiating at different stages of the fatigue life, the above experiment is done in an interrupted manner. As shown in Figure 5-7(a, b), the tensile strain increases in the first 1×10^5 cycles of the fatigue test and correspondingly there is a slight reduction in the longitudinal stiffness. Hence, the fatigue test was interrupted for microscopic inspection at different intervals of the fatigue life starting at 1000 cycles, 1×10^5 and finally at 1.42×10^6 cycles.

[†] Linear regression of the complete stress-strain curve

[‡] Modulus computed between the origin and the maximum stress after each load cycle.

From the microscopic observation at the end of 1000 cycles (Figure 5-8a), the only damage observed on the composite polished edge is the weft yarn cracking. At 1×10^5 cycles, the microscopic analysis reveals that the damage in the satin weave composite under the fatigue load exhibits many forms such as: a) broken load carrying fibres (Figure 5-8b); b) meta-delaminations (Figure 5-8c); c) crack conjunction at different levels. The observed micro-scale damage mechanisms explain the reduction in the longitudinal modulus of the composite.

a)
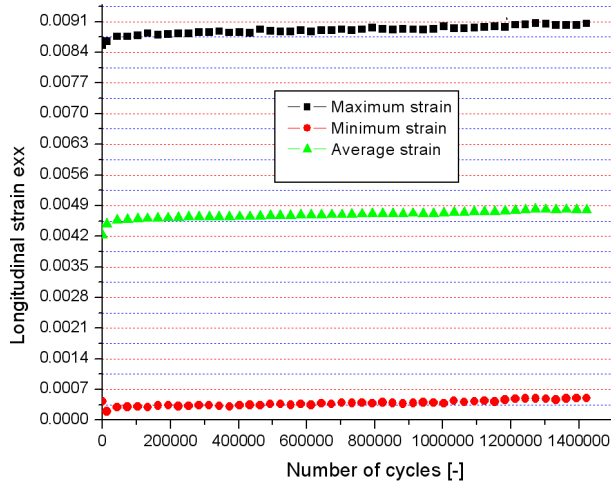
b)
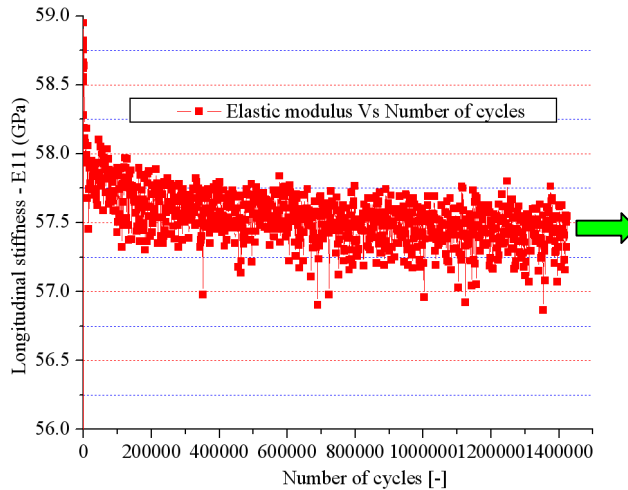
Figure 5-7.   Fatigue test at 500 MPa stress and at 5Hz frequency: a) evolution of the strain values; b) evolution of the composite in-plane stiffness.

a)
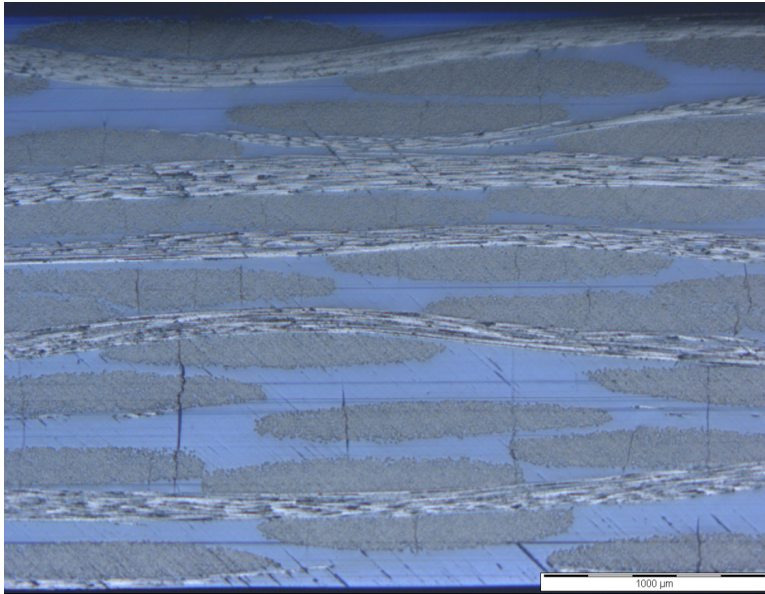
b)
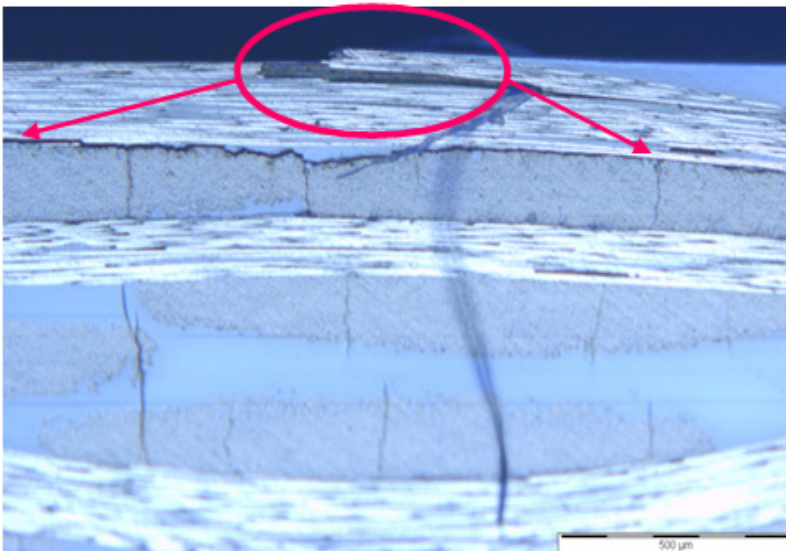
c)
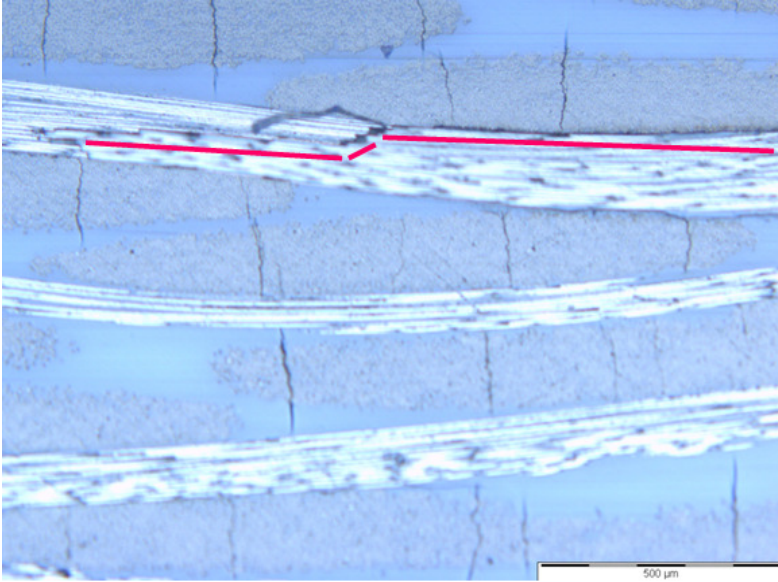
Figure 5-8.   **Microscopic damage analysis of the composite polished edges at 500 MPa stress and at 5Hz frequency: a) weft yarn damage at 1000 cycles; b) broken axial fibres and meta-delamination; c) crack conjunction at 1×10^5 cycles.**

Finally, at around 1.42×10^6 cycles, the end tabs of the composite specimen debonded and the fatigue test was aborted automatically. At this stage, in addition to the above specified damage events (Figure 5-8a-c), microscopic inspection reveals that the inter-ply delaminations (red marks in Figure 5-9a) as well as numerous axial fibre breaks and meta-delamination were observed (Figure 5-9b). Moreover, one should note that the large black areas shown in Figure 5-9(a, b) indicate that the broken axial fibres on the polished surface. Once the fibre failure occurred, the subsequent tensile load process retract the broken fibres in the load direction and hence the unpolished surface becomes visible.

a)
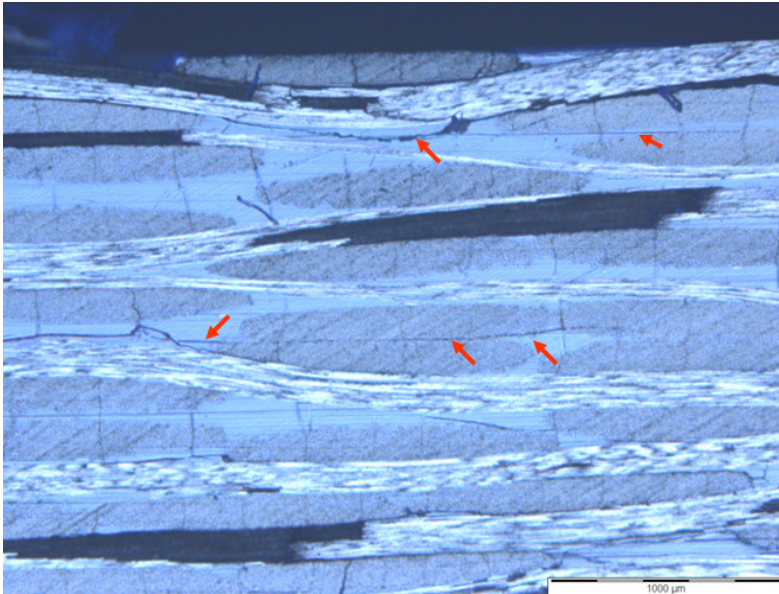
b)
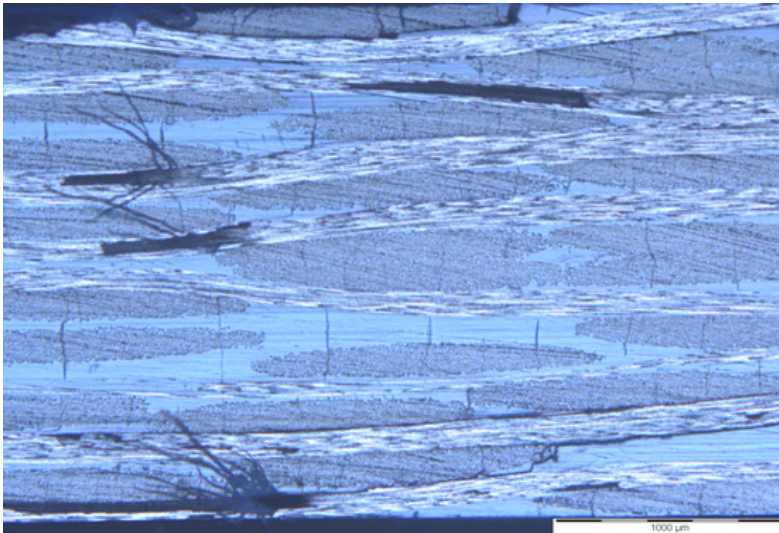
Figure 5-9. **Microscopic damage analysis of the composite polished edges at 500 MPa stress and at 5Hz frequency: a) inter-ply delamination; b) broken axial fibres and meta-delamination.**

In addition to the above mentioned tests, fatigue damage analysis of the carbon-PPS satin weave laminate at 550 MPa stress and at 5Hz frequency reveals a similar damage behaviour. The above discussed fatigue tests are either terminated intentionally at around 1×10^6 cycles for the residual strength analysis or prematurely failed near the tab area (above 550 MPa stress). Finally, Figure 5-10 shows the most commonly occurring macroscopic fatigue failure of the composite specimens, which is mainly concentrated around the tab area.
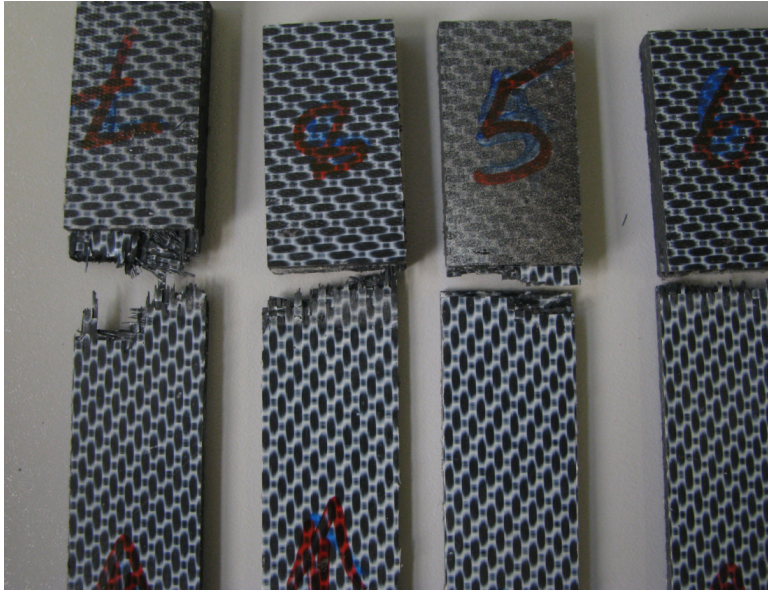
Figure 5-10.   **Macro-scale fatigue failure of the rectangular composite specimens.**

5. 3. 2.   Fatigue damage analysis using dog-bone test specimens

As mentioned above, most of the test specimens prepared according to the ASTM standard tends to fail very early in the fatigue test or during the run-in process, at around 550 MPa and the above stress levels. Moreover, failure of the composite specimen is occurring near the end tabs, caused by the stress concentration that is inherent in the rectangular test specimens [10] (Figure 5-11). As shown in Figure 5-11, debonding between the tab and the specimen starts at the early stage of the load process. Once the global stress level reaches at around 550 MPa or above, the composite specimen pull-out of the end tabs or failure within the tab area.

Furthermore, the failure of the adhesive layer and debonding of the tab also results in premature failure. In order to find a suitable combination of end tab material such as, geometry and adhesive, several experiments were performed by De Baere et al. [9]. After considering different adhesives and using various mechanical methods to glue the end tabs to the specimen, it is concluded that, due to non-reactive nature of the PPS with the adhesive combined with the inherent stress concentration near the end tabs causes the adhesive failure at the elevated loads. This phenomenon hinders the further fatigue testing at the higher load levels and underestimates the fatigue performance of the carbon-PPS satin weave composite. Using the rectangular test specimens prepared according to the ASTM standard, the fatigue behaviour of the satin weave composite is tested up to 75% of the static tensile strength. However, for the carbon fibre composites the fatigue limit is around 80-90% of the static tensile strength [11]. In order to understand the material behaviour at higher load levels, and to avoid the damage in the end tabs, milled dog-bone specimens are used for the further fatigue tests.

Start, σ = 0 MPa   σ = 200 MPa   Fracture, σ = 650 MPa
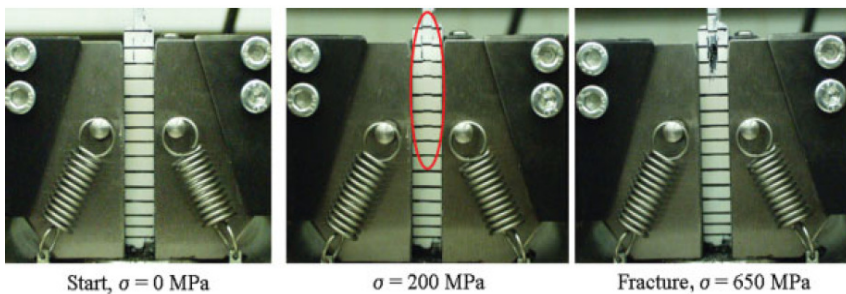
Figure 5-11.   **Illustration of the breaking of the bond between the tabs and the specimen, resulting in tab failure [12].**

The idea behind using the dog-bone specimens is to have a slight curvature in the specimen, so that this stress concentration at the end tabs is compensated by having a less wide specimen at the centre of the composite test coupon [1, 6, 11] (Figure 5-12). Moreover, it should be noted that the test specimen geometry used in the current experiments differs from the ones mostly found in literature: in most cases, there is a constant section in between the two curved areas. Whereas here, the curved section has a constant radius and thus a constantly varying width. The reason for the constant radius is clearly explained by De Baere et al.[13] based on the stress calculations made by considering stress concentration in the end tab as well as the dimensions of the composite specimen.
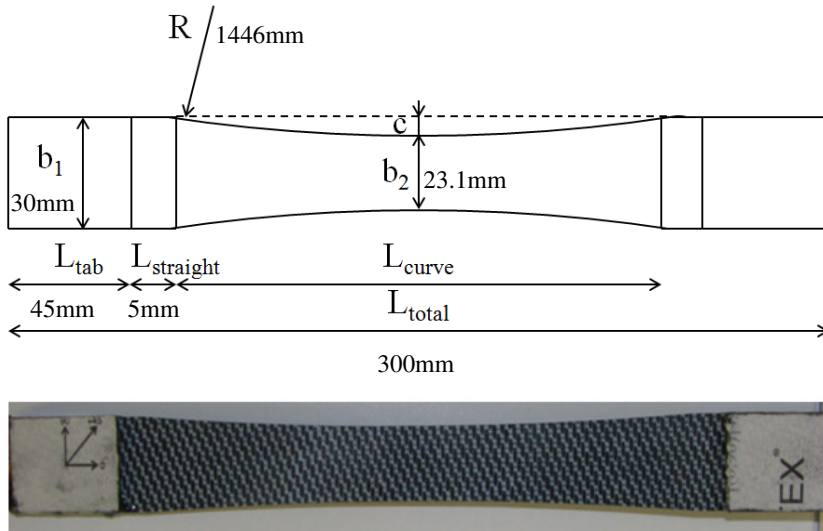
Figure 5-12.   Dog-bone specimen used for the fatigue test.

Finally, one could state that because the width is not constant in the centre of the specimen, there will be a variation in the longitudinal strain in that area. Since the strain will be measured with an extensometer during the fatigue experiments, this could influence the measurement because this device measures the strain over a certain length and therefore averages out the variations.

In order to calculate the strain variation in the centre of the dog-bone specimen, FE simulations are performed by [10] with one quarter of the dog-bone specimen along with the application of 100 MPa tensile stress. Moreover, symmetry boundary conditions are applied to the FE model (arrow marked faces in Figure 5-13). From the aforementioned simulation, as can be seen in the longitudinal strain distribution (Figure 5-13), the variation of longitudinal strain is minimal for radius of curvature R = 1446 mm and a width of 30 mm dog-bone specimen. Over a length 8.12 mm away from the centre of the specimen, so over 16.24 mm in the centre in total, the strain has a uniform distribution between 0.001734 and 0.001757, corresponding to the imposed 100 MPa longitudinal stress. Since the extensometer will be mounted in the centre of the specimen and failure is therefore very likely to occur between the two blades of the extensometer, a gauge length of 10 mm will be used. This length is smaller than the 16.24 mm of uniform strain field, so a correct strain measurement is expected.

ε_{11} [-]

+1.780e-03
+1.757e-03
+1.734e-03
+1.710e-03
+1.687e-03
+1.664e-03
+1.640e-03
+1.617e-03
+1.593e-03
+1.570e-03
+1.547e-03
+1.523e-03
+1.500e-03
+9.506e-04

8.12 mm
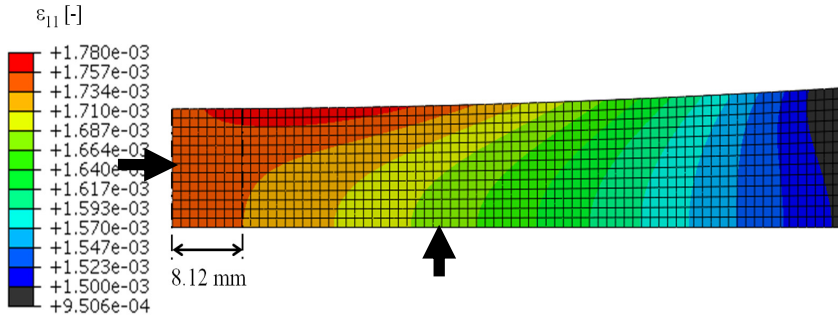
Figure 5-13.   Longitudinal strain distribution for the geometry with R equal to 1446 mm [10].

Based on the above discussion, the geometry with L_{total} = 300 mm and R = 1446 mm will be used for the experimental fatigue tests. The dog-bone specimens are cut out of a big laminate using a water jet, which uses a CAD/CAM system so that the imposed geometry is followed accurately, within the tolerance limits of ± 0.02mm in width direction. In addition, extra precautions were taken so that no delaminations originated during the water jet cutting.

5. 3. 2. a. Comparative study between rectangular vs. dog-bone specimens

Using the above specified dog-bone shaped specimens, which are not in accordance with the ASTM standards, initial fatigue tests were conducted as a comparative study between the rectangular (ASTM) to the dog-bone shaped specimen. Comparing the evolution of the longitudinal stiffness (Figure 5-14) at 500 MPa stress and at 5Hz frequency reveals that the change in the test specimen geometry does not show any influence on the composite structural response under the fatigue load [13]. Subsequently, the following sections are devoted to evaluate the composite structural response at the higher stress levels ($\geq 550MPa$) using the dog-bone specimens. Using the dog-bone shaped specimen, the final failure in the composite end tabs is eliminated. Moreover, at higher stress levels ($\geq 550MPa$) longer fatigue life is achieved.
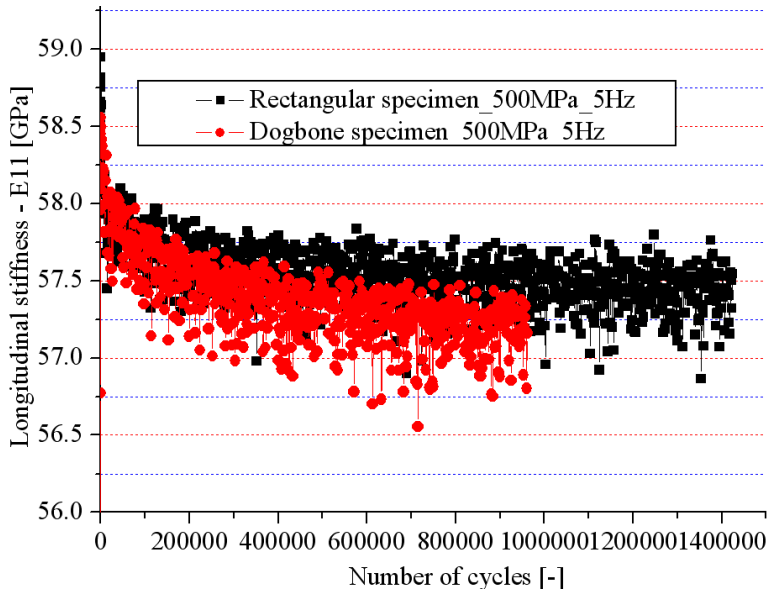
Figure 5-14.   **Evolution of the longitudinal stiffness: a comparison between the rectangular vs. dog-bone shape test specimen.**

5. 4.   Fatigue damage analysis at elevated loads

Using the dog-bone specimens, tension-tension fatigue experiments were conducted and the results are presented in the current section. The maximum tensile stress of 600 MPa (80% static tensile strength) was applied to the test specimen at 2Hz frequency. As it can be observed that, at elevated loads the test frequency is set at 2Hz instead of 5Hz. This is due to the fact that at higher stress levels with 5Hz frequency test specimen failed within few cycles, without any indication of the progressive failure.

Finally, Figure 5-15(a, b) shows the evolution of the longitudinal strain as well as the longitudinal stiffness of the composite specimen up to 1.1×10^6 cycles. Initially, the maximum longitudinal strain value increases from 0.98 to 1% around 1×10^5 cycles. Thereafter, it stays almost constant till the end of the fatigue test. Corresponding to the increase in strain value, the longitudinal stiffness of the composite reduces from 61 GPa to 59 GPa at the end of 1.1×10^6 cycles. Moreover, at this load level, microscopic analysis of the composite specimen reveals initial fibre breaks as well as meta-delaminations were detected on the composite polished edges at around 1000 cycles.

a)

b)
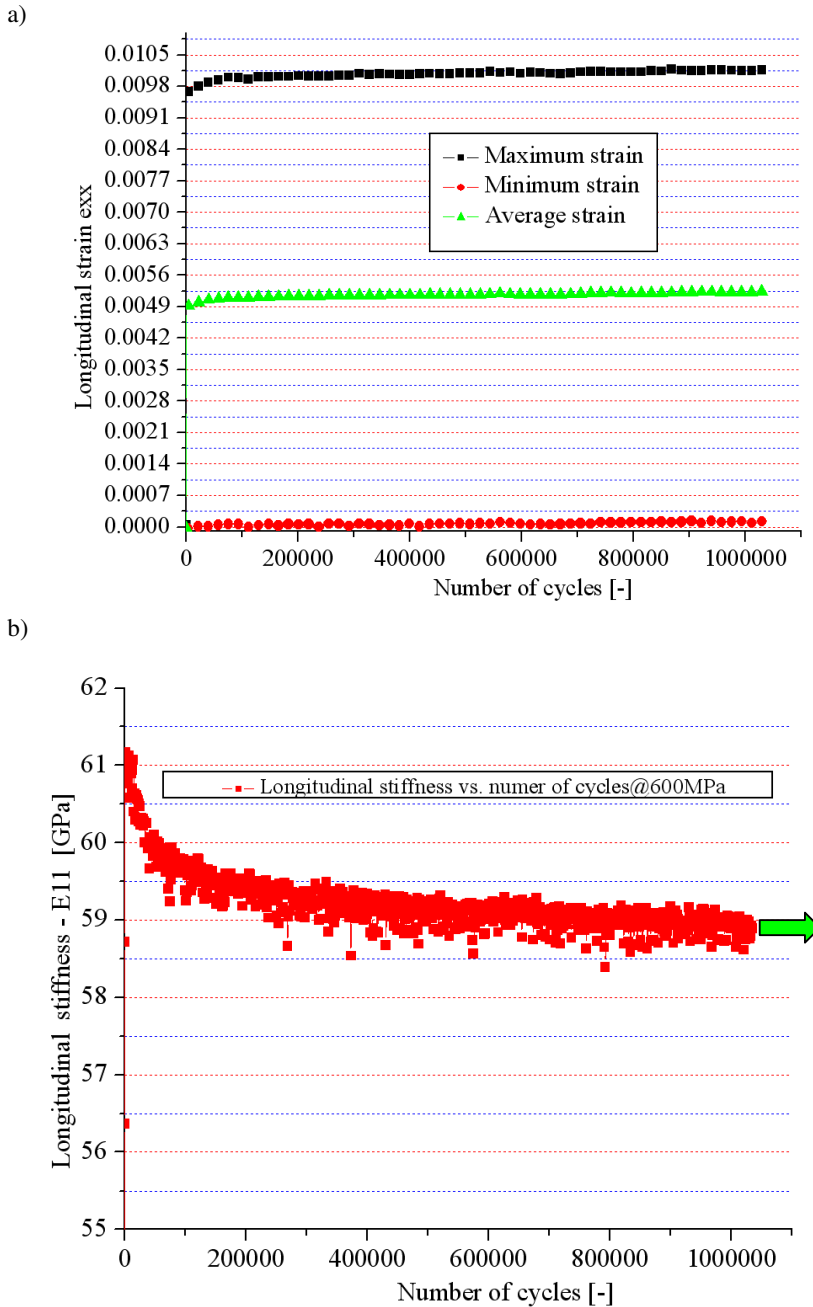
Figure 5-15.   **Fatigue test at 600 MPa and at 2Hz frequency: a) evolution of the strain values; b) evolution of the composite in-plane stiffness.**

In the above section, the fatigue test is intentionally terminated at around 1.1×10^6 cycles to determine the residual stress-strain behaviour of the composite, which is presented in the later sections of this chapter.

Figure 5-16a shows the longitudinal strain behaviour of the composite specimen at 625 MPa and at 2 Hz frequency until the composite final failure (1.9×10^6 cycles). As shown in Figure 5-16a, the maximum and minimum strain values obtained from the extensometer at the beginning of the fatigue test are little higher than the theoretical values. The higher strain values registered by the extensometer might be caused by the slight movement of the rubber bands holding the extensometer on the composite specimen, due to the fibre breaks at the edges. However, the global trend in the strain value clearly shows that the increase in strain value during the fatigue test is gradual.

a)
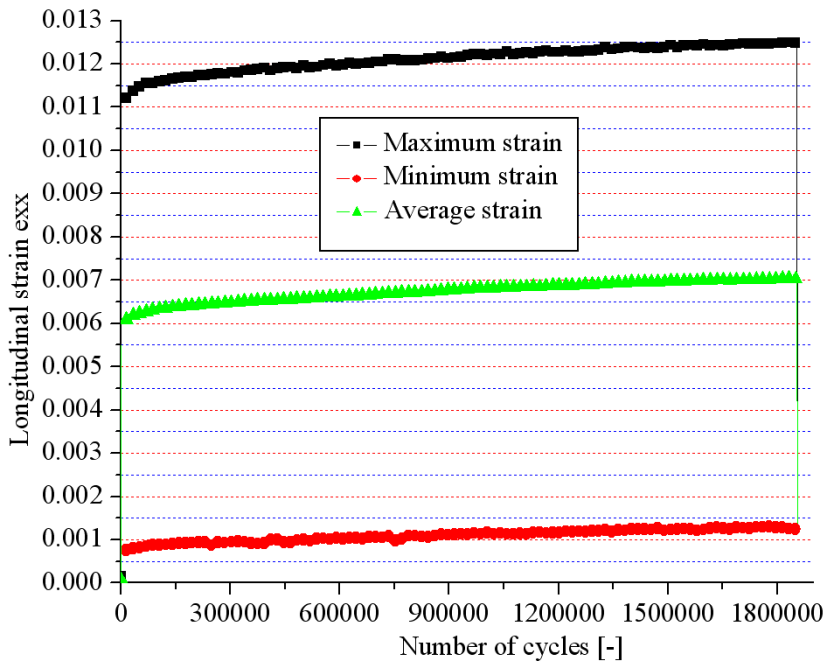
b)
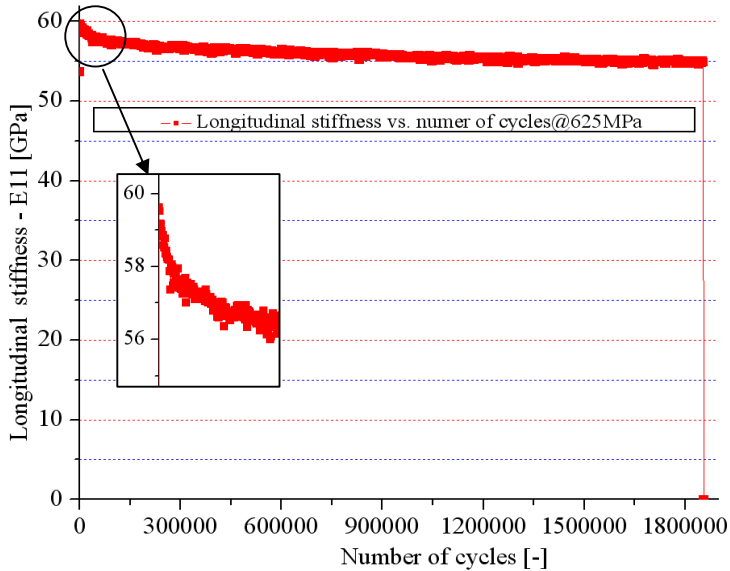
Figure 5-16.   **Fatigue test at 625 MPa and at 2Hz frequency: a) evolution of the strain values; b) evolution of the composite longitudinal stiffness.**

From Figure 5-16b it is evident that the composite longitudinal stiffness reduces from 60 GPa for the virgin specimen to 55 GPa at the end of the fatigue test at around 1.9×10^6 cycles. Finally, the fatigue test at 700 MPa with 2 Hz frequency lasts only for a few cycles with the sudden composite failure, without the indication of progressive failure.

5. 5.   Detailed micro-structural analysis

The above discussed sections mainly present the fatigue damage initiation and propagation on the polished edges of the composite specimen. However, in order to estimate the free-edge effects on the fatigue damage process, the current section presents the detailed damage analysis in the laminate inner layers (Figure 5-17). For the above mentioned purpose, tension-tension fatigue analysis is conducted on the composite specimen at 625 MPa stress and at 2Hz frequency. For the microscopic inspection, the fatigue test is terminated at around 7×10^5 cycles and the microscopic analysis is performed on the cut-sections of the composite specimen.
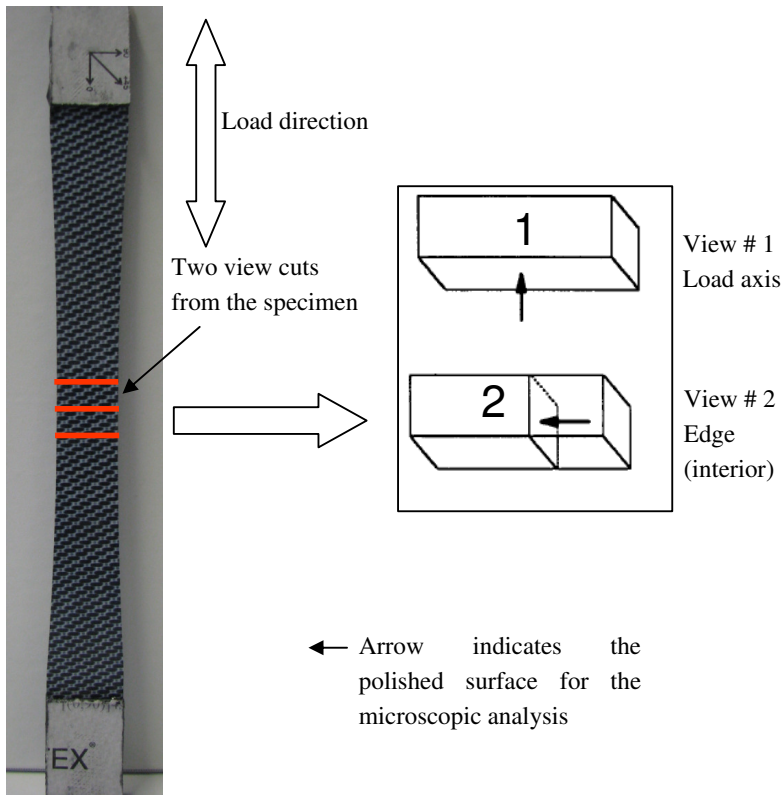
Figure 5-17. **Schematic displaying of the various views for micro-structural analysis.**

As shown in Figure 5-17, one cross-section in the load axis and one from interior edge of the composite specimen are selected at the centre of the composite specimen. Figure 5-18(a, b) shows the damage caused by the fatigue load process in the load direction. In the view cut 1, along with the weft yarn damage (Figure 5-18b), there are numerous meta-delaminations (Figure 5-18a) as well as splitting of the load carrying warp yarn is observed.

a)
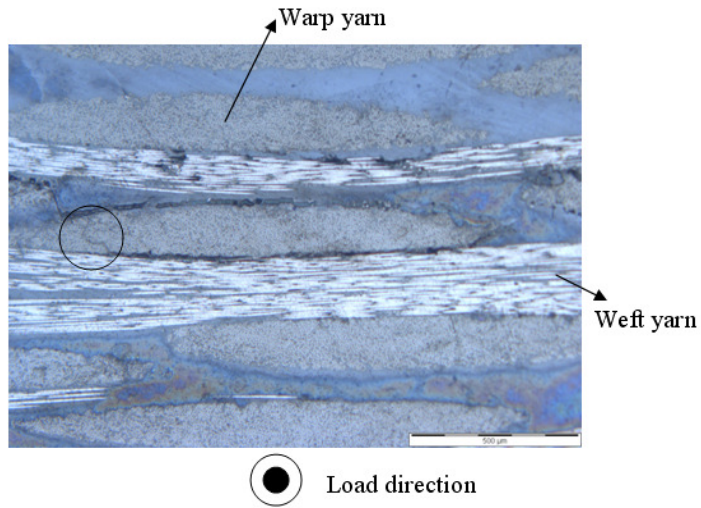
b)
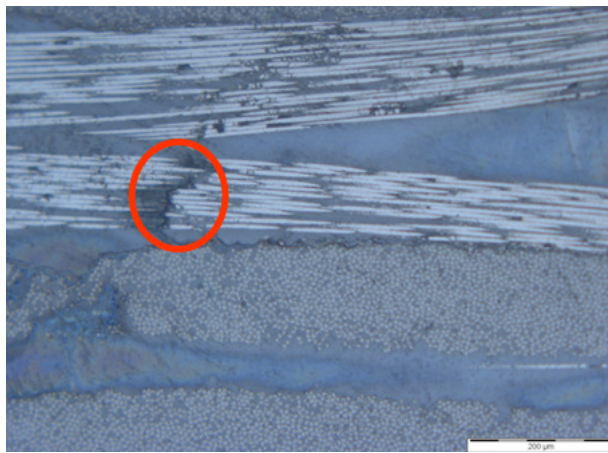
Figure 5-18.   Microscopic fatigue damage analysis in the load direction (View#1): a) meta-delamination and fibre splitting of the warp yarn; b) weft yarn splitting.

In correlation with the exterior edge damage phenomena (Figure 5-9), the laminate inner layers (view#2) shows the fibre fracture in the load carrying warp yarn (Figure 5-19). Comparison of the exterior and the interior edge damage phenomena reveal that the inter-ply delaminations are limited only to the free edges. For the statistical significance of the above observation, eight unit cells are used for the microscopic analysis from the interior edges of the composite. With the background of the effect of tension-tension fatigue on the micro- as well as macro-level structural response, the following sections present the detailed study of the post-fatigue structural behaviour of the 5-harness satin weave composite.
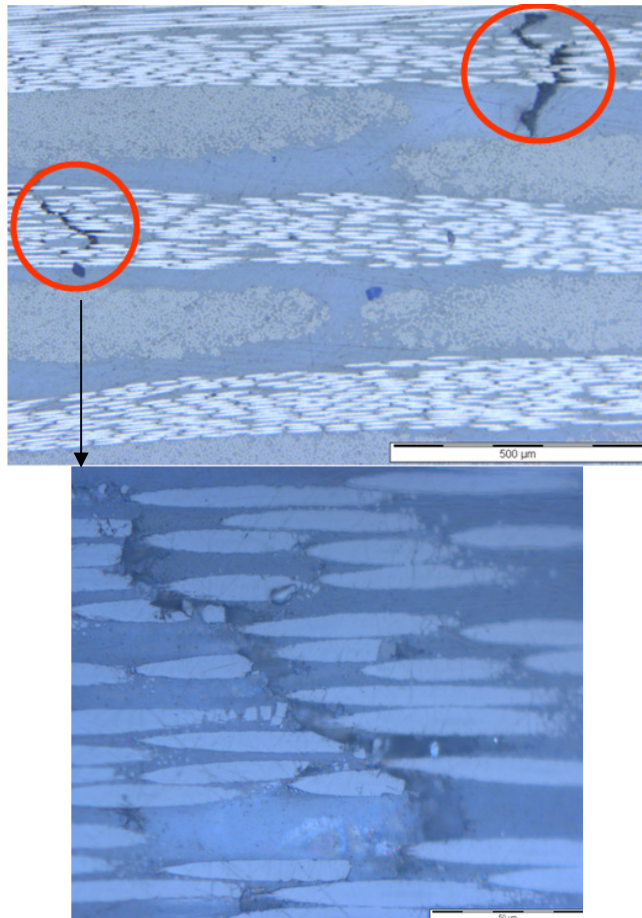
Figure 5-19   Warp yarn splitting in the interior (edge) sections of the composite laminate (View#2) (Oblique cut).

5. 6.   Residual strength analysis

In order to measure the residual strength of the fatigue tested composite specimens, the above specified fatigue tests starting from 500 MPa at 5Hz, 600 MPa at 2 Hz and 625 MPa at 2Hz were terminated at around 10^6 cycles. Figure 5-20a compares the stress-strain behaviour of the virgin samples to the test coupons used for the fatigue tests at various load levels as well as at different frequencies. From the residual strength tests (Table 5-1), it is evident that the observed microscopic damage under fatigue load does not show any influence on the strength of the composite. The reason for the same strength of the virgin as well as the fatigue samples is explored hereafter.

Table 5-1.   **Comparison between the static and post-fatigue structural behaviour.**

	Strength, MPa	Strain at failure, %	Stiffness, GPa	Stiffening
Static tensile test	754 ± 10	1.1 ± 0.1	57 ± 1	6-8%
Post-fatigue behaviour				
At 65% of the static strength- 10^6 cycles at 5Hz frequency	755	1.24	57.5	11-19%
At 80% of static strength-10^6 cycles at 2Hz frequency	769 ± 10	1.4 ± 0.1	56.5 ± 1	

For the uni-directional carbon fibre composites, the main source of degradation of the tensile strength of the composite is considered to be fibre damage caused by the matrix cracking. This means that if fibres can be protected from the damage caused by matrix cracks, the tensile strength of the carbon fibre composite potentially stays the same or increased. This protection might occur when the fibre matrix interfaces are damaged [11]. Moreover, as explained by Dreumel et al. [14], unlike metals where as the stress peaks smoothed by plastic deformation, heavily loaded areas in carbon fibre reinforced materials will behave stiffer and attract more load. In the case of UD carbon fibre composite the increase in the stiffness is about 30% between the zero load to the ultimate tensile strength [14]. Also, similar behaviour for dry carbon fibres is reported by [15]. The above mentioned phenomenon is the so called fibre stiffening effect and reported in the literature [16, 17].

However, for woven composites with carbon fabric as reinforcement, strength enhancing mechanisms are reported by [18, 19]. According to Chawla et al. [18] damage induced in between the fibre bundles (bundle debond or meta-delminations) allows large deformation in the initially curved load carrying fibre bundles of the weave structure: i.e. stretching of the curved bundles (which is observed during the fatigue test on the carbon-PPS laminate surface layer at the edges of the composite with bare eye). Thus the full potential strength of the load-bearing fibre bundles is achieved by straightening their curvatures. Figure 5-20b presents the deformation mechanism for woven composite proposed by Shuler et al. [19] that shows the weave alignment and straightening mechanism that occurs during the fatigue of woven composite. Because of the thermoplastic matrix in the satin weave composite, stretching and aligning mechanisms can easily occur, with the relief of strain mismatches allowing the longitudinal bundles to stretch while the transverse bundle to align themselves.

Moreover, from the fatigue tested samples a higher strain to failure was achieved (Figure 5-20a) due to the stretching of the weave; i.e. because fatigue damage likely redistributes and reduces the severity of the localized stress in the composite, more uniform loading of the bundle might occur.

a)
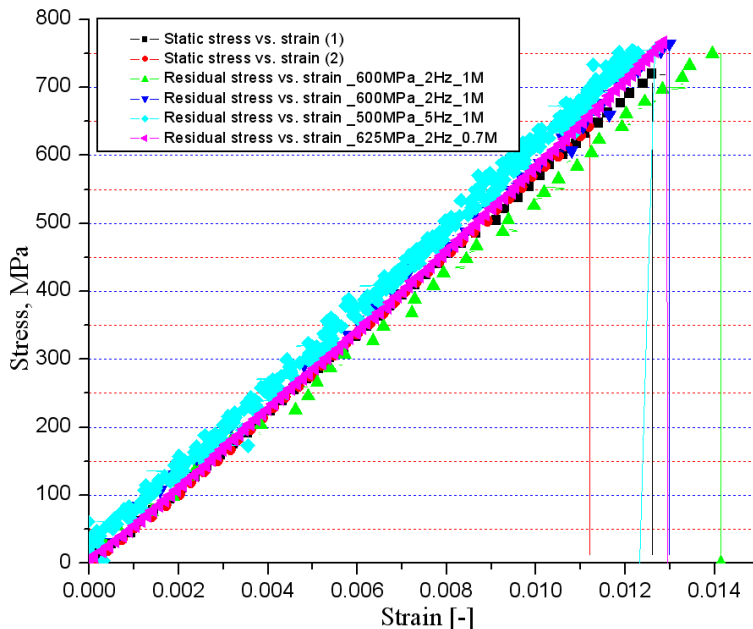
b)
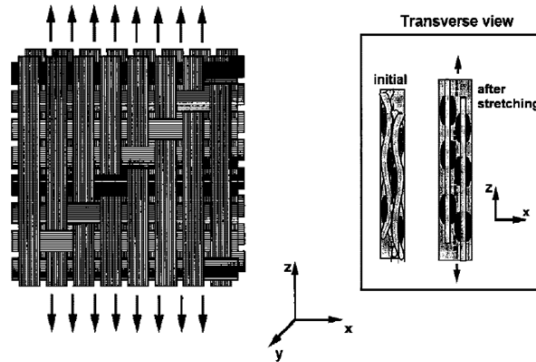
Figure 5-20.   Residual stress–strain tests: a) stress-strain behaviour; b) schematic of the stretching of the weave and realignment of transverse fibre bundles [18].

From the above discussed post-fatigue static tensile tests, it is evident that the induced fatigue damage in the composite specimen does not show any influence on the strength of the composite specimen. Nevertheless, considering the local derivatives on the stress-strain curve of the post-fatigue specimen, considerable stiffening of the composite specimen is observed from the beginning till end of the tension test. As shown in Figure 5-21a, in the beginning of the stress-strain curve, the longitudinal stiffness of the fatigue tested specimen is around 52.3 GPa. Consequent tensile load causes the straightening of the load carrying warp yarns supported by meta delmaminations as well as the local carbon fibre stiffening due to the local damage induced by the fatigue load. Hence, the derivative of the stress-strain curve at the final part indicates that the composite stiffness end up around 63.6 GPa.

In order to compare the stiffening of the virgin specimen to the fatigue tested specimen, as already shown in chapter 4, Figure 5-21b shows tangential modulus of the virgin specimen at various parts of the stress-strain curve. The local derivatives of the stress-strain curve indicate that the composite stiffness increases from (55.1 GPa) initial loading to the final failure (61.3 GPa) of the composite. At this moment, one should notice that the static damage analysis on the satin weave composite (Chapter 4) shows that the only observed damage is weft yarn cracking. Hence, the major contribution for the stiffening observed in the virgin specimen stress-strain curve might be obtained from straightening of the load carrying warp yarns under the applied external tensile load. Finally, the comparison of stiffening between the virgin specimens and the fatigue specimens is listed in Table 5-1.
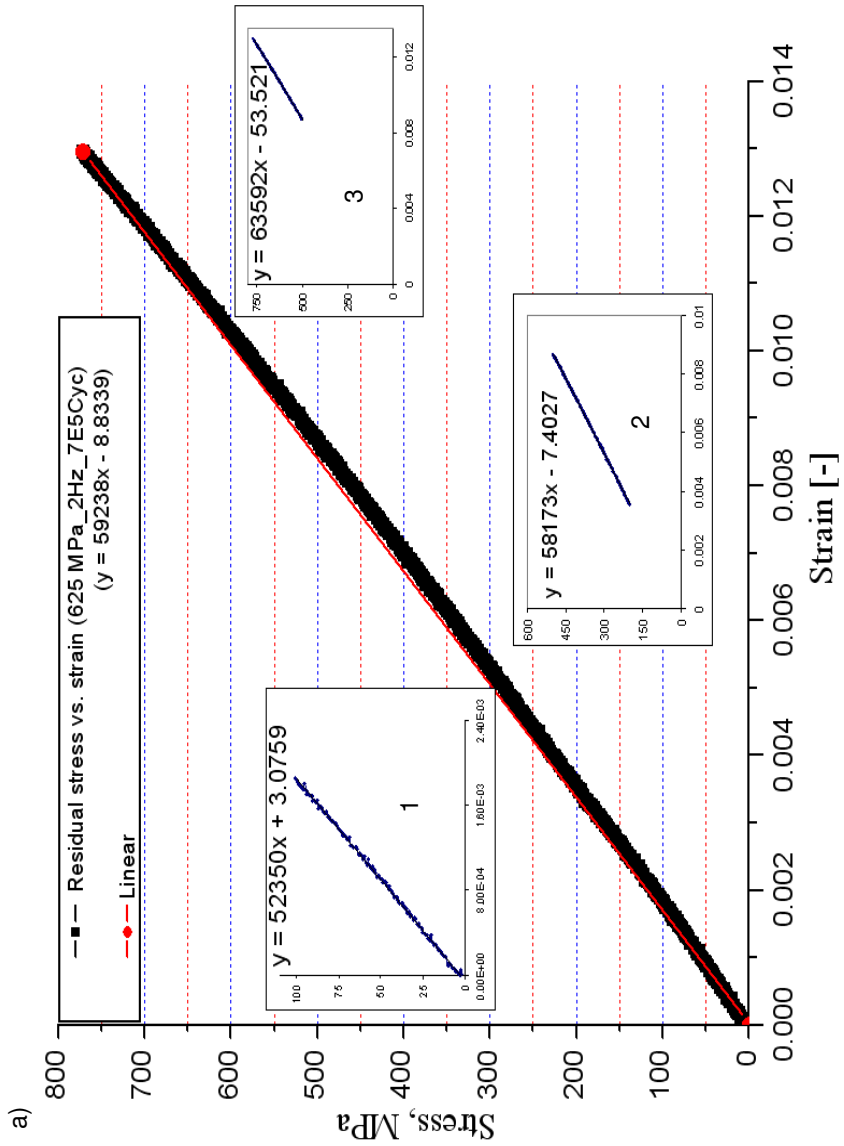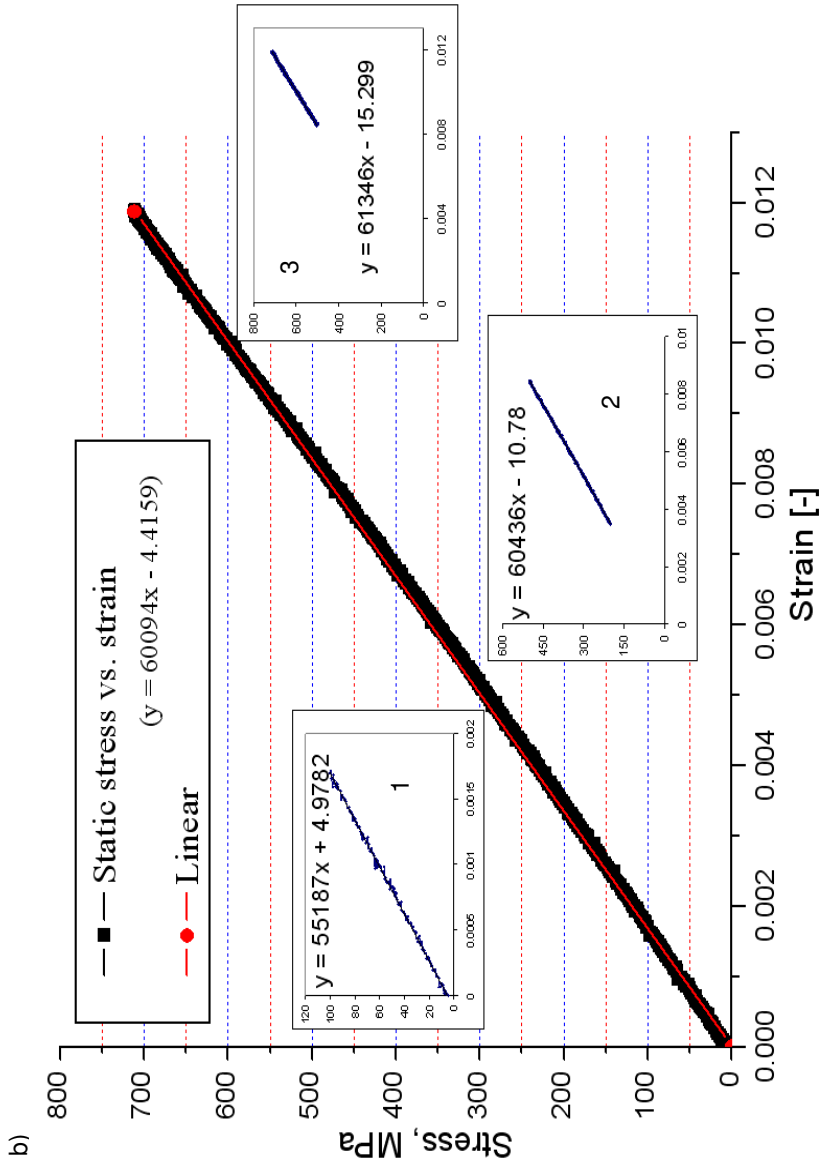
Figure 5-21.   **Analysis of the composite stiffening under static tensile load:**
a) post-fatigue stress-strain behaviour of the composite
specimen; b) stress-strain behaviour of the virgin specimen.

Finally, Figure 5-22 depicts the macro-level composite fatigue failure at the centre of the dog-bone specimen, which is in contrast to the rectangular specimen failure.
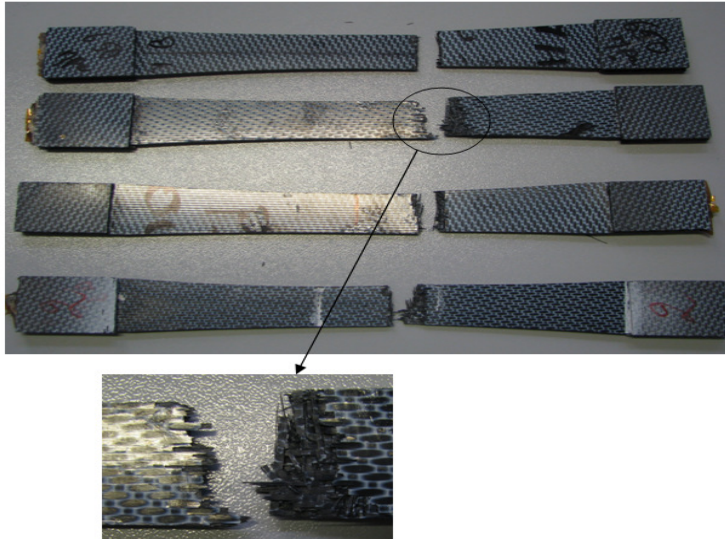
Figure 5-22.   Composite failure at the macro-level with dog-bone specimens

5. 7.   Conclusion

Comprehensive fatigue damage analysis is performed on a thermoplastic 5-harness satin weave composite under tension-tension fatigue. Initially, fatigue damage analysis is performed with the test specimens prepared according to the ASTM standard. Due to the premature failure of the rectangular test specimens at the higher stress levels, dog-bone shaped specimens with constant curvature are used for the fatigue test. Apart from monitoring the macro-scale structural response, aim of this work is to investigate the influence of the micro-scale damage events on the macro-level structural response. For the aforementioned purpose, strain in the composite specimen during the fatigue testing was registered using a dynamic extensometer. To detect the damage locations, microscopic analysis was performed using both destructive as well as non-destructive testing process. The detailed experimental analysis leads to the following conclusions:

- Experimental fatigue damage analysis on the rectangular specimens (ASTM standard) up to 550 MPa maximum stress at 5Hz frequency reveals that, during the initial phase of the cyclic load process (below 1×10^5 cycles) the longitudinal strain values increase and correspondingly, the longitudinal stiffness of the composite reduces approximately by 5%.

- In correlation with the change in the longitudinal strain and stiffness, the micro-scale damage events that are detected in the satin weave composite take many forms starting from the weft yarn damage, followed by the random breaking of the weaker load carrying fibres, and meta-delaminations. The aforementioned damage events cause the initial reduction in the composite stiffness. With the increase in the number of fatigue cycles, greater number of load carrying fibres is damaged. In addition, inter-ply delaminations are also observed.

- By the application of higher fatigue stress levels (higher than 75% of the static tensile strength of the composite), the test specimens prepared according to the ASTM standard failed in the tab area, or the adhesive that bonds the end tabs to the specimen debonded gradually. Hence, the fatigue test was aborted prematurely. To avoid this problem, dog-bone shape specimens with constant curvature are used for the fatigue tests.

- Fatigue damage analysis at higher loads with the dog-bone shaped specimens shows similar macro-scale structural response compared to the rectangular specimens. Although the cyclic load process causes many damage events, the residual strength tests reveal that the induced fatigue damage does not show any influence on the strength of the composite specimen.

- Microscopic observation of the satin weave composite during tensile load indicates that the straightening of the load carrying warp yarns is much higher in the tension-tension fatigue compared to static tensile test. The aforementioned composite behaviour is caused by large number of meta delaminations formed during the fatigue load.

- Finally, comparison between the stiffening of the virgin composite specimen to the fatigue tested specimen under static tension test indicates that the induced fatigue damage in the composite specimen causes 7-8% higher stiffening (local). The aforementioned phenomena occurred upon the reduction of the initial stiffness caused by the fatigue damage, while achieving similar failure stress in comparison to the virgin specimen.

5. 8.   References

[1]   Gyekenyesi, A.L., *Isothermal Fatigue, Damage Accumulation, and Life Prediction of a Woven PMC.* NASA/CR—1998-206593, 1998.

[2]   Pandita, S.D. and I. Verpoest, *Tension-tension fatigue behaviour of knitted fabric composites.* Composite Structures, 2004. **64**(2): p. 199-209.

[3]   Harik, V.M., J.R. Klinger, and T.A. Bogetti, *Low Cycle Fatigue of Unidirectional Laminates: Stress Ratio Effects.* 2000, ASME. p. 415-419.

[4]   Talreja, R., *Damage and fatigue in composites - A personal account.* Composites Science and Technology, 2008. **68**(13): p. 2585-2591.

[5]   Pandita, S.D., et al., *Tensile fatigue behaviour of glass plain-weave fabric composites in on- and off-axis directions.* Composites Part A: Applied Science and Manufacturing, 2001. **32**(10): p. 1533-1539.

[6]   Ferreira, J.A.M., et al., *Analysis of fatigue and damage in glass-fibre-reinforced polypropylene composite materials.* Composites Science and Technology, 1999. **59**(10): p. 1461-1467.

[7]   Ruggles-Wrenn, M.B., G. Hetrick, and S.S. Baek, *Effects of frequency and environment on fatigue behavior of an oxide-oxide ceramic composite at 1200 °C.* International Journal of Fatigue, 2008. **30**(3): p. 502-516.

[8]   VanPaepegem, W., *Development and finite element implementation of a damage model for fatigue of fibre-reinforced polymers.* PhD Thesis; Ghent University Architectural and Engineering Press, 2002.

[9]   De Baere, I., *Experimental and Numerical Study of Different Setups for Conducting and Monitoring Fatigue Experiments of Fibre-Reinforced Thermoplastics.* PhD Thesis, Gent university, 2008.

[10]   De Baere, I., et al., *On the tension-tension fatigue behaviour of a carbon reinforced thermoplastic part I: limitations of the ASTM D3039/D3479 standard.* SUBMITTED to International Journal of Fatigue, 2010.

[11]   Goto, K., et al., *Tensile fatigue of a laminated carbon-carbon composite at room temperature.* Carbon, 2003. **41**(6): p. 1249-1255.

[12]   De Baere, I., W. Van Paepegem, and J. Degrieck, *On the design of end tabs for quasi-static and fatigue testing of fibre-reinforced composites.* Polymer Composites, 2009. **30**(4): p. 381-390.

[13]   De Baere, I., et al., *On the tension-tension fatigue behaviour of a carbon reinforced thermoplastic part II: evaluation of a dogbone-shaped specimen.* SUBMITTED to International Journal of Fatigue, 2010.

[14]   Dreumel. W. H. M. and Kamp. J. L. M., *Non Hookean behaviour in the fibre direction of carbon-fibre composites and the influence of fibre waviness on the tensile properties.* Delft University of Technology - the Netherlands, July 1977.

[15]   Isidoe M. D., Daniela R. S., and M.M. S, *Non-linear elastic behaviour of carbon fibres of different structural and mechanical characteristic.* J. Serb. Chem. Soc. 72 (5) 513–521 2007.

[16]   Toyama, N. and J. Takatsubo, *An investigation of non-linear elastic behavior of CFRP laminates and strain measurement using Lamb waves.* Composites Science and Technology, 2004. **64**(16): p. 2509-2516.

[17]   Gao, F., et al., *Damage accumulation in woven-fabric CFRP laminates under tensile loading: Part 1. Observations of damage accumulation.* Composites Science and Technology, 1999. **59**(1): p. 123-136.

[18]   Chawla, N., et al., *High-Frequency Fatigue Behavior of Woven-Fiber-Fabric-Reinforced Polymer-Derived Ceramic-Matrix Composites.* Journal of the American Ceramic Society, 1998. **81**(5): p. 1221-1230.

[19]   Shuler, S.F., et al., *Influence of Loading Frequency on the Room-Temperature Fatigue of a Carbon-Fiber/SiC-Matrix Composite.* Journal of the American Ceramic Society, 1993. **76**(9): p. 2327-2336.

Chapter 6

CONCLUSIONS AND FUTURE WORK

This chapter is divided into two parts. The first part of this chapter presents the conclusions based on the extensive experimental and numerical study of the satin weave composite (CETEX®) *under uni-axial tensile load. In order to continue with the meso-FE simulations for predicting the progressive damage behavior, the second part of this chapter presents some recommendations for the future work.*

6. 1.   Conclusions

The yarn interlacing pattern followed by the traditional composite manufacturing process introduces the complex local deformation behavior under the applied tensile load, which is caused by the interaction of the differently placed plies in a textile composite laminate. The aforementioned deformation produces a complex strain (stress) and damage behavior in the plies of a textile composite. Hence, understanding the local structural response and the factors influencing their variation under the external load becomes necessary to develop a physically based meso-FE analysis procedure.

For the above said goal, usage of the existing meso-FE analysis procedure and advanced experimental techniques is a starting point for this research work. As it was mentioned in the previous chapters, the concept of meso-FE modeling is based on the spatial periodicity of the mesoscopic unit cells and the local uniformity of macroscopic fields within each unit cell. Nevertheless, general microscopic analysis of the tensile tested textile composite laminates suggests that the damage initiation and propagation breaks the periodicity of the textile reinforcement [1-3], thus indicating the non-periodic spatial variation of the stress-strain behavior throughout the composite.

Within the ultimate goal of predicting the progressive damage behavior of textile reinforced composites using meso-FE simulations, in the current research work, a unit cell based meso-FE analysis approach is employed. The local stress-strain profiles and their spatial distribution obtained from the unit cell meso-FE simulations are carefully evaluated and validated against the suitable experimental techniques. For the aforementioned purpose, in order to create the unit cell geometrical model, the internal description of the yarns in the satin weave reinforcement is accurately captured by the micro-CT technique. The calculated textile parameters are implemented into the geometrical modeler software 'WiseTex' [4, 5]. Using the 'WiseTex' generated geometrical model, a unit cell finite element mesh is generated with the 'MeshTex' software [6]. In order to account for the yarn crimp in the FE model, homogenized micro-mechanical (UD) material properties are assigned to the yarn cross-sections in their local coordinate system. In the process of validating the stress-strain and damage profiles obtained from the unit cell meso-FE simulations, various experimental techniques are used. Based on the feedback from comparison between the experimental and traditional meso-FE simulation results, modifications are accomplished to the existing unit cell FE analysis procedure. Extensive experimental and numerical analysis of the satin weave composite leads to the following conclusions.

6. 1. 1.   Experimental analysis

i.   In order to validate the meso-FE strain profiles and their spatial distribution, full-field strain analysis is conducted on the composite traction free surface in the width direction. Experimental local strain analysis leads to the following conclusions: a) the maximum in-plane longitudinal strain occurs at the centre of the weft yarn at the yarn crimp location, while the resin pockets sustain the minimum strain;

b) in addition, the maximum compressive transverse strain is observed at the centre of the load carrying warp yarn, and the positive transverse strain is detected at the weft yarn at the yarn crimp location; c) finally, the maximum in-plane shear strain under the applied tensile load is detected in the resin pockets [7].

ii.   The general microscopic observations of the satin weave laminate in the through-the-thickness direction indicate that the random textile lay-up and the subsequent compression of the layers during the composite manufacturing process cause a random shift between the adjacent plies, and also causes the interpenetration of the yarns between the adjacent plies (nesting). The above process disturbs the periodicity of the textile reinforcement in the composite thickness direction and may cause the complex strain field in the laminate inner layers.

iii.   In order to validate the above hypothesis, local strain behavior in the laminate inner layers is estimated using the embedded fibre optic sensors. Comparison between the surface layers and the laminate inner layers local strain profiles indicates that the effect of internal ply shifting does not show any influence on the local longitudinal strain behavior of the composite [7].

iv.   In order to estimate the local damage behavior in the plies of a satin weave composite under static tensile load, acoustic emission as well as microscopic analysis is used. Both damage monitoring techniques indicate that the initiation of the damage in the plies of a satin weave composite is a sequential process. Moreover, microscopic analysis of the tensile tested composite indicates that the internal ply shifting shows major influence on the local weft yarn damage. The initial damage events are detected in the laminate inner layers, followed by the damage initiation on the surface layer weft yarns. In correlation with the observed maximum strain location from the full-field strain measuring technique, damage initiation on the surface layers is detected at the centre of the weft yarns at the yarn crimp location.

v.   From the microscopic analysis of the tensile tested composite specimen, starting from low stress levels (at around 40 MPa) until the satin weave composite final failure (at around 750 MPa) crack density is increased in the perpendicular weft yarns. However, there is no observable macroscopic stiffness degradation in the satin weave composite. On the contrary, composite stiffening is observed starting from initial load to the composite final failure. The above specified non-Hookean behavior of the carbon-fibre reinforced woven composites is triggered by: i) the inherent stiffening behavior of the carbon fibre caused by its ability to attract more load under severe loading conditions [8, 9]; ii) in woven composites, apart from the material stiffening (carbon fibre), the inherent yarn crimp and subsequent straightening of the yarns caused by the external tensile load causes the initially crimped yarns to achieve their full load carrying capacity [10-12]. From the above discussion it can be concluded that the induced sequential weft yarn damage under static tensile load (in the fibre direction) does not alter the global composite stiffness. Instead, the applied tensile load causes the progressive stiffening of the satin weave composite.

vi.   Under tension-tension fatigue, the reduction in the composite in-plane stiffness of the satin weave composite occurs in the first few hundred thousand cycles. Consequently, the damage mechanisms such as fibre fracture and meta-delaminations are observed. Although the subsequent fatigue load process induces many more new damage locations until the composite final failure, their influence on the composite stiffness behavior is negligible. More importantly, the observed microscopic damage under fatigue load in various plies of the satin weave laminate seems to be governed by the stochastic material and laminate parameters rather than the periodicity of the textile reinforcement.

vii.   To the author's knowledge, carbon-PPS satin weave composite material (CETEX®) is designed for operating at strain levels around 0.4%. From the fatigue tests at the elevated loads and the subsequent residual stress-strain analysis, it can be concluded that once the satin weave composite is subjected to higher stress levels and returns to the normal operating loads, the structural behavior of the composite is changed substantially. This behavior is manifested by the lower stiffness (at around 52 GPa) in the first part of the residual stress-strain curve.

6. 1. 2.   Numerical analysis

Numerical meso-FE analysis using the satin weave unit cell is started with the prediction of the homogenized elastic properties of the satin weave composite. Later, unit cell FE simulations are extended to the local stress-strain and the local damage analysis. Detailed numerical investigation of the local structural parameters and subsequent comparison with the experimental results leads to the following conclusions:

   i. Good correlation is observed between the numerical elastic constants computed using the traditional meso-FE simulations compared to the experimental elastic constants.

   ii. Comparison of the experimental local surface strain profiles to the single unit cell meso-FE strain profiles indicates that the applied boundary conditions and the used geometrical model shows considerable influence on the spatial strain distribution. The difference in the spatial strain distribution between the experimental and numerical results indicates the necessity for improvement in the meso-FE analysis procedure. Moreover, it is important to predict the maximum strain locations correctly, due to the fact that the maximum strain and damage in the unit cell are situated at the same location.

   iii. In order to improve the unit cell FE simulation results, instead of using a strain profile obtained from the single unit cell with the infinite laminate conditions to compare with the experimental strain profile obtained from the randomly shifted textile laminate, various unit cell stacks with different ply configurations are constructed for the FE analysis. Using the above created unit cell stack FE simulations, the bounding limits for the local strain variation of the satin weave composite are computed under the applied static tensile load [13]. Moreover, effect of the ply shifting and the applied boundary conditions on the spatial surface strain variation is realized.

   iv. Finally, in order to predict the sequential weft yarn damage in different plies of the satin weave laminate at various applied strain levels as observed in the experimental damage analysis, different unit cell models with suitable boundary conditions are used for the meso-FE analysis. In correlation with the experimental observations, meso-FE simulations indicate that the damage initiation strain and its location in the weft yarn depends on the allowed deformation of the weft yarn at the yarn crimp location, which intern depends on the ply position in the laminate.

More importantly the local stress analysis at the damaged elements provides the stress components that are responsible for the sequential damage initiation.

v.   From the detailed stress analysis at the damage regions using meso-FE simulations, it can be concluded that the active stress components that are responsible for the weft yarn damage in different plies are: i) in-plane transverse stress; ii) out-of-plane normal stress; iii) out-of-plane shear stress. The above mentioned stress components are active due to the interlacement pattern of the yarns in the satin weave composite [14], and are also influenced by the local ply constraints posed by the surrounding layers. As a conclusion, depending on the ply position in the laminate, the local deformation behavior of the textile fabric varies so as the local stress components, and hence the local damage behavior.

vi. In brief, the damage mechanism in the satin weave composite under static and fatigue loads is summarized as follows: For the woven composites, the nonuniform stress-strain distributions develop at different scales in three orthogonal directions. At meso-scale, the yarn interlacement pattern produces nonuniform strain (stress) distributions along the axial (fibre) and width (transverse) directions within the individual plies. At macro-scale, the random stacking of the plies produces the nonuniform stress distribution in the thickness direction of the specimen. Moreover, non-uniform stretching caused by the random stacking of the plies produces a shear stress in the contact surface of the plies, resulting in delamination between the plies [12]. At micro-scale, the straightening of the individual load carrying fibres and simultaneous bending of the perpendicular weft yarns produces the micro-scale damage.

vii. Within the timeframe of this current research work, the author tried to understand the observed experimental local damage in a deterministic manner by studying the various local parameters in a stochastic (textile lay-up) and inhomogeneous (material) satin weave composite. Detailed structural behavior of the satin weave composite is studied using the local response parameters such as strain and damage. Effect of the adjacent layers on the local ply structural behavior is highlighted.

Detailed analysis of the structural response using experimental and numerical simulations starting from the deformation, strain (stress) and damage provides a unified knowledge regarding the local damage behavior in the plies of a satin weave composite. In this process, the conventional single unit cell meso-FE analysis procedure is modified substantially to capture the non-uniform stress distribution in different plies at different locations of the textile laminate.

viii. Finally, the progressive damage modeling under fatigue load using the conventional meso-FE simulations procedure is a challenging task from the geometrical as well as the material model point of view.

       a. From the experimental fatigue damage analysis it is observed that the main source of the geometrical stiffening is caused by the straightening of the load carrying fibres induced by meta-delaminations at the yarn crimp region. This phenomenon can not be captured with the existing unit cell geometrical models.

       b. As stated in the previous section, the observed microscopic damage under fatigue load seems to be caused by the stochastic geometrical and material parameters rather than the periodicity of the textile reinforcement. This phenomenon further complicates the conventional (deterministic) unit cell meso-FE analysis under fatigue loads.

       c. From the material point of view, the amount of stiffening observed in the satin weave composite is a combination of material (carbon fibre [9]) and geometrical (straightening of the crimps [15]) stiffening. In order to use the stiffening percentage during progressive damage modeling, one should decouple them and apply the appropriate stiffening according to the observed damage location in the unit cell. This procedure requires further experimental testing of the material under static and fatigue loads.

6. 2.   Future work

For the better understanding of the textile composite mechanical behavior, following recommendations are suggested for the future research work.

6. 2. 1.   Residual thermal strain analysis

As stated in the previous chapter, the stress-strain mechanics of polymer composites starts with the composite manufacturing process without the application of any external structural load. Due to the significantly larger shrinkage of the polymer matrix compared to the reinforcing fibres, residual strains arise in composites during processing and subsequent cooling from the processing to the service temperature. Owing to the composites inherent inhomogeneous nature, these process-induced residual strains occur in all fibre reinforced polymers and significantly influence the properties of the composite structures. Therefore, it is important to take the residual strains and their effects into account during the design of composite structures [16].

In this regard, extensive experimental work has been conducted by Parlevliet et al. [17-20] on the formation of the thermal strains and instrumenting them during the composite manufacturing process. The induced thermal stresses cause the warping of the composite plates as well as the fibre matrix debonding prior to the application of the structural load (graphite fibre and polyimide composite) [21]. In addition, based on the finite element analysis of the thermal residual stresses by Zhao et al. [21] leads to the conclusion that, with and without considering the thermal residual stress in the unit cell for the structural FE analysis, there is almost 30% difference in the failure initiation strain. In addition, finite element analysis of the carbon-carbon satin weave composite using different unit cell stacks in the presence of only thermal load indicates that the crack initiation and propagation depends on the stacking configuration [22].

In the context of the current research work, the author tried to simulate the thermal stress behavior in the carbon-PPS satin weave composite using unit cell meso-FE simulations. The intention is to incorporate the induced thermal stresses in the unit cell for the subsequent stress and damage analysis under uni-axial tensile load. In the aforementioned process, homogenization of the CTE as well as the restarting the ABAQUS simulations after each temperature load step is successfully accomplished. However, the following challenges were encountered:

i. The major challenge is the measurement of the accurate material properties such as thermal expansion coefficient and elastic modulus of the carbon fibre and PPS resin at the elevated temperature during the composite manufacturing process.

ii. From the meso-FE analysis point of view, unit cell FE simulation of the thermal stress behavior requires the application of the PBCs along with the average strain experienced by the composite during the manufacturing process, which is extremely difficult to measure.

iii. In the future research work, it is recommended to measure the residual thermal strains using the embedded fibre optic sensors (temperature and strain) in between the composite plies during the composite manufacturing process. In this way average thermal strain during the composite manufacturing process can be estimated at different temperature levels.

Using the numerical meso-FE simulations, performing the thermal strain analysis using the data obtained from the fibre optic sensors and the subsequent structural analysis facilitates the thorough understanding of the influence of the thermal residual stresses on the composite structural response.

6. 2. 2.   Structural and material behavior

Apart from the above mentioned thermal analysis, the following structural analysis should provide valuable information to understand as well as to develop a procedure for predicting the progressive damage behavior in textile composites.

- Starting from the static load, the straightening mechanism of the yarn crimp regions is responsible for the local damage in the weft yarns as well as the stiffness enhancing in the satin weave composite. Hence, characterization of the out-of-plane deformation of the textile composite under tensile load using DIC becomes necessary [23].

- From the static as well as fatigue tension tests, the observed stiffening of the carbon-PPS satin weave composite seems to be difficult to understand in a deterministic way. In the future research work, it is recommended to study the carbon-PPS UD composite under static and fatigue tensile load followed by the experimental analysis of the satin weave carbon-PPS composite under static and fatigue tension load. In the above said way, the contribution of the stiffening obtained from the material (carbon fibre) and the yarn crimps (geometric stiffening) can be decoupled.

- As explained by Jekabsons et al. [15], the stiffness components (Q matrix) of the woven composite highly depend on the number of plies in the laminate. For instance, experimental tensile tests on the carbon fibre (Tenax HTA) woven composite with single layer and eight layered laminate indicate that there is almost 30% difference in the longitudinal stiffness [15] (31 GPa for single layer and 50 GPa for eight layer). Moreover, the authors [15] have reported a considerable increase in the tangent modulus due to the straightening of the crimped yarns along the load process. In addition, multi-layered composites seem to exhibit a more linear stress-strain response compared to the single layer composites. In comparison to the residual stress-strain analysis of the fatigue tested satin weave composite (Figure 5-19 a), single layer woven composites exhibit non-linear stress-strain behavior during the load process with low tangential modulus at beginning and high at the end, indicating the substantial stiffening of the carbon fabric. From the above discussion, in the future research work it is recommended to perform the static tensile tests in a loading and un-loading manner by varying the number of plies in the woven composite. In the aforementioned way, effect of the adjacent layers as well as number of plies on the composite stiffening can be realized.

6. 3.   References

[1]   Roy, A.K., *Comparison of in situ damage assessment in unbalanced fabric composite and model laminate of planar (one-directional) crimping.* Composites Science and Technology, 1998. **58**(11): p. 1793-1801.

[2]   Duplessis Kergomard, Y., et al., *Intralaminar and interlaminar damage in quasi-unidirectional stratified composite structures: Experimental analysis.* Composites Science and Technology. **70**(10): p. 1504-1512.

[3]   Ivanov, d.S., *Damage analysis in textile composites.* PhD Thesis; KU Leuven - Faculty of Engineering, May 2009.

[4]   Lomov, S.V., et al., *Textile composites: modelling strategies.* Composites Part A: Applied Science and Manufacturing, 2001. **32**(10): p. 1379-1394.

[5]   Verpoest, I. and S.V. Lomov, *Virtual textile composites software WiseTex: Integration with micro-mechanical, permeability and structural analysis.* Composites Science and Technology, 2005. **65**(15-16): p. 2563-2574.

[6]   Lomov, S.V., et al., *Meso-FE modelling of textile composites: Road map, data flow and algorithms.* Composites Science and Technology, 2007. **67**(9): p. 1870-1891.

[7]   Daggumati, S., et al., *Local strain in a 5-harness satin weave composite: part I - experimental analysis.* Accepted for Composites Science and Technology, 2011.

[8]   Isidoe M. D., Daniela R. S., and M.M. S, *Non-linear elastic behaviour of carbon fibres of different structural and mechanical characteristic.* J. Serb. Chem. Soc. 72 (5) 513–521 2007.

[9]   Dreumel. W. H. M. and Kamp. J. L. M., *Non Hookean behaviour in the fibre direction of carbon-fibre composites and the influence of fibre waviness on the tensile properties.* Delt University of Tecnnology - the Netherlands, July 1977.

[10]   Gao, F., et al., *Damage accumulation in woven-fabric CFRP laminates under tensile loading: Part 1. Observations of damage accumulation.* Composites Science and Technology, 1999. **59**(1): p. 123-136.

[11]   Chawla, N., et al., *High-Frequency Fatigue Behavior of Woven-Fiber-Fabric-Reinforced Polymer-Derived Ceramic-Matrix Composites.* Journal of the American Ceramic Society, 1998. **81**(5): p. 1221-1230.

[12]   Shuler, S.F., et al., *Influence of Loading Frequency on the Room-Temperature Fatigue of a Carbon-Fiber/SiC-Matrix Composite.* Journal of the American Ceramic Society, 1993. **76**(9): p. 2327-2336.

[13]   Daggumati, S., et al., *Local strain analysis in a 5-harness satin weave composite under static tension : part II-meso-FE analysis.* Accepted for Composites Science and Technology, 2011.

[14]   Cox, B.N. and G. Flanagan, *Handbook of Analytical Methods for textile composite.* NASA Contractor Report 4750, 1997.

[15]   Jekabsons, N. and J. Byström, *On the effect of stacked fabric layers on the stiffness of a woven composite.* Composites Part B: Engineering, 2002. **33**(8): p. 619-629.

[16]   Parlevliet, P.P., *Residual Strains in Thick Thermoplastic Composites - an Experimental Approach.* PhD Thesis; Delft University of Technology, 2010.

[17]   Parlevliet, P.P., H.E.N. Bersee, and A. Beukers, *Measurement of (post-)curing strain development with fibre Bragg gratings.* Polymer Testing. **29**(3): p. 291-301.

[18]   Parlevliet, P.P., H.E.N. Bersee, and A. Beukers, *Residual stresses in thermoplastic composites--A study of the literature--Part I: Formation of residual stresses.* Composites Part A: Applied Science and Manufacturing, 2006. **37**(11): p. 1847-1857.

[19]   Parlevliet, P.P., H.E.N. Bersee, and A. Beukers, *Residual stresses in thermoplastic composites - a study of the literature. Part III: Effects of thermal residual stresses.* Composites Part A: Applied Science and Manufacturing, 2007. **38**(6): p. 1581-1596.

[20]   Parlevliet, P.P., H.E.N. Bersee, and A. Beukers, *Residual stresses in thermoplastic composites--A study of the literature--Part II: Experimental techniques.* Composites Part A: Applied Science and Manufacturing, 2007. **38**(3): p. 651-665.

[21]   Zhao, L.G., N.A. Warrior, and A.C. Long, *A micromechanical study of residual stress and its effect on transverse failure in polymer-matrix composites.* International Journal of Solids and Structures, 2006. **43**(18-19): p. 5449-5467.

[22]   Clinton D. Chapman, J.D.W., *Thermally Induced Damage Initiation and Growth in Plain and Satin Weave Carbon-Carbon Composites.* Mechanics of advanced materials and structures, 2000.

[23]   Littell, J.D. and W.K. Binienda, *Characterization of Damage in Triaxial Braid Composites Under Tensile Loading.* NASA/TM—2009-215645, May 2009.

APPENDIX A

A.1. Kinematic boundary conditions and surface reactions

The prescription of appropriate BC's is essential for the homogenization process. Determination of the effective elastic constants relies on the conservation of energy principle. It is first observed that for given BC's, the variation of the total mechanical work done in the unit cell may be computed from the microscopic stress and strain field via

$$\delta W = \int_V \sigma . \delta \varepsilon \, \mathrm{d}v \qquad (A.1)$$

On the other hand, the total mechanical work in the unit cell (V) when the original heterogeneous material is replaced by the effective one is given by

$$\delta w^* = \left| V \right| \sigma^* . \delta \varepsilon^* \qquad (A.2)$$

By imposing the micro-macro work balance, i.e. that the variation of the total mechanical work is conserved in the transition from the heterogeneous to the homogenized case, then one obtains the following Hill energy criterion:

$$\sigma^* . \varepsilon^* = \left\langle \sigma . \varepsilon \right\rangle \qquad (A.3)$$

The above shown equality (equation 2.9) has a physical meaning only for elastically deforming structures for which it would amount to saying that the strain energy should be conserved in the micro-macro transition. Moreover, the above statement is a restriction, in the sense that it specifies the types of BC's that may be applied to the unit cell [1]. Initially, linear displacement BC's that are applicable for the unit cell FE analysis is tested with the Hill energy criterion as follows:

In general, linear displacement BC's are defined as follows:

$$u = HX \qquad \text{on } \partial V \qquad (A.4)$$

Where 'u' is the displacement, 'H' is the deformation gradient and 'X' is the unit cell length.

From the average energy theorem one obtains:

$$\langle \sigma.\varepsilon \rangle = \frac{1}{|V|} \int_{\delta v} t.u \, da = \frac{1}{|V|} \int_{\delta V} t.HX \, da \qquad (A.5)$$

And the above equation can be rearranged into:

$$\frac{1}{|V|} \int_{\delta V} (X \otimes t).H^T \, da = \langle \sigma \rangle.H^T = \langle \sigma \rangle.\langle \varepsilon \rangle \qquad (A.6)$$

Where t is the traction, da is the traction surface.

From the above derivation it is evident that the linear displacement boundary conditions satisfy the Hill energy criterion (micro-macro work balance). Consequently, linear displacements BC's are applied to the satin weave unit cell for the FE analysis and results are presented in the following section.

A.1.1 Normal load applied to the unit cell

In order to estimate the normal elastic components of the satin weave composite, initially, three independent unit normal load cases (shown below) are applied to the unit cell FE model (Figure A-1) in x, y, z directions.

$$\varepsilon_{11} = 1\%, \qquad \varepsilon_{22} = \varepsilon_{33} = \gamma_{23} = \gamma_{13} = \gamma_{12} = 0$$
$$\varepsilon_{22} = 1\%, \qquad \varepsilon_{11} = \varepsilon_{33} = \gamma_{23} = \gamma_{13} = \gamma_{12} = 0$$
$$\varepsilon_{33} = 1\%, \qquad \varepsilon_{11} = \varepsilon_{22} = \gamma_{23} = \gamma_{13} = \gamma_{12} = 0$$

With the application of the above shown kinematic constraints, after solving each load case, equating the external work done on the unit cell to the stored energy in the unit cell, one obtains the relation between macroscopic (m-level) in-plane stresses to the strains [2].
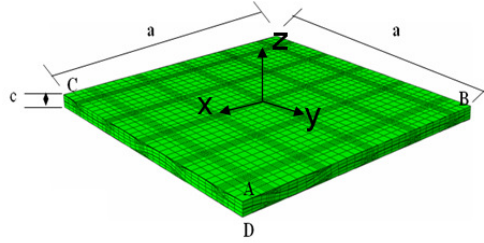
Figure A-1. **5-harness satin weave RUC.**

In general, the stress–strain state for the general orthotropic material is related through the below equation:

$$
\begin{Bmatrix} \sigma_{11} \\ \sigma_{22} \\ \sigma_{33} \\ \tau_{23} \\ \tau_{13} \\ \tau_{12} \end{Bmatrix} = \begin{bmatrix} E_{11}\dfrac{1-\nu_{23}\nu_{32}}{\Delta} & E_{11}\dfrac{\nu_{21}+\nu_{31}\nu_{23}}{\Delta} & E_{11}\dfrac{\nu_{31}+\nu_{21}\nu_{32}}{\Delta} & 0 & 0 & 0 \\ E_{11}\dfrac{\nu_{21}+\nu_{31}\nu_{23}}{\Delta} & E_{22}\dfrac{1-\nu_{13}\nu_{31}}{\Delta} & E_{22}\dfrac{\nu_{32}+\nu_{12}\nu_{31}}{\Delta} & 0 & 0 & 0 \\ E_{11}\dfrac{\nu_{31}+\nu_{21}\nu_{32}}{\Delta} & E_{22}\dfrac{\nu_{32}+\nu_{12}\nu_{31}}{\Delta} & E_{33}\dfrac{1-\nu_{12}\nu_{21}}{\Delta} & 0 & 0 & 0 \\ 0 & 0 & 0 & G_{23} & 0 & 0 \\ 0 & 0 & 0 & 0 & G_{13} & 0 \\ 0 & 0 & 0 & 0 & 0 & G_{12} \end{bmatrix} \begin{Bmatrix} \varepsilon_{11} \\ \varepsilon_{22} \\ \varepsilon_{33} \\ \gamma_{23} \\ \gamma_{13} \\ \gamma_{12} \end{Bmatrix}
\qquad (A.7)
$$

Where $\Delta = 1 - \nu_{12}\nu_{21} - \nu_{23}\nu_{32} - \nu_{31}\nu_{13} - 2\nu_{21}\nu_{32}\nu_{13}$

After solving each normal load case, surface reactions are computed from the constrained unit cell faces. Using the obtained reaction forces, nine normal components of the constitutive matrix (red box in Equation A.7) are estimated using the formulations shown in Table A-1 [2-6]. Subsequently, the following section explains the calculation of the shear components of the orthotropic material constitutive matrix (equation A.7).

Table A-1.   **Normal components of the orthotropic constitutive matrix.**

ε_x	ε_y	ε_z
$A_{11} = \dfrac{N_x}{c.\delta}$	$A_{21} = \dfrac{N_y}{c.\delta}$	$A_{31} = \dfrac{N_x}{c.\delta}$
$A_{12} = \dfrac{N_y}{c.\delta}$	$A_{22} = \dfrac{N_x}{c.\delta}$	$A_{32} = \dfrac{N_y}{c.\delta}$
$A_{13} = \dfrac{N_z}{a.\delta}$	$A_{23} = \dfrac{N_z}{a.\delta}$	$A_{33} = \dfrac{N_x.c}{\delta.a.a}$

In the above table, N_x, N_y, N_z are the reaction forces measured over the constrained x, y, z surfaces of the of the unit cell shown in Figure 2-8. Where as a and c are the width and thickness of the unit cell. And δ is the elongation in the respective unit cell direction.

A.1.2   Longitudinal shear load

After calculating the normal components, the shear components of the constitutive matrix should be evaluated. The assumption of constant shear load applied to the unit cell is based on the hypothesis that the longitudinal shear strain in the matrix is equal to the fabric shear strain ($\gamma_L^{yarn} = \gamma_L^{matrix}$). This is incorrect, since the fibre being much stiffer than the matrix, should exhibit less shear strain [4]. The strain field in a composite subjected to longitudinal loading is two-dimensional in nature, i.e. it is independent of the axial coordinate (x-coordinate). To impose this constraint to the unit cell, the front and the back faces of the unit cell (Figure A-2) are required to undergo identical displacement, i.e. points on the front ($x = a$) and the back ($x = 0$) faces with the same y and z coordinates are constrained to have the same displacements in all three directions.

With the above procedure, the shear stiffness components of the orthotropic material matrix (equation A.7) are computed as explained below:

The average longitudinal shear strain on the unit cell is given by (Figure A-2):

$$\bar{\gamma}_{12} = \frac{1}{V}\int_V \gamma_{12}\,dV = \frac{2}{V}\int_V \varepsilon_{12}\,dV \qquad (A.8)$$

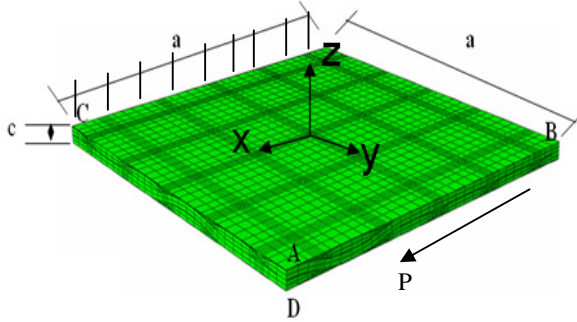Equating the external work done to the strain energy in the system, one obtains:

$$\frac{1}{2}P\delta = \frac{1}{2} < \sigma_{12} >< \gamma_{12} > V \qquad (A.9)$$

Where P - reaction force of the constrained surface (Figure A-2)

δ - applied small deformation

For the boundary conditions applied to the unit cell (Figure A-2) the shear strain equation is reduced to:

$$\overline{\gamma}_{12} = \frac{\delta}{2b} \qquad (A.10)$$

Figure A-2. **RUC under longitudinal shear loading[4].**

Using equations (A.9) and (A.10), the average stress and longitudinal shear modulus is given by:

$$< \sigma_{12} >= \frac{P}{2ac} \qquad (A.11)$$

$$G_{12} = \frac{< \sigma_{12} >}{\gamma_{12}} = \frac{Pb}{ac\delta} \qquad (A.12)$$

In a similar way, the other two shear moduli can be derived. As mentioned above, after solving the six initial boundary value problems (IBVP's), the full constitutive components of the orthotropic material were obtained. By inverting the stiffness matrix (equation A.13), the compliance components are calculated, which takes the following form:

$$
\begin{Bmatrix} \varepsilon_{11} \\ \varepsilon_{22} \\ \varepsilon_{33} \\ \gamma_{23} \\ \gamma_{13} \\ \gamma_{12} \end{Bmatrix} = \begin{bmatrix} \dfrac{1}{E_{11}} & \dfrac{-\nu_{12}}{E_{11}} & \dfrac{-\nu_{13}}{E_{11}} & 0 & 0 & 0 \\ \dfrac{-\nu_{21}}{E_{22}} & \dfrac{1}{E_{22}} & \dfrac{-\nu_{23}}{E_{22}} & 0 & 0 & 0 \\ \dfrac{-\nu_{31}}{E_{33}} & \dfrac{-\nu_{32}}{E_{33}} & \dfrac{1}{E_{33}} & 0 & 0 & 0 \\ 0 & 0 & 0 & \dfrac{1}{G_{23}} & 0 & 0 \\ 0 & 0 & 0 & 0 & \dfrac{1}{G_{13}} & 0 \\ 0 & 0 & 0 & 0 & 0 & \dfrac{1}{G_{12}} \end{bmatrix} \begin{Bmatrix} \sigma_{11} \\ \sigma_{22} \\ \sigma_{33} \\ \tau_{23} \\ \tau_{13} \\ \tau_{12} \end{Bmatrix} \qquad (A.13)
$$

From the above matrix (Equation A.13), six homogenized elastic constants (three normal, three shear) along with the three Poisson's ratio's are calculated and are listed in the Table 2-8 (*column 3*). Due to the numerical error, there will always be a slight difference between C_{12} and C_{21}. For the evaluation of the Poisons ratio's, the averaged value of C_{12} and C_{21} is used [7].

In the above section, unit cell FE analysis is accomplished using kinematic BC's. Although kinematic BC's satisfy the Hill energy criterion, they may not produce periodic stress and strain fields [1, 8] which is the critical issue for analysis of the local strain and damage patterns of the satin weave unit cell (discussed in the later chapters of this manuscript). Thus, in order to dictate the unit cell boundary deformation not by equivalent homogeneity conditions, but by the actual micro-structural content, periodic boundary conditions should be applied to the unit cell faces. Hence, the following sections provide the detailed discussion regarding the concept of the periodic boundary conditions as well as the volume averaging technique.

A.2. Asymptotic homogenization method (AHM)

The current section deals with the derivation of the mathematical homogenization theory. In order to introduce the concept of the periodic boundary conditions (PBCs), AHM is presented in the current section. The aforementioned theory uses asymptotic expansion of displacement, stress and strain fields about the macroscopic values, which has been used for analyzing two scale responses in the composites [9-15]. In general, periodic structure for the textile composite is made up of many unit cells and uses the periodic homogenization. Provided that the scale associated with the unit cell is well separated from the overall structure, linear elastic properties of the composite are estimated from the unit cell FE simulations [16].

AHM not only allows us to find the effective elastic constants, but also allows one to estimate the stress in the constituent materials at the micro-scale. Consider a composite, wherein micro-structure is periodically distributed in the plane $x_2 - x_3$ (Figure A-3) defined by global co-ordinates (x_2, x_3) and fast co-ordinates at the unit cell scale are defined by (y_2, y_3) (Figure A-3).

a)   b)
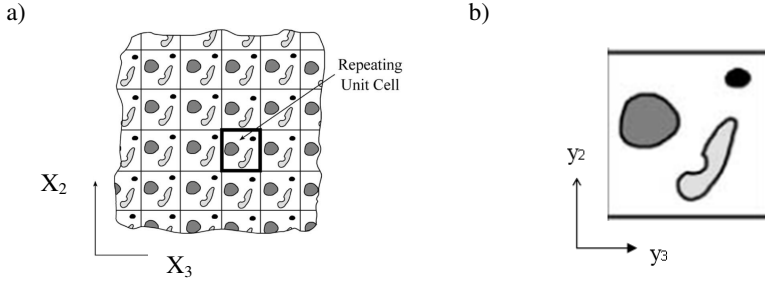
Figure A-3.   Periodic structure with two levels: a) global scale; b) local scale.

One important assumption for asymptotic analysis is that it must be possible to distinguish two length scales associated with the macroscopic and microscopic phenomena. The ratio of these scales defines the small parameter ε. And the two sets of the coordinates are related by equation A-14.

$$y = \frac{x}{\varepsilon} \qquad (A.14)$$

The above equation A-14 implies that the movement of an order of unity on the local scale corresponds to a very small movement on the global scale. For heterogeneous body depicted in Figure A-3 deforming in elastic range is defined by the following continuum equations:

Equilibrium equation:
$$\sigma_{ij,j}^{\varepsilon}(x) + f_i(x) = 0 \qquad (A.15)$$

Kinematics:
$$e_{kl}(u^{\varepsilon}(x)) = \frac{1}{2}(\nabla^{\varepsilon}u(x) + \nabla^{\varepsilon T}u(x)) \quad (A.16)$$

Constitutive equation:
$$\sigma_{ij}^{\varepsilon}(x) = a_{ijkl}^{\varepsilon}e_{kl}(u^{\varepsilon}(x)) \qquad (A.17)$$

The superscripts (ε) used in the above equations indicate the variables of the problem relates the unit cell dimensions to the global length. And $\sigma_{ij}(x)$ represents the stress tensor, e_{kl} represents the linear strain and a_{ijkl} denotes the elasticity tensor. The asymptotic expansion of the displacement, stress and strain leads to the following equations:

$$u^\varepsilon(x) = u^0(x) + \varepsilon u^1(x, y) + \varepsilon^2 u^2(x, y) + \ldots \ldots \varepsilon^k u^k(x, y) \qquad \text{(A.18)}$$

$$\sigma^\varepsilon(x) = \sigma^0(x) + \varepsilon \sigma^1(x, y) + \varepsilon^2 \sigma^2(x, y) + \ldots .. \varepsilon^k \sigma^k(x, y) \qquad \text{(A.19)}$$

$$e^\varepsilon(x) = e^0(x) + \varepsilon e^1(x, y) + \varepsilon^2 e^2(x, y) + \ldots \ldots \varepsilon^k e^k(x, y) \qquad \text{(A.20)}$$

In the above equations superscript '0' refers to the effective or macroscopic fields and superscripts 1 and 2 represent the first and second order perturbations caused by the micro-structure, which are assumed to vary periodically. And u^k, σ^k, e^k for k>0 are Y-periodic (on meso-scale) i.e. take the same values on the opposite sides of the unit cell periodicity. Consequently, the material periodicity imposes the constraint $u^{\varepsilon i}(x, y) = u^{\varepsilon i}(x, y + n_p d_p)$ where n_p is an arbitrary integer number and d_p characterizes the periodicity [17]. By introducing the equations (A.18-A.20) into (A.15-A.17) and using the chain rule with the following notation:

$$\frac{\partial}{\partial x_i} f = (\frac{\partial}{\partial x_i} + \frac{1}{\varepsilon} \frac{\partial}{\partial y_i}) f = f,i(x) + \frac{1}{\varepsilon} f,i(y) \qquad \text{(A.21)}$$

Segregating the terms (the terms of the same powers of ε are segregated and equated to zero), then the equilibrium equation becomes:

$$\sigma_{ij}^{(0)}(x, y) = a_{ijkl}(y)(e_{kl}(x)(u^0) + e_{kl}(y)(u^1)) \qquad \text{(A.22)}$$

$$\sigma_{ij}^{(1)}(x, y) = a_{ijkl}(y)(e_{kl}(x)(u^1) + e_{kl}(y)(u^2)) \qquad \text{(A.23)}$$

Due to the linear elastic problem, the microscopic equilibrium condition can be expressed as:

$$\sigma_{ij}^1 = \sigma_{ij}^{kl}(y) \frac{\partial u_k^0}{\partial x_l}, u_i^1 = \chi_i^{kl}(y) \frac{\partial u_k^0}{\partial x_l} \qquad \text{(A.24)}$$

In equation A.24, σ_{ij}^{kl} is a Y-periodic function and χ_i^{kl} is a Y-periodic functions representing characteristic modes of the deformation in the RUC (three normal and three shear modes). Substituting equation A.24 into equation A.15-A.17 yields the microscopic constitutive relation as [16, 18]:

$$\sigma_{ij}^{kl}(y) = a_{ipjm}^{\varepsilon}[\delta_{kp}\delta_{lm} + \frac{\partial\chi_p^{kl}}{\partial y_m}] \qquad (A.25)$$

Where δ_{ij} is the Kronecker delta. The mean of the equation (2.31) yields the elastic modulus for the use of macroscopic analysis, in the form of:

$$a_{ijkl}^{H} = \left\langle \sigma_{ij}^{kl} \right\rangle_{Y} = \frac{1}{|Y|}\int_{y}\sigma_{ij}^{kl}\,dY \qquad (A.26)$$

a_{ijkl}^{H} - Homogenized elastic constant on the meso-scale

$|Y|$ - indicate the volume of the RUC

A.2.1   Periodic boundary conditions

As introduced in the above section, for a general textile composite unit cell the boundary conditions are completely periodic. This means that any displacement on one side must be the same on the opposite side plus or minus some constant [19]. Any periodic loading can be applied to the full unit cell with these boundary conditions. Since the distance between any one face and its opposite face is always constant after load has been applied, i.e. at equilibrium, the macroscopic displacement gradients of the unit cell can be calculated. These are given for the unit cell shown in Figure A-1:

$$\left(\frac{\partial u}{\partial x}\right)_0 = \frac{u_A - u_B}{a}; \left(\frac{\partial u}{\partial y}\right)_0 = \frac{u_A - u_C}{a}; \left(\frac{\partial u}{\partial z}\right)_0 = \frac{u_A - u_D}{c}; \qquad (A.27)$$

$$\left(\frac{\partial v}{\partial x}\right)_0 = \frac{v_A - v_B}{a}; \left(\frac{\partial v}{\partial y}\right)_0 = \frac{v_A - v_C}{a}; \left(\frac{\partial v}{\partial z}\right)_0 = \frac{v_A - v_D}{c}; \qquad (A.28)$$

$$\left(\frac{\partial w}{\partial x}\right)_0 = \frac{w_A - w_B}{a}; \left(\frac{\partial u}{\partial y}\right)_0 = \frac{w_A - w_C}{a}; \left(\frac{\partial u}{\partial z}\right)_0 = \frac{w_A - w_D}{c}; \qquad (A.29)$$

In the above equations, $AB = AC = a$ = width of the unit cell and $AD = c$ = unit cell height. Substituting equations (A.27), (A.28), (A.29) into the periodic conditions gives the following nine periodic boundary conditions (Table A-2). Using Table A-2, PBCs for any unit cell (half or quarter unit cell…) under extension and shear loading can be derived [20]. And the obtained PBCs are applied to the unit cell using equation command in ABAQUS®. By specifying the boundary conditions, as explained in the previous sections, it is possible to solve six boundary value problems of the unit cell (3 normal and 3 shear load cases).

Table A-2. **Summary of periodic boundary conditions for the unit cell.**

$x = \pm \dfrac{a}{2}$	$y = \pm \dfrac{a}{2}$	$z = \pm \dfrac{c}{2}$
$u(\frac{a}{2}, y, z) = u(-\frac{a}{2}, y, z) + u_A - u_B$	$u(x, \frac{a}{2}, z) = u(x, -\frac{a}{2}, z) + u_A - u_C$	$u(x, y, \frac{c}{2}) = u(x, y, -\frac{c}{2}) + u_A - u_D$
$v(\frac{a}{2}, y, z) = v(-\frac{a}{2}, y, z) + v_A - v_B$	$v(x, \frac{a}{2}, z) = v(x, -\frac{a}{2}, z) + v_A - v_C$	$v(x, y, \frac{c}{2}) = v(x, y, -\frac{c}{2}) + v_A - v_D$
$w(\frac{a}{2}, y, z) = w(-\frac{a}{2}, y, z) + w_A - w_B$	$w(x, \frac{a}{2}, z) = w(x, -\frac{a}{2}, z) + w_A - w_C$	$w(x, y, \frac{c}{2}) = w(x, y, -\frac{c}{2}) + w_A - w_D$

A.3.   REFERENCES

[1]   I.Temizer, *Micromechanics - Analysis of heterogeneous materials.* Institute of Mechanics and Computational Mechanics, Leibniz University of Hannover, 2007.

[2]   Yang, Q.-S. and W. Becker, *Numerical investigation for stress, strain and energy homogenization of orthotropic composite with periodic microstructure and non-symmetric inclusions.* Computational Materials Science, 2004. **31**(1-2): p. 169-180.

[3]   He, H., Y.C. Roth, and N. Himmel, *Elastic constants estimation of stitched NCF CFRP laminates based on a finite element unit-cell model.* Composites Science and Technology, 2007. **67**(6): p. 1081-1095.

[4]   Sun, C.T. and R.S. Vaidya, *Prediction of composite properties from a representative volume element.* Composites Science and Technology, 1996. **56**(2): p. 171-179.

[5]   Jean-sebastien gerard, S.c., Roger assaker, Julian santiago prowald, *Multi-scale modeling of triaxial woven fabric. application to satellite antenna.* e-Xstream engineering SA, Rue du Bosquet7, B-1348 Louvain-la-Neuve, Belgium.

[6]   Searles, K., G. Odegard, and M. Kumosa, *Micro- and mesomechanics of 8-harness satin woven fabric composites: I -- evaluation of elastic behavior.* Composites Part A: Applied Science and Manufacturing, 2001. **32**(11): p. 1627-1655.

[7]   Bogdanovich, A.E., *Multi-scale modeling, stress and failure analyses of 3-D woven composites.* Journal of Materials Science, 2006.

[8]   Pindera, M.-J., et al., *Micromechanics of spatially uniform heterogeneous media: A critical review and emerging approaches.* Composites Part B: Engineering, 2009. **40**(5): p. 349-378.

[9]   Rodriguez-Ramos, R., et al., *Closed-form expressions for the effective coefficients of a fiber-reinforced composite with transversely isotropic constituents - I. Elastic and square symmetry.* Mechanics of Materials, 2001. **33**(4): p. 223-235.

[10]   K.Tamma, K., P. W.Chung, and *Woven Fabric Composites-Developments In Engineering Bounds Homogenization and Applications.* International Journal on Numerical Methods in Engineering, 1999.

[11]   Takano, N., et al., *Microstructure-based evaluation of the influence of woven architecture on permeability by asymptotic homogenization theory.* Composites Science and Technology, 2002. **62**(10-11): p. 1347-1356.

[12]   Takano, N., et al., *The formulation of homogenization method applied to large deformation problem for composite materials.* International Journal of Solids and Structures, 2000. **37**(44): p. 6517-6535.

[13]   Zako, N.T.a.M., *Hierarchical modelling of textile composite materials and structures by the homogenization method.* Simul. Mater. Sci. Eng 1998.

[14]   Takano, N. and Y. Okuno, *Three-scale finite element analysis of heterogeneous media by asymptotic homogenization and mesh superposition methods.* International Journal of Solids and Structures, 2004. **41**(15): p. 4121-4135.

[15]   Byström, J., N. Jekabsons, and J. Varna, *An evaluation of different models for prediction of elastic properties of woven composites.* Composites Part B: Engineering, 2000. **31**(1): p. 7-20.

[16]   Kanouté, P., et al., *Multiscale Methods for Composites: A Review.* Archives of Computational Methods in Engineering, 2009. **16**(1): p. 31-75.

[17]   Aboudi, J., M.-J. Pindera, and S.M. Arnold, *Higher-order theory for periodic multiphase materials with inelastic phases.* International Journal of Plasticity, 2003. **19**(6): p. 805-847.

[18]   Ghosh, S., K. Lee, and P. Raghavan, *A multi-level computational model for multi-scale damage analysis in composite and porous materials.* International Journal of Solids and Structures, 2001. **38**(14): p. 2335-2385.

[19]   Chapman, C.D., *Effect of assumed Tow architecture on the predicted moduli and stress in woven composites* NASA Contractor Report 195310, 1994.

[20]   Whitcomb, J.D., C.D. Chapman, and X. Tang, *Derivation of Boundary Conditions for Micromechanics Analyses of Plain and Satin Weave Composites.* 2000. p. 724-747.